

# *Control and Operation of a Spinning Disc Reactor*

*by*

*Dena Ghiasy*

---

*Thesis submitted for the degree of Doctor of Philosophy  
in the Faculty of Science, Agriculture and Engineering  
of the Newcastle University*

---

*School of Chemical Engineering and Advanced Materials  
Newcastle University  
Newcastle upon Tyne, U.K.*

*December 2012*

## *Acknowledgements*

I owe my deepest gratitude to my supervisors, Dr Kamelia Boodhoo and Dr Ming Tham, for their support, guidance and encouragement throughout this project. The financial support provided by an EPSRC Doctoral Training Award is also gratefully acknowledged.

The assistance provided by the technical staff at SCEAM is sincerely appreciated. In particular, I would like to thank Mr. Brian Grover and Mr. Simon Daley for their valuable contributions regarding the setup and troubleshooting of the experimental apparatus.

I also wish to express my heartfelt gratitude to all my colleagues and friends in Newcastle and Singapore, for providing me with unfailing moral support and making my journey more worthwhile. Special thanks to Noushin, Kamelia and Jon for their companionship, good humour and uplifting optimism.

A special thought goes to my family for their enduring love, patience and understanding throughout my life. I am truly indebted to my parents for inspiring me to learn and to pursue my goals. I would also like to thank my uncle Shahram and his family for their unreserved support and motivations during the past few years.

Last but not least, to Lawrence who has been an enriching source of enthusiasm in my life and has continuously given me strength and hope, especially when the times were tough.

## *Abstract*

The aim of the present research is to assess the control and operation of a Spinning Disc Reactor (SDR), carried out via four separate investigations. Firstly, the effect of equipment size reduction on control is studied by comparing the performance of a PID controller applied to simulated intensified and conventional processes. It was found that superior control performance in terms of Integral of Absolute Error (IAE) is achieved for the simulated intensified system. However, the results showed that intensified systems are more susceptible to disturbances and the controlled variable exhibits larger overshoots. Furthermore, the frequency response analysis of the two systems showed that the simulated intensified system has reduced stability margins.

The second part of the research investigates the task of pH control in a SDR using a PID controller by means of simulation and experimental studies. The effectiveness of a disturbance observer (DO) and a pH characteriser to compensate for the severe pH system nonlinearity is also explored in detail. The experimental studies showed that a PID controller provides adequate setpoint tracking and disturbance rejection performances. However, sluggish transient responses prevailed and the effluent pH limit cycled around the setpoint. There were indications of unstable behaviour at lower flowrates, which implied more advanced control schemas may be required to adapt to various operating regions dictated by the complex thin film hydrodynamics. The addition of the DO scheme improved the control performance by reducing the limit cycles.

In the third segment of the investigations, the potential of exploiting the disc rotational speed as a manipulated variable is assessed for the process of barium sulphate precipitation. A PI controller is successfully used to regulate the conductivity of the effluent stream by adjusting the disc rotational speed. The results are immensely encouraging and show that the disc speed may be used as an extra degree of freedom in control system design.

Finally, the flow regimes and wave characteristics of thin liquid films produced in a SDR are investigated by means of a thermal imaging camera. The film hydrodynamics strongly affect the heat and mass transfer processes within the processing films, and thus the intensification aspects of SDRs. Therefore, effective control and operation of such units is significantly dependent on the knowledge of film hydrodynamics and the underlying impact of the operating parameters and the manipulated variables on a given process. The results provided an interesting insight and unveiled promising potentials for characterisation of thin liquid film flow and temperature profiles across the disc by means of thermographic techniques.

The present study reveals both challenges and opportunities regarding the control aspects of SDRs. It is recommended that equipment design and process control need to be considered simultaneously during the early stages of the future developments. Furthermore, intensified sensors and advanced controllers may be required to achieve an optimum control capability. Currently, the control performance is inhibited by the lack of sufficient considerations during the SDR design and manufacturing stages, and also by the characteristics of the commercially available instrumentation.

## ***Table of Contents***

Acknowledgements.....	i
Abstract.....	ii
List of Figures.....	vi
List of Tables.....	xi
<b>Chapter 1. Introduction</b>	<b>1</b>
1.1 Research Motivations.....	1
1.2 Aims and Objectives.....	2
1.3 Outline of the Approach and Methodology.....	3
1.4 Thesis Layout.....	6
<b>Chapter 2. Literature Review</b>	<b>8</b>
2.1 Process Intensification (PI).....	8
2.1.1 Principles and Design Strategies.....	9
2.1.2 Advantages of PI.....	12
2.1.3 Applications of PI.....	13
2.1.4 Barriers and the Future of PI.....	13
2.2 Spinning Disc Reactor.....	14
2.2.1 Operation.....	14
2.2.2 Features.....	15
2.2.3 Hydrodynamics of Thin Film Flow.....	17
2.2.4 Heat Transfer.....	19
2.2.5 Mass Transfer.....	20
2.2.6 Applications.....	21
2.3 Control of Process Intensified Systems.....	23
2.3.1 Potential Difficulties.....	23
2.3.2 Control of SDRs.....	26
2.4 pH Control.....	26
2.4.1 Difficulties in pH Control.....	27
2.4.2 pH Control Strategies.....	28
2.5 Precipitation Process.....	31
2.5.1 Precipitation of Barium Sulphate.....	32
2.5.2 Effect of Mixing.....	34
2.5.3 Effect of Residence Time.....	36
2.5.4 Intensified Reactors and Precipitation Processes.....	37
2.5.5 Control of the Precipitation Process.....	38
2.6 Thermographic Analysis of Thin Liquid Films.....	39
2.6.1 Thermographic Measurements.....	40
2.7 Summary.....	42
<b>Chapter 3. Preliminary Studies</b>	<b>44</b>
3.1 Controller Design.....	45
3.2 Model Order Reduction.....	46
3.2.1 Step Response.....	46
3.2.2 Frequency Response.....	47
3.2.3 Isaksson and Graebe's Method.....	49
3.2.4 Skogestad's Method.....	50
3.2.5 Maclaurin Series Expansion.....	51

3.2.6	Frequency Response Analysis of Reduced Models.....	52
3.3	Controller Performance .....	55
3.3.1	Assessment Criteria .....	56
3.3.2	Setpoint Tracking .....	57
3.3.3	Disturbance Rejection .....	59
3.3.4	Simulated Conventional versus Intensified Systems.....	61
3.4	Summary .....	63
<b>Chapter 4. Apparatus and Procedures</b> .....		<b>64</b>
4.1	Apparatus.....	64
4.1.1	Spinning Disc Reactor .....	65
4.1.2	Liquid Feed Arrangements .....	68
4.1.3	Temperature Control Units.....	70
4.1.4	SDR Control System .....	70
4.1.5	Feed and Product Vessels .....	71
4.1.6	Pumps .....	71
4.1.7	Sensors and Transmitter .....	72
4.1.8	Data Acquisition Devices .....	73
4.1.9	Matlab/Simulink Software.....	74
4.1.10	LabVIEW Software .....	75
4.1.11	Computer System .....	75
4.1.12	Thermal Imaging Camera.....	75
4.1.13	ThermaCAM Researcher Software .....	76
4.2	Procedures .....	76
4.2.1	Safety Evaluation.....	76
4.2.2	Implementation of Control Loops in LabVIEW .....	77
4.2.3	Conductivity Signal Conditioning.....	82
4.2.4	Implementation of pH Control Loop in Simulink .....	82
4.2.5	pH Control Experiments.....	84
4.2.6	Conductivity Control Experiments using the Rotational Speed.....	85
4.2.7	Thermal Imaging Experiments .....	86
4.3	Summary .....	90
<b>Chapter 5. pH Control</b> .....		<b>91</b>
5.1	Process Model .....	91
5.1.1	Titration Curve .....	91
5.1.2	Dynamic Model of the Process.....	92
5.2	Simulation Studies.....	95
5.2.1	Control Strategies .....	95
5.2.2	Optimal Disturbance Observer Design.....	99
5.2.3	Performance Evaluation .....	104
5.2.4	Disturbance Rejection Performances .....	105
5.2.5	Setpoint Tracking Performances .....	109
5.2.6	Robustness Assessment.....	113
5.3	Experimental pH Control .....	115
5.3.1	Control Loop Setup .....	115
5.3.2	Controller Tuning .....	116
5.3.3	Selection of DO Filter Time Constant.....	119
5.3.4	Performance Evaluation .....	121
5.3.5	Disturbance Rejection Performance .....	121

5.3.6	Setpoint Tracking Performance .....	123
5.3.7	Repeatability Assessment .....	125
5.3.8	Effect of Rotational Speed.....	127
5.4	Summary .....	128
<b>Chapter 6. Control using Disc Rotational Speed</b>		<b>130</b>
6.1	Input-Output Model.....	130
6.2	Control Loop Setup .....	133
6.3	Controller Tuning .....	134
6.4	Selection of DO Filter Time Constant.....	136
6.5	Setpoint Tracking Performance .....	137
6.6	Repeatability Assessment.....	138
6.7	Analysis of Results .....	142
6.7.1	System Constraint.....	142
6.7.2	Effect of Mixing .....	144
6.7.3	Effect of Residence Time .....	147
6.8	Summary .....	150
<b>Chapter 7. Thermographic Studies</b>		<b>152</b>
7.1	Effect of Flowrate and Rotational Speed .....	153
7.1.1	Water Films .....	153
7.1.2	Therminol SP Films.....	159
7.2	Effect of Viscosity.....	162
7.3	Effect of Disc Temperature .....	166
7.4	Effect of Feed Configuration.....	167
7.5	Effect of Heat of Reaction.....	170
7.6	Comparison with a Theoretical Model .....	172
7.7	Summary .....	177
<b>Chapter 8. Conclusions and Recommendations</b>		<b>179</b>
8.1	Conclusions .....	179
8.2	Recommendations for Future Work .....	182
Nomenclature.....		185
References.....		189
Appendices.....		199
Appendix A. PID Controller .....		199
Appendix B. Controller Design by Direct Synthesis Method.....		200
Appendix C. Controller Model Order Reduction by Maclaurin Series Expansion .....		202
Appendix D. Order Reduction for Simulated Intensified & Conventional Systems .....		203
Appendix E. pH Control Loop in Simulink .....		209
Appendix F. pH Control Loop in LabVIEW .....		213
Appendix G. Conductivity Control Loop in LabVIEW.....		216
Appendix H. Calculation of Diffusion Coefficient.....		218
Appendix I. Calculation of Activity Coefficient.....		219
Appendix J. Semi-Analytical Model of Barium Sulphate Precipitation .....		221
Appendix K. Therminol SP Properties .....		222
Appendix L. Presentations and Publications.....		223

## *List of Figures*

Figure 2-1. Process intensification components (adapted from ref. [9]) .....	9
Figure 2-2. SDR schematic [54] .....	15
Figure 2-3. Wave formation on a rotating surface at different angular velocities [16] .....	16
Figure 2-4. Schematic of forces exerted on a fluid element .....	18
Figure 2-5. Local liquid film heat transfer coefficient on smooth disc [16].....	20
Figure 2-6. Local mass transfer coefficients at various rotational speeds with water flow rate of 80 cm <sup>3</sup> /s [16].....	21
Figure 2-7. Mass transfer coefficients at the completion of the reaction [68].....	21
Figure 2-8. Example titration curves [87].....	27
Figure 2-9. Titration curves of samples taken from an industrial pH process during different upstream conditions [88].....	28
Figure 2-10. pH characteriser [23].....	30
Figure 2-11. Disturbance observer [19] .....	31
Figure 2-12. Morphology of barium sulphate at various initial supersaturations.....	33
Figure 2-13. Barium sulphate crystal size distributions [133].....	36
Figure 3-1. Closed-loop block diagram .....	44
Figure 3-2. Open-loop block diagram.....	47
Figure 3-3. Step response.....	47
Figure 3-4. Frequency Response.....	49
Figure 3-5. Conventional system Bode plots .....	54
Figure 3-6. Intensified system Bode plots .....	55
Figure 3-7. Closed-loop system with a PID <sup>2</sup> controller .....	56
Figure 3-8. Setpoint tracking performance for the simulated conventional system .....	57
Figure 3-9. Setpoint tracking performance for the simulated intensified system .....	58
Figure 3-10. IAE values for setpoint tracking performance .....	59
Figure 3-11. Disturbance rejection performance for the simulated conventional system .....	60
Figure 3-12. Disturbance rejection performance for the simulated intensified system .....	60
Figure 3-13. IAE values for disturbance rejection performance.....	61
Figure 3-14. Gain and phase margins .....	62
Figure 4-1. Experimental set up.....	65
Figure 4-2. Top view of the disc and heat transfer channels .....	66
Figure 4-3. Schematic diagram of the SDR .....	67
Figure 4-4. Reactor housing.....	67
Figure 4-5. Reactor lid .....	68
Figure 4-6. Single point injections.....	69
Figure 4-7. Distributor system .....	69
Figure 4-8. Schematic diagram of distributor system.....	69
Figure 4-9. Disc rotational speed calibration data .....	70
Figure 4-10. Peristaltic pump calibration data .....	71

Figure 4-11. Gear pump calibration data .....	72
Figure 4-12. pH probe.....	72
Figure 4-13. Conductivity probe [Courtesy of Mettler-Toledo].....	73
Figure 4-14. USB6211 .....	73
Figure 4-15. Simulink Library Browser.....	74
Figure 4-16. LabVIEW .....	75
Figure 4-17. IR camera setup.....	76
Figure 4-18. Data acquisition block diagram.....	77
Figure 4-19. PID controller VI.....	77
Figure 4-20. Unit conversion VIs .....	78
Figure 4-21. Write to Spreadsheet VI.....	78
Figure 4-22. DAQmx Timing (Sample Clock) VI.....	79
Figure 4-23. Simulation parameters configuration window .....	81
Figure 4-24. CD Convert Continuous to Discrete VI .....	82
Figure 4-25. Lookup Table block .....	83
Figure 4-26. pH control loop .....	83
Figure 4-27. Water film thickness profile.....	87
Figure 4-28. Therminol SP film thickness profile .....	88
Figure 4-29. Emissivity as a function of film thickness on polished stainless steel surface at 77K [156].....	88
Figure 4-30. Effect of emissivity on temperature measurement, $T_d=70^\circ\text{C}$ .....	89
Figure 4-31. Methods of evaluating emissivity .....	89
Figure 5-1 Schematic of pH control loop .....	91
Figure 5-2 Laboratory generated titration curve .....	92
Figure 5-3. Input-output data .....	93
Figure 5-4. Process model and experimental pH responses .....	94
Figure 5-5. Implementation of the process model .....	94
Figure 5-6. Feedback control scheme block diagram .....	95
Figure 5-7. pH Characteriser.....	96
Figure 5-8. Disturbance Observer: delay-free .....	97
Figure 5-9. Disturbance Observer (practical representation): delay-free .....	97
Figure 5-10. Disturbance observer: time-delay implementation 1 .....	97
Figure 5-11. Disturbance observer: time-delay implementation 2 .....	98
Figure 5-12. DO1 scheme, $\theta = 1\text{s}$ , $\tau_f = 18\text{s}$ .....	99
Figure 5-13. DO2 scheme, $\theta = 1\text{s}$ , $\tau_f = 18\text{s}$ .....	100
Figure 5-14. DO3 scheme, $\theta = 1\text{s}$ , $\tau_f = 18\text{s}$ .....	100
Figure 5-15. All DO cases with low order filters, $\theta = 1\text{s}$ , $\tau_f = 18\text{s}$ .....	101
Figure 5-16. All DO cases with low order filters, $\theta = 5\text{s}$ , $\tau_f = 18\text{s}$ .....	102
Figure 5-17. DO1 with low order filter, $\theta = 1\text{s}$ .....	103
Figure 5-18. DO1 with low order filter, $\theta = 5\text{s}$ .....	104
Figure 5-19. Characteriser mismatch.....	105



Figure 5-20. Disturbance rejection performance [ $\theta = 1\text{s}$ , direct synthesis] .....	106
Figure 5-21. Disturbance rejection performance [ $\theta = 1\text{s}$ , manual tuning] .....	106
Figure 5-22. Disturbance rejection performance [ $\theta = 5\text{s}$ , direct synthesis] .....	108
Figure 5-23. Disturbance rejection performance [ $\theta = 5\text{s}$ , manual tuning] .....	108
Figure 5-24. Setpoint tracking performance [ $\theta = 1\text{s}$ , direct synthesis] .....	110
Figure 5-25. Setpoint tracking performance [ $\theta = 1\text{s}$ , manual tuning] .....	110
Figure 5-26. Setpoint tracking performance [ $\theta = 5\text{s}$ , direct synthesis] .....	111
Figure 5-27. Setpoint tracking performance [ $\theta = 5\text{s}$ , manual tuning] .....	112
Figure 5-28. PI plus characteriser robustness .....	113
Figure 5-29. PI plus disturbance observer robustness .....	114
Figure 5-30. PI plus characteriser and disturbance observer robustness .....	114
Figure 5-31. pH control loop elements .....	116
Figure 5-32. Controller tuning [ $K_c = 0.15$ , $T_i = 0.3$ min, $T_d = 0$ ] .....	117
Figure 5-33. Controller tuning [ $K_c = 0.015$ , $T_i = 0.3$ min, $T_d = 0$ ] .....	118
Figure 5-34. Controller tuning [ $K_c = 0.023$ , $T_i = 0.708$ min, $T_d = 0$ ] .....	118
Figure 5-35. Controller tuning [ $K_c = 0.03$ , $T_i = 0.43$ min, $T_d = 0.11$ min] .....	119
Figure 5-36. Controller tuning [ $K_c = 0.025$ , $T_i = 0.43$ min, $T_d = 0.11$ min] .....	119
Figure 5-37. DO filter time constant selection [ $\tau_f = 1.8\text{s}$ ] .....	120
Figure 5-38. DO filter time constant selection [ $\tau_f = 18\text{s}$ ] .....	120
Figure 5-39. DO filter time constant selection [ $\tau_f = 180\text{s}$ ] .....	121
Figure 5-40. PID controller disturbance rejection performance .....	122
Figure 5-41. PID controller and disturbance observer disturbance rejection performance ...	122
Figure 5-42. PID controller setpoint tracking performance [IAE = 1,439] .....	124
Figure 5-43. PID controller setpoint tracking performance .....	124
Figure 5-44. PID controller and disturbance observer setpoint tracking performance .....	125
Figure 5-45. PID controller repeat run .....	126
Figure 5-46. PID controller and disturbance observer repeat run .....	126
Figure 5-47. PID controller disturbance rejection, disc speed = 1500 rpm .....	127
Figure 5-48. PID controller and DO disturbance rejection, disc speed = 1500 rpm .....	127
Figure 6-1. Schematic of conductivity control loop .....	130
Figure 6-2. Input-output data .....	131
Figure 6-3. Modelled and experimental data for the first two steps .....	132
Figure 6-4. Modelled and experimental data for the second two steps .....	132
Figure 6-5. Modelled and experimental data [ $k = -0.025$ ( $\mu\text{S}/\text{cm}$ )/rpm, $\tau = 15\text{s}$ , $\theta = 18\text{s}$ ] .....	133
Figure 6-6. Conductivity control loop elements .....	134
Figure 6-7. PI controller tuning [ $K_c = -34$ , $T_i = 0.25$ min] .....	135
Figure 6-8. PI controller tuning [ $K_c = -20$ , $T_i = 0.25$ min] .....	135
Figure 6-9. PI controller tuning [ $K_c = -10$ , $T_i = 0.25$ min] .....	136
Figure 6-10. DO filter time constant selection [ $\tau_f = 90\text{s}$ ] .....	136
Figure 6-11. DO filter time constant selection [ $\tau_f = 180\text{s}$ ] .....	137
Figure 6-12. PI controller setpoint tracking performance .....	137

Figure 6-13. PI controller plus disturbance observer setpoint tracking performance.....	138
Figure 6-14. Time-varying characteristics of the conductivity signal .....	139
Figure 6-15. Conductivity versus concentration (at 25°C) .....	139
Figure 6-16. Changes in conductivity due to variation of feed molar concentration .....	140
Figure 6-17. Barium sulphate particles build up on the disc .....	140
Figure 6-18. Effect of disc/probe cleanliness on effluent conductivity [0.01M feed].....	141
Figure 6-19. Effect of disc/probe cleanliness on effluent conductivity [0.1M feed].....	142
Figure 6-20. Conductivity versus disc rotational speed.....	143
Figure 6-21. Film thickness at various disc rotational speeds .....	144
Figure 6-22. Influence of disc speed on micromixing time constant.....	146
Figure 6-23. Residence time at various disc rotational speeds .....	148
Figure 6-24. Concentration versus time.....	148
Figure 7-1. Thermograms of water films at various operating conditions .....	154
Figure 7-2. Effect of feed flowrate and disc speed on water film temperatures.....	156
Figure 7-3. Effect of film thickness on water film temperatures.....	157
Figure 7-4. Effect of residence time on water film temperatures .....	157
Figure 7-5. Water film temperatures versus Fourier number .....	159
Figure 7-6. Thermograms of Therminol films at various operating conditions .....	160
Figure 7-7. Effect of feed flowrate and disc speed on Therminol film temperatures.....	161
Figure 7-8. Effect of film thickness on Therminol film temperatures.....	161
Figure 7-9. Effect of residence time on Therminol film temperatures .....	162
Figure 7-10. Therminol film temperatures versus Fourier number .....	162
Figure 7-11. Viscosity versus temperature data.....	163
Figure 7-12. Surface tension versus temperature data .....	163
Figure 7-13. Thermograms of water vs. water & Glycerol films .....	165
Figure 7-14. Effect of disc temperature on water film temperatures.....	166
Figure 7-15. Effect of disc temperature on Therminol film temperatures.....	166
Figure 7-16. Heat transfer efficiency versus disc temperature .....	167
Figure 7-17. Thermograms of water films for two different feed configurations .....	168
Figure 7-18. Thermograms of Therminol films for two different feed configurations .....	169
Figure 7-19. Effect of heat of reaction on film temperature .....	171
Figure 7-20. Water film temperature profiles .....	174
Figure 7-21. Water film temperature profiles .....	174
Figure 7-22. Therminol film temperature profiles.....	176
Figure 7-23. Therminol film temperature profiles.....	176
Figure A-1. Feedback control block diagram.....	196
Figure B-1. Closed loop block diagram.....	197
Figure D-1. Step response of the simulated conventional system.....	200
Figure D-2. Step response of the simulated intensified system.....	201
Figure D-3. Frequency response of the simulated conventional system.....	202
Figure D-4. Frequency response of the simulated intensified system.....	203

Figure E-1. Feedback control loop [PI controller].....	206
Figure E-2. Feedback control loop [PI controller plus pH characteriser] .....	207
Figure E-3. Feedback control loop [PI controller plus DO] .....	208
Figure E-4. Feedback control loop [PI controller plus pH characteriser and DO].....	209
Figure F-1. LabVIEW block diagram [PID controller].....	210
Figure F-2. LabVIEW block diagram [PID controller plus DO].....	211
Figure F-3. LabVIEW front panel.....	212
Figure G-1. LabVIEW block diagram [PI controller].....	213
Figure G-2. LabVIEW block diagram [PI controller plus DO].....	214

## *List of Tables*

Table 2-1. Response time of loop elements (adopted from ref. [3]).....	24
Table 3-1. Control loop elements.....	52
Table 3-2. Original and reduced order models .....	53
Table 3-3. Controller parameters .....	56
Table 4-1. DAQ specifications .....	74
Table 4-2. DAQ VIs.....	78
Table 4-3 Operating conditions .....	86
Table 4-4. Emissivity of lubricating oil [171] .....	88
Table 5-1. PI controller tuning parameters (direct synthesis).....	96
Table 5-2. DO filter design .....	98
Table 5-3. Disturbance rejection IAE values ( $\theta = 1s$ ) .....	107
Table 5-4. Disturbance rejection IAE values ( $\theta = 5s$ ) .....	109
Table 5-5. Setpoint tracking IAE values ( $\theta = 1s$ ) .....	111
Table 5-6. Setpoint tracking IAE values ( $\theta = 5s$ ) .....	112
Table 5-7. Ziegler-Nichols tuning method.....	118
Table 6-1. Induction times .....	147
Table 6-2. Chemical conversion times.....	149
Table 7-1. Physical properties at 40°C and 1bar.....	153
Table D-1. Control loop elements.....	200
Table I-1. Individual ion values in an aqueous solution at 25°C.....	216
Table J-1. Simulation parameters.....	218

# Chapter 1. Introduction

Process Intensification (*PI*) is one of the contemporary concepts in the field of chemical and process engineering, which aims to revolutionise the process industry by introducing a paradigm shift, wherein new products and processes are invented to meet the market needs. Amongst many developments in the past few decades, the Spinning Disc Reactors (SDR) is one of the most prominent examples of process intensification with widely demonstrated capabilities and unique features. However, despite abundant research on intensification aspects of SDRs, such as improvements in yield and selectivity as well as reductions in processing time, very little has been done on devising appropriate control schemas for such devices. The present research is focused on investigating the operation and control aspects of SDRs by means of simulation and experimental studies.

The present chapter highlights the driving forces for undertaking the research along with the aims and objectives of the project. This contribution covers several subject areas, as discussed later in this chapter. Finally, an outline of the thesis is provided to conclude the introduction chapter.

## 1.1 Research Motivations

The literature available in the field of process intensification is exceptionally rich, as outlined in several text books published on the subject [1-3]. In the past three decades numerous studies on feasibility of the design concepts and the potential applications of the process intensifying methods and equipment have been carried out, including a number of industrially adopted technologies such as reactive distillation [4] and microreactors [5]. It is expected that challenges in operation and control of some *PI* technologies, such as multifunctional equipment, may arise due to their increased level of complexity and interactions within the system. Furthermore, control and operational difficulties may prevail due to the fast dynamics and high responsiveness of miniaturised *PI* equipment.

There is a significant amount of research on control aspects of the reactive distillation process, as outlined in a recent review by Sharma and Singh [6]. This is attributed to the fact that the reactive distillation technology has been adopted for several industrial applications [7]. Nikacevic et al. [8] review the available work on control of intensified equipment including reactive distillation, divided wall columns and microreactors. However, the field of process control for intensified systems is currently far from a mature state and deserves more research attention.

Nikacevic et al. [8] state that full integration of process design, operation and control in the earliest phases of the conceptual design is an essential part of the future developments in the field of process intensification. Furthermore, there is concern that the commercially available controllers, sensors and actuators may not be compatible with *PI* equipment. Therefore, novel sensors capable of obtaining online measurements of fast changing process

variables, in systems that are either miniaturised or have complex multifunctional structures, in conjunction with faster, more advanced controllers may need to be developed.

The present research investigates the operation and control aspects of a spinning disc reactor, as an example of miniaturised reactor technology. A PI/PID controller coupled with commercially available sensors and actuators is used to achieve the control objectives. The current research evaluates the challenges and limitations that may be encountered in operation and control of low volume *PI* equipment using the available instrumentation and commonly used control schemes, as outlined in the following sections.

## ***1.2 Aims and Objectives***

The primary focus of the present study is to investigate the control and operational aspects of miniaturised intensified equipment, in particular spinning disc reactors. The research involves both simulation and experimental studies aimed at a number of areas which have not received a great deal of research endeavours so far. This contribution is expected to shed more light on the selected subjects and also to promote additional research interest in the area of control of intensified units. The current research may be categorised into four groups:

- 1) Preliminary studies
- 2) pH control
- 3) Control using the disc rotational speed
- 4) Thermographic analysis of thin liquid films

The preliminary studies involve an illustration of the potential impacts of intensification in general on process control by means of simulation. Process intensification is often defined as a major reduction in equipment size, without compromising the throughput, which is afforded by improvements in processing efficiency and performance [9]. This major reduction in size, whilst keeping the production capacity constant, means that the residence times of intensified units are much smaller than those of their conventional counterparts. For instance the residence time in a stirred tank reactor may be tens of minutes whereas the residence time in a smaller volume SDR for the same production capacity could be just a few seconds. This implies that intensified equipment have faster dynamics and are more responsive to process disturbances. The aim of the preliminary studies is to emphasise the impact of equipment size reduction on control by means of simulation.

The objective of the pH control studies is to assess the control and operation of a SDR when it is used as a neutralisation reactor. A PID controller is coupled with commercially available instrumentation to regulate the pH of the effluent stream by manipulating the reagent flowrate. At present, process control and equipment design are not considered simultaneously during the conceptual design of SDRs, thus the effectiveness of a control strategy is inhibited by the limitations in SDRs design and also by the characteristics of the available instrumentation. The pH control studies aim to highlight the potential challenges of controlling a fast dynamic intensified unit by means of conventional control system design.

It is known that some intensified equipment offer an extra degree of freedom in their design, which may be exploited to transform the way process equipment are operated and

controlled. For instance, the disc rotational speed in a SDR is a readily controllable parameter, which has an influence on the liquid residence time on the disc, as well as the mixing intensity within the thin liquid films. Therefore, adjusting the disc rotational speed could influence conversion, selectivity, or particle size. This presents a new prospect to achieve a given control task by manipulation of the disc speed, rather than the conventional methods of adjusting the flowrate for example. The objective of the third phase of the present research is to assess the feasibility of the described control approach in a SDR for an example process.

The hydrodynamics of thin liquid films on rotating surfaces have been studied experimentally [10-12] and by means of modelling [13, 14]. The heat transfer performances from rotating surfaces to thin liquid films have also been studied [15, 16] by previous researchers. It is expected that the thin film flow regime and the characteristics of the surface instabilities strongly influence the mass and heat transfer processes within the thin processing films, and thus the process intensifying features of the SDRs. Therefore, characterising the operating conditions which give rise to the desired flow regimes and surface waves is a critical consideration for optimal operation and control of processes in SDRs. In the present work a novel approach for studying the liquid film hydrodynamics and hence the heat transfer performance of SDRs is proposed by means of an infrared camera. The objective of the final section of the present research is to determine the relative merits and the practicality of using thermographic measurements of thin liquid films to define the desired operational window and consequently improve process control.

### ***1.3 Outline of the Approach and Methodology***

As mentioned previously the control investigations are carried out by means of simulations and experimental studies. The simulations are performed using Matlab/Simulink, whilst the experimental feedback control runs are carried out in a laboratory/industrial scale SDR unit coupled with commercially available instrumentation. Throughout the present work when process control is concerned, some form of a PID controller is adopted to achieve the control task. This is because PID controllers are the most widely used controllers in industry, with proven reliability and robustness. Further, PID controllers are often well understood and readily tuned by the plant operators due to their simplicity.

However, the philosophy of using the most widely used controller was not to simplify the investigations. Rather, it was believed that achieving a challenging control objective in a SDR by means of a commonly used controller, combined with conventional sensors and actuators could help the industrial acceptance of such units. The industry's conservatism has been identified as one of the barriers to hamper the adaptation of intensified equipment [17]. Therefore, it can be imagined that the commercial viability of such equipment could be hindered if they have to be coupled with complex control algorithms and/or sophisticated instrumentation to achieve a control task. Nevertheless, the work does not try to project PID controllers as the only solution and degrade the importance and applicability of the numerous advanced control strategies developed over the past few decades. The proposed approach will enable identification of any potential challenges/limitations that may be encountered for

control of fast dynamic systems using the most commonly used controller and instrumentation.

The PID controller for the online tests is implemented using the LabVIEW software on a PC running Windows Vista. Therefore, a software controller is used to control a hardware plant. This method may be favoured in many applications where the high cost of real-time operating hardware controllers is not justified, and/or when more flexibility to manipulate the controller algorithm is desired. In the present study a combination of these two factors were at play, which led to the adopted rapid control prototyping approach.

The opportunity of including a ‘Disturbance Observer’ (DO) scheme [18] in addition to the PID controller which could, in theory, improve the control performance presented an interesting prospect. The DO scheme is designed to estimate the disturbances affecting the system and subsequently eliminate them. The DO was initially applied to mechatronic systems, but more recent literature [19, 20] suggested that the control performance in chemical processes may also benefit from the scheme. Furthermore, simulation studies in previous research [21, 22] have shown that DOs can mitigate the undesired effects of the system nonlinearity. Therefore, the DO approach could be well suited to the intensified units where the reduced equipment size means that the system might be more responsive, and thus more susceptible to disturbances. The system nonlinearity observed in a pH process as well as many other industrial processes makes further investigation of DOs of great interest. To the best of the author’s knowledge no online implementation of a DO scheme for a chemical process has been carried out, whilst the previous research have mainly focused on simulations and theoretical aspects of the strategy. Thus, further experimental investigation of DOs seems to present an attractive research opportunity with potential contributions not only to intensified systems but also to the field of process control in general. Therefore, the performance of the DO scheme coupled with a PID controller is assessed as part of control investigations in a SDR. Another approach to compensate for the nonlinear characteristics of a pH process, namely the inclusion of a pH characteriser [23], is also investigated by means of simulations.

The commonly used model based PID tuning methods are often based on a first or second order process model whilst the instrumentation dynamics are negligible in comparison to the process. However, since for an intensified system, the process, sensors and actuators have dynamics of the same order of magnitude, the overall process model tends to be represented by a high order dynamic model. As part of the preliminary studies a number of model order reduction techniques are outlined to approximate the overall plant model by a lower order transfer function. The relative merits and accuracy of the listed techniques are examined by means of frequency response analysis, as part of the preliminary studies carried out in this work.

The second segment of the research looks at a specific control task in a SDR. For this part the pH control in neutralisation reaction of a strong acid (HCl) and a strong base (NaOH) is considered. The control objective, which is to maintain the pH of the effluent stream at the neutral point of 7, is achieved by manipulating the flowrate of the base stream in a feedback control loop structure. A number of factors led to the selection of the named control problem.



Firstly, the neutralisation reaction is inherently fast and is suited to the short residence times in a SDR. Further online measurements of pH can readily be achieved by means of a pH probe and transmitter. Additionally, pH control is selected as it is widely recognised as a challenging control task, mainly due to the severe system nonlinearity characterised by the S-shaped titration curve [24]. Also, if it can be shown that solving a difficult control problem such as pH control in a SDR is achievable, it would imply that less challenging control tasks may also be readily accomplished by the same approach. The pH control investigations commence by carrying out an experimental input-output test to characterise the overall system dynamics, wherein step changes in the base flowrate are introduced and the corresponding changes in the effluent pH are recorded. This input-output model, which approximates the behaviour of the actuator, process and measurement device, provides a platform for simulating the control performance.

The neutralisation reaction which facilitated the pH control investigations did not show a great deal of sensitivity to the disc rotational speed, thus a number of other processes were screened in search of an appropriate reaction. The precipitation reaction between barium chloride and sodium sulphate which produces barium sulphate particles was identified as a suitable candidate for the purpose of the current investigations. The precipitation reaction is known to be intrinsically fast and often only limited by the mixing characteristics of the crystallizer [25]. Therefore, it is well suited for carrying out in a SDR where short residence times and enhanced mixing characteristics prevail.

As the precipitation reaction proceeds, the reacting ions are removed from the solution to form the barium sulphate precipitates and no longer contribute to the solution conductivity. Hence, concentration and conversion can be inferred from conductivity measurements of the input and output streams. The conductivity signals can be readily obtained online and provide a feedback signal for establishing a closed loop control. Additionally, previous research has shown that fine barium sulphate particles of 0.7  $\mu\text{m}$  diameter with a narrow particle size distribution can be produced on a spinning disc reactor [26]; therefore, examining some control aspects of this process seems appropriate. In the third phase of the current study the precipitation reaction between barium chloride and sodium sulphate is carried out on the experimental SDR whilst the conductivity of the product stream is controlled by adjusting the disc rotational speed. If successful, the results will prove that the innovative control approach of using the disc rotational speed as manipulated variable can be utilised in practice.

The final segment of the present research involves the thermographic analysis of heating thin liquid films in a SDR. It is well established that many chemical processes are temperature-dependent to varying extent. The direct and invasive methods of measuring the liquid film temperature on rotating surfaces are often not preferred. This is because slight disturbances induced, for instance, by inserting a thermocouple on the disc top surface, could lead to breakage of the thin liquid films and consequently impede the heat and mass transfer capabilities of SDRs. Therefore, in most currently available SDRs the film temperature is inferred from indirect measurements such as the disc temperatures or the temperature of the heating media. It is assumed that the thin highly sheared films get up to the disc temperature very quickly as they flow towards the disc edges. If this assumption does not hold true the

implications in terms of reaction rate, performance and also process control could be significant. Thermal imaging cameras provide a non-invasive method of temperature measurement which is well suited for studying thin liquid films. Therefore, as part of this study the temperature profiles across the heating liquid films are examined by means of a thermal imaging camera to gain a better understanding of the mechanisms involved.

In addition to analysis of the temperature profiles across thin liquid films at various operating conditions, the corresponding film hydrodynamics may also be investigated using thermographic techniques. The film flow regime and the surface wave characteristics are known to significantly influence the intensification aspects of SDRs. Therefore, defining an operational envelope which leads to the desired film hydrodynamics is greatly beneficial for operation and control of SDRs. It is worth pointing out that the two manipulated variables considered in this study, namely the feed flowrate and the disc rotational speed, invariably alter the characteristics of thin film flow and the surface waves. Therefore, since the controller command directly influences the film hydrodynamics, and thus the intensification capability of SDRs, it is essential to define the thin film flow characteristics with respect to the operating parameters and manipulated variables, as enabled by the thermographic images.

## ***1.4 Thesis Layout***

This chapter introduced the principal research motivations, the aims and objectives of the work along with the approaches for carrying out the investigations. The next chapter provides a critical review of the literature available on the prime topics of the present research. The literature survey includes a review of the concept of process intensification with more attention focused on spinning disc reactors. The challenges and control strategies for pH control are then discussed in more detail. An overview of barium sulphate precipitation process is then provided, followed by some notes on the theory of thermography and its potential applications.

The results and discussion of the preliminary investigations into the control of fast dynamic equipment together with a number of PID tuning approaches for high order systems are provided in Chapter 3. The apparatus used to carry out the research which includes software platforms and hardware components are described in detail in Chapter 4. Additionally, the procedures employed to perform the simulations and the experimental investigations are also outlined in the same chapter.

The simulation and experimental results of the pH control in a SDR are presented and discussed in Chapter 5, whereby the application of two nonlinear compensation methods (pH characteriser and DO) are studied via simulation and one method (DO) is also implemented online. The results of the feedback control experiments, where the aim is to maintain the conductivity of the effluent stream in barium sulphate precipitation process using the disc rotational speed, are provided in Chapter 6. Detailed analysis and discussion of the results obtained are also presented in the same chapter.

Chapter 7 presents the results and discussion of the thermographic studies which provide an interesting insight into the hydrodynamics of thin liquid films along with the interactions

of the film temperature profiles with the operating parameters. Finally, the conclusions and recommendations for future investigations are presented in Chapter 8.

## Chapter 2. Literature Review

The objective of the present chapter is to provide some background information and to familiarise the reader with the relevant advances in the subject literature. This chapter begins with a review of process intensification (*PI*) including the drivers behind the development, the resulting benefits, the barriers and the future work required for full implementation of *PI* technologies on an industrial scale. Then the features and applications of spinning disc reactors (SDRs), as a classic example of process intensification and the main focus of the present research, are discussed in more detail.

Later in this chapter, the potential issues regarding the operation and control of process intensified systems are outlined. In the current study, two processes namely pH control in a neutralisation reaction and conductivity control in a precipitation reaction are selected to evaluate the control aspects of SDRs by simulation and by experimental trials. Therefore a literature survey concerning the aforementioned processes is necessary to summarise the mechanisms and challenges involved as well as the commonly used control strategies.

Chemical processes, especially reaction systems, are often affected by the operating temperature. Furthermore, the liquid film hydrodynamics and surface characteristic in SDRs significantly influence the heat and mass transfer processes. Therefore the operation and control of SDRs may be directly influenced by the film hydrodynamics and temperature profiles. In this work a thermal imaging camera is used to study the surface temperatures and the hydrodynamics of thin liquid films at various operating conditions. Therefore, an introduction to thermographic measurement techniques is also provided at the end of this chapter.

### 2.1 Process Intensification (*PI*)

Process intensification was pioneered by Colin Ramshaw and his colleagues at ICI in the late 1970s [3], and currently seems to be one of the most significant trends in chemical and process engineering, as evidenced by the increasingly large number of literature sources that have appeared on the subject in the last decade [1, 3]. Various definitions of *PI* have been proposed, with a common emphasis on development of “novel” technologies, which lead to “substantial” improvements. Stankiewicz and Moulijn [9] offer the following definition:

“Process intensification consists of the development of novel apparatuses and techniques that are expected to bring dramatic improvements in manufacturing and processing, substantially decreasing equipment-size/production-capacity ratio, energy consumption, or waste production, and ultimately resulting in cheaper, sustainable technologies”

Significant developments in the field of *PI* along with some very encouraging results have been achieved over the past few decades. Nevertheless, there are still some barriers that may need to be overcome if *PI* is to emerge as a fully developed technology [9, 17, 27-30].

### 2.1.1 Principles and Design Strategies

The main objectives of intensification strategies are to maximise efficiency and remove any heat/mass transfer limitations in order to greatly increase the rate of physical and chemical processes. Stankiewicz and Moulijn [9] divide the *PI* concepts into two main areas: a) process-intensifying equipment and b) process-intensifying methods as shown in Figure 2-1.

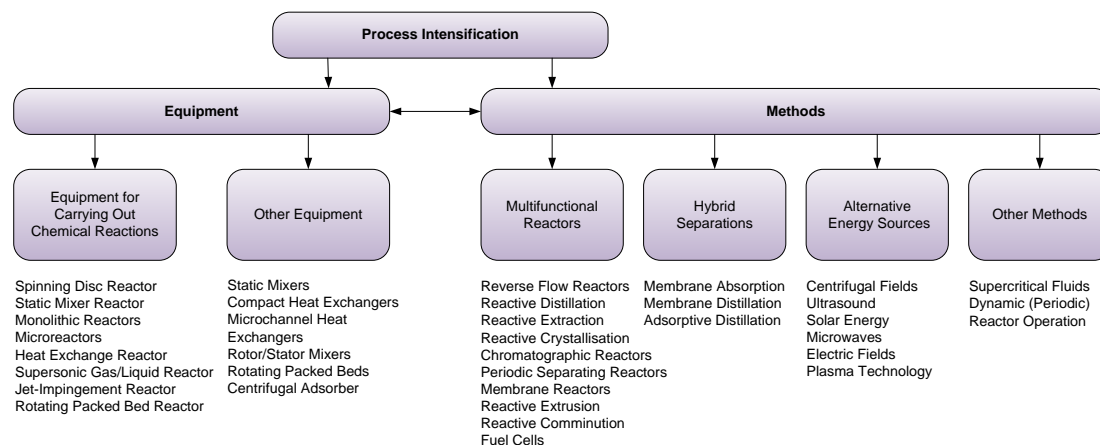


Figure 2-1. Process intensification components (adapted from ref. [9])

Some of such novel process-intensifying equipment and methods, for instance, rotating packed beds [31], reactive distillation [4] and microreactors [5] have been fully developed and commercialised, whilst others are still in a premature phase and require more research and development. Some of the most common *PI* design strategies are briefly outlined next.

#### 2.1.1.1 Multifunctional Units

Process intensification may be achieved by combining a number of unit operations into one so-called multifunctional unit, which commonly involves integration of reaction with at least one more function such as heat transfer or separation. The potential advantages of combining a number of unit operations into one unit include enhanced reaction rates, increased conversion/selectivity, reduced energy consumption and capital cost [3]. However, there are a number of disadvantages involved in the commercialisation of such units, which include, for instance, significant development costs, increased scale-up risks and increased operational complexity [3].

#### 2.1.1.2 Alternative Sources of Energy

Alternative sources and forms of energy have been identified to intensify chemical and biochemical processes, some of which are discussed below. Stankiewicz [32] provides more details of enhancement by means of alternative sources of energy.

*a) Energy of High-Gravity Fields*

A wide range of industrial processes involve handling multiphase systems, such as distillation, condensation, and fluidisation. The fluid dynamic behaviour of such systems is controlled by the buoyancy term ( $\Delta\rho g$ ), where  $\Delta\rho$  denotes density difference and  $g$  the acceleration due to gravity. Applying higher accelerations (typically 1000g) increases the buoyancy force, which results in thinner films and smaller bubbles [3]. Rotating packed beds and spinning disc reactors, also referred to as HiGee devices, are examples of novel equipment which exploit centrifugal force to drastically enhance heat and mass transfer performances. HiGee technologies are often only suitable for fast processes due to the typically short residence times. More details of the mechanism involved and characteristics of thin films are provided later in this chapter.

*b) Energy of Electric Fields*

Ptasinski and Kerkhof [33] provide a review of electric field applications to enhance separation processes. It is suggested that applying an electric field to multiphase systems interacts selectively with the interface, creating turbulence within and around the dispersed phase. Furthermore, the use of electric fields can also result in bubble disengagement or rupture, thus increasing the interfacial area available for transfer. These factors result in significant mass transfer enhancements. Electric field driven separation processes are expected to be much more energy efficient than the conventional thermal or mechanical counterparts due to the selective nature of electric stresses. A study on falling film and spray evaporation [34] showed that application of electric fields can result in up to seven-fold enhancement of the heat transfer coefficient. The augmented heat transfer observed was due to the formation of thin liquid films, small liquid droplets and surface waves as a result of applied electric stresses.

*c) Energy of Electromagnetic Radiation (Microwaves and Light)*

The exceptionally rich literature available on microwave processing suggests that microwave radiation is an alternative source of energy which may be used to provide direct and rapid means of supplying heat via dipole rotations and ionic movements on the irradiated medium. It has been reported [35] that microwave processing also accelerates organic reactions and, in some cases, increases the product yield. The large scale application of the technique, however, is scarce due to existing barriers and limitations, such as problems with scale up due to the low penetration depth of microwaves. Light may also be used to intensify processes by potentially increasing selectivity [36], and also by decreasing the non-renewable energy consumption due to exploiting solar light [37].

*d) Energy of Acoustic Fields*

Exposing liquid phase systems to ultrasound results in cavitation phenomena, in which bubbles (cavities) form, grow and subsequently collapse. The implosions of micro bubbles lead to large amounts of local energy being released and generation of local hot spots (high

temperature and pressure). It has been established that energy of sound increases the rate of formation of free radicals [38] and also enhances mass transfer and reaction rates in liquid-solid systems [39]. Nevertheless, as with the application of microwave and light, there are still barriers impeding the feasibility of large scale designs. The limitations include equipment erosion due to cavitation and the small penetration depth of acoustic waves.

### 2.1.1.3 Passive Enhancements

Passive techniques used to intensify heat and mass transfer are those which require no direct application of power, such as extended surfaces (fins) and static mixers. Extended surfaces are known to significantly enhance heat transfer in gas phase systems by increasing the heat transfer area available [3]. Static mixers are typically in the form of tube inserts, which promote mixing and heat/mass transfer by continually disrupting the flow streamlines [3]. It can be argued, however, that static mixers cannot strictly be considered as passive enhancement devices with no additional energy input because they often result in increased pressure drops compared to an empty tube [40].

### 2.1.1.4 Moving from Batch to Continuous Processing

A *PI* philosophy is also to move from batch to continuous processing as this enables residence times to be matched to the desired reaction times. Clear benefits of continuous processing generally include reduced equipment size, capital and operating cost savings, increased efficiency, better control of process variables, enhanced process safety, less scale up issues and lower levels of waste [41]. However, the uptake of continuous processing has been slow in the pharmaceutical and fine chemicals sectors. The reasons for this include the potential development cost and plant flexibility implications, as continuous equipment are more specialised than batch, and interruptions to one part of a continuous process can impact on the entire production sequence [42].

### 2.1.1.5 Minimising Diffusion/Conduction Paths

Minimising diffusion/conduction path length is proven to enhance heat and mass transfer performances drastically. This concept is the basis of microscale technologies which allow the reactions to be performed under more aggressive conditions, resulting in higher yields and selectivities [43, 44]. The fluid behaviour in such devices is dominated by laminar flow, wherein diffusion is the only mixing mechanism. Rapid mixing and excellent thermal management in microscale devices are attributed to their significantly increased specific surface area (of the order of  $30,000 \text{ m}^2/\text{m}^3$ ) compared to that of conventional and larger equipment [44]. Microreactors can achieve complete mixing in microseconds, whilst heat transfer coefficients as high as  $25 \text{ kW}/\text{m}^2\text{K}$  are also possible [44]. Pennemann et al. [45] compare the performances of both microflow devices and the conventional equipment across a wide range of processes and throughputs, outlining the enhanced performance and efficiency of microscale technologies.

## 2.1.2 Advantages of PI

The benefits of *PI* may be categorised into three groups: *business, process and environment*, as discussed below.

### 2.1.2.1 Business

*PI* can be advantageous from a business vantage point, as plant miniaturisation could result in major savings in capital (e.g. piping, support structures, land) and operating (e.g. utilities, labour, waste stream processing) costs. Furthermore, desktop plants may enable distributed manufacturing, resulting in transport cost savings and improved safety, especially for highly reactive and toxic materials such as cyanide and peroxides [3].

It is sometimes required to test a new product at laboratory, pilot and industrial scales before it can be introduced to the market. *PI* can provide the opportunity for several extra years of production, by eliminating these scale-up stages. This is because continuous intensified equipment used for laboratory trials may well be capable of full scale production. This is particularly beneficial to the pharmaceutical sector, as it can maximise the profitable manufacturing period, before the patent life of a new product expires. Adopting *PI* principles in order to move towards sustainable processing could also improve the corporate image in the eyes of the general public [1, 3]

### 2.1.2.2 Process

In intensified processes yield, selectivity and conversion of the desired reaction is improved, hence product purity is enhanced and the need for an expensive sequence of downstream processing is reduced. Such improvements may also lead to a reduction in energy consumption [46] and waste disposal costs. Moreover, significantly smaller equipment size implies that the inventories of hazardous substances are dramatically reduced, hence improving the intrinsic safety of the process. Further, the number of process operations can also be reduced by designing novel multifunctional equipment, leading to less pipe work and hence reduced potential sources of leakage. However, the inherent safety of some *PI* technologies has been disputed in some studies as discussed in section 2.1.4.

In conventional processing, the operating temperatures and pressures as well as the reagent concentrations are often not at optimal values, due to limiting capabilities of the system, such as poor mixing and inefficient energy transfer. In contrast, heat and mass transfer coefficients in intensified systems are dramatically enhanced enabling wider and more economic processing conditions to be applied [47]. Thus, for instance, more concentrated solutions of reagents can be applied in microreactors [48] or spinning disc reactors [49] whilst still being able to efficiently control the process by removing the additional heat of reaction quickly, due to the high surface area per unit volume in these units.



### 2.1.2.3 Environment

Small plants occupy a reduced area of land and are less obtrusive on the landscape. Additionally, as mentioned previously, the improved chemistry of a process may lead to significant reductions in energy and solvent usage. Moving from batch to continuous processing also offers potentials for energy savings; for example the energy losses are reduced due to shorter processing times and there is more scope for heat recovery. Reductions in energy usage lead to reductions in greenhouse gas emissions and more sustainable processing. Moreover, due to improved product yield and reduced solvent usage, the amount of waste produced can be dramatically reduced [1, 3].

### 2.1.3 Applications of *PI*

Numerous applications of *PI* across a wide range of industries have been documented in the literature. Some technologies have been successfully demonstrated at industrial scale, whilst others remain research projects with potentials. Chapters 8 to 11 of the textbook by Reay et al. [3] catalogue the *PI* application areas in various sectors including:

- Bulk chemicals
- Fine chemicals/ pharmaceuticals
- Offshore processing
- Nuclear industry
- Food and drink
- Textiles
- Metals
- Glass and ceramics
- Effluent treatment
- Power generation

The applications concern intensified equipment such as HiGee units, static mixers, oscillatory baffle reactors, as well as novel processing methods. Applications of spinning disc reactors are discussed later in section 2.2.6.

### 2.1.4 Barriers and the Future of *PI*

Although intensified systems are cheaper, safer, and more efficient than their conventional counterparts there are a number of technical and non-technical obstacles [1, 17] which need to be overcome in order to speed up the adoption of *PI* in industry. The non-technical barriers include industries' conservative culture and limited awareness of *PI* whilst the technical barriers include, for example, the lack of design codes for intensified equipment. Furthermore, some *PI* technologies are not fully developed, and feasible designs for the full production scales are yet to emerge.

Despite the governing view that *PI* technologies are inherently safer, there are a number of studies which suggest otherwise, posing an additional hurdle to adaptation of such

technologies. For instance, it is suggested that safety issues may arise for *PI* technologies which involve high-energy inputs such as microwaves and electromagnetic radiation [50]. Also due to small hold ups in some intensified units, disturbances can cause rapid changes within the process which may lead to safety constraints being approached rapidly [51]. Reaction runaway due to operating at more severe operating conditions [52] and the risk of explosive atmospheres in microreactors [53] have also been identified as potential hazards.

The following future developments are some examples which could mitigate both technical and nontechnical barriers to *PI*:

- Raise awareness of *PI* through conferences, publications and universities.
- Involvement and support of governments in development and commercialisation of *PI* technology.
- Collaboration of chemical engineers, chemists and scientists.
- Development of tools, such as design codes, to enable simulation and design of *PI* equipment.
- Design of a wider range of technically and economically feasible, large scale novel equipments.
- Allocate more research efforts to areas which have received the least attention, but may be of critical importance, such as control and operation of intensified units.

## ***2.2 Spinning Disc Reactor***

Spinning Disc Reactors are classic examples of process intensification [54]. Although abundant experimental work is available in the literature on intensification aspects of SDRs, as discussed next, very little has been done on devising appropriate control strategies for the unit. Since the present work is focused on operation and control of a SDR the subsequent sections are dedicated to a discussion on the operating principles, characteristics, mass/heat transfer performance and applications of SDRs.

### ***2.2.1 Operation***

The general operating principle of SDRs is to generate high acceleration environments by rotating a disc surface using a motor. The spinning disc is typically a horizontally mounted plate which may have a smooth, textured or grooved surface. The liquid feed streams are pumped into a well in the centre of the disc, which acts as a reservoir system to enable uniform distribution of the feeds across the disc surface. Under the action of high centrifugal fields, the liquid travels rapidly towards the disc edges and forms a very thin, highly sheared film. At the disc periphery the liquid is thrown out and hits the stationary walls of the reactor housing. An example of a SDR is schematically presented in Figure 2-2.

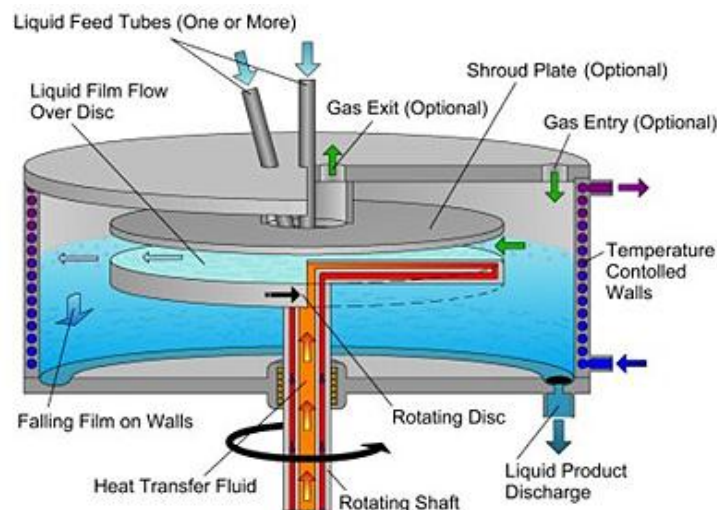


Figure 2-2. SDR schematic [54]

The disc may contain internal channels for flow of a heat transfer fluid, providing heating or cooling. For example, the heat transfer fluid may be delivered to the centre of the bottom surface of the disc through an internal pipe within the rotation shaft. The heating/cooling fluid moves towards the disc edges and exits the chamber before it gets recirculated through the system via a temperature controlled bath. The stationary reactor housing may have the facility for one or more liquid feed streams and perhaps an optional gas inlet/outlet. Provisions for purging the system with an inert gas may also be incorporated in the reactor set up. The walls of the reactor housing may be cooled to rapidly remove any excess heat from the product, in order to stop further reactions taking place before product collection.

## 2.2.2 Features

The key features of the SDR, which offer advantages, particularly for systems that are conventionally heat/mass transfer limited, are listed below.

### 2.2.2.1 Thin Film Flow

Formation of very thin films (typically 50 to 600  $\mu\text{m}$  [55]) on a rotating disc minimises the conduction/diffusion path lengths. Furthermore, the high centrifugal fields subject the liquid film to high shear stress and create unstable waves which promote good mixing and high heat/mass transfer rates. This phenomenon is illustrated in Figure 2-3 which shows the behaviour of a liquid film at two different disc rotational speeds. The studies of thin liquid films on a smooth rotating disc, e.g. [10, 11], suggest that different types of waves (concentric, spiral or irregular), of various intensities, are formed depending on the rotational speed, flow rate and fluid physical properties, such as surface tension and viscosity. The type and intensity of surface waves are also affected by the surface characteristics of the disc [15] and entrance conditions such as feed tube diameter [12]. When the film becomes sufficiently thin (below 20  $\mu\text{m}$  [11]) it starts to break up into rivulets, thus hampering the SDR's potential for heat and mass transfer enhancement. The thin liquid films formed on rotating surfaces

also provide short UV penetrations paths, making the SDR particularly suitable for photochemical reactions.

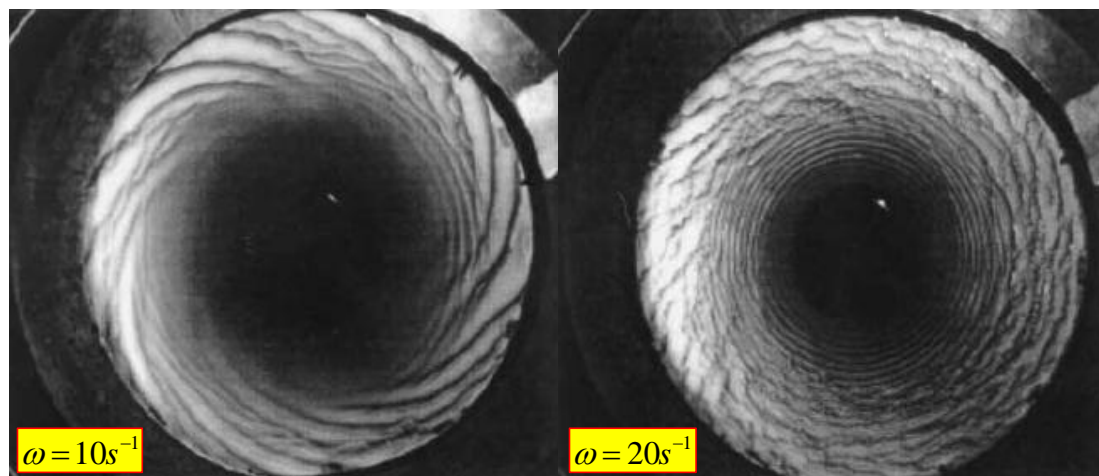


Figure 2-3. Wave formation on a rotating surface at different angular velocities [16]

#### 2.2.2.2 Short Residence Times

Fluid residence time on the disc is determined by the fluid flowrate and viscosity, as well as the disc diameter and rotational speed. Typically, very short residence times of 0.1s up to 5s are achieved [54]. This feature is of considerable interest for improving the selectivity of the desired product [56]. It also enables the processing of heat-sensitive materials and the exploitation of higher reaction temperatures with reduced risks of product degradation.

#### 2.2.2.3 Variable Rotational Speed

The disc rotational speed offers an extra degree of freedom in equipment design, a feature which may be exploited to control the fluid residence time on the disc, as well as the mixing intensity. As the speed of rotation increases, enhanced mixing within highly sheared films are achieved; therefore, the rate of a mixing-limited reaction is expected to increase. However, beyond an optimal value of the rotational speed, the residence time on the disc becomes too short, which may cause a reduction in conversion for some processes. Conversion may also be inversely affected if the liquid film breaks down into rivulets and the disc is not fully wetted as a result of increased rotational speed.

#### 2.2.2.4 Plug Flow Characteristics

Film flow characteristics on a rotating surface is more analogous to the plug flow regime [57, 58] as continuous flow with very little back mixing in the radial direction and excellent degrees of mixing in the axial direction is achieved. The plug flow regime is desirable for some processes in order to limit formation of unwanted by products, as well as, controlling product properties such as molecular weight distribution.

### 2.2.2.5 Catalyst Immobilisation

The disc may be coated with a thin layer of catalyst [56, 59] in order to eliminate the need for downstream separation of the catalyst from the reaction medium, leading to a more environmental friendly and cost-effective process.

### 2.2.2.6 Low Energy Consumption

Jachuck et al. [60] estimate that using the spinning disc technology for polymerisation reactions could result in up to 40% energy savings, in comparison to a conventional batch reactor due to the more efficient processing capabilities of the former system.

### 2.2.2.7 Handling Viscous Material and Slurries

SDRs are capable of processing viscous liquids, such as monomer-polymer mixtures. It is suggested [54] that the shear forces acting on the shear thinning fluids result in an apparent reduction in viscosity. This is a key feature of SDRs which offers a vast opportunity for carrying out polymerisation reactions, since the conventional CSTRs become less effective as reaction proceeds and the melt viscosity builds up. Further, the disc is resistant to plugging and may therefore be suitable for handling slurries.

## 2.2.3 Hydrodynamics of Thin Film Flow

The centrifugal model as outlined by Boodhoo [61] provides a simplified representation of the hydrodynamics of thin film flow on a smooth disc. The basis of the model is a balance between the centrifugal force and the opposing viscous forces in the radial direction, as schematically shown in Figure 2-4:

$$-\frac{v_{\theta}^2}{r} = \nu \frac{\partial^2 v_r}{\partial z^2} \quad (2-1)$$

where,  $v_{\theta}$  = angular velocity [m/s]

$r$  = radial distance from the disc centre [m]

$\nu$  = kinematic viscosity [m<sup>2</sup>/s]

$v_r$  = radial velocity [m/s]

$z$  = vertical distance along the z-axis [m]

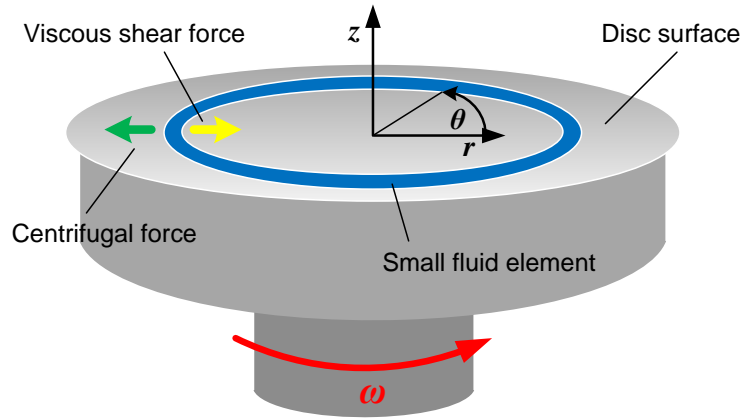


Figure 2-4. Schematic of forces exerted on a fluid element

The underlying assumptions in development of the centrifugal model are:

1. The radial velocity,  $v_r$ , is negligibly small compared to the angular velocity,  $v_\theta$ .
2. The angular rate of rotation of the liquid is equal to the rate of rotation of the disc at all radii so that  $v_\theta = r \omega$ .

Expressions for various parameters, such as radial velocity profile, film thickness, residence time, shear rate, and Reynolds number, have also been developed [61] as presented below:

$$v_r = \frac{\omega^2 r}{\nu} \left( \delta z - \frac{z^2}{2} \right) \quad (2-2)$$

$$\delta = \left( \frac{3Q\nu}{2\pi\omega^2 r^2} \right)^{1/3} \quad (2-3)$$

$$t_{\text{res}} = \left( \frac{81 \pi^2 \nu}{16 \omega^2 Q^2} \right)^{1/3} \left( r_o^{4/3} - r_i^{4/3} \right) \quad (2-4)$$

$$\gamma = \frac{\omega^2 r}{\nu} (\delta - z) \quad (2-5)$$

$$\text{Re} = \frac{4Q}{\pi d \nu} \quad (2-6)$$

where,  $\omega$  = angular velocity [rad/s], ( $\omega = 2\pi N/60$ ,  $N$ =disc rotational speed [rpm])

$\delta$  = film thickness [m]

$Q$  = volumetric flowrate [ $\text{m}^3/\text{s}$ ]

$t_{\text{res}}$  = mean residence time [s]

$r_i$  = radial distance of the inlet from the disc centre [m]

$r_o$  = radius at exit [m]

$\gamma$  = shear rate [ $\text{s}^{-1}$ ]

$\text{Re}$  = Reynolds number

The above simplified representations of the hydrodynamics of thin films on a rotating surface are based on the Nusselt model for a fully developed laminar flow, which neglects the effect of surface instabilities and inertia on flow regimes. Burns et al. [62] measured the film thickness over a range of conditions and found that on average, the ratio of experimental film

thickness to Nusselt prediction is 0.91. Much larger deviations between calculated and measured values were observed at lower Ekman numbers, where inertia influences are strong and a significant portion of the disc radius is required to accelerate the film up to the disc speed. Matar et al. [14] provide a comprehensive review of the experimental and modelling developments of continuous film flow over a rotating surface, including more advanced models to account for the complex hydrodynamic and the effects of surface instabilities.

### 2.2.4 Heat Transfer

The improved heat transfer performance of the SDR is due to the reduced conduction path lengths between the disc and the process fluid, enhanced mixing and increased surface area per unit volume within the thin films. It is also suggested [15] that the presence of surface imperfections such as grooves promote the formation of a large number of small waves, which create instabilities in the film and enhance heat transfer rates.

Jachuck and Ramshaw [15] measured heat transfer coefficients from a brass disc to thin water films over a range of flowrates and rotational speeds. They also investigated the effects of different disc surface configurations on heat transfer performance of spinning discs. The results indicated that the heat transfer coefficient depends on both liquid film thickness and surface waves or instabilities in the liquid film. Generally a thin film with numerous surface ripples should provide the best conditions for heat transfer. Increasing the disc rotational speed produces thinner films; however, beyond a particular value extremely thin liquid films without any surface waves are produced, which may result in a drop in the value of heat transfer coefficient.

Additionally, the results showed that increasing the fluid flowrate generally leads to an increase in the heat transfer coefficients for the range of parameters studied, which is attributed to more waves being formed at higher flowrates which induce more efficient mixing. However, film thickness increases with increasing flowrate, thus beyond a certain flowrate heat transfer coefficients start to fall. Therefore, to achieve the best results, a compromise between film thickness and surface waves may be necessary. The authors however do not consider the effect of residence time when explaining their experimental trends. Both flowrate and rotational speed also influence the fluid's contact time on the disc, and may also influence the heat transfer performance. Average heat transfer coefficients as high as 19.9 kW/m<sup>2</sup>K are reported for a grooved disc corresponding to a rotational speed of 650 rpm and a flowrate of 60 cc/s. Ozar et al. [63] also found that increasing the rotational speed and flowrate both result in an increase in the local heat transfer coefficients.

Aoune and Ramshaw [16] present the following expression for calculating the local film heat transfer coefficient based on the Nusselt theory:

$$h = \frac{5k}{3\delta} \quad (2-7)$$

where, k = Thermal conductivity [W/mK]

$\delta$  = Film thickness [m]

The above expression does not take the effect of surface waves into account. Therefore, theoretically it should result in conservative values for water like liquids which may exhibit numerous surface waves. However, comparing the experimental data provided in the same study with those predicted based on the Nusselt theory do not show a good agreement, as shown in Figure 2-5.

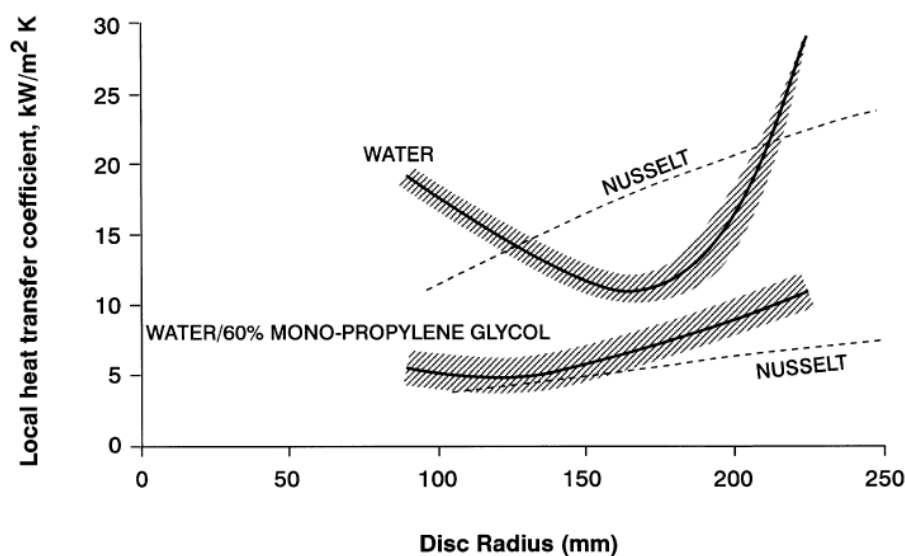


Figure 2-5. Local liquid film heat transfer coefficient on smooth disc [16]  
(flowrate:  $35 \text{ cm}^3/\text{s}$ , angular velocity  $60 \text{ s}^{-1}$ )

The comparison of experimental data and that predicted by the Nusselt model shows that the measured heat transfer coefficients are only more conservative near the disc centre and at the disc periphery, whilst the Nusselt model over predicts the heat transfer coefficient for most of the disc surface. The large values of local heat transfer coefficient measured near the disc centre are attributed to the extra film disturbances involved in bringing the feed liquid to the local disc angular velocity. However, at higher viscosities, the measured and predicted data show a more reasonable agreement whilst, much lower heat transfer performances are obtained. More recent studies by Quinn and Cetegen extend the investigation of heat transfer from a rotating disc to boiling [64] and evaporating [65] liquid films.

### 2.2.5 Mass Transfer

Enhanced mass transfer performance is achieved in a SDR as the diffusion path lengths between the liquid and gas phases, in thin films are dramatically reduced. Additionally the high shear stresses exerted on liquid films promote the formation of surface instabilities and lead to enhanced mixing. These features make SDRs particularly suited for carrying out reactions whose rates are impeded in conventional reactors, due to mixing/mass transfer limitations.

Early studies of mass transfer from gas phase into thin liquid films include the work of Lim [66] and Moore [67]. More recently Aoune and Ramshaw [16] measured the local mass transfer coefficients for absorption of  $\text{O}_2$  into thin liquid films. The data shows a strong



correlation with the disc rotational speed, wherein enhanced performance was achieved at higher angular velocities which provide higher mixing intensities, as shown in Figure 2-6.

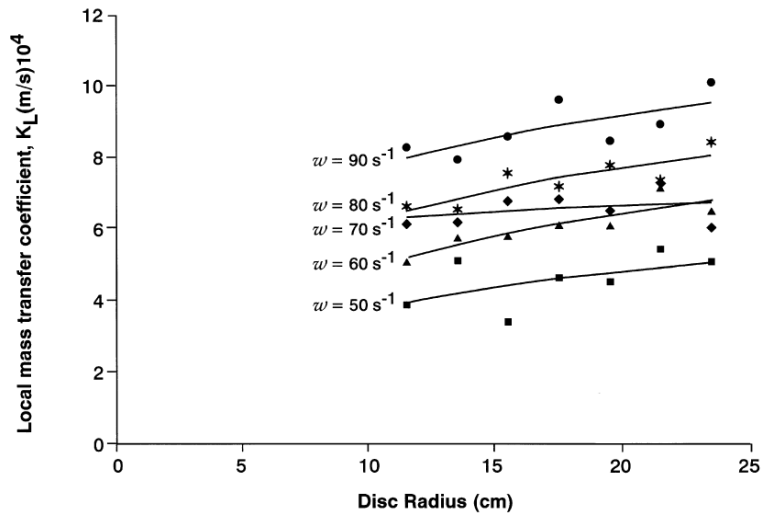


Figure 2-6. Local mass transfer coefficients at various rotational speeds with water flow rate of  $80 \text{ cm}^3/\text{s}$  [16]

Burns and Jachuck [68] reported a range of mass transfer coefficients for absorption of  $\text{CO}_2$  into a thin liquid film which increased with higher flowrates and higher rotational speeds as shown in Figure 2-7. Simulation studies of mass transfer in thin liquid films over rotating surfaces [13, 69] have also shown that the presence of surface waves lead to augmentation of mass transfer.

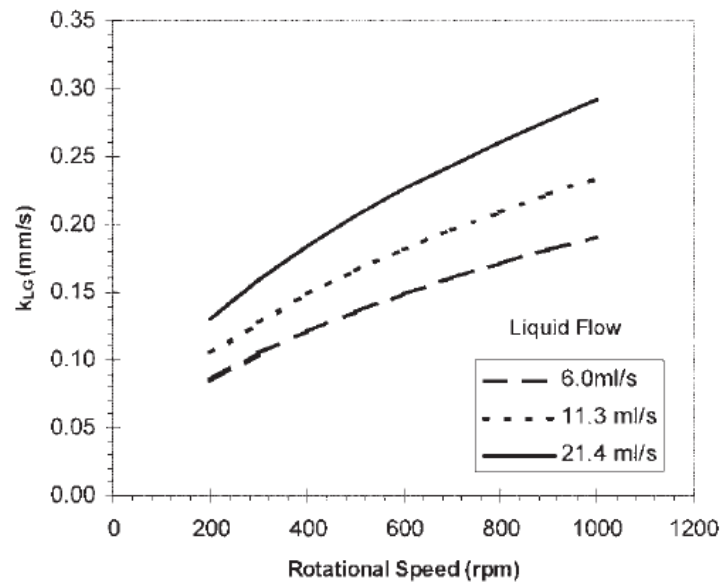


Figure 2-7. Mass transfer coefficients at the completion of the reaction [68]

## 2.2.6 Applications

SDRs are particularly favoured for carrying out inherently fast, highly exothermic reactions, such as neutralisation and polymerisation, as well as reactions requiring rapid mixing, for instance, crystallization. SDRs can also offer benefits to processes involving heat-

sensitive materials, due to very short, controllable residence times. Some examples and case studies are presented below.

SmithKlineBeecham investigated the use of a SDR for the phase-transfer-catalysed Darzen's reaction to produce a drug intermediate [57] and reported very encouraging results. The reaction time was reduced by 99.9%, reactor volume by 99%, and impurity level by 93%, compared to the conventional batch process. The study showed that a 15cm diameter SDR can manufacture around 8 tonnes of product per year, proving that the laboratory scale can be the full scale.

SDRs have also been successfully used to carry out a range of polymerisation reactions, such as styrene polymerisation [70] and condensation polymerisation [71]. In conventional processing, difficulties arise as the polymerisation reactions proceed, whereby efficient mixing and heat transfer become increasingly difficult as the polymer melt becomes more viscous. Non-uniform temperature profiles cause broadening of the molecular weight distribution, hence, reducing product quality. In extreme cases, loss of temperature control and reaction runaway may also occur. Diffusion and mass transfer are also impaired at high viscosities, causing a significant drop in the rate of reaction. In general, the SDR with its excellent mixing and heat/mass transfer characteristics offers higher polymerisation rate and conversion, enhanced product quality (tighter molecular weight distribution), improved safety, and lower risk of polymer degradation due to short residence times. The higher polymerisation rates achieved lead to significant reductions in processing time and therefore improved process economics [70, 71]. Another advantage is that the thin films produced on a rotating disc enable efficient UV light penetration for photo-initiated polymerisation and photocatalytic processes [59, 72, 73].

SDRs also offer considerable improvements in precipitation and crystallisation [57]. This is generally attributed to the intense mixing achieved in thin highly sheared films. The good mixing ensures homogeneous nucleation and thus, tighter particle size distribution and improved product quality. An experimental study of the precipitation of barium sulphate [26] also suggests that the SDR requires significantly lower energy to achieve high rates of precipitation, compared to a tubular T-mixers and Y-mixers. SDRs may also be applied for production of particles in the nano-size range, as discussed in section 2.5.4.

The food industry may also benefit from SDRs. Akhtar et al. [74] report the application of a SDR for the production of ice-cream base, which leads to significant reductions in the processing time and energy consumption compared to conventional processing methods. The observed reduction in ice-cream base processing time is attributed to micromixing and the creation of large interfacial areas for protein-emulsifier adsorption. It was also speculated that macromolecules are stretched and untangled under high centrifugal forces, leading to increased surface activities.

The application of a SDR to an organic catalytic reaction using immobilised catalyst [56] demonstrated improved selectivity due to short and controllable residence times and faster reaction rates, compared to that achieved in batch processes. Employing a heterogeneous catalyst eliminated the need for downstream separation of the catalyst from the product, resulting in a greener process. It was also envisaged that the high shear rates prevailing on the

spinning disc shift the product molecules away from the active catalyst sites, leading to improved catalyst activity.

## ***2.3 Control of Process Intensified Systems***

Process control is an essential part of any chemical plant to ensure that all processing units are operated within their safety envelopes. Further it is desired to effectively control the production rate and the product quality in order to meet specifications. Control systems are also used to ensure that the plant is operating within the legal framework, for instance, in terms of discharges of wastes to the environment.

Although some compelling advantages of intensified systems have been demonstrated, there is concern that existing control strategies and instrumentation may not provide a satisfactory performance when applied to such processing units. Barzin et al. [75] provide a brief overview of the potential difficulties involved, which call for more investigations into the control and operation of intensified equipment.

### ***2.3.1 Potential Difficulties***

Barzin et al. [75] conveniently categorise the challenges of controlling intensified units into two groups. The first category consists of issues arising from integration of a number of process unit operations into one unit. This is because multifunctional equipment are often more complex and their design suffers from losses of degrees of freedom. The second group includes the difficulties encountered in control of low volume, high throughput, equipment due to the high responsiveness and fast dynamics of such units. The potential challenges of controlling intensified equipment are outlined in more detail next.

#### **2.3.1.1 Multifunctional Equipment**

Synergy is one of the fundamental principles of *PI* which involves combining a number of unit operations into one single unit. Due to the more complex behaviour of such units, including strong interactions of different process quantities and the presence of multiple steady states, dynamic modelling, design, operation and control of multifunctional units become more challenging tasks [76]. In particular, more elaborate automatic control schemes may be required [77].

Another issue with multifunctional units is that the availability of measurement information and the number of manipulated variables are reduced. For example, if a reactor outlet is fed to a distillation column via a pipe, the flowrate, temperature and even composition of the stream can be measured and may subsequently be used in feed-forward control of the column. However, if the reactor and column are integrated, no information on the distillation feed can be obtained, thus the degrees of freedom available for control are reduced [78].

Haugwitz et al. [79] provide details of developing a suitable control strategy for an open plate reactor, which is an efficient heat exchanger reactor particularly suited for carrying out

highly exothermic or endothermic reactions. The authors propose a model predictive control strategy to ensure safe operation whilst maximising conversion. The simulation results show satisfactory control performance in presence of disturbances. Kiss and Bildea [80] have recently investigated the control of dividing wall columns (DWC) in detail. In a DWC, separation of a ternary mixture is achieved in a single distillation column with a split middle section, whilst in a conventional approach two stand-alone columns are required to achieve the separation. Despite clear advantages of DWCs in terms of significant energy savings and capital costs reduction, their industrial scale applications has been hindered due to uncertainties in their operation and control. Kiss and Bildea [80] provide a guideline for selecting appropriate control strategies for DWCs and show that good control may be achieved if appropriate control structures are selected. They investigate a range of control schemes of varying complexity and show that superior control is achieved using a multiple input multiple output (MIMO) model predictive control strategy, compared to PID controllers within a multiloop structure.

Similar investigations into the control of multifunctional and integrated units are scarce in the subject literature. More research in this field for a wider range of equipment along with experimental validation of simulation studies is required to increase the commercial attractiveness of such novel technologies.

### 2.3.1.2 Miniaturised Equipment

One of the primary objectives of *PI* is to dramatically reduce the equipment size/capacity ratio; as a consequence, compared to conventional equipment, the residence times of intensified units are significantly shorter. This may introduce unprecedented challenges in operation and control of such units. For example, sensors and actuators commonly used in industry may be too slow in contrast with the very quick response times of low volume equipment. Typical time constants of conventional control loop elements are displayed in Table 2-1.

Table 2-1. Response time of loop elements (adopted from ref. [3])

<i>Loop element</i>	<i>Typical response time</i>
Signal transmitter	1-5s (pneumatic) Instantaneous (electrical)
Signal converter	0.5-1.0s (electronic to pneumatic)
Final control element	1-4s
Thermocouple	Almost instantaneous (bare) 5-20s (in thermowell)
Flow, pressure, level sensor	Several seconds
Analysers	5-30 minutes or longer

A smaller equipment size also results in reduced inventories and holdups, thus faster dynamics. This means that disturbances can cause rapid changes within the system, leading to larger deviations in process variables [51] and consequently compromising safety and

product quality. Further, using a conventional sensor for low volume equipment might also imply that the external sensor housing chamber may have a larger volume than the intensified equipment liquid holdup, leading to large measurement lags and significant deterioration of the control performance.

Moreover, in designing control systems for conventional processes, the instrumentation dynamics are often neglected, as the process dynamics are dominant. This simplification, however, is not justified for intensified systems, as process and instrumentation dynamics are of the same order of magnitude. The resulting problem is that the order of the system is increased; hence, most commonly used model based PID controller tuning methods may no longer be suitable for intensified systems. However, simulation work carried out by Jones and Tham [81], suggests that simplifying the process model by truncating high order terms does not compromise the controller performance. The authors conclude that the IMC (Internal Model Control) approach can still be employed to derive appropriate settings for classical/industrial PID algorithms for application to intensified processes.

Wille et al. [82] report satisfactory control of a pigment synthesis process in an experimental microreactor using conventional and commercially available instrumentation including pressure and flow meters. Quiram et al. [83] also utilised a control scheme for an experimental microreactor system used for a gas-phased catalytic reaction. They used commercially available hardware including a programmable logic control system, signal acquisition devices and sensors to control the gas flowrate and the reaction temperature in a parallel system of microreactors. It was shown that the PID algorithm was adequate for maintaining the temperature of the microreactors. However, the authors found that implementation of the control strategy was more challenging than those encountered for more conventional reactor systems.

However, Barzin et al. [84] suggest that non-conventional sensors which have extremely fast response times, result in small measurement delays and are compact in size with low holdups should be used for effective control of low volume intensified equipment. The authors present an experimental case study in which a spectrophotometric sensor is used to control the pH of a neutralisation reaction carried out in a microreactor. Such sensors are capable of providing fast concentration measurements of different compounds in a solution and require very small volume of the liquid for the analytical measurements. The authors report a measurement delay and time constant of 0.7 s and 5-10 ms respectively, which is much shorter than that of a conventional pH probe. Satisfactory control was achieved using an embedded PID controller plus first order low pass filter in Matlab. Ferstl et al. [85] also report using microstructured temperature, pressure and mass flow sensors in an automated microreaction system for monitoring and control of the process parameters.

Similar to the case of intensified multifunctional equipment, more investigations are required to assess the impact of intensification on the control of miniaturised equipment. Spinning disc reactors are an example of low volume equipment which exhibit fast dynamics and high responsiveness. In the present study the control aspects of SDRs are studied in more details for two example processes via simulation and experimental studies using commercially available instrumentation.

### 2.3.2 Control of SDRs

The previous section provided a brief overview of the difficulties that may be encountered in control of intensified units in general. In this section, the potential advantages and disadvantages of SDRs from a control point of view are considered. Effective control of SDRs may be challenging due to their fast dynamics and short residence times, for example because the conventional sensors and actuators may be too slow, as discussed previously. However, some key features of SDRs may prove to be advantageous for achieving a given control task. For example, the rotational speed of the disc offers an extra degree of freedom in control system design, since the residence time and mixing intensity, and therefore the conversion and particle size, may be controlled by adjusting the rotational velocity, instead of more commonly used methods of varying reactant flowrates. This aspect is explored in more detail for a precipitation reaction in section 2.5.

In conventional reactors, mixing limitations may introduce large lags in implementing the controller's command. In contrast, the enhanced mixing achievable in a SDR could ensure that the controller's corrective actions bring the controlled variable back to setpoint with practically no delays. Further, the enhanced heat transfer characteristics of SDRs could enable tight and rapid temperature control of the liquid film on the disc surface which is likely to be highly beneficial should there be any temperature fluctuations in the feed.

Studying the control aspects of SDRs forms the primary objective of the present study. pH control of a strong acid/strong base neutralisation reaction and conductivity control in a precipitation reaction are chosen to facilitate this assessment. Therefore, it is appropriate to introduce the two selected processes along with their characteristics and common control strategies next.

## 2.4 pH Control

pH is an important process variable in the (bio)chemical industry. pH regulation may be necessary for any of the following reasons [86]:

1. To enable microorganism growth and metabolism in food, beverage and pharmaceutical industries.
2. Corrosion prevention.
3. Environmental monitoring of plant effluent to ensure legal requirements are satisfied. e.g. control pH to minimise solubility of pollutants such as heavy metals in waste streams.
4. Neutralization of waste water streams which may be recycled as process or boiler feed water.

pH is a measure of acidity or alkalinity of a solution and is a function of hydrogen ion activity by the following expression:

$$pH = -\log \alpha_{H^+} \quad (2-8)$$

Hydrogen ion activity  $\alpha_{\text{H}^+}$  is the product of the activity coefficient and concentration of hydrogen ion. If the activity coefficient is assumed to be unity the activity term may be substituted by a concentration term  $C_{\text{H}^+}$  in the above equation. The validity of this assumption is diminished when the concentration of ions, hence the interactions between them, increases in a solution. The challenges of measurement and control of pH as well as the strategies to achieve satisfactory pH regulation are discussed in the subsequent sections.

### 2.4.1 Difficulties in pH Control

pH control is often a challenging task due to both the non-linear and time-varying characteristics of the system. Non-linearity is due to the logarithmic relationship between pH and hydrogen ion concentration, generally defined by the S-shaped titration curves, as illustrated in Figure 2-8. It can be seen that for a strong acid/base system the titration curve is fairly flat at the extreme ends of the pH spectrum, whilst the slope of the curve is significantly steeper for a large portion of the pH scale, around the neutral point. In contrast, the titration curve varies more gradually for a weak acid/base system with increasing reagent concentration.

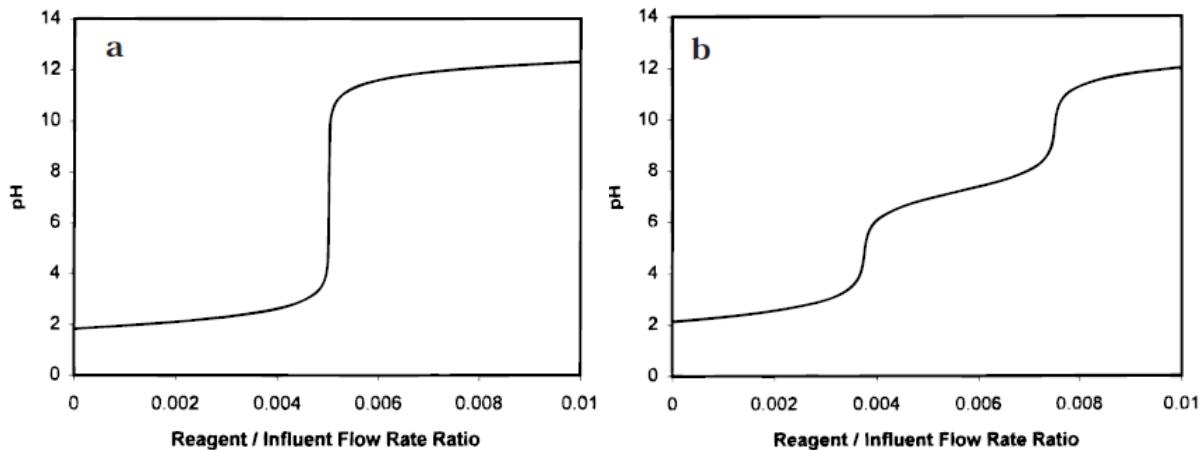


Figure 2-8. Example titration curves [87]

[a) strong acid/strong base system (unbuffered); b) weak acid/weak base system (buffered)]

The time-varying nature of a pH system is due to the changes in its buffering capacity and thus variations of the shape/slope of the titration curve with time. Figure 2-9 shows the changes in titration characteristics of an industrial process at different upstream conditions. It can be seen that the slope of the titration curve and the reagent demand can vary significantly with time. The dynamics of pH probes and the accuracy of measurement may also change with time in the absence of regular maintenance and calibration. These characteristics make the pH control a challenging problem as non-linear compensation and adaptive control may be required to achieve satisfactory control performance.

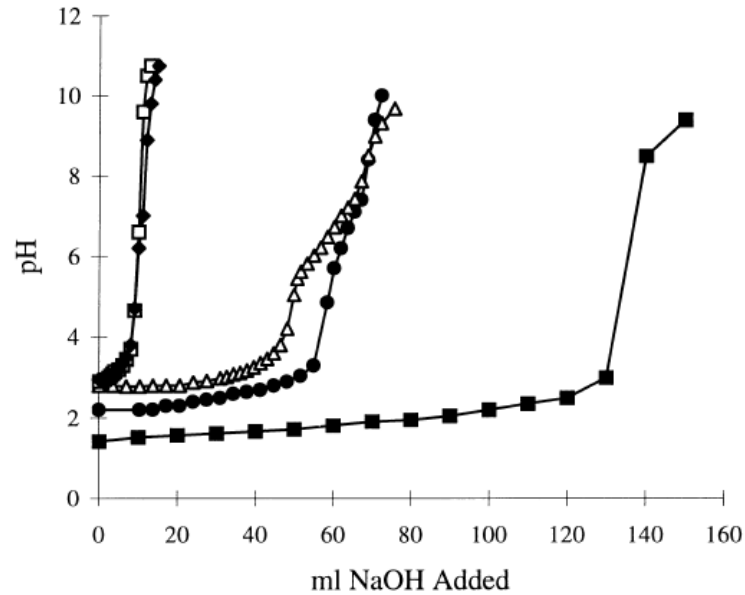


Figure 2-9. Titration curves of samples taken from an industrial pH process during different upstream conditions [88]

The tremendous sensitivity and rangeability of pH measurements also result in further challenges. For a strong acid/strong base system, the reagent control valve must have a rangeability greater than 10,000,000:1 to bring an influent stream with a pH of zero up to a setpoint of 7. This is because pH has a logarithmic relationship with concentration and the reagent flow demand is proportional to the difference in hydrogen ion concentration of the process stream and the setpoint [24]. However, the rangeability of control valves with positioners only reaches 100:1, and that of metering pumps is typically 20:1 [87]. Thus, for strong acid/strong base systems precision and rangeability of control valves and metering pumps can considerably influence the pH control performance.

Due to the highly non-linear dynamics of neutralisation processes, limit cycles (uniform oscillations with fixed magnitude) are common occurrences in a pH control loop [89], which can substantially increase reagent consumption. Finally, processes requiring pH regulation such as neutralisation of waste water with multiple feed streams of unknown, time varying compositions are frequently of a complex nature and often subjected to large unmeasured disturbances.

### 2.4.2 pH Control Strategies

Nearly all pH control systems utilise some form of feedback control. Feed-forward control may also be added to compensate for disturbances arising from changes in feed flow rate, in a cascade or ratio arrangement [24]. Numerous strategies, with varying degrees of complexity, have been proposed for effective pH monitoring and control. Henson and Seborg [90] classify pH control strategies into four broad groups: non-adaptive linear, adaptive linear, non-adaptive nonlinear and adaptive non-linear. The authors suggest that control strategies which are both nonlinear and adaptive are required to account for the nonlinearity and time-varying characteristics of pH systems respectively.



Non-adaptive linear controllers such as those based on a PID algorithm, are the simplest strategy for pH control, operating on a fixed set of tuning parameters. In a pH system, the process gain is equal to the slope of the titration curve which may vary significantly at different operating regions, particularly for strong acid/base systems where the non-linearity is more pronounced. The controller gain is usually inversely proportional to the process gain; therefore, at steep regions of the titration curve where the process gain is high, the controller gain should be set low to maintain stability. Conversely, at flat regions of the titration curve where the process gain is low, the controller gain may be set higher to achieve a faster response without approaching the stability margins. Theoretically, a non-adaptive linear PID controller provides adequate performance only if the process is operated within a narrow region where the controller is tuned for and if the buffering variations are small [91].

A range of linear adaptive control schemes have been developed to handle the time varying characteristics of pH processes, including gain scheduled PID [87, 92] and self-tuning PID [93] control algorithms. The limitation of these schemes is that they are based on a linear process model and therefore may not be efficient in dealing with the severe non-linearity of pH processes. Nonlinear control strategies, barring those developed for strong acid/base systems, are often based on state space estimation of the process model [94]. For strong acid/base systems, state estimations are not required as a nonlinear model may be developed based on pH measurements [95]. However, such control schemes are not applicable to buffered solutions. Gustafsson et al. [96] developed a general model for pH processes in terms of reaction invariants, estimated by a least squares method. The resulting nonlinearity is then fed back in the control loop to linearise the system.

Wright et al. [86, 97] developed and experimentally demonstrated the Strong Acid Equivalent (SAE) approach, which consists of defining an alternative equivalent control objective that is linear in the states. Therefore a linear control law in terms of this new linear control objective may be used to control pH. The authors point out that although pH is a good measure of how many active hydrogen ions are present in the solution, the error in pH is not a good measure of how far the system is from the setpoint. For example going from pH 3 to 7 will require a different amount of base depending on the buffering capacity of the system. In contrast, the SAE is directly related to the amount of reagent that must be added in order to bring the system to the desirable level of acidity. The SAE is calculated online from pH measurements, given a nominal titration curve of the process stream. A controller based on this approach was developed and successfully implemented for a complex industrial process with unknown chemical composition [88]. Advanced nonlinear control schemes such as internal model control [98, 99], fuzzy logic [100] and neural networks [101] have also been proposed for pH control.

Despite the advent of many advanced control theories, controllers based on the simple PID algorithm (see Appendix A) are still widely used in industry. In fact, more than 90% of all control loops in industry use some form of a PID controller [102]. This is because the principles of PID control are simple and easy to understand. Moreover, the robustness and reliability of PID controllers have been proven by many successful industrial applications. Thus, it may be more desirable to employ a PI/PID controller to regulate pH. Brandes [103]

provides details of a simple yet robust approach to control neutralization of a strongly acidic wastewater with a strong base, using a PI controller. The titration curve was linearised by empirical treatment and correlation of experimental data. The system was implemented industrially and acceptable performance was achieved.

In the present study, the advanced control algorithms proposed for pH control will not be adopted, as the objective is to examine the control aspects of spinning disc reactors using commercially available instrumentation and a PID controller. The pH system was selected as the neutralisation reaction is inherently fast and well suited to the short residence times of SDRs. Furthermore, as pH control has a challenging nature it allows the extension of the research findings to other control tasks with equal or less challenging characteristics. Two relatively simple nonlinear compensation techniques namely the application of a ‘characteriser’ and a ‘disturbance observer’ algorithm have been identified as suitable approaches to improve the performance of a PID controller for the present study. These two techniques are outlined briefly next.

Shinsky [23] offers a simple solution by adding a characteriser or a complementary nonlinear function in the path of the pH measurement and the set point, with the objective of linearising the loop. The pH characteriser is the titration curve rotated, as shown in Figure 2-10.

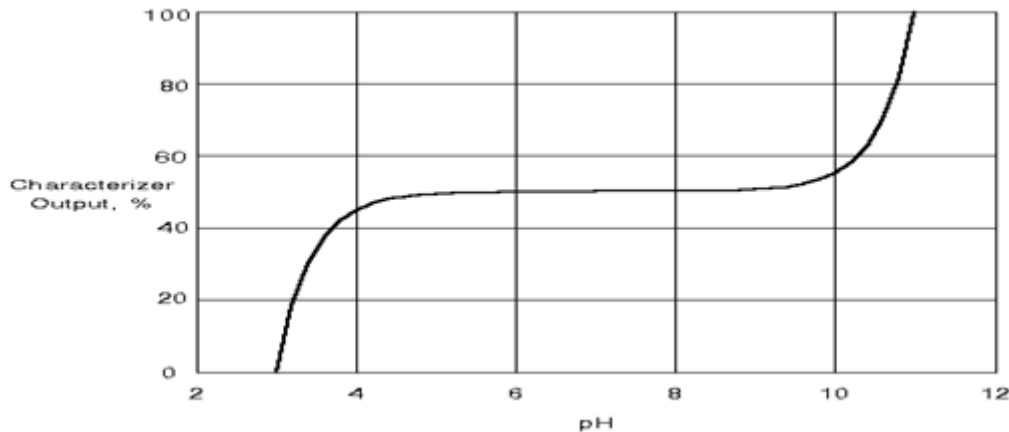


Figure 2-10. pH characteriser [23]

Shinsky [23] shows that the pH control performance using a PI controller is improved when the characteriser is placed in the measurement path to linearise the loop. However, detailed discussion of his results is not provided in the article and other reports on the application of this technique are scarce in the literature. Nevertheless, the approach can be readily implemented without extra computational costs and the underlying concept of linearising the pH control loop with an inverse of the titrations curve seems logical. Therefore, the characteriser scheme was selected for further testing in the present study.

The Disturbance Observer (DO) is a complementary algorithm which may be employed to cancel out the unmeasured disturbances. The DO concept was originally presented by Ohnishi [18] to estimate and reject disturbances in controlling a DC motor. DOs are commonly used to improve the disturbance rejection capabilities of mechatronic servo control systems [104, 105]. More relevant to the present study is the application of a DO

algorithm to suppress the undesired effects of system nonlinearity reported by Shahrzuz et al. [21, 22]. The authors investigated the effectiveness of the algorithm in suppressing the limit cycles observed in control of backlash in gear systems. The results indicated that DO structures are effective means of suppressing system nonlinearities.

Jones and Tham [19] extended the application of the DO algorithm from mechatronic systems to process control, using the general structure presented in Figure 2-11. The authors explain that DO closes an inner loop around the controlled plant,  $G_p(s)$  and by passing the output signal,  $y$ , through the inverse of the nominal plant model,  $G_n^{-1}(s)$ , the disturbance,  $d$ , may be estimated and subsequently rejected. The DO design is analogous to internal model control as they both use the inverse of the nominal plant model. The signal,  $c$ , is usually provided by an outer loop controller, such as a PID. The DO design involves specification of a low pass filter,  $Q(s)$ , such that  $Q(s) / G_n(s)$  is realisable, followed by choosing the filter parameters to provide a balance between disturbance rejection performance versus stability robustness [19].

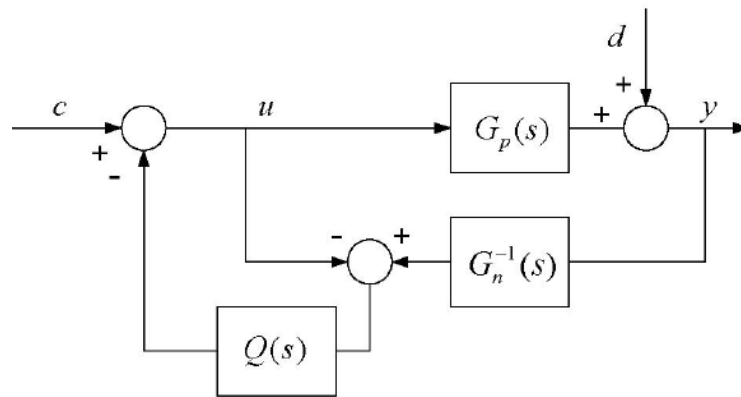


Figure 2-11. Disturbance observer [19]

In a later study, Jones and Tham [20] considered DO designs for continuous systems with delays and presented two implementation approaches. More recently, Tham et al. [106] applied the DO algorithm to a simulated, nonlinear multivariable distillation system to assess its potentials for mitigating control loop interactions. The results suggested that DOs can provide more robust performance in a nonlinear environment even in presence of modelling mismatch, compared to that achieved by the traditional decoupling control.

Although the DO algorithm has not been explicitly applied to a pH control problem, the available results in the literature indicate that there are potentials for its application to pH control. Evaluating the performance of a DO strategy combined with a PID control algorithm is of great interest in the present study and will be investigated extensively via simulation and online implementation.

## 2.5 Precipitation Process

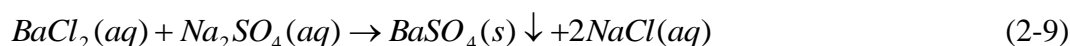
As discussed in Chapter 1, it is of great research interest to examine the possibility and also the relative merits of using the disc rotational speed as manipulated variable, instead of the more conventional methods of for example varying the reagent flowrate. However, the

acid/ base neutralisation process was found to be insensitive to the disc rotational speed, as no significant changes in effluent pH were observed at various disc speeds, whilst the feed flowrates were kept constant. Upon considering a number of mixing sensitive processes, the precipitation process was found to be a suitable candidate for the present investigations.

Most crystallisation reactions have fast kinetics implying that the rate of reaction can be influenced by how effectively the reactants are mixed on the molecular scale. Burns and Jachuck [68] studied the precipitation of  $\text{CaCO}_3$  on a spinning disc reactor and found that conversion was affected by both feed flowrate and disc rotational speed. Cafiero et al. [26] also showed that the  $\text{BaSO}_4$  crystal production rate increases with increasing rotational speed whilst the average crystal size decreases. Reactive crystallisation of barium sulphate was selected as an example process to study the potential of exploiting SDRs rotational speed as a manipulated variable to achieve a given control task. A literature survey of barium sulphate precipitation including the influence of mixing and residence time, and common control strategies is provided in the following sections.

### ***2.5.1 Precipitation of Barium Sulphate***

The precipitation of barium sulphate from barium chloride and sodium sulphate proceeds according to the following reaction:



Barium sulphate is sparingly soluble in water, and hence, it precipitates as soon as it is formed. During barium sulphate precipitation, a number of processes occur almost simultaneously, including mixing of the reactants, chemical reaction, nucleation and growth of the solid particles. Secondary processes such as agglomeration, ripening and breakage may also occur [26].

The mechanism and kinetics of nucleation and growth are mainly controlled by the degree of supersaturation. Upon mixing of the reagents, supersaturation starts to build up; nucleation is then triggered as the supersaturation increases and the formed nuclei start to grow. Therefore, at the start of the precipitation process, supersaturation increases via mixing of the reagents whilst it also decreases simultaneously as nucleation and growth progress. When supersaturation is reduced to saturation, the precipitation process is complete [107]

A high quality barium sulphate product is often characterised by a low mean particle size and narrow crystal size distribution (CSD). The shape of the crystals and their purity level may also be important. Precipitation of barium sulphate is an industrially important process and is also widely used as a model system for precipitation studies. However, the literature available are contradictory with respect to its nucleation mechanism, growth kinetics and the degree of agglomeration, as pointed out by Sohnle and Garside [108]. This inconsistency has been attributed to differences in conditions of the precipitation process, mainly the supersaturation, the presence of impurities and different experimental techniques.

The nucleation process can occur as primary homogeneous in the absence of a solid interface, primary heterogeneous in the presence of a solid interface of a foreign particle and

secondary nucleation in the presence of a solute-particle interface [109]. Crystal growth mechanism occurs in various stages including the transport of solute from the bulk solution to the crystal surface, adsorption on the surface, diffusion over the surface and liberation of heat of crystallization. Hence, the rate of crystal growth is often controlled by mass transport limitations [109]. There are several experimental studies concerning the kinetics of barium sulphate precipitation available in literature [110-112].

Agglomeration may occur in some crystallization processes if crystals ‘stick’ together to form larger particles. If the cohesion forces are weak, the agglomeration is called coagulation and if the process occurs without supersaturation it is referred to as aggregation. The key factors that influence agglomeration include hydrodynamic conditions, physical properties of the solvent, size and habit of the crystals, population density of the crystals and supersaturation [113]. Ripening occurs when small particles dissolve and the solute is subsequently deposited on larger particles. The driving force for this process is the difference in solubility of small and large particles. Additives such as gelatine can be used to retard the ripening process [107].

As discussed previously, supersaturation controls the precipitation process and strongly influences the size and habit of the product. Judat and Kind [114] studied the morphology and internal structure of barium sulphate particles and illustrated the strong dependence of particle size and morphology on supersaturation, as shown in Figure 2-12.

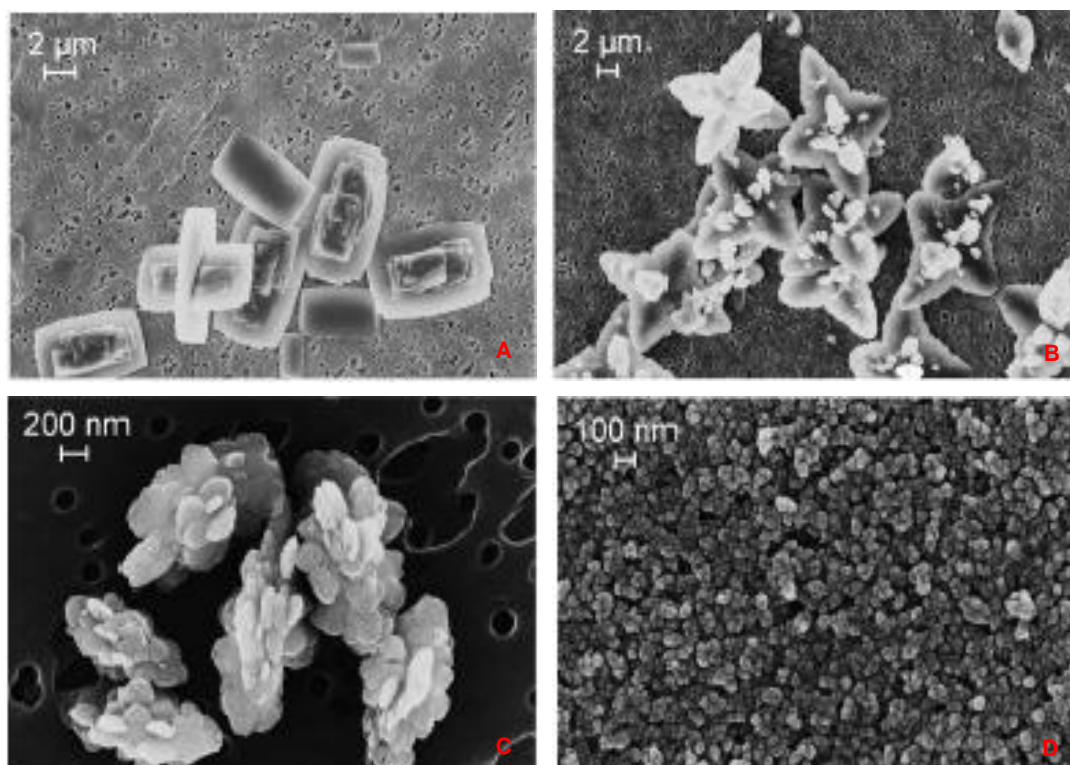


Figure 2-12. Morphology of barium sulphate at various initial supersaturations  
[Initial supersaturation: A: 50 B: 250 C: 2500 D: 5000]

### 2.5.2 Effect of Mixing

The effect of mixing on precipitation has been widely studied over the past few decades, both experimentally and by simulation. Mixing affects the kinetics of crystal growth by enhancing mass transfer and diffusion whilst it affects the nucleation rate mainly by controlling the generation and distribution of supersaturation. Modelling the precipitation process, particularly for prediction of the crystal size and CSD at various operating conditions, is of key practical importance, as it facilitates the optimal design, operation and control of the process. Precipitation of barium sulphate is commonly chosen as an example process to develop and validate simulation models for precipitation.

The effect of process parameters on precipitation has commonly been investigated with the help of computational fluid dynamics (CFD) [115-119]. Modelling the precipitation process requires solving a group of complex partial differential equations which describe the system, including momentum and mass transport equations, the moment equations for crystal population balance, precipitation kinetics and mixing characteristics.

Mixing at micro-, meso- and macroscales can influence the size and morphology of the produced crystals, and thus the quality of the product. Micromixing occurs at the molecular level, whilst macromixing involves mixing at the full equipment scale and mesomixing signifies mixing between micro and macro scales, such as mixing at the localised feed point. Macromixing determines the environment concentration for meso- and micromixing. As the precipitation process involving chemical reaction, nucleation and crystal growth occurs at molecular level, micromixing is often regarded as the mechanism which directly influences the course of precipitation [120].

Baldyga et al. [120, 121] developed a mixing precipitation model which involves the interactions between mixing of macro, meso, and micro scales in combination with the population balance model of crystallization and kinetics of precipitation. The model allows the determination of mixing time constants at different scales. Comparing the time constants of micro- and mesomixing provides an insight into which mechanism is more dominant. If the mesomixing time constant is much larger than that of micromixing, mesomixing is the controlling step and vice versa. If the time constants for meso- and micromixing are equal or comparable, both mechanisms are important and need to be considered. In order to evaluate the effect of mixing on the course of precipitation, the mixing time constants are commonly compared to the induction time which is the time elapsed between the creation of supersaturation and the formation of first particle of detectable size [107, 122].

The effect of mixing on the precipitation process has been broadly studied. However, various authors have reported contradictory theoretical and experimental trends about the impact of mixing on precipitation, and therefore the particle size. For example, the early work of Pohorecki and Baldyga [123] showed that the mean particle size decreases with increasing impeller speed for batch precipitation. In a later study [124] the same authors observed the opposite trend in a continuous stirred tank reactor in which the particle size increased with increasing mixing intensity.

An increase in the particle size with increasing stirrer speed was also reported for double feed semi-batch precipitation by Baldyga et al. [120, 125] and for a single feed semi-batch process by Phillips et al. [126]. However, the data reported by Chen et al. [127] for a semi-batch reactor show that there is a critical stirrer speed at which a minimum particle size is achieved. Below the critical speed, the crystal size was found to reduce with increasing mixing intensity, whilst above the critical speed the opposite trend was noted. The appearance of the critical phenomenon was attributed to the contradictory interactions of micro- and macromixing which reach equilibrium at the critical rotational speed.

Schwarzer and Peukert [128] produced nanoparticles in a T-mixer and showed that increasing the flowrate and consequently enhancing the mixing intensity yields smaller particles with a narrower size distribution. The same trend was observed by Wang et al. [129] whereby increasing the total flowrate and decreasing the micropore size in a tube-in-tube microreactor led to a reduction in the average particle size.

Therefore, based on the research available in the subject literature, enhanced mixing may increase and/or decrease the particle size. This discrepancy may have resulted from the differences in supersaturation levels, operating conditions and mode of operation adopted in various studies. An investigation of the relevance of micromixing to barium sulphate precipitation [130] confirmed that the role of micromixing varies depends on the operating conditions, including reactant concentrations and mixing conditions in a semi-batch reactor. The results showed that the effect of micromixing is significant when the feed injection time is very fast and comparable to the micromixing time, and also when the reaction is fast as a result of high reactant concentrations.

Öncül et al. [131] also investigated the effect of micromixing by means of simulation, using various micromixing models. The models did not show a perfect agreement with the experimental data available in the literature for all cases and configurations. The authors concluded that the influence of micromixing might be negligible at high Reynolds numbers or low supersaturation ratios. The conclusion that micromixing is more applicable for high supersaturation ratios seems intuitive, since the slowest mechanism controls the process. Thus, the micromixing time must be comparable or larger than the reaction time to have a significant effect on the course of the reaction. At high Reynolds numbers, more efficient macromixing is achieved due to more turbulent conditions; therefore the effect of micromixing might decrease.

To summarise, mixing at the micro scale directly influences the course of precipitation as the reaction, nucleation and growth processes all occur at molecular level. Comparing the mixing time constants at various scales provides a means for determining if micromixing is the dominant mechanism. Secondly a process is sensitive to micromixing if the reaction time is faster than the micromixing characteristic time constant, i.e. at high supersaturation levels. Dramatic reductions in mixing times (at every mixing scale) are achieved by increasing the specific turbulent energy dissipation rate [132]. In SDRs enhanced micromixing and molecular diffusion, at Kolmogorov and Batchelor scales respectively, are achieved with increasing disc rotational speed. The effect of micromixing on the course of precipitation and particle size based on the literature available for intensified systems in provided section 2.5.4.

One objective of the present research is to study the control of SDRs by manipulating the rotational speed. The rotational speed impacts the mixing intensity of thin films which is known to affect the precipitation process. Additionally, the rotational speed has an influence on the fluid residence time, which may in turn impact the precipitation process, as discussed next.

### 2.5.3 Effect of Residence Time

The effect of residence time on particle size depends on the relative kinetic order of nucleation and growth and usually is not an effective means for adjusting the product crystal size [107]. The results presented by Matynia et al. [133] for continuous barium sulphate precipitation show that the particle size and variance increase with increasing residence time as shown in Figure 2-13.

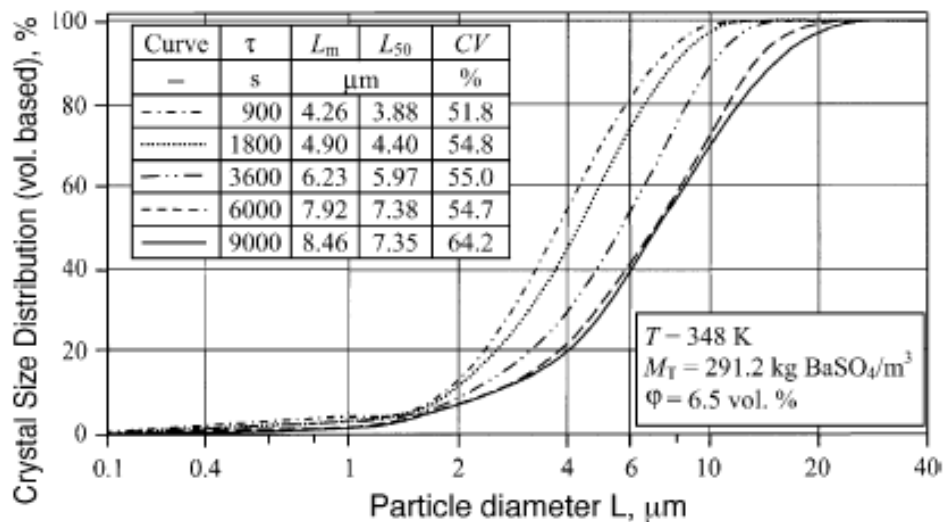


Figure 2-13. Barium sulphate crystal size distributions [133]

[ $\tau$ : mean residence time,  $L_m$ : mean crystal size,  $L_{50}$ : median crystal size,  $CV$ : coefficient of variation,  $M_T$ : suspension density,  $\phi$ : volumetric concentration of crystals in suspension]

Supersaturation level decreases with time as the ions are consumed by the precipitation reaction. Consequently, the rate of nucleation and growth decrease with increasing residence time, but to different extents. At low supersaturation levels (corresponding to longer residence times), the crystal growth rate is often faster than the nucleation rate and therefore, larger crystals are produced. Conversely, at high supersaturation levels (shorter residence times), the nucleation rate is often faster than the linear growth rate - therefore finer particles are produced [133]. Increasing particle size with increasing residence time in continuous precipitation of barium sulphate is also evident in the experimental data presented by Pohorecki and Baldyga [124].

Wong et al. [134] studied the size evolution of  $\text{BaSO}_4$  particles over time, for a series of double feed semi-batch experiments and observed that in most cases, the CSD shifted to longer sizes with respect to time. However, in one test condition, in the presence of ion excess, CSD remained constant with respect to time, which seems to suggest that in presence of ion excess, the supersaturation is mainly consumed through nucleation. Therefore the increased retention time does not result in particle growth.



The effect of residence time on conversion depends on the degree of mixing within the crystallisation vessel. If mixing limitations are removed, the consumption of reacting ions via nucleation and growth is generally very fast, thus the impact of residence time on the extent of reaction becomes less notable.

### ***2.5.4 Intensified Reactors and Precipitation Processes***

Nanoscale materials have attracted great scientific interest due to the resulting advantages of the reduced size. To achieve nano-sized precipitation crystals, high supersaturation levels, generated by enhanced mixing, as well as control and prevention of particle agglomeration are necessary [128]. Therefore, intensified reactors such as SDRs and microreactors offer great potentials for production of nanoparticles as they provide good micromixing to enhance the nucleation rate, in addition to short and controllable residence times to limit particle growth. Such miniaturised reactors provide a more homogeneous reaction environment in terms of concentration, temperature and mass transfer, therefore particle size and distribution can be tightly controlled. This concept is validated by the production of BaSO<sub>4</sub> nanoparticles using microemulsion systems [135, 136] where the confined geometry of water droplets provides a very homogenous mixing environment and therefore tight control of the precipitation process and particle size.

Lim [66] and Auone and Ramshaw [16] studied the gas-liquid mass transfer performance of SDRs for absorption of O<sub>2</sub> into thin liquid films. Their results implied a strong link between the disc rotational speed and achieved mass transfer coefficient. More recently, Burns and Jachuck [68] studied the precipitation of CaCO<sub>3</sub> on a spinning disc reactor and found that conversion was affected by both feed flowrate and disc rotational speed. Cafiero et al. [26] produced BaSO<sub>4</sub> particles of 0.7 μm in size on a spinning disc reactor. The results showed that the crystal production rate increases with increasing rotational speed whilst the average crystal size decreases. A more recent investigation [137] also confirmed that the mean particle size is inversely proportional to the disc rotational speed for production of hydroxyapatite nanoparticles in a SDR.

McCarthy et al. [132] produced barium sulphate particles in narrow channel reactors, with mean crystal sizes as fine as 0.2 μm. The results indicated that high supersaturation ratios and high channel velocities, obtained at higher liquid flowrates and smaller channel diameters, lead to production of small particle sizes. Additionally, the channel diameter was found to determine the crystal morphology, whereby spherical particles were formed in the smallest channels, whilst coarse, tabular crystals were produced in larger diameters.

A more recent contribution by Wang et al. [129] reports the production of barium sulphate nanoparticles with an average size of 37 nm and narrow CSD in a tube-in-tube microchannel reactor. The reactor consisted of two coaxial tubes which form an annular microchannel. The liquid flowing inside the inner tube can disperse into the annular chamber from the microporous section of the pipe and mix with the other liquid stream. The particle size was controlled by adjusting the feed concentration, total flow rate and the pore size. Increasing the total flowrate and reducing the pore size resulted in enhanced mixing and thus smaller particle sizes were achieved. Stoller et al. [138] also report the production of TiO<sub>2</sub>

nanoparticles on a spinning disc reactor and the effect of feed location on particle size. The use of microreactors to produce nanoparticles of semiconductors [139] and metals [140] is also reported in the literature.

The available literature suggests that the hydrodynamics of the reaction media affects both the production rate and the crystal size. In intensified reactor technologies such as narrow channel reactors and SDRs, the hydrodynamics characteristics are readily controlled by adjusting the liquid flowrate, channel diameter in narrow channel reactors and rotational speed in SDRs. These offer extra degrees of freedom and more flexibility in controlling the precipitation process, including the crystal size and morphology. Considering the evidence, SDRs are strong candidates for the production of particles in nano-size range. Therefore, control of the particle size using the rotational speed is of great scientific interest.

### ***2.5.5 Control of the Precipitation Process***

The control objective in a crystallisation process is to achieve a certain product specification in terms of particle size, CSD, purity, yield or morphology. The particle size not only determines the product quality but also affects the downstream processes such as dewatering, filtration and drying. Therefore, it is desired to control the particle size within a specific range. As discussed previously, supersaturation drives the crystallisation process and thus is the most important factor which affects the properties of the crystals. Therefore the control objectives may be achieved by controlling the supersaturation levels in a crystalliser. Disturbances to the process may include changes in the mixing intensity and variations in the feed temperature and composition [113].

Braatz [141] summarizes the challenges of controlling the crystallization process as being due to significant uncertainties in the kinetics, the ambiguity in effects of mixing, process nonlinearity and sensor limitations. For effective identification and control of the precipitation process, measurements of the solution concentration and crystal size distribution are required. Attenuated Total Reflection - Fourier Transform Infrared (ATR-FTIR) and Raman spectroscopy have been used to measure the solution concentration for feedback control of crystallisation processes [142, 143]. Devices based on the laser backscattering approach may be used to provide in-situ measurement of the particle size and distribution [144]. Chianese and Kramer [145] provide a comprehensive catalogue of the instrumentation and methodologies available for online or in situ monitoring of the relevant process variables in a crystallisation process, which if coupled with a suitable control recipe can ensure effective control of such processes at an industrial scale. However, according to Mersmann [113] in most industrial crystallisation processes only easily measurable parameters such as temperature, flowrate, level and pressure are used to control the process, whilst online measurements of particle size and solution concentration are seldom used as feedback signals in the control loop.

During any precipitation reaction, a change in conductivity is observed due to the addition of the feed streams and subsequent consumption of the ions to form the precipitate product. Concentration, and therefore supersaturation, may be inferred from conductivity

measurements and used as a feedback control signal. This approach, adopted in the present study, is discussed in more details in the following section.

### 2.5.5.1 Conductivity Measurements

During any precipitation reaction, the solution conductivity is reduced as the reacting ions precipitate out and no longer contribute to the solution's conductivity. Depending on the feed addition mode and mixing characteristics of the crystalliser, the solution conductivity may initially increase at low reaction rates.

For very dilute solutions of a strong electrolyte (one that freely dissociates), conductivity increases with increasing concentration of ions linearly. The conductivity-concentration relationship becomes progressively nonlinear as the ion concentrations in the solution increase, due to increased level of ion interactions. In very concentrated solutions, the attractive forces between charged ions can give rise to ion association and formation of neutral particles, thus, conductivity begins to fall [146].

Taguchi et al. [147] used conductivity measurements to calculate the thermodynamic supersaturation in a series of barium sulphate batch precipitation reactions. The calculated saturation profiles showed measureable sensitivity to the stirrer speed, wherein the rate of decay of supersaturation was faster at higher rotational speeds. Stanley [148] also used conductivity measurements to monitor the concentration variations in semi-batch precipitations of barium sulphate. The results indicated sensitivity of the conductivity profile to stirrer speed, where faster reaction rates prevailed at higher agitation intensities. The same trend is also reported by Rodgers et al. [149] for precipitation of barium sulphate in a semi-batch stirred vessel. Burns and Jachuck [68] also monitored the production of  $\text{CaCO}_3$  on a spinning disc reactor by inferring the product concentration from conductivity measurements.

The main drawback of using conductivity measurements to infer concentration of reacting ions is that other non-reacting ions and impurities can also influence the conductivity readings and therefore deteriorate the control performance. Further, the correlation between conductivity measurements and supersaturation may be time-varying as a result of process disturbances. Therefore, the application of conductivity measurements for control of an industrial precipitation process may not be straight forward. However, for the purpose of the current research in a controlled lab environment, conductivity measurements for feedback control of the process are the most attractive and affordable approach.

## 2.6 *Thermographic Analysis of Thin Liquid Films*

An Infrared (IR) camera is adopted in the present work to study the film hydrodynamics as well as the temperature profiles across heating liquid films, at various operating conditions. The flow patterns and surface characteristics of thin liquid films strongly influence the heat and mass transfer processes in SDRs, and thus the intensification capability of such units. Therefore, it is often essential to define an operation window which entails the desired flow regimes and surface characteristics. Thermographic techniques may provide a useful insight

for achieving effective control and operation of SDRs by shedding more light on flow characteristics and heat transfer performance at various operating conditions.

Thermocouples are commonly used to measure fluid temperatures. However, measuring the film temperature by this invasive technique requires the thermocouple to protrude through the film which may disturb the continuous flow of fluid, especially in the case of a SDR where fluid films are very thin. Further, the thin films may not provide sufficient immersion depth for the thermocouple tip to acquire accurate measurements. The only temperature measurements available in SDRs are commonly provided by thermocouples inserted in the disc via a slip ring assembly [16, 61, 63, 64] or immersed in the heat transfer fluid [57], whereby the film temperature has to be inferred from such indirect measurements. In contrast an IR thermal imager provides non-contact means of determining the temperature profiles across thin liquid films.

Tight temperature control of the liquid films produced on SDRs may be important in a number of ways. Firstly, as temperature often has a significant effect on the rate of chemical reactions, quantified by the Arrhenius equation, the actual film temperature may directly influence the conversion and selectivity achieved in SDRs. Further, accurate control of the film temperature may be essential in some applications due to safety implications. SDRs also offer great potentials for processing viscous materials such as polymer melts. The actual film temperature plays an important role in the efficiency of processing such materials, indicating again that monitoring and control of the film temperature, which is directly linked to film hydrodynamics, is of great importance in SDR operation. A brief overview of thermographic techniques is provided next.

### ***2.6.1 Thermographic Measurements***

All objects emit infrared radiation at temperatures above absolute zero and the amount of radiation increases with temperature. Thermal imaging cameras [150, 151] detect infrared radiation and produce a visual image, referred to as a thermogram, which depicts the thermal variations within the object being measured. Thermography is applied in a wide variety of different fields such as military and security services, building and infrastructure, research and industry, as well as medical applications and many more [152].

The thermal imaging camera, or IR camera, receives IR radiation from the object being measured, plus those from its surroundings reflected onto the target object's surface. These radiation components are attenuated to some extent as they pass through the atmosphere due to absorption by gases and scattering by particles. Since the atmosphere can absorb part of the radiation energy, it can also radiate some itself [153]. The accuracy of the object temperature estimated by the camera is often closely linked to how accurately the following input parameters to the thermal imaging camera are specified:

1. The emissivity of the object
2. The reflected apparent temperature
3. The distance between the object and the camera
4. The relative humidity

## 5. Temperature of the atmosphere

The emissivity value of the object is typically the most important parameter which needs to be determined accurately. The accuracy of the input parameters becomes less critical if the target object has high emissivity and is significantly hotter than its surroundings [152].

### 2.6.1.1 Emissivity

Emissivity is a measure of how much radiation is emitted from the object, compared to that from a blackbody of the same temperature. Therefore, theoretically, emissivity values range from 0 to 1. Accurate temperature measurements using an IR camera requires accurate knowledge of the object's emissivity value. Emissivity values for common materials are available in the literature; however, these values pertain to specific measurement conditions and should therefore be used with caution. Further, the knowledge of emissivity at different temperatures and for the liquid phase is rare. Emissivity values are affected by the factors listed below [152] :

1. Material (metals/non-metals): a non-metal emitter often has an emissivity value above 0.8. Conversely, metals are generally highly reflective and exhibit low values of emissivity, often below 0.2.
2. Surface condition (rough/ polished): polished surfaces may have emissivity values as low as 0.02, but the emissivity of the same material with a roughened surface, can be much higher and even reach values above 0.8. For instance, the emissivity of polished steel is reported as 0.07 whereas the corresponding value for steel with a roughened surface is 0.81 [154].
3. Regular geometry (grooves, cavities, etc.): Regular surface structures typically increase the value of emissivity.
4. Viewing angle: an object which is observed from a direction perpendicular to its surface has higher emissivity than when observed at oblique angles.
5. Wavelength: the emissivity of metals usually decreases with wavelength, whereas non metals can show increases as well.
6. Temperature: emissivity usually varies with temperature.

A study of infrared characteristics of thin polymer films [155] showed that emissivity is also dependent on film thickness (increases with increasing film thickness). The same pattern was also observed for several thin films applied to a stationary stainless steel surface at cryogenic temperatures [156].

Emissivity can directly be measured using several techniques. The easiest method is to attach tape or paint of known emissivity to the object being measured. A thin opaque adhesive tape, such as a black electrical tape (typical emissivity of 0.97) is suited for this purpose. The object's emissivity value can be found by varying the emissivity parameter in the camera software until the object's temperature matches the known surface temperature of the tape/paint, assuming the temperature distribution across adjacent surfaces is uniform and there is thermal equilibrium between the tape/paint and the object [152]. This method is, however, only applicable to solid surfaces. Pyrolaser and Pyrofiber [157] infrared

thermometer instruments are capable of real time emissivity measurement by measuring the target's diffuse reflectivity. Martan et al. [158] calculated a view factor from a set of calibration curves for known metallic samples and the literature value of their emissivity. The view factor was then used to calculate the emissivity of tungsten thin films and the liquid phase emissivity of various metals and silicone.

### 2.6.1.2 Errors and Uncertainties

Sources of errors in temperature measurements by means of thermographic techniques can be categorised into three groups as outlined below [159]:

1. Method: resulting from incorrect evaluation of input parameters such as object's emissivity, atmospheric temperature, relative humidity, etc.
2. Calibration: errors can result from different measurement conditions for the calibration data and each experiment, such as different camera to object distance. Accuracy of the reference standard, number of calibration points and interpolation can also influence the accuracy of the final temperature measurement.
3. Electronic path: factors such as detector noise can also influence the temperature measurements.

Incorrect setting of the object emissivity is known to be the main cause of significant temperature measurement errors. In the present work, the main uncertainty in the measured values is believed to be caused by the estimation of emissivity values for thin liquid films on a rotating disc.

## 2.7 Summary

This chapter provided an overview of the concept of process intensification, outlining various technologies that can potentially lead to major improvements in processing efficiency and ultimately more sustainable developments. The key features and applications of an intensified reactor technology, namely spinning disc reactor, were discussed in more detail. A survey of the available literature on control of intensified equipment, including the potential challenges, was then outlined in this chapter.

The objective of the present research is to provide a better understanding of the control aspects of an intensified unit with fast dynamics, i.e. the spinning disc reactor. Two processes have been selected to facilitate the proposed investigations: a) pH control of a strong acid/base neutralisation reaction, b) control of supersaturation level inferred from conductivity measurements in barium sulphate precipitation. Both are typical processes that may be carried out in a SDR. The former control task is achieved by adjusting the reagent flowrate, whilst the latter involves exploiting the disc rotational speed as the control manipulated variable. A literature review of the two mentioned processes including their characteristics and the common control strategies was also provided in the present chapter.

The use of an infrared thermal imaging camera is proposed as part of the current research to study the liquid film hydrodynamics and temperature profiles, which can strongly influence

the operation and control of SDRs. Therefore, in this chapter a brief introduction of thermographic techniques was also provided.

## Chapter 3. Preliminary Studies

As discussed in the previous chapter, the increased level of complexity and the degree of interactions in some intensified equipment may lead to more challenging operation and control of such units. Furthermore, the control difficulties may arise from the fast dynamics and short residence times of low volume intensified equipment, which is the focus of the present investigation. One of the consequences of significant equipment size reduction is that the dynamics of commercially available instrumentation may become comparable or even slower than that of the process. Therefore, the instrumentation dynamics might have a significant impact on the control performance and should be accounted for in the design of an appropriate control scheme. Including instrumentation dynamics in a model based controller design leads to high order, unconventional controllers.

Abd Shukor and Tham [160] employed the ‘Direct Synthesis’ method to design a controller for a general feedback loop including the dynamics of the actuator and the sensor, as shown in Figure 3-1. If a first order Taylor series approximation for the time delay element is applied, this approach leads to a PIDD<sup>2</sup> controller in series with a first order low pass filter whereby the second order derivative term ( $D^2$ ) is a direct result of including the instrumentation dynamics.

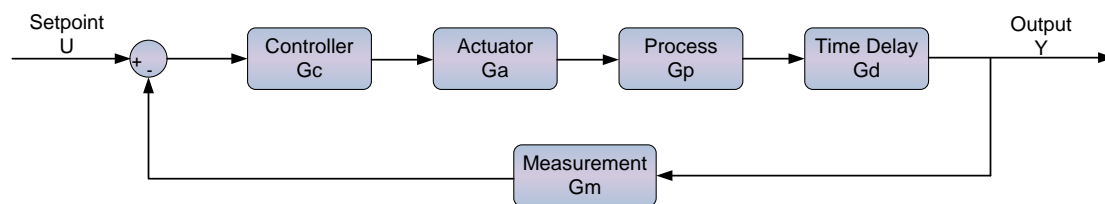


Figure 3-1. Closed-loop block diagram

The applied methodology results in controllers that cancel the dynamics of both process and actuators in the forward path. This implies that only the sensor dynamics and the process time delay influence the control performance. Analytical analysis of the control performance for various values of sensor time constant and time delay has shown that the controller is relatively insensitive to variations in those two parameters, provided the sensor time constant and process time delay are smaller than 0.2s and 1s respectively. However, the overall controller performance deteriorates exponentially as the transmitter time constant and process delay become larger [160].

Jones and Tham [81] also derived a PIDD<sup>2</sup> controller using an IMC design for a general feedback loop which included the sensor and actuator dynamics. The authors compared the performance of the high order controller with a reduced order classical and industrial PID controller, which were designed by truncating the high order term ( $D^2$ ) in the original design. The simulations were carried out for an intensified system in which the response times of the process, actuator and sensor were equal. The results indicated that overall, the performance of the original high order control and the reduced order PID controllers are very similar, where



the additional second order derivative term provided slightly more smoothing of the setpoint transient response.

In this chapter a model based controller design for a feedback control loop which includes the instrumentation dynamics is outlined first. Then several model order reduction techniques are considered which lead to design of a conventional PI/PID algorithm. The controllers are subsequently applied to a simulated intensified and conventional system firstly to evaluate the model order reduction techniques and secondly to highlight the potential impacts of equipment size reduction on control performance.

### 3.1 Controller Design

In the present study, the direct synthesis approach [161] which is a model based controller tuning method is applied to a general feedback system in order to design applicable control algorithms. Briefly, this approach enables the synthesis of a controller that can produce a specific closed loop response, based on the dynamics of the system. If the overall process is described by a First Order Plus Dead Time (FOPDT) or a Second Order Plus Dead Time (SOPDT) model, then the direct synthesis method yields a PI or PID control algorithm respectively, which are the most commonly used controllers in industry [102]. However, applying the direct synthesis approach to a model higher than second order leads to a non-standard high order controller, which may not be practical to implement industrially. In the present study assuming that the actuator, process and measurement dynamics are first order then the overall open loop system dynamics is described by a third order model. Applying a model based controller design such as the direct synthesis to a third order model yields a PIDD<sup>2</sup> controller of the following format (see Appendix B):

$$G_c = K_c \left( 1 + \frac{1}{T_I s} + T_D s + T_D^2 s^2 \right) \quad (3-1)$$

where,  $K_c$  = controller gain

$T_I$  = integral time constant

$T_D$  = derivative time constant

$T_D^2$  = second order derivative time constant

The overall performance of a controller with a first order, plus a second order derivative term is expected to be rather poor. This is attributed to large derivative kicks, due to increased sensitivity of the system to measurement noise and sudden changes in the setpoint, as discussed by Abd Shukor [162]. Additionally, such high order controllers are not commercially available, implying that their implementation may not be practical. However, if the original high order process model can be approximated by a SOPDT or a FOPDT model, then the direct synthesis approach leads to a PID or a PI controller respectively with the following structures (refer to Appendix B):

$$G_c = K_c \left( 1 + \frac{1}{T_I s} + T_D s \right) \quad (3-2)$$

Or,

$$G_c = K_c \left( 1 + \frac{1}{T_I s} \right) \quad (3-3)$$

The controllers gain and time constants are calculated based on the parameters of the process model, in addition to a user specified closed loop time constant,  $\lambda$ , which is the only tuning parameter in the direct synthesis method. As outlined above, including the instrumentation dynamics leads to a high order overall process model which in turn leads to design of high order non-standard controllers if a model based tuning method is adopted. Most commonly used PI or PID controllers may be utilized if the original high order models are reduced in order. A number of order reduction techniques to enable the design and application of standard controllers are discussed next.

### ***3.2 Model Order Reduction***

As discussed previously, including the instrumentation dynamics in a model based controller design approach results in high order non-standard control structures. However, PID controllers are the most common controllers used in industry due to their simplicity, robustness and established credibility from successful applications. Thus, it is often desired to employ standard PID controllers to achieve the control objectives. To obtain PID controller settings for a high order model, using a model based tuning method, two approaches may be adopted:

1. Reduce the high order process model to a first or a second order form, and then apply a model based controller design to obtain a PI or a PID controller respectively. Or,
2. Design a high order controller based on the full order of the process and then apply a model order reduction technique to the controller's design equation to achieve a PI/PID structure.

In the present study, four model order reduction techniques to approximate the behaviour of the full order process model, along with one method to reduce the controller's order are employed. The model order reduction techniques investigated in this study are:

1. Step Response
2. Frequency Response
3. Isaksson and Graebe's Method
4. Skogestad's Method

whilst the method to reduce the controller's order is based on the Maclaurin's expansion series. Note that relatively simple methods which can be easily implemented are selected here, as described next.

#### ***3.2.1 Step Response***

The step response test [163] also referred to as process reaction curve, is a system identification technique which may be used to reduce the process model order. This method aims at obtaining a FOPDT model via an open loop step input test. An open-loop system

includes the dynamics of the actuator, process and measurement as well as the time delay, as illustrated in Figure 3-2.

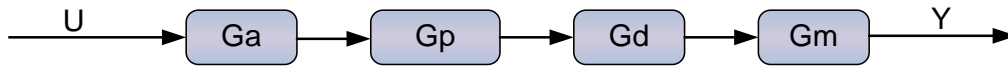


Figure 3-2. Open-loop block diagram

A unit step change  $U$  is introduced to the system and the output response  $Y$  is observed in order to enable approximation of the system behaviour by a first order plus delay model, presented below:

$$\frac{Y}{U} = \frac{k}{\tau s + 1} e^{-\theta s} \quad (3-4)$$

An overall gain, time constant and time delay may be estimated from the open loop step test response, as graphically illustrated in Figure 3-3 for an example system. The system gain,  $k$ , is equal to the final change in output per unit step input. The time delay,  $\theta$ , is the point at which the gradient line drawn on the steepest section of the graph intersects with the time axis, whilst the time constant,  $\tau$ , is equal to the time taken to reach 63.2% of the final response.

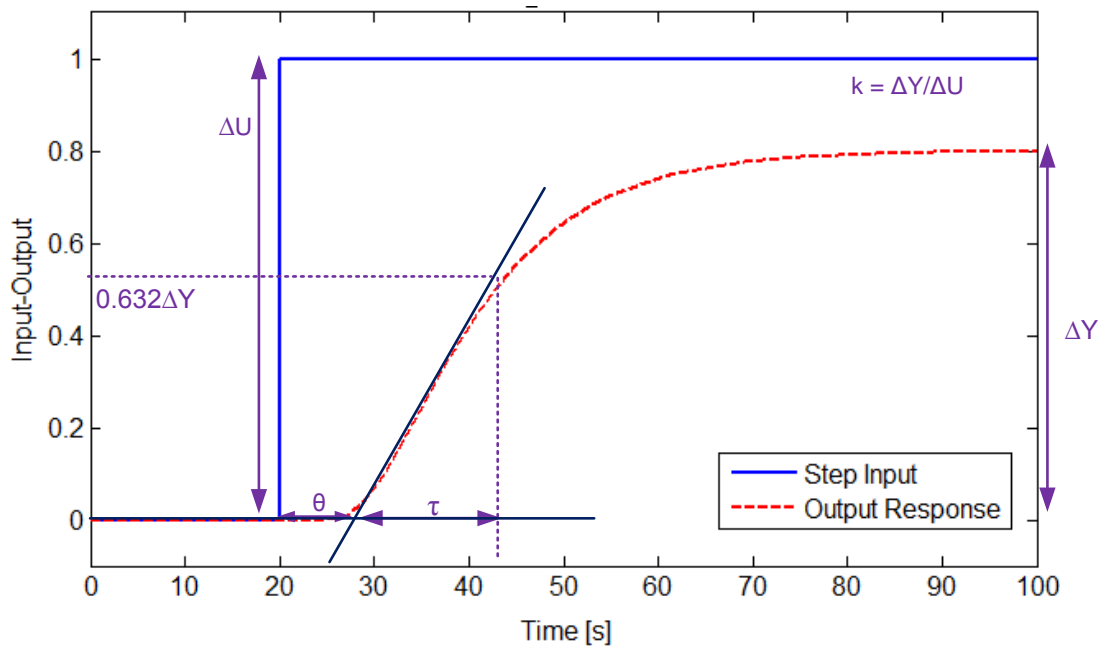


Figure 3-3. Step response

### 3.2.2 Frequency Response

The frequency response [163] of a high order process may also be used to approximate the system to a FOPDT model. For a stable linear system, given a sinusoidal input in the form  $u(t) = A \sin(\omega t)$ , the resulting output is  $y(t) = B \sin(\omega t + \phi)$ . The ratio  $B/A$  is referred to as the ‘Amplitude Ratio’ indicating the degree by which the input signal is magnified when it passes through the system; whilst,  $\phi$  is the degree of shift in the input signal termed as ‘Phase Shift’.

For any transfer function,  $G(s)$ , substituting the Laplace operator,  $s$ , with ' $j\omega$ ' transforms the system from the Laplace domain to the frequency domain. Where,  $j$  is the complex operator  $\sqrt{-1}$  and  $\omega$  is the frequency of oscillations. The amplitude ratio (AR) and phase shift ( $\phi$ ) are calculated according to the following equations:

$$AR = |G(j\omega)| = \sqrt{(\text{Real part of } G(j\omega))^2 + (\text{Imaginary part of } G(j\omega))^2} \quad (3-5)$$

$$\phi = \angle G(j\omega) = \tan^{-1} \left( \frac{\text{Imaginary part of } G(j\omega)}{\text{Real part of } G(j\omega)} \right) \quad (3-6)$$

The amplitude ratio and phase shift are determined solely by the process parameters (gain, time constant and delay) and frequency of the input signal, therefore the frequency response may be employed for system identification purposes. The frequency response of a system to a sinusoidal input change is commonly illustrated graphically by means of a Bode plot which consists of two graphs: amplitude ratio vs. frequency and phase shift vs. frequency. The amplitude ratio is commonly expressed in units of decibel (dB) and the phase shift in degrees. The Bode plot of a system may be used to approximate the process to a FOPDT model as outlined below.

For a first order plus delay model,

$$G = \frac{k}{\tau s + 1} e^{-\theta s}$$

The amplitude ratio and phase shift are given by the following expressions:

$$AR = \frac{k}{\sqrt{1 + \tau^2 \omega^2}} \quad (3-7)$$

$$\phi = -\tan^{-1}(\tau\omega) - 57.3\theta\omega \quad (3-8)$$

Therefore, the frequency response of a high order process may be used to estimate an overall gain, time constant and delay to approximate the system with a FOPDT model. From the above expression for AR it can be seen that the amplitude ratio is equal to the overall gain when frequency approaches zero. Therefore, the overall gain is the point where the low frequency asymptote on the amplitude ratio graph cuts the y-axis, (see Figure 3-4). The overall time constant is equal to the inverse of the corner frequency,  $\omega_c$ , which is the frequency at which the low and high frequency asymptotes on the amplitude ratio graph intersect. Finally, evaluating the phase shift at the corner frequency enables the calculation of the time delay according to the following equation:

$$\theta = -\frac{\phi(\omega_c) + 45}{57.3\omega_c} \quad (3-9)$$

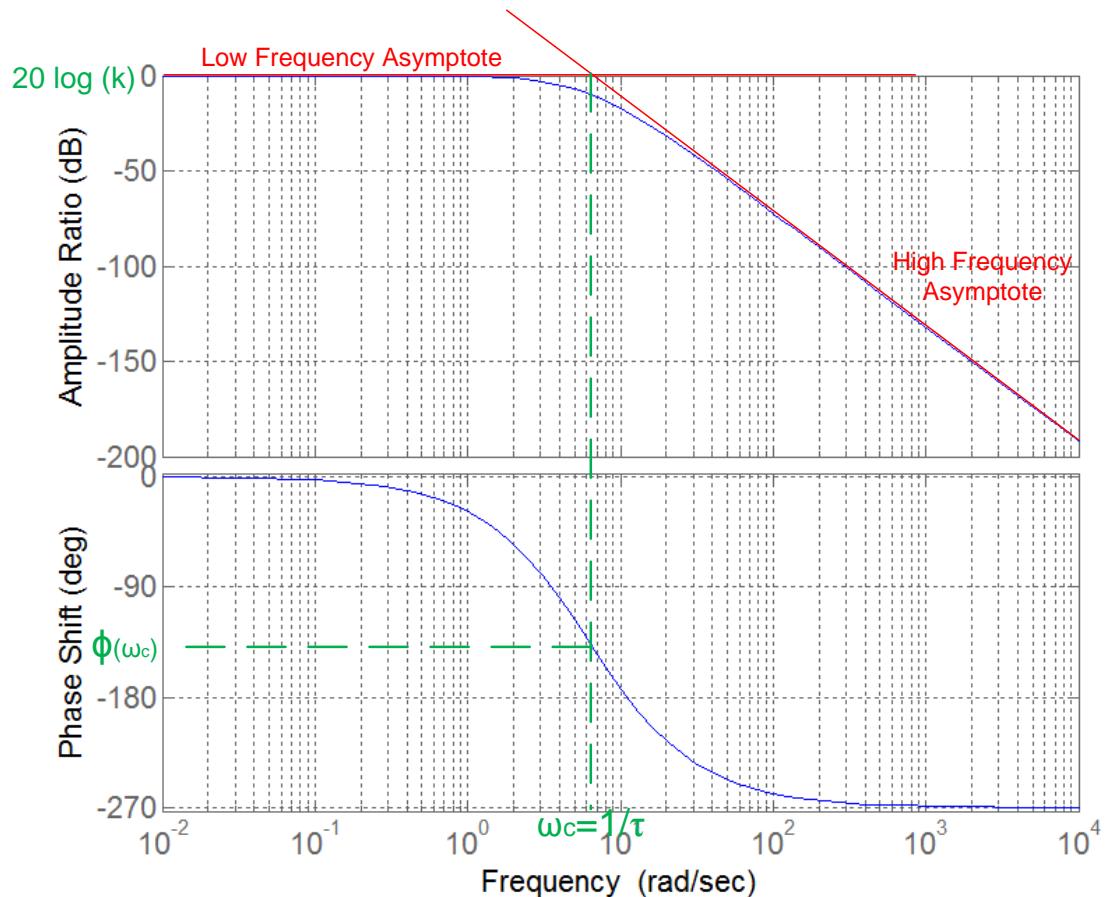


Figure 3-4. Frequency Response

The process model order reduction by analysis of the frequency response leads to a FOPDT model for which a PI controller is readily obtained via a model based controller design technique. For the first two model order reduction techniques described here, namely step response and frequency response, if the high order process model is known, the step and frequency responses of the system can be readily formulated via simulation. However, if the original full order process model is not known, the step and frequency responses of the process can be determined experimentally, allowing identification of the overall process behaviour by a reduced order model. The empirical low order model of the system may then be used as a platform for analysis and determination of a suitable set of controller parameters. However, the next two model order reduction techniques to be described are based on an analytical approach, and thus require prior knowledge of the original model.

### 3.2.3 Isaksson and Graebe's Method

The technique proposed by Isaksson and Graebe [164] is also based on reducing the process model to a suitable format for PID design. However, unlike the previous two methods this analytical approach requires knowledge of the original high order process model. The method considers the numerator and denominator of a transfer function separately and involves determining the dominant poles and low order coefficients of the plant. If the original high order model is described by the following transfer function,

$$G(s) = \frac{B(s)}{A(s)}$$

Then the reduced order approximation of the system is equal to:

$$G^*(s) = \frac{\frac{1}{2}(B_1(s) + B_2(s))}{\frac{1}{2}(A_1(s) + A_2(s))} \quad (3-10)$$

where,  $B_1$  and  $A_1$  are polynomial that retain only the slowest roots (dominant poles) in the numerator and denominator of the original model respectively. Whilst,  $B_2$  and  $A_2$  are polynomial that retain the low order coefficients of the numerator and denominator of the initial model. If the original model contains a delay term, then the delay free portion of the model may be reduced using the above procedure. Subsequently, the initial delay term may be added to the approximated model. Alternatively, the delay term may be included in the transfer function of the original process using a Pade approximation before the reduction procedure is applied. The Isaksson and Graebe's method is simple and easy to implement, provided that the process model is known.

### 3.2.4 Skogestad's Method

Skogestad [165] also proposed a method to reduce the order of the process model by applying the 'half rule' which is based on evenly distributing the largest neglected (denominator) time constant between the effective time delay and the smallest retained time constant. In this method each numerator term ( $T_0s+1$ ) with  $T_0 > 0$  of the high order model is first simplified with a denominator term ( $\tau_0s+1$ ),  $\tau_0 > 0$  using the following rules:

$$\frac{T_0s+1}{\tau_0s+1} \approx \begin{cases} T_0/\tau_0 & \text{for } T_0 \geq \tau_0 \geq \theta \\ T_0/\theta & \text{for } T_0 \geq \theta \geq \tau_0 \\ 1 & \text{for } \theta \geq T_0 \geq \tau_0 \\ T_0/\tau_0 & \text{for } \tau_0 \geq T_0 \geq 5\theta \\ \frac{(\tilde{\tau}_0/\tau_0)}{(\tilde{\tau}_0 - T_0)s + 1} & \text{for } \tilde{\tau}_0 = \min(\tau_0, 5\theta) \geq T_0 \end{cases} \quad (3-11)$$

where  $\theta$  is the final effective delay whose exact value depends on the subsequent approximations. Therefore, it may be required to initially guess  $\theta$  and iterate the procedure until the guessed and estimated values are equal.  $\tau_0$  is usually chosen as the closest denominator time constant to  $T_0$ . Once this process is carried out for all of the positive numerator time constants, the process transfer function will have the following form:

$$\frac{\prod_j (-T_{j0}s + 1)}{\prod_i (\tau_{i0}s + 1)} e^{-\theta_0 s} \quad (3-12)$$

where,  $T_{j0} > 0$  and the time constants are ordered in descending magnitude. The process time constant and effective time delay for a FOPDT model are approximated as:

$$\tau = \tau_{10} + \frac{\tau_{20}}{2} \quad (3-13)$$

$$\theta = \theta_0 + \frac{\tau_{20}}{2} + \sum_{i \geq 3} \tau_{i0} + \sum_j T_{j0} + \frac{T_s}{2} \quad (3-14)$$

where  $T_s$  is the sampling period for cases with digital implementation. Similarly, to obtain the time constants and effective delay of a SOPDT model the following approximations are applied:

$$\tau_1 = \tau_{10} \quad (3-15)$$

$$\tau_2 = \tau_{20} + \frac{\tau_{30}}{2} \quad (3-16)$$

$$\theta = \theta_0 + \frac{\tau_{30}}{2} + \sum_{i \geq 4} \tau_{i0} + \sum_j T_{j0} + \frac{T_s}{2} \quad (3-17)$$

As with Isaksson and Graebe's method, the model order reduction based on the half rule requires knowledge of the original high order process model. Skogestad's method may be more difficult to implement compared to the technique proposed by Isaksson and Graebe, due to the possible iterations in the model reduction algorithm. One advantage of Skogstad's method is that the approach accounts for the contribution from the sampling period in a digital control loop.

The four model order reduction methods outlined so far primarily focus on reducing the order of the original process model to enable design of a PI or PID controller via a model based design approach. In contrast, the next method discussed in this chapter is aimed at directly approximating a high order controller to a PI or a PID controller.

### 3.2.5 Maclaurin Series Expansion

As discussed earlier in this chapter including the instrumentation dynamics in a model based controller design leads to non-standard high order controllers such as a PIDD<sup>2</sup> controller. If the high order controller is rearranged into the following format,

$$G_c = \frac{f(s)}{s} \quad (3-18)$$

Approximation of  $f(s)$  by the first three terms of a Maclaurin series expansion yields a PID controller algorithm of the form,

$$G_c^* = \frac{1}{s} \left[ f(0) + f'(0)s + \frac{f''(0)}{2!} s^2 \right] \quad (3-19)$$

where,  $f'$  and  $f''$  are the first and second order derivatives of the controller function  $f$  with respect to the Laplace operator  $s$ . It can be noted that considering only the first two terms of a Maclaurin series expansion leads to a PI controller design. It can be readily shown that

approximating a high order controller, such as a PIDD<sup>2</sup>, to a PID controller using the Maclaurin series expansion is equivalent to truncating the high order terms in the original controller design equation (see Appendix C).

So far in this chapter, four approaches for approximation of a high order process model to a first or a second order process model, along with a method of reducing a high order controller to a PI or PID format have been presented and discussed. In the next section, the reduced order process models obtained from different methods are compared to the original high order model by means of frequency response analysis.

### 3.2.6 Frequency Response Analysis of Reduced Models

The process model order reduction techniques discussed previously, namely the step response, frequency response, Isaksson and Graebe's and Skogestad's methods are evaluated by means of frequency response analysis. A high order model of a system would be approximated sufficiently well by a reduced order model, if the Bode plots of the two systems are identical, or similar, over a given range of frequencies. For control purposes it is most critical to have a good approximation of the system at the bandwidth [165].

In the present study two example process models are considered, to simulate a conventional and an intensified system. Time constants of 10 and 0.1 seconds are selected for the former and latter systems respectively. The relative magnitude of the conventional and intensified process time constants represents a 100 fold reduction in the equipment size whilst the production rate is kept constant. The dynamics of the actuator and measurement device for the intensified and conventional systems are selected to be identical, implying that the intensified system is coupled with commercially available instrumentation. The time constants of the actuator and sensor for both systems were selected as 0.2 seconds and a delay of 1 second was also included in the process model. These values were identified [160] as thresholds beyond which (i.e. larger transmitter time constant and time delay) the control performance starts to deteriorate exponentially. The process, actuator and measurement device were assumed to have a unity gain as outlined in Table 3-1.

Table 3-1. Control loop elements

	<i>Conventional</i>	<i>Intensified</i>
<i>Process</i>	$\frac{e^{-s}}{10s+1}$	$\frac{e^{-s}}{0.1s+1}$
<i>Actuator</i>	$\frac{1}{0.2s+1}$	$\frac{1}{0.2s+1}$
<i>Measurement device</i>	$\frac{1}{0.2s+1}$	$\frac{1}{0.2s+1}$

The overall process models for intensified and conventional systems along with the approximated low order models obtained from four different process model order reduction techniques are presented in Table 3-2. The derivations of the low order approximations are given in Appendix D. It can be noted that the low order approximations of the original



models obtained from various methods are very similar except for those achieved by the frequency response technique. In the latter case, the process time constant is significantly smaller than that obtained by other methods, particularly for the case of the example conventional system. However, it should be noted that the estimated delays obtained from the frequency response of the systems are larger, implying that a portion of the lag time constant is approximated as time delay.

Table 3-2. Original and reduced order models

	<i>Conventional system</i>	<i>Intensified system</i>
<i>Original model</i>	$G = \frac{1}{(10s + 1)(0.2s + 1)^2} e^{-s}$	$G = \frac{1}{(0.2s + 1)^2(0.1s + 1)} e^{-s}$
<i>Step response</i>	$G^* = \frac{1}{10.4s + 1} e^{-s}$	$G^* = \frac{1}{0.5s + 1} e^{-s}$
<i>Frequency response</i>	$G^* = \frac{1}{0.77s + 1} e^{-1.94s}$	$G^* = \frac{1}{0.17s + 1} e^{-1.25s}$
<i>Isaksson &amp; Graebe's method (1<sup>st</sup> order)</i>	$G^* = \frac{1}{10.2s + 1} e^{-s}$	$G^* = \frac{1}{0.35s + 1} e^{-s}$
<i>Isaksson &amp; Graebe's method (2<sup>nd</sup> order)</i>	$G^* = \frac{1}{2.02s^2 + 10.2s + 1} e^{-s}$	$G^* = \frac{1}{0.04s^2 + 0.35s + 1} e^{-s}$
<i>Skogestad's method (1<sup>st</sup> order)</i>	$G^* = \frac{1}{10.1s + 1} e^{-1.3s}$	$G^* = \frac{1}{0.3s + 1} e^{-1.2s}$
<i>Skogestad's method (2<sup>nd</sup> order)</i>	$G^* = \frac{1}{(10s + 1)(0.3s + 1)} e^{-1.1s}$	$G^* = \frac{1}{(0.2s + 1)(0.25s + 1)} e^{-1.05s}$

The delay free portions of the above models are used to compare the frequency responses of the original model with the reduced order approximations. It should be noted that the delay terms have no influence on the amplitude ratio and solely contribute to the value of the phase lag. The impact of delay on the phase diagram is only significant at high frequencies which are outside the range of interest in the current analysis. Therefore, as lower frequencies (around the bandwidth) are of prime focus in this study, excluding the delay terms does not diminish the validity of the analysis presented here.

Figure 3-5 illustrates the frequency responses of the original model and the reduced order models for a simulated conventional system. It can be seen that at the bandwidth frequency (0.1 rad/s), amplitude ratio and phase shift responses of the original process model are identical for all reduced order models barring the approximation by the frequency response. Applying the frequency response system identification yielded a FOPDT model with a time constant of 0.77 second (see Table 3-2) which is much smaller than the dominant process time constant of 10 seconds in the original model. This explains the rather large differences observed in the frequency responses of the original and reduced order models. It can be concluded that the step response, Isaksson and Graebe's and Skogestad's methods all provide sufficiently accurate approximations of the original model of a simulated conventional system and can be 'safely' used to obtain PI or PID controller tuning parameters to control the original process.

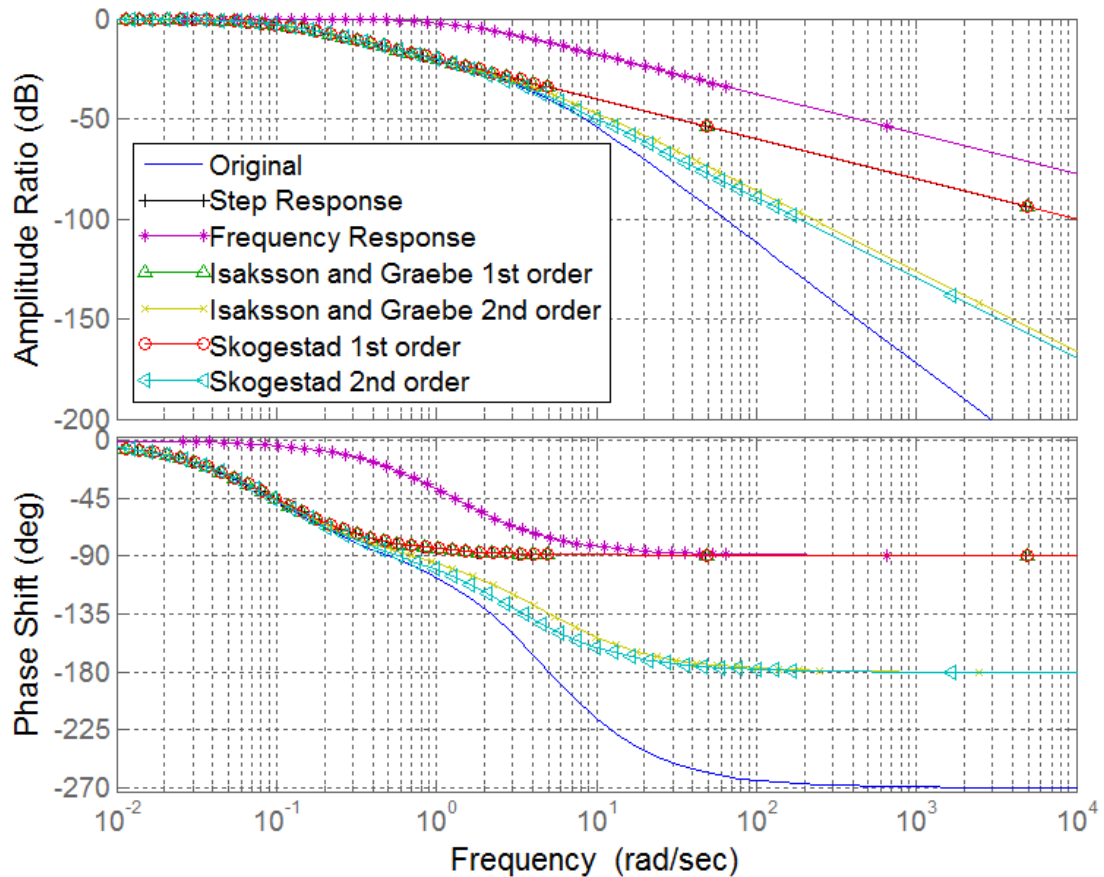


Figure 3-5. Conventional system Bode plots

Figure 3-6 presents the frequency responses of the original model simulating an intensified system and the corresponding reduced order models. The amplitude ratio of the high order and reduced order models are similar at the bandwidth frequency (3 rad/s), however the phase shifts of the reduced order models show larger deviations from the original model at the bandwidth frequency compared to that observed for the simulated conventional system. Overall, the frequency response of the approximated models show satisfactory agreement with the original model at the bandwidth frequency and may be safely used to obtain tuning parameters for a PI/PID controller.

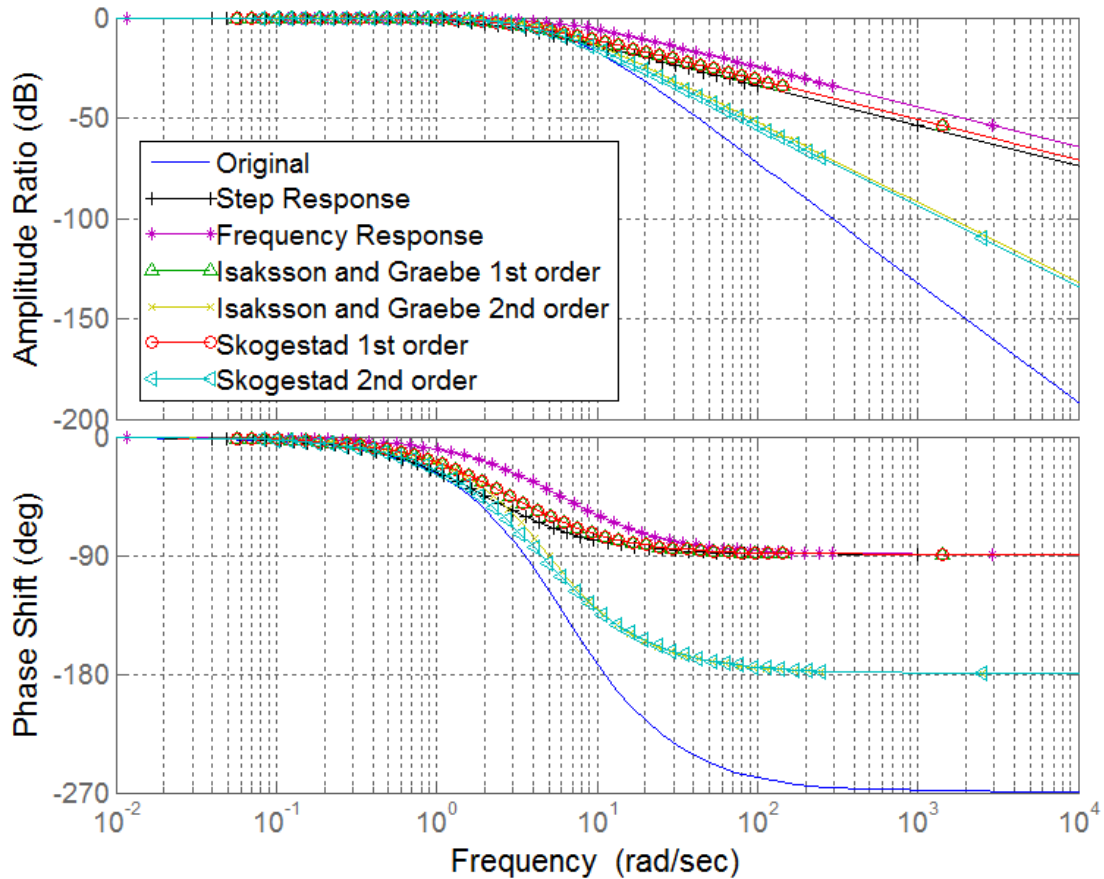


Figure 3-6. Intensified system Bode plots

For the simulated conventional system, the amplitude ratio and phase shift of the reduced order models (apart from the frequency response method) are identical to the original model at the bandwidth frequency (Figure 3-5). This is attributed to the presence of a dominant process time constant, explaining why the instrumentation dynamics are seldom included in a model based controller design for a conventional system. Conversely, the deviations of the reduced order approximations from the original model at the bandwidth frequency are more notable in the frequency response of the intensified system (Figure 3-6). This is because the dynamics of the process and instrumentation are similar in magnitude and contribute equally.

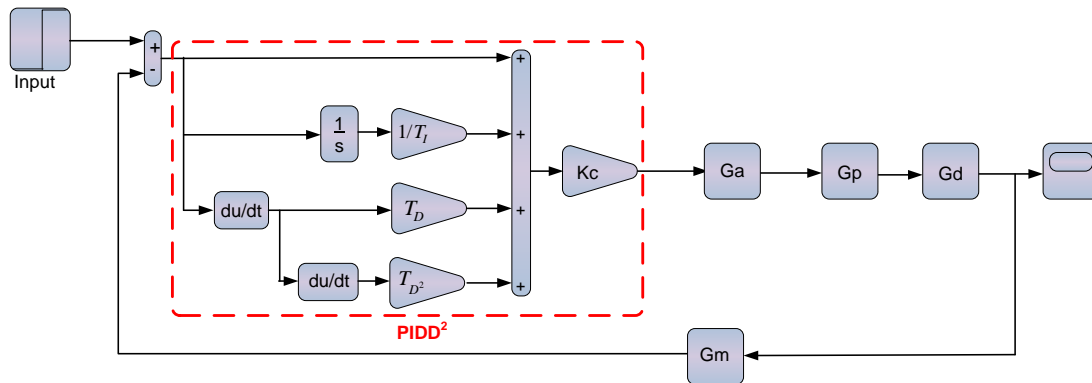
### 3.3 Controller Performance

The direct synthesis method is employed to derive control algorithms for the high order and reduced order models of the simulated intensified and conventional systems described in section 3.2.6. The only tuning parameter for the controllers is the closed loop time constant  $\lambda$ , which is selected as half of the process time constant, namely 5 and 0.05 for the simulated conventional and intensified systems respectively. The resulting controller parameters are outlined in Table 3-3.

Table 3-3. Controller parameters

	<i>Conventional</i>				<i>Intensified</i>			
	$K_C$	$T_I$	$T_D$	$T_D^2$	$K_C$	$T_I$	$T_D$	$T_D^2$
<i>Original (PIDD<sup>2</sup> + filter)</i>	1.733	10.4	0.388	0.038	0.476	0.5	0.16	0.008
<i>Step Response (PI)</i>	1.733	10.4			0.476	0.5		
<i>Frequency Response (PI)</i>	0.11	0.77			0.13	0.17		
<i>Isaksson &amp; Graebe (PI)</i>	1.7	10.2			0.33	0.35		
<i>Isaksson &amp; Graebe (PID)</i>	1.7	10.2	0.198		0.33	0.35	0.114	
<i>Skogestad (PI)</i>	1.6	10.1			0.24	0.3		
<i>Skogestad (PID)</i>	1.69	10.3	0.291		0.41	0.45	0.111	
<i>Maclaurin series (PI)</i>	1.733	10.4			0.476	0.5		
<i>Maclaurin series (PID)</i>	1.733	10.4	0.388		0.476	0.5	0.16	

The feedback control loop shown in Figure 3-1 is implemented in Simulink to assess the performance of various controllers derived for the cases of simulated conventional and intensified systems. The PI/PID control parameters are implemented using the built-in ‘PID controller’ block available in Simulink. However the non-standard PIDD<sup>2</sup> controllers are modelled according to the block diagram in Figure 3-7.

Figure 3-7. Closed-loop system with a PIDD<sup>2</sup> controller

The simulations involving the PIDD<sup>2</sup> controller were found to be more ‘stiff’ compared to the other cases. Therefore, to ensure numerical accuracy a fixed step integrator was selected for PIDD<sup>2</sup> simulations with a step size of 0.0008. Choosing a very small step size makes the simulation more computationally demanding thus the rest of the ‘non-stiff’ cases were simulated using variable-step integration. The variable and fixed step solvers were selected as ode45 and ode3 respectively.

### 3.3.1 Assessment Criteria

The closed loop systems are subjected to step changes in the setpoint as well as load disturbances, to evaluate the setpoint tracking and disturbance rejection performances of the controllers with various tuning parameters. The performance assessment is carried out by visual inspection of the controlled variable response in terms of overshoot, rise time,

oscillations, etc. Additionally, the Integral of Absolute Error (IAE) criterion is selected to allow a quantitative evaluation of the controllers' performance. The IAE is calculated according to,

$$IAE = \int_0^T |e(t)| dt \quad (3-20)$$

where,  $e(t)$  is the difference between the measured value of controlled variable and the desired value or setpoint at any point in time. Therefore, IAE is an indication of how efficiently the controller maintains the process variable at the desired value. Clearly smaller values of IAE indicate tighter control.

### 3.3.2 Setpoint Tracking

The setpoints of the simulated closed loop systems were increased from zero to one at time equal to 20 seconds. The setpoint tracking performance of various controllers for the simulated conventional and intensified systems are presented in Figure 3-8 and Figure 3-9 respectively.

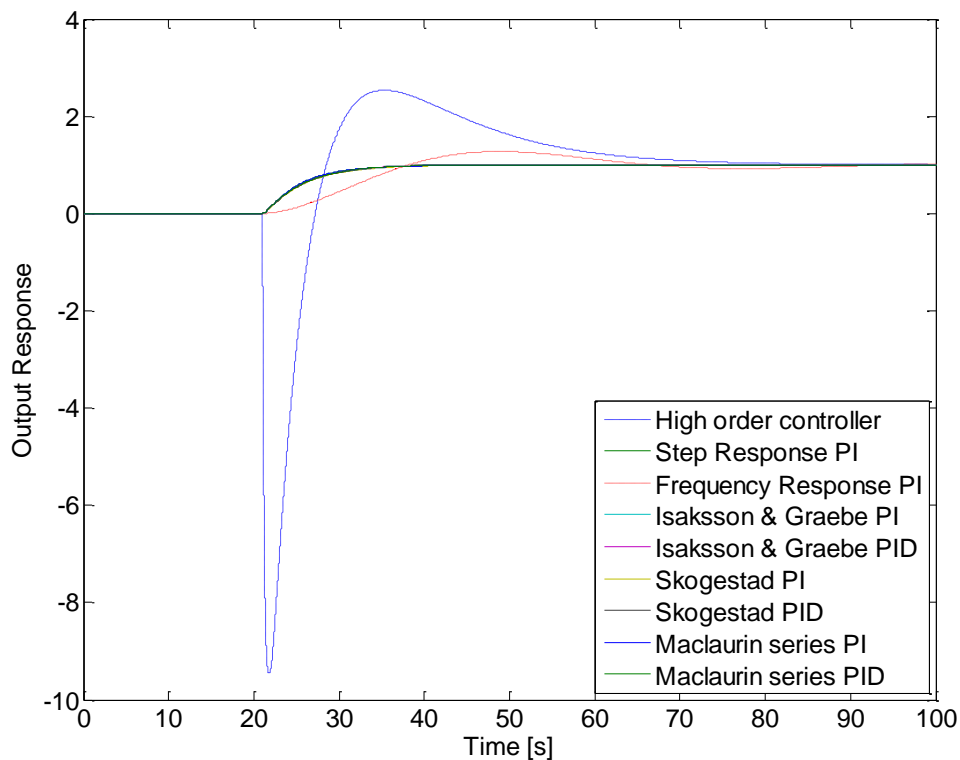


Figure 3-8. Setpoint tracking performance for the simulated conventional system

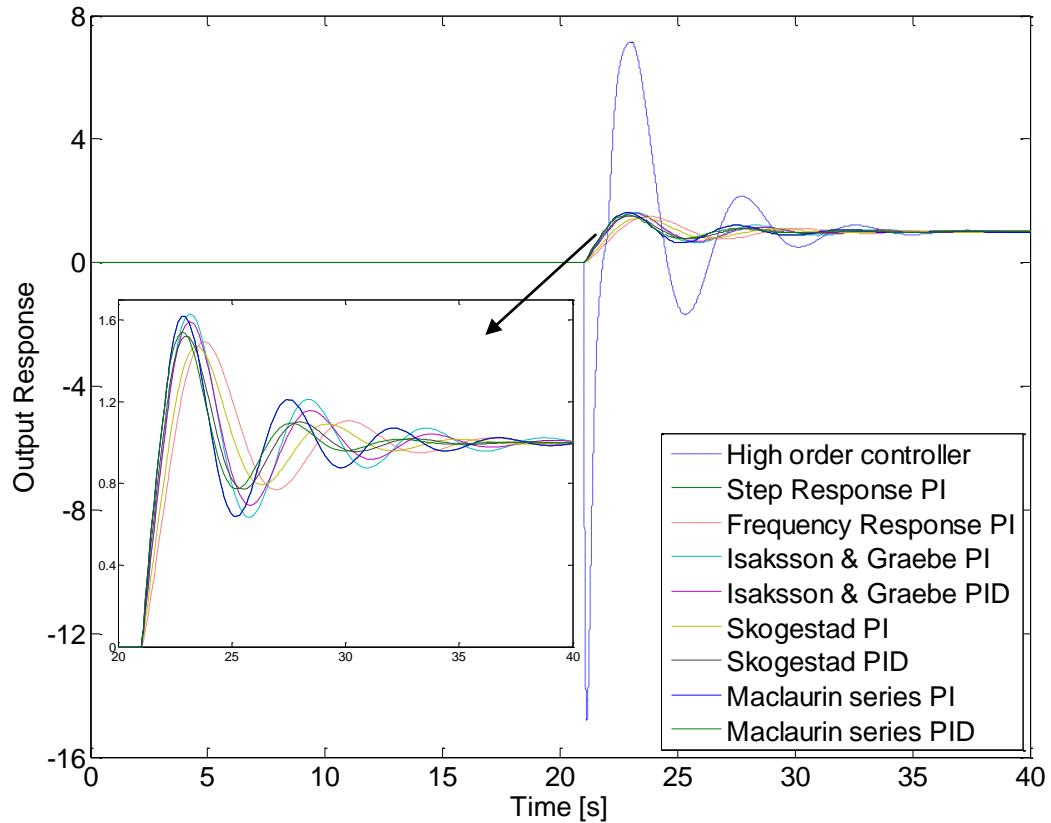


Figure 3-9. Setpoint tracking performance for the simulated intensified system

For both systems the high order controllers provide the least satisfactory performances; high overshoots and inverse responses are evident in the output responses. These undesirable characteristics commonly referred to as ‘derivative kicks’, are attributed to the second order derivative term of the  $PIDD^2$  controller. The derivative kicks have a detrimental effect on instrumentation and control performance, which may be mitigated by implementation of a low pass filter and fine tuning the controller. It can be noted that the overshoot and inverse response resulting from the high order derivative terms are more significant for the simulated intensified system whilst the output response of the conventional system is more sluggish, due to the slower process dynamics.

The results indicate that the derivative kicks are significantly reduced and no inverse responses are present for all PI and PID controllers obtained from the order reduction techniques. Overall, the output response of the simulated conventional system is over-damped for all controller tuning methods. Conversely, the output response of the intensified system is under-damped for all cases and overshoots of 50-60% are observed even with the reduced order controllers.

The IAE performances of the designed controllers for both systems are presented in Figure 3-10. The IAE values indicate that the control performance is improved when standard PI/PID controllers are used instead of the original high order controller. For the simulated conventional system the tuning parameters obtained by the frequency response yield the highest value of IAE amongst the reduced order controllers, also notable in Figure 3-8. The performances of the remaining reduced order controllers are not vastly different, all returning substantially smaller IAE values compared to the performance of the high order controller.

One interesting observation is that all controllers applied to the example intensified system result in smaller values of IAE compared to those achieved in the simulated conventional system. This is attributed to the smaller time constant of the intensified system which leads to a faster control response.

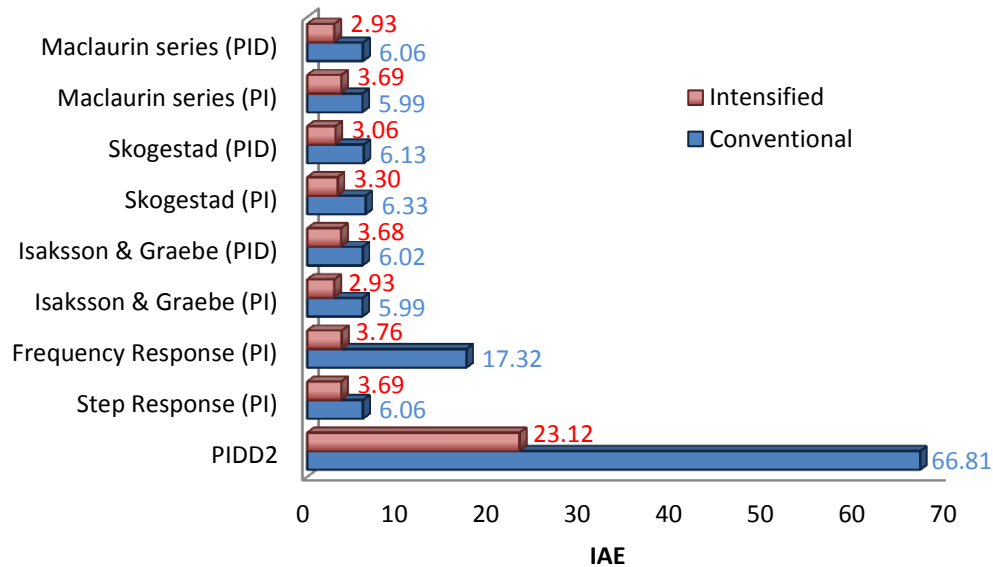


Figure 3-10. IAE values for setpoint tracking performance

### 3.3.3 Disturbance Rejection

The simulated closed loop systems were subjected to a step load disturbance at time equal to 20 seconds. The disturbance was modelled as an input variable to the process with a magnitude of 1. The output responses of the simulated conventional and intensified systems are presented in Figure 3-11 and Figure 3-12 respectively. It can be seen that the disturbance rejection performance of the high order controller is comparable to those achieved by the reduced order controllers. However, the PI controller obtained by the frequency response provides an inferior performance compared to the rest of the controllers for the conventional system. This is due to the fact that the overall time constant estimated by this method is more than an order of magnitude smaller than the dominant process time constant of 10. The smaller value of time constant leads to specification of a faster integral time constant which resulted in a larger contribution from the integral term causing an overshoot in the response.

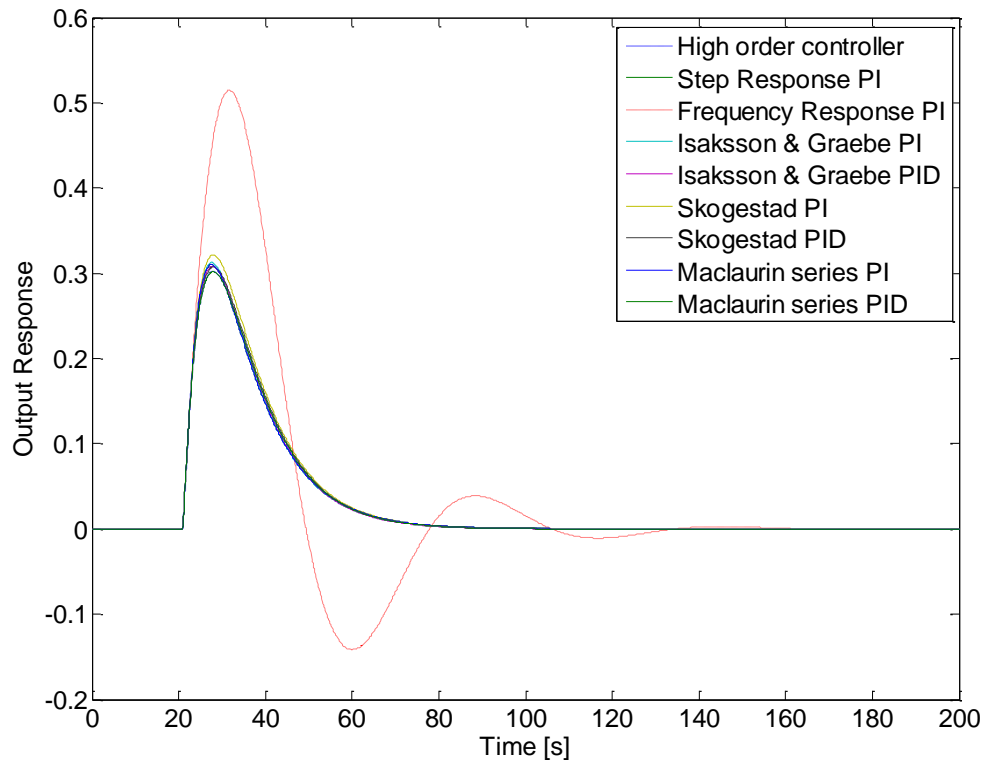


Figure 3-11. Disturbance rejection performance for the simulated conventional system

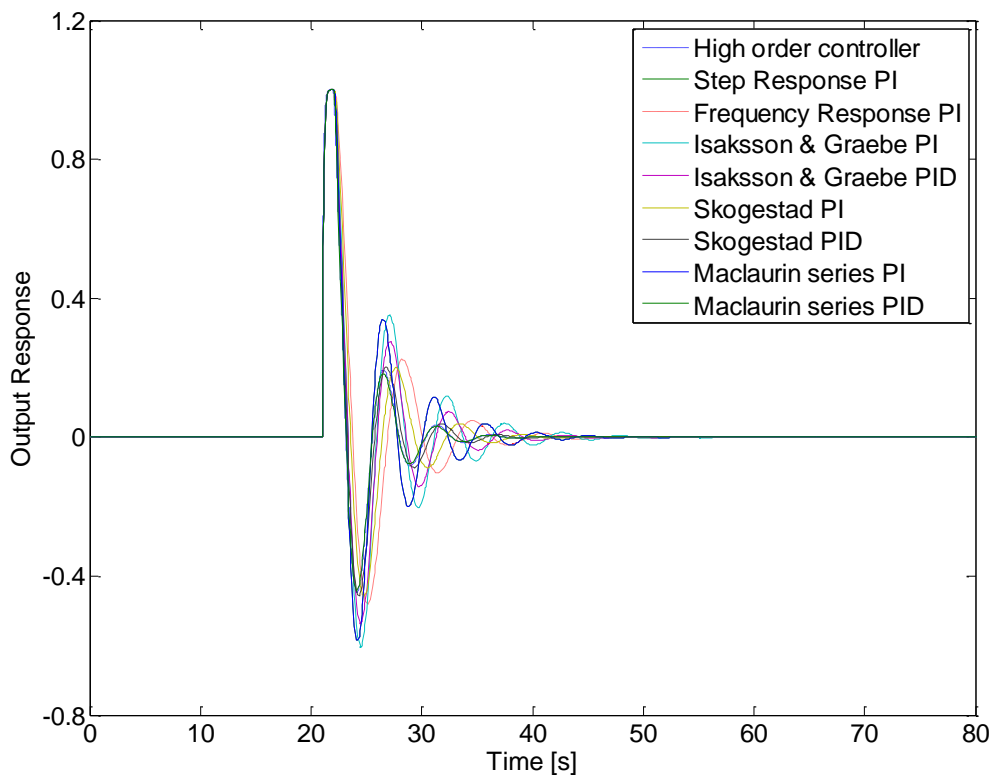


Figure 3-12. Disturbance rejection performance for the simulated intensified system

Similar to the trends observed for the setpoint tracking performance, the disturbance rejection response of the simulated conventional process is over-damped and sluggish, whilst the response of the simulated intensified system is under-damped and exhibits decaying oscillations. It is observed that the magnitude of the overshoot as a result of a load



disturbance for the intensified system is three times larger than that observed for the conventional system (excluding the frequency response tuning), indicating that the intensified system is more susceptible to disturbances.

The plot of IAE values presented in Figure 3-13 reinforces the observation that the controller parameters obtained by the frequency response provide a poor performance for the conventional system. This was also highlighted by the frequency response analysis of the reduced order model provided in Section 3.2.6. Further, as observed for the setpoint tracking responses, the IAE values of the example intensified system are smaller than those associated with the simulated conventional system.

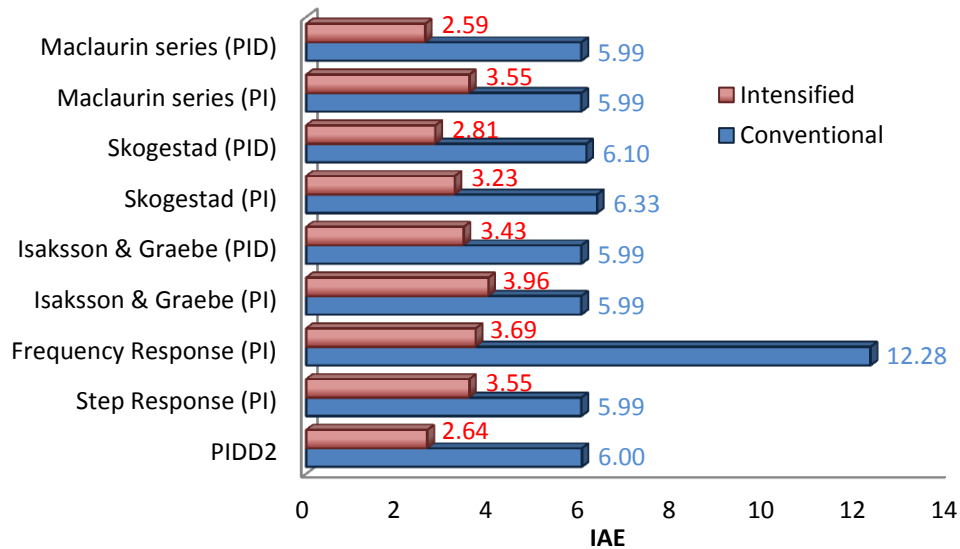


Figure 3-13. IAE values for disturbance rejection performance

### 3.3.4 Simulated Conventional versus Intensified Systems

The assessment of setpoint tracking and disturbance rejection performances of the simulated conventional and intensified systems led to a number of observations as summarised below:

1. Applying the same control synthesis approach with the tuning parameter  $\lambda$  equal to half of the process time constants of the respective systems, resulted in under-damped responses for the intensified system whilst the response of the conventional system was rather sluggish.
2. The setpoint change applied to the intensified process resulted in 50 to 60% overshoots for all reduced order controllers, which is higher than the usually acceptable levels of 10 to 20%.
3. The intensified system showed more sensitivity to load disturbances as the magnitude of the initial rise in the output response was three times higher than that observed for the simulated conventional system.
4. The IAE values for the intensified system were lower than that of conventional system implying a faster and more efficient control.

The overall control performance in terms of IAE for an intensified system is superior to that obtained in a conventional system, as the former process is more responsive, thus faster control can be achieved. However, the faster responses are achieved at the expense of higher overshoots. To further investigate the potential impacts of reducing the equipment residence time on control, the stability of the simulated intensified and conventional processes are compared next.

The frequency response of an open loop system may be used to determine the stability of the closed loop system. The frequency responses of the overall intensified and conventional models may be used to obtain the gain and phase margins of the respective systems. For this analysis PID controllers with tuning parameters obtained from the Maclaurin series expansion (see Table 3-3) are coupled with the process models. The gain and phase margins ( $G_m$  and  $\phi_m$ ) indicate the stability margins of a system, namely the amount of gain and phase shift that the system can tolerate before the closed loop response becomes unstable. As presented in Figure 3-14 the gain margin of the simulated intensified system in series with a PID controller, is smaller than that of the conventional process examined. This implies that reducing the process time constant brings the closed loop system closer to instability.

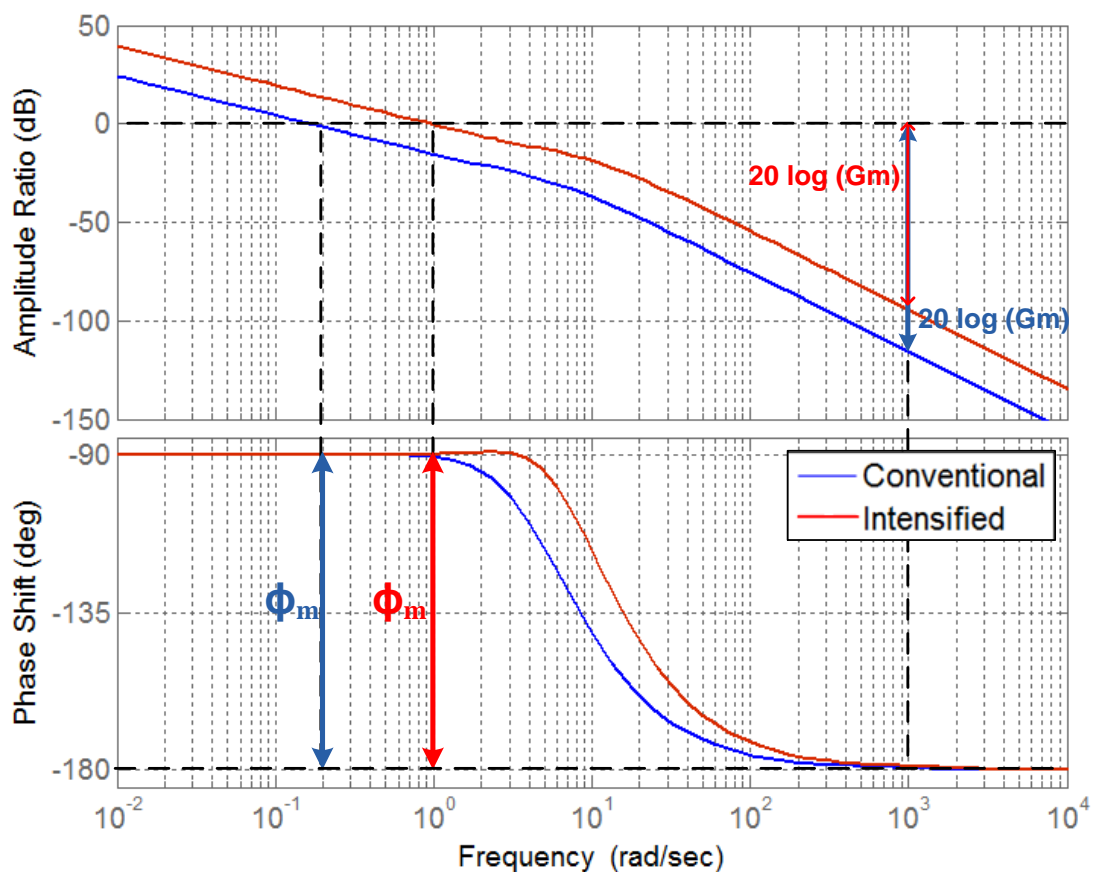


Figure 3-14. Gain and phase margins

Reducing the time constant of processing units makes them more sensitive to load disturbances; additionally larger overshoots and smaller stability margins may prevail. The comparison between the simulated conventional and intensified systems indicates that more care is required in control and operation of fast dynamic intensified units.

### **3.4 Summary**

In conventional processing the main unit operations often have residence times of tens of minutes, thus the instrumentation dynamics may be neglected in design of a suitable control schema. However, as the equipment size is reduced for a constant production capacity, the residence time of the unit operation is drastically reduced to even fractions of a second in some intensified units. Therefore, the commercially available instrumentation dynamics become more significant in comparison to the process dynamics and may greatly influence the control performance. Including the instrumentation dynamics in a model based controller design results in non-standard high order controllers, which may not be practical for industrial implementation. In order to achieve the control objectives using the most commonly used PI/PID controllers a model reduction technique may be applied to either the process or the controller transfer function. The present chapter outlined a number of such model order reduction techniques.

The potential impacts of equipment size reduction on control were studied by simulating example conventional and intensified systems, whereby the time constant of the former system was 100 folds larger than that of the latter. The performance of the high order controller in terms of setpoint tracking was poor for both intensified and conventional systems, as the second order derivative term makes the controller more susceptible to sudden changes of setpoint and measurement noise. The performance of a PI/PID controller obtained via various model order reduction techniques provided superior setpoint tracking compared to the high order controller. However, the disturbance rejection performances of high and reduced order controllers were generally very similar. A superior control performance in terms of IAE was achieved for the simulated intensified system, compared to that achieved for the conventional counterpart. However, the intensified system suffered from larger overshoots and was more sensitive to load disturbances. Further, the frequency response of the open loop systems indicated that smaller stability margins are obtained for the intensified system compared to the conventional system.

In this chapter preliminary simulation studies were carried out to investigate the potential impacts of faster dynamics on control. Further, various model order reduction techniques for controller tuning were outlined and subsequently analysed. The outcome provides an important foundation for detailed analysis of specific control tasks which are carried out via simulation and online application to a spinning disc reactor in the present research. The next chapter provides details of the experimental apparatus and the procedures involved in conducting further investigations of control of intensified equipment with fast dynamics.

## ***Chapter 4. Apparatus and Procedures***

This chapter outlines the apparatus and procedures employed to carry out the present research project. The investigations presented in the following chapters can be divided into three parts:

1. pH control by manipulation of base stream flowrate
2. Conductivity control using the disc rotational speed
3. Thermographic analysis of thin liquid films

The neutralisation of hydrochloric acid with sodium hydroxide is selected to facilitate the pH control investigations in SDRs. The second part of the control studies concerning the exploitation of the disc rotational speed as the manipulated variable is carried out using the barium sulphate precipitation process. Here, individual feed solutions containing barium chloride and sodium sulphate are pumped to the SDR and the conductivity of the effluent stream is controlled using the disc rotational speed. It is expected that the actual temperatures as well as the hydrodynamics of the thin liquid films formed in SDRs have a strong impact on any process, and thus the effective control of such units. Therefore, the temperature profiles along with the flow and wave patterns of the thin liquid films are investigated with the aid of an infrared thermal imaging camera.

For the control studies, first order approximations of the process models are obtained from open loop step tests. The process models are then used for analysis of the interactions within the system and also for obtaining controller tuning parameters via a model based tuning approach. Furthermore, the process model of the pH process is used to study a number of control strategies via simulation. Feedback control loops which include a PI/PID controller with and without a disturbance observer are implemented and tested online for both cases of pH and conductivity control. The apparatus used to carry out the experimental and simulation studies includes hardware and software components, as outlined next.

### ***4.1 Apparatus***

The experimental work is carried out in a spinning disc reactor which is coupled with external temperature control units and a computer control system. The overview of the experimental rig set up is shown in Figure 4-1. Details of all hardware and software components used in the present work are outlined in the subsequent sections.

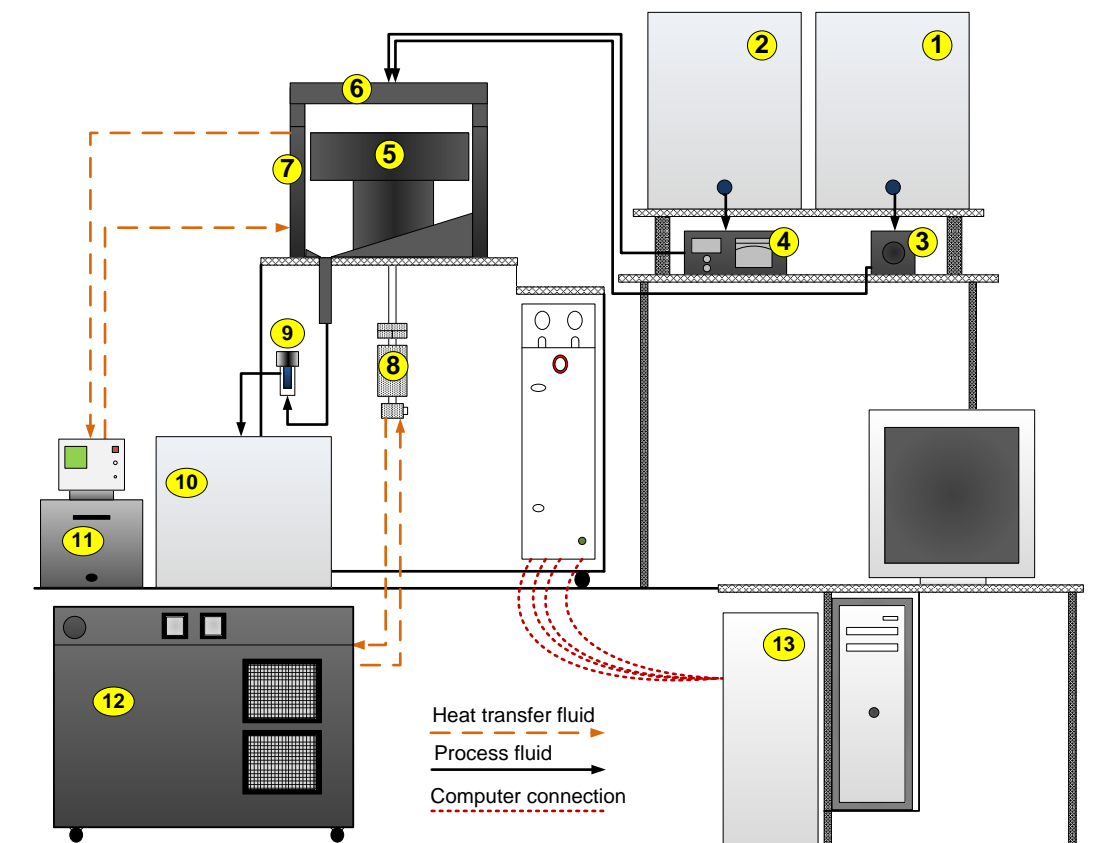


Figure 4-1. Experimental set up

[1) & 2) feed vessels, 3) gear pump, 4) peristaltic pump, 5) spinning disc, 6) reactor lid, 7) reactor stationary housing, 8) motor, 9) sample cell, 10) product receiver, 11) water bath, 12) heater/chiller unit, 13) SDR control system]

### 4.1.1 Spinning Disc Reactor

The spinning disc reactor comprises of three distinct parts: the rotating disc, the reactor housing and the lid (Figure 4-1, components 5, 6 & 7). The main component of the SDR is a horizontally mounted smooth stainless steel disc with a diameter of 16 cm. The disc is connected to a shaft which is rotated by an electrically driven motor. The liquid feed streams are pumped into a well in the centre of the top surface of the disc. As the disc rotates the well acts as a reservoir system to enable uniform distribution of the processing fluid across the disc surface. Under the action of high centrifugal fields exerted by rotating the disc at various rotational speeds (200 to 2000 rpm), the liquid travels rapidly towards the disc edges and forms a very thin, highly sheared film typically covered with numerous surface ripples. Underneath the disc, there are internal channels for flow of a heat transfer fluid, providing heating or cooling, as shown in Figure 4-2.

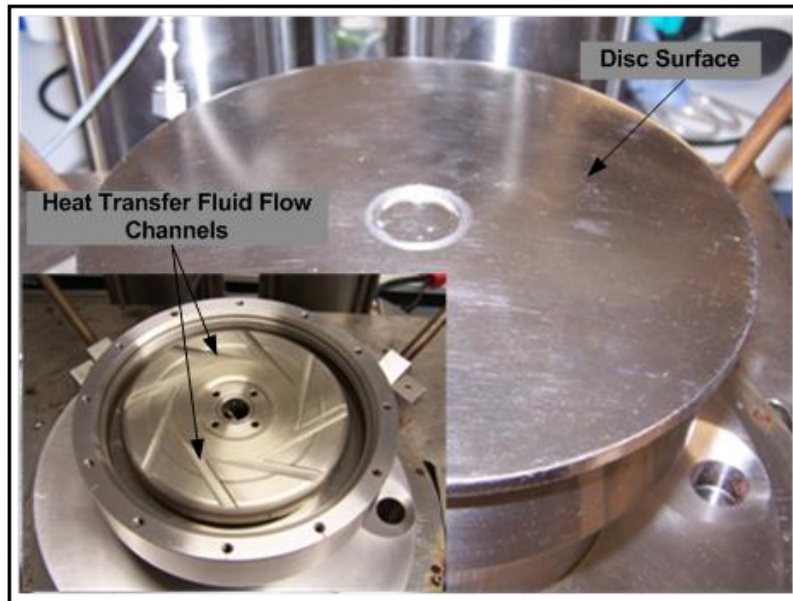


Figure 4-2. Top view of the disc and heat transfer channels

The heat transfer fluid is delivered to the centre of the bottom surface of the disc through an internal pipe within the rotating shaft. The heating/cooling fluid moves towards the disc edges and exits the chamber before it gets recirculated through the system via a temperature controlled heat transfer unit, as schematically shown in Figure 4-3. The disc temperature is inferred from two thermocouples inserted in the inlet and outlet heat transfer fluid pipes to the SDR unit. At steady state conditions the stainless steel disc is expected to reach the temperature of the heat transfer fluid flowing in the narrow channels underneath the disc. The mass of the processing fluid on the disc at any one time is very small in comparison with the mass of the disc. Thus the amount of heat transferred to the thin liquid film is not likely to be significant enough to cause any large variations in the temperatures across the disc. Therefore the disc temperature is taken to be uniform and equal to that of the heat transfer fluid flowing underneath the disc.

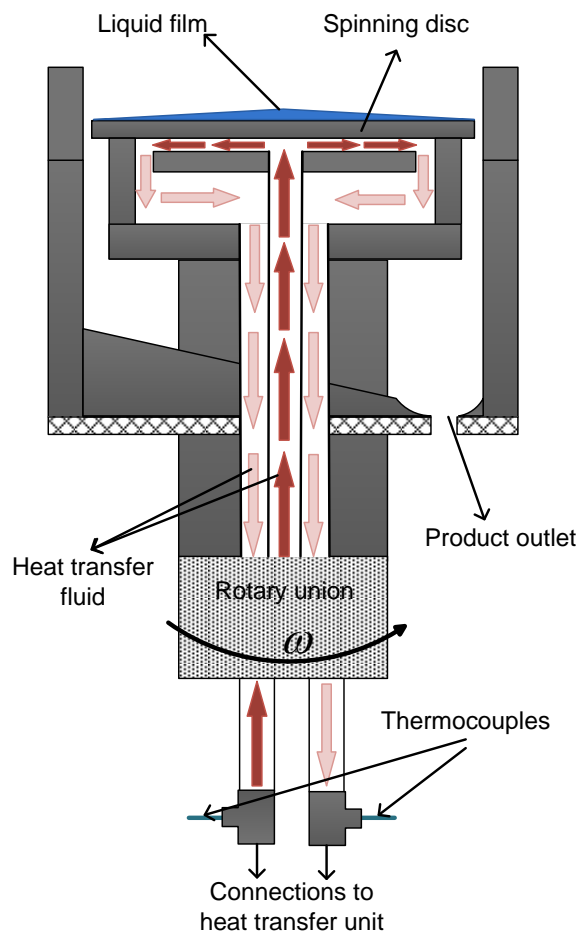


Figure 4-3. Schematic diagram of the SDR

In addition to the disc, the SDR is composed of a housing chamber and a lid made of stainless steel. As discussed previously, the liquid film travels rapidly on the disc under the action of centrifugal force. At the disc periphery the liquid is thrown out and hits the stationary walls of the reactor housing. The housing consists of two jackets with capabilities to heat or cool the product after it leaves the disc. Both parts of the jacket may be connected to external temperature control units to circulate a heat transfer fluid within the hollow walls of the reactor housing, as shown in Figure 4-4.



Figure 4-4. Reactor housing

The reactor lid contains three liquid feed ports which are aligned with the disc centre. There are two additional ports which may be used for flow of gaseous feed/products or a nitrogen sweep. A pressure sensor is also incorporated on the lid to provide an indication of the pressure within the vessel. The lid also contains two glass windows for observation of the liquid films formed on the rotating disc.

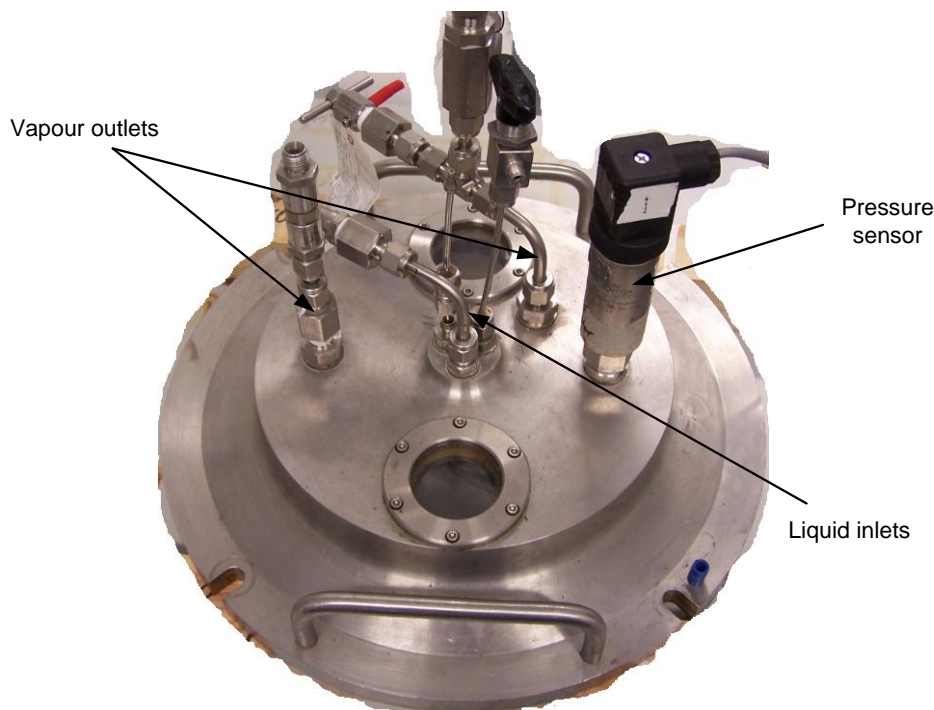


Figure 4-5. Reactor lid

### 4.1.2 Liquid Feed Arrangements

For the control experiments involving the neutralisation and precipitation reactions, the liquid feed ports which are fitted on the reactor lid (see Figure 4-5) are used to deliver the reagent solutions to the SDR. However, for the thermographic analysis of the thin liquid films the reactor lid has to be removed. Initially, the fabrication of a new lid using an IR transparent material was considered; this however could not be realised mainly due to the prohibitively high cost of such specialised materials. It is to be noted that materials that are transparent to visible light such as glass or perspex are infrared opaque. Therefore, as the system is operated without any lid for the thermographic investigations, new feeding arrangements were designed to allow the delivery of the processing fluid to the centre of the disc. Two feeding configurations are tested in the present study. The first arrangement involves two 2.4 mm ID pipes which are bolted to the walls of the stationary reactor housing, as shown in Figure 4-6. The feed tubes are extended across the disc and deliver the feed solutions to the disc centre, approximately 3 mm away from the surface. This arrangement is referred to as ‘single point injections’.



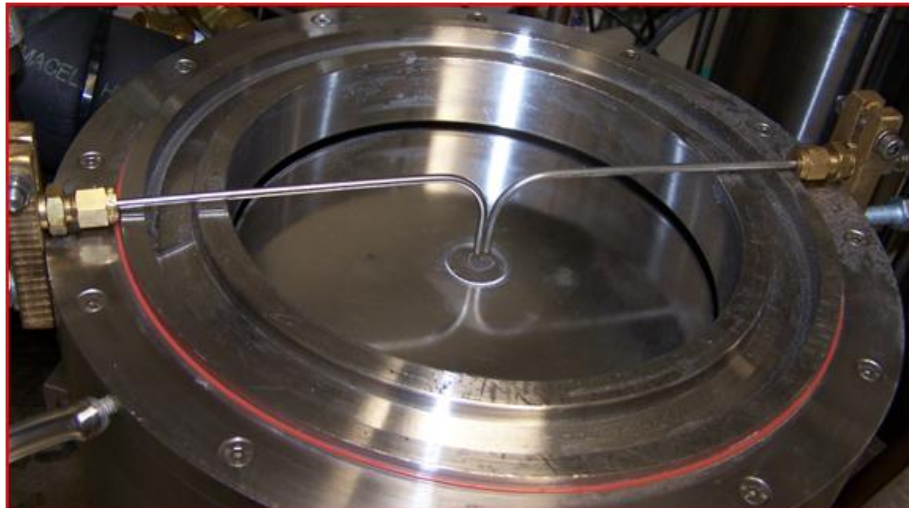


Figure 4-6. Single point injections

Another feed configuration referred to as ‘distributor system’ was also designed, as shown in Figure 4-7. In this arrangement one of the liquid feeds is delivered to the disc centre in a circular pipe, whilst, the second feed is distributed through an annular gap of 0.1 mm located around the first feed, as illustrated schematically in Figure 4-8. The main purpose of testing this feeding arrangement, in addition to the previous design, is to establish whether different feeding configurations lead to different outcomes in terms of the temperature profiles or flow patterns across the liquid film.

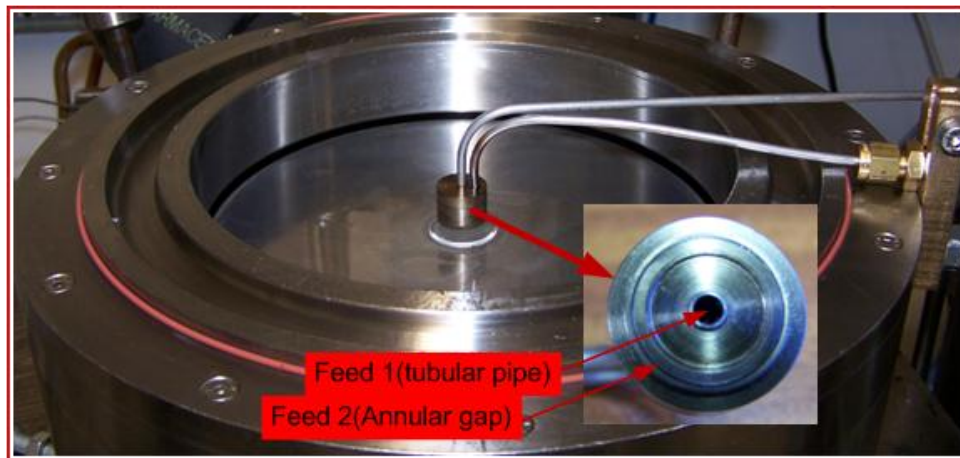


Figure 4-7. Distributor system

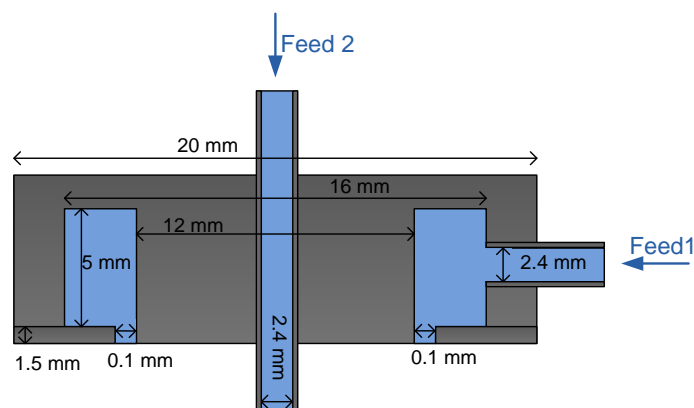


Figure 4-8. Schematic diagram of distributor system

### 4.1.3 Temperature Control Units

The rotating disc/shaft system is connected to a heater/chiller unit (Figure 4-1, component 12) which circulates Baysilone M10 heat transfer fluid around the system. The bottom section of the reactor housing jacket is connected to a temperature controlled water bath (Figure 4-1, component 11). Reactions are carried out within the short residence times of the processing fluid on the rotating disc. Therefore, tight control of the disc temperature allows control of the reaction temperature. The ability to heat or cool the reactor housing walls is also greatly beneficial for some processes. For instance, if a temperature sensitive reaction is carried out in the SDR, the reactor housing walls may be chilled to stop the reaction immediately after the processing fluid leaves the disc. This could in turn minimise the formation of unwanted by-products.

### 4.1.4 SDR Control System

The SDR control system is composed of two elements: an electronics console and a computer system hosting the SDR operational software (Figure 4-1, component 13). The software provides an interface for control of the disc rotational speed and temperature. In the pH control and thermal imaging runs the disc rotational speed is maintained at the desired value via the SDR control software. However, for the conductivity control runs it is required to automatically adjust the disc rotational speed based on the computed value of the controller output, following each execution of the control loop. Therefore, the SDR control system was modified such that the disc speed was controlled via a voltage signal generated by a data acquisition device (Section 4.1.8) instead of the original SDR software. The calibration data presented in Figure 4-9 are obtained by sending various voltage signals to the SDR variable speed drive unit and measuring the corresponding disc rotational speed using a tachometer.

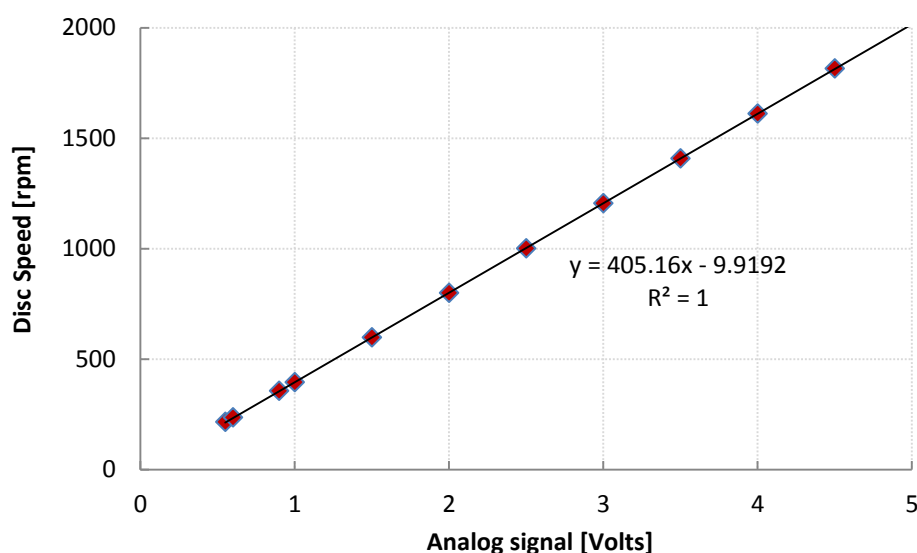


Figure 4-9. Disc rotational speed calibration data

### 4.1.5 Feed and Product Vessels

The two feed vessels (Figure 4-1, components 1 & 2) are made of high density polyethylene with a capacity of 25 litres. The feed vessels have good chemical and thermal resistances and contain provisions for fitting stopcock valve connections to control the flow of the feed solutions out of the vessel. The product is collected in a canister (Figure 4-1, component 10) for appropriate disposal.

### 4.1.6 Pumps

Two pumps namely a Watson-Marlow peristaltic pump (model 323E) and a Cole-Palmer gear pump (model 75211-41) are used to deliver the liquid feeds from the feed vessels to the SDR (Figure 4-1, components 3 & 4). The gear pump has the capability of being remotely driven by an analog current signal, thus it is used as the actuator delivering the base stream to the SDR in the pH control runs. The calibration data for the two pumps are presented in Figure 4-10 and Figure 4-11.

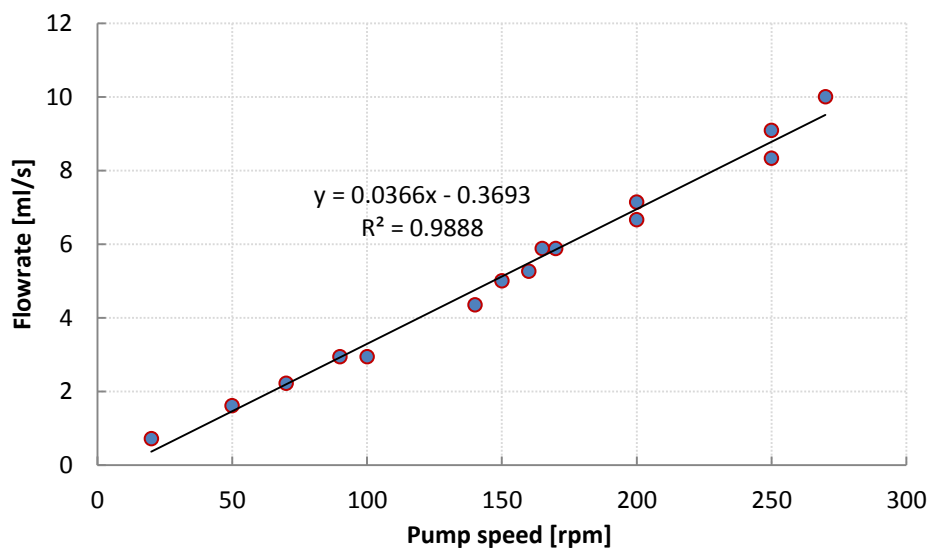


Figure 4-10. Peristaltic pump calibration data

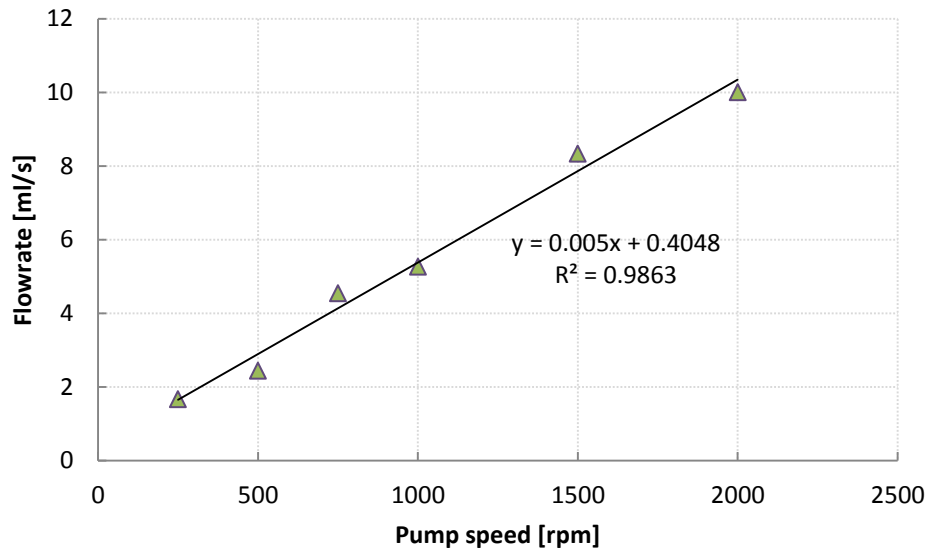


Figure 4-11. Gear pump calibration data

### 4.1.7 Sensors and Transmitter

For measurement of the effluent pH, a Mettler-Toledo pH probe (model InPro 3253i/SG/120) is used. The probe is placed in a sample cell made of Perspex (see Figure 4-12) which is situated downstream of the SDR in the product outlet path (see Figure 4-1, component 9). The probe's response time (98% between pH 4 and 7) is quoted to be 20 seconds by the manufacturer. Note that the probe response time is considerably larger than the value selected for a generic sensor (0.2s) in the previous chapter. The sample cell is designed with minimal liquid hold-up to minimise the transport time delays in the system as much as possible.

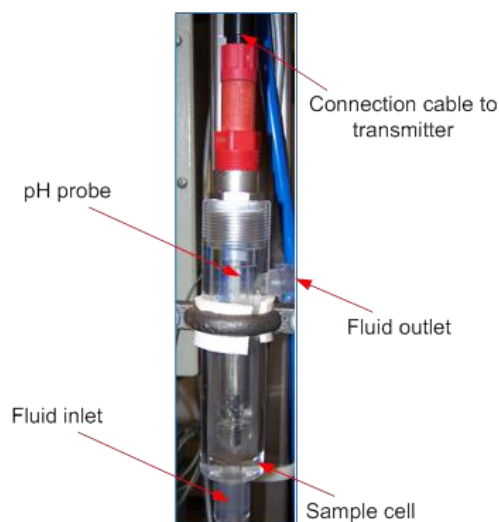


Figure 4-12. pH probe

The conductivity of the effluent stream is measured using a 4 pole Mettler-Toledo conductivity probe (model InPro7100i) with a range of 0.02 – 400 mS/cm, as shown in Figure 4-13. The conductivity probe has the same dimensions as the pH probe and is fitted in the same sample cell downstream of the SDR for the conductivity control runs. The actual

response time of the probe is not provided by the manufacturer; however, a fast response time is one of the characteristic features of this particular probe. The pH and conductivity probes are both compatible with the Mettler-Toledo M300 transmitter used in this study.



Figure 4-13. Conductivity probe [Courtesy of Mettler-Toledo]

### 4.1.8 Data Acquisition Devices

The effluent pH for the open loop step tests is recorded by a LASCAR electronics data logger (model EI-USB-4). For the pH closed loop runs a National Instruments data acquisition device (model USB6211) is used to acquire/generate the process/control signals. As shown in Figure 4-14, the data acquisition (DAQ) device contains a number of analog input and output ports and is connected to a PC via a USB connection.

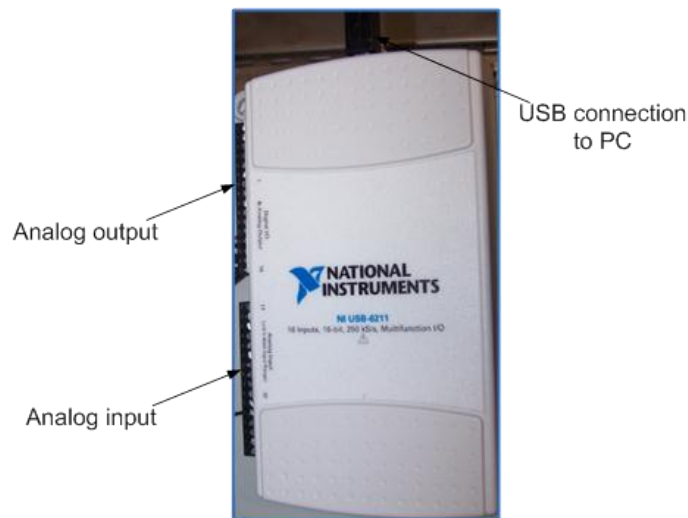


Figure 4-14. USB6211

The conductivity signal was initially acquired by the same DAQ device used for the pH control (NI-USB6211). However, there were often large amplitude spikes in the measured signal. A less sensitive device (NI-USB6008) was used instead and this eliminated the measurement spikes. The USB6008 data acquisition device is used to acquire the conductivity signal for the open/closed loop tests, and also used to generate an analog output signal to the actuator for the closed loop conductivity control runs. As outlined in Table 4-1 the USB6211 offers faster sampling and more accurate measurements. Nevertheless, the USB6008 provides adequate functionality for the purpose of the current data acquisition task.

Table 4-1. DAQ specifications

	USB-6211	USB-6008
Analog input channels	16	8
Analog output channels	2	2
Resolution [bits]	16	12
Sample rate (analog input) [samples/s]	250,000	10,000
Update rate (analog output) [samples/s]	250,000	150
On-board memory (samples)	4095	512

### 4.1.9 Matlab/Simulink Software

Matlab (Matrix Laboratory) version R2008b developed by MathWorks which is a numerical computing environment [166] is used in the present work. The Simulink package [167] within Matlab which has a graphical block diagramming interface is used in particular for the simulations studies carried out here. A wide range of programmed blocks are available from Simulink Library Browser (see Figure 4-15) which may be used to perform various process modelling and simulation tasks.

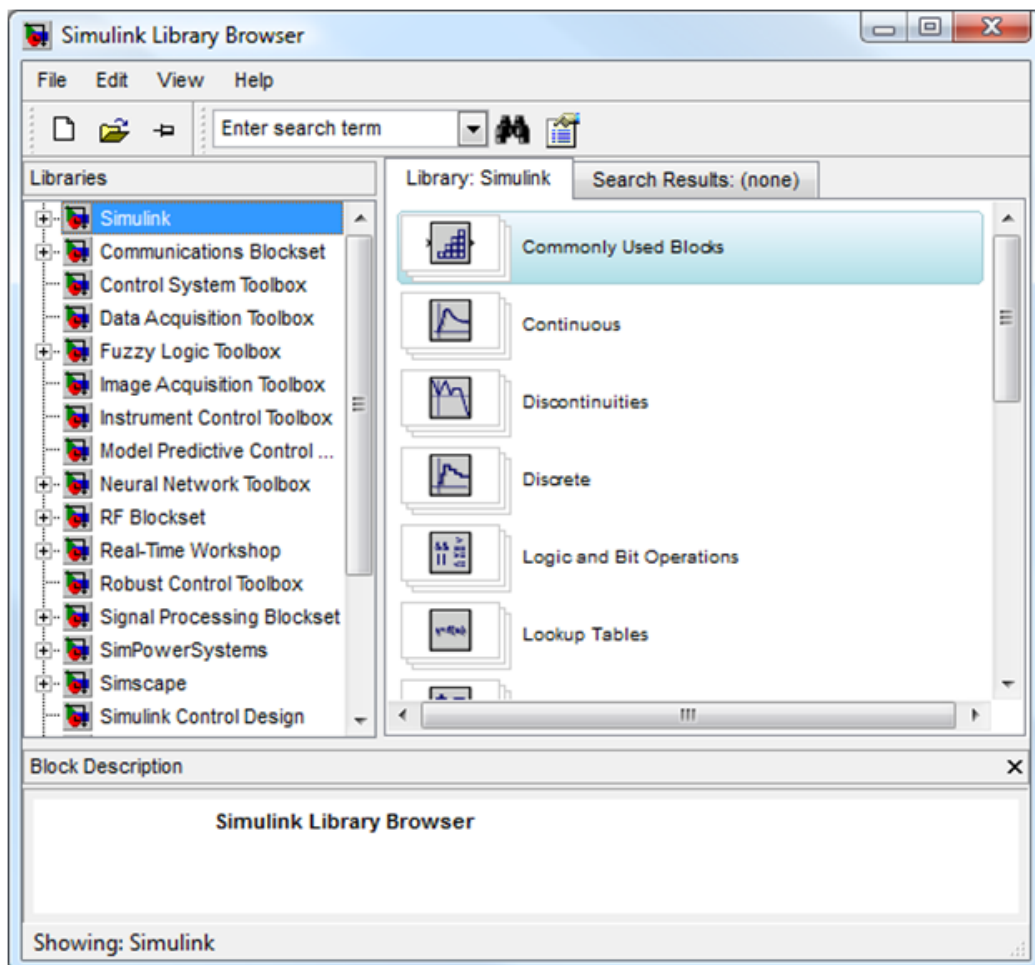


Figure 4-15. Simulink Library Browser

### 4.1.10 *LabVIEW Software*

The control loops are implemented in National Instrument's LabVIEW (Laboratory Virtual Instrumentation Engineering Workbench) [168] version 2009 SP1 which is a platform for the graphical programming language, G. The LabVIEW environment consists of two windows: the 'Front Panel' which acts as a user interface and the 'Block Diagram' which contains all the graphical codes. Programs are developed using the 'Controls' and 'Functions' palettes which are available in the front panel and block diagram windows respectively, as shown in Figure 4-16. The front panel provides a user interface which can be customised for monitoring the variables of interest as well as interacting with the program as it is running. The building blocks of LabVIEW programs are called Virtual Instruments (VIs).

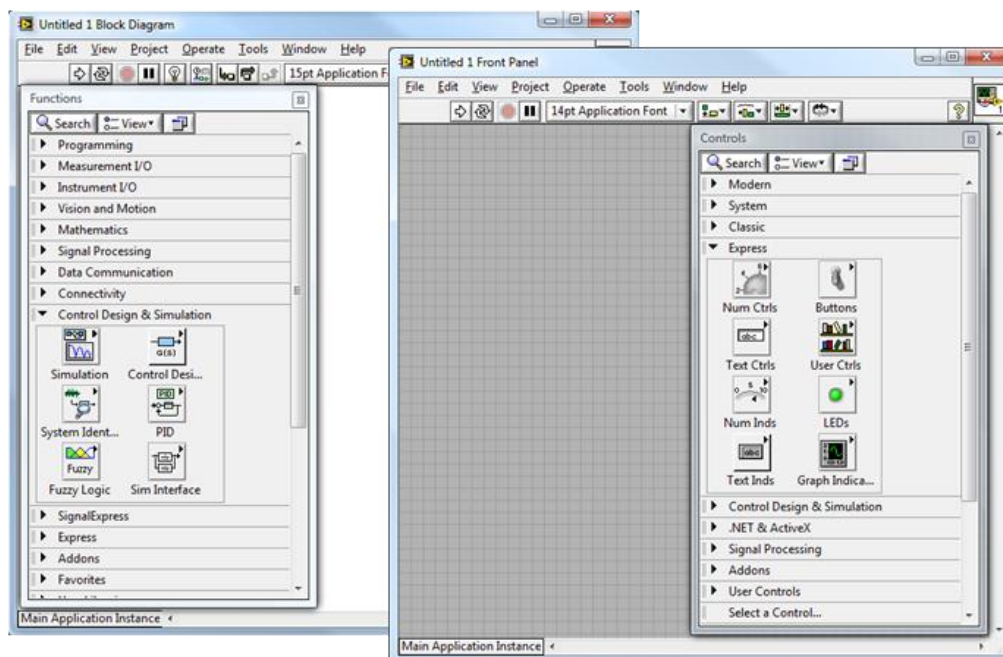


Figure 4-16. LabVIEW

### 4.1.11 *Computer System*

The computer system used for implementation of the software controller and communication with the data acquisition devices is a Toshiba Satellite Pro laptop model L300-2E5. The laptop has an Intel Core 2 duo processor at 2GHz with a 4GB RAM which is operated under Windows Vista. The simulation studies are also carried out using the same system.

### 4.1.12 *Thermal Imaging Camera*

The thermal imager used in this study is a FLIR ThermaCAM SC640 [153] which is a long wave band (7-13 $\mu$ m), capable of real time scanning and analysis, or capturing images at up to 30 frames per second for subsequent analysis. A 19mm/45° IR lens is used to capture the images in the present work. The camera is fixed to a support structure above the SDR unit as shown in Figure 4-17 and is connected to a laptop via a firewire cable for remote operation.

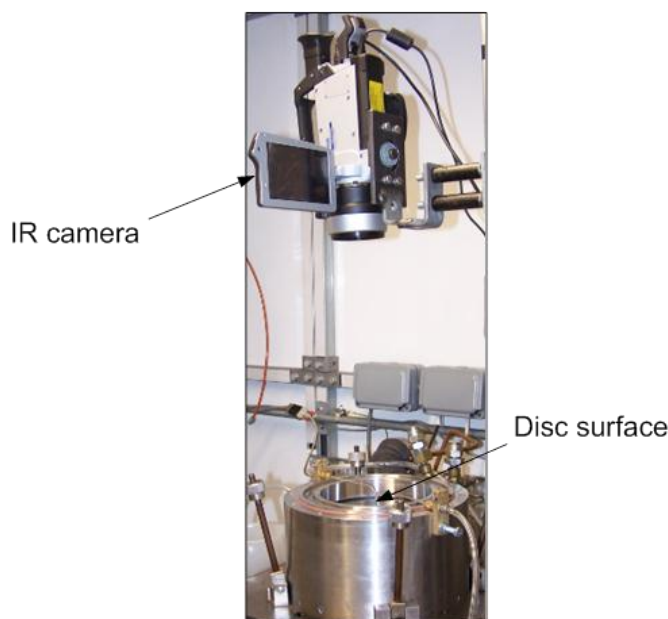


Figure 4-17. IR camera setup

### **4.1.13 *ThermaCAM Researcher Software***

The ThermaCAM Researcher software allows remote operation of the IR camera from a PC. Version Pro 2.10 of the software is used in the present work to operate the camera and to subsequently store and analyse the thermographic images. Object parameters such as emissivity, distance from the object, etc. can be modified using the software even after an image has been taken and stored. Various measurement tools such as a spot, line or area can be added to an IR image for temperature analysis and transfer of data to other file formats such as Excel.

## **4.2 *Procedures***

The apparatus employed to carry out the present work was outlined in the previous sections. The rest of this chapter is focused on the procedures applied for setting up and conducting the experimental and simulation studies.

### **4.2.1 *Safety Evaluation***

A risk assessment of the possible hazards arising from the chemicals and equipment used is carried out prior to commencing the experimental work. The assessment includes identifying the potential hazards and outlining the appropriate prevention and control measures that are in place. As the experimental work involves working with potentially hazardous chemicals all procedures are carried out to conform to the COSHH regulations.



## 4.2.2 Implementation of Control Loops in LabVIEW

In all closed loop control applications, a process signal is measured and a control signal is generated to manipulate a variable. In the present study, the control strategies which include a PI/PID controller with and without a disturbance observer are implemented in LabVIEW. The software controller communicates with the hardware plant via the data acquisition device as outlined in Figure 4-18. The DAQ device is used to acquire the pH or conductivity signals from the transmitter. The controller compares the measured process signal with a desired value and computes an appropriate control signal which is then conveyed to the actuator (base stream pump or disc variable speed drive) for implementation of the controller command. The building blocks for the control loops, which include a number of PID and data acquisition VIs, are presented in this section together with the applied procedures.

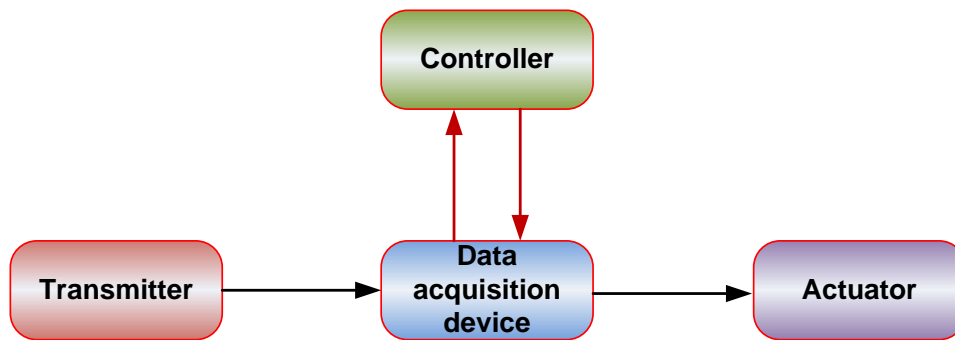


Figure 4-18. Data acquisition block diagram

The PID palette of the ‘Control Design & Simulation’ module within LabVIEW features a range of VIs for PID control including gain scheduling and auto-tuning PID controllers. In this study however the basic PID.vi is used as shown in Figure 4-19.

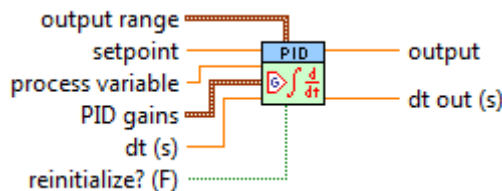


Figure 4-19. PID controller VI

The PID controller calculates the controller action  $c(t)$  using the following algorithm:

$$c(t) = K_c \left( e + \frac{1}{T_i} \int_0^t e dt + T_d \frac{de}{dt} \right) \quad (4-1)$$

Where,  $K_c$  = controller gain [%/%]

$T_i$  = integral time [min]

$T_d$  = derivative time [min]

$e$  = error (setpoint minus process variable) [%]

The default ranges for the setpoint, process variable and output of the PID VIs correspond to percentage values. Therefore, the inputs must be scaled from engineering units to percentage and the outputs need to be scaled from percentage to engineering units. There are two VIs available in the PID palette to achieve these unit conversions, as shown in Figure 4-20.

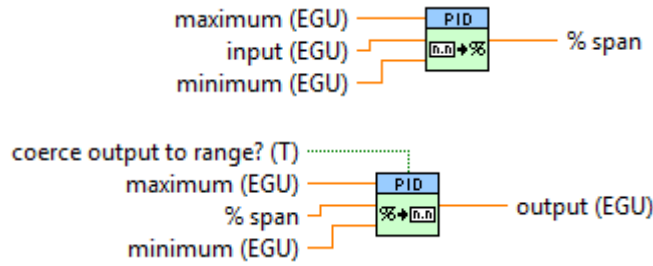


Figure 4-20. Unit conversion VIs

For the case of pH control, a controller bias of 24% is added to the controller. The flowrate of the acid stream in absence of process disturbances is approximately 5 ml/s. The bias of 24% brings the flowrate of base stream to around 5 ml/s. As the concentrations of both acid and base streams are equal, this should maintain the process variable steady at pH 7. The controller output is specified to range from -24 to 76%, hence, when the bias is added to the controller output, the resulting range is a full 0 to 100% scale. No controller bias is used for the conductivity control using the disc rotational speed and the controller output range is specified as 0-100%. For each control experiment, the values of the setpoint, process variable and controller output are written to an excel spreadsheet file each time the loop is executed using the ‘Write to Spreadsheet’ VI shown in Figure 4-21.

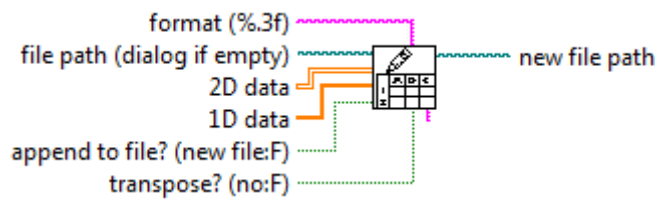






Figure 4-21. Write to Spreadsheet VI

In addition to the PID VIs a number of data acquisition VIs (see Table 4-2) are used to construct the feedback control loop. The DAQ VIs are available from the Function palette >Measurement I/O>NI-DAQmx >Data Acquisition.

Table 4-2. DAQ VIs

VI	Description
 DAQmx Create Virtual Channel.vi	Creates channel(s) to measure voltage.
 DAQmx Read.vi	Reads samples from the specified task or virtual channel.
 DAQmx Write.vi	Writes samples to a task that contains an analog output channel.
 DAQmx Timing.vi	Sets the source and rate of the sample clock, and the number of samples to acquire or generate.

Data acquisition occurs in two stages: in the first stage data is transferred from the DAQ device (USB6211 or USB6008) into the memory (RAM) of the computer. This stage is controlled by the DAQmx Timing VI which configures the mode and the number of samples to acquire or generate. A buffer size is specified by the value of ‘samples per channel’ input of DAQmx Timing VI (see Figure 4-22), whilst, the time taken to fill the buffer is equal to the buffer size divided by sampling rate. The DAQ devices use onboard First-In-First-Out (FIFO) buffers as an intermediate place to store the acquired data.

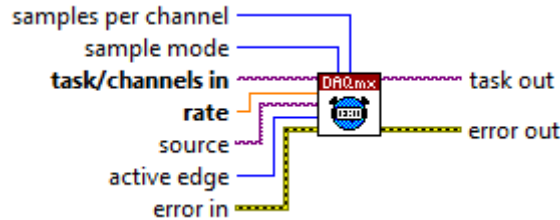


Figure 4-22. DAQmx Timing (Sample Clock) VI

The second stage of data transfer involves conveying the data from the PC buffer (RAM) into the Application Development Environment (ADE) memory of the LabVIEW software, which is managed by the DAQmx Read VI. Therefore, the read loop rate must be fast enough so that the buffer does not overflow. The DAQmx Write Function moves samples from the ADE memory to the PC buffer in RAM. These samples are then transferred from the PC buffer to the DAQ board FIFO in order to be sent to the actuator.

The pH and conductivity signals sent from the transmitter are current signals in the range of 4 - 20 mA. These signals pass through a 250 Ohms resistor before entering the DAQ devices in form of analog voltage signals in the range of 1 – 5 Volts. These analog signals are then converted to a digital signal by the DAQ devices before being sent to the computer. Sampling rate can be defined as how often an analog to digital conversion (A/D) takes place with units of Hz; whilst, sampling period is the inverse of sampling rate with units of seconds. A Sample Clock accurately times the occurrence of each A/D conversion. The required sampling rate is a function of the type and the characteristics of the signal being measured as well as the dynamics of the process to be controlled.

A signal needs to be adequately sampled in order to preserve the information it conveys, whereby, inadequate sampling causes distortion of the signal or aliasing [169]. According to Nyquist's theorem to avoid aliasing the sampling rate must be greater than twice the maximum frequency component in the measured signal. However, this theorem is only concerned with preserving the frequency content of the signal. In order to accurately represent the shape of the signal, the sample rate should be at least 5 or 10 times the maximum frequency component of the signal [169].

However, sampling rate is not critical if the measured signal is DC (low frequency) which varies less than once every second. In this study the pH and conductivity signals can be regarded as analog DC signals as the speed of any measured changes are limited by the response times of the pH and conductivity electrodes. In control theory, the guideline is that a control system should sample a physical process at a rate about 10 times faster than the fastest time constant in the physical process [170]. The sampling rate also depends on the

capability of the DAQ device and the computer system on which the LabVIEW data acquisition code is executed. In the present work, a sampling rate of 10 Hz in continuous sampling mode is used for the pH control. However this sampling rate is too fast for the conductivity closed loop runs in which USB-6008 DAQ device is used; thus, a value of 2 Hz was selected for the sampling rate.

Since this control setup involves both hardware and software, it is critical to ensure that the respective operations are adequately synchronised. ‘Determinism’ allows accurate determination and control of the timing for execution of different sections of a program, and is perhaps the most important factor in defining a ‘real-time’ application [168]. It should be noted that a PC operating under Windows is not real-time due to timing uncertainties caused by the computer operating system. To achieve determinism, a real-time operating system (RTOS) along with specific hardware components is required. For a real-time application, the LabVIEW RT development environment can be used. LabVIEW RT runs on a Windows host, where the host only provides local storage and user interface. When the run button is pressed the developed code is downloaded to an embedded target with a dedicated processor on a RTOS [168].

The hardware required for implementation of LabVIEW RT is not available for this study. However, in development of the LabVIEW code, an effort is made to make the program efficient and correlate software and hardware operations using software timing. For software-timed analog control loops the data acquisition and control loop rates are controlled by a software timer. Some of the common software timers available in LabVIEW are:

- Wait (ms).vi
- Wait Until Next ms Multiple.vi
- Timed loop
- Simulation loop

The ‘Wait (ms)’ function ensures that a certain amount of time has elapsed between loop iterations, without reference to an absolute time. Whereas the ‘Wait Until Next ms Multiple’ function controls the loop execution rate with respect to a millisecond timer, therefore more suited for synchronising activities. The ‘Timed loop’ and ‘Simulation loop’ also provide fairly deterministic software timing mechanisms for data acquisition tasks. The determinism and resolution of the above timers are dependent on the operating system. LabVIEW’s built-in timing function uses the PC’s real-time clock, which is based on milliseconds. Therefore, timing loops of up to 1 kHz can theoretically be achieved by software timing.

For the pH control loop involving a PID controller a timed loop is used to provide software timing, whilst for the conductivity control using a PI controller a simulation loop is used to facilitate the inclusion of a low pass filter on the process signal (see Section 4.2.3). The simulation loops are also used for the cases involving a DO scheme instead of timed loops. This is because the online implementation of the DO scheme involves implementing the nominal plant model and the low pass filter using Laplace transfer functions. For the pH control the rate of the loop execution (loop period) is selected as 100 ms which is equal to the sampling rate (10 Hz) controlled by the Sample Clock. Similarly the loop period for the

conductivity control is set to 500 ms to match the sampling rate of 2 Hz. Therefore the control loops are executed once for each sample point that is acquired.

The simulated elements are included in the code using the ‘Control Design & Simulation’ module within LabVIEW. To achieve some degree of determinism, fixed step ODE solvers with an appropriate step size should to be used. In this study Runge-Kutta 4 which is a high order fixed step ODE solver is selected. The step size is the interval between the times at which the ODE solver evaluates the model and updates the model output. By setting the step size of the ODE solver equal to the simulation period, the simulation runs in almost real-time. If no timing is reinforced the simulation loop will solve as fast as the CPU can handle. As shown in Figure 4-23, for the pH control loop including the DO scheme the ODE step size is selected as 0.1s which is equal to the loop period of 100 ms specified using the simulation parameter window. The step size and loop period for the conductivity control including DO scheme are 0.5s and 500ms respectively.

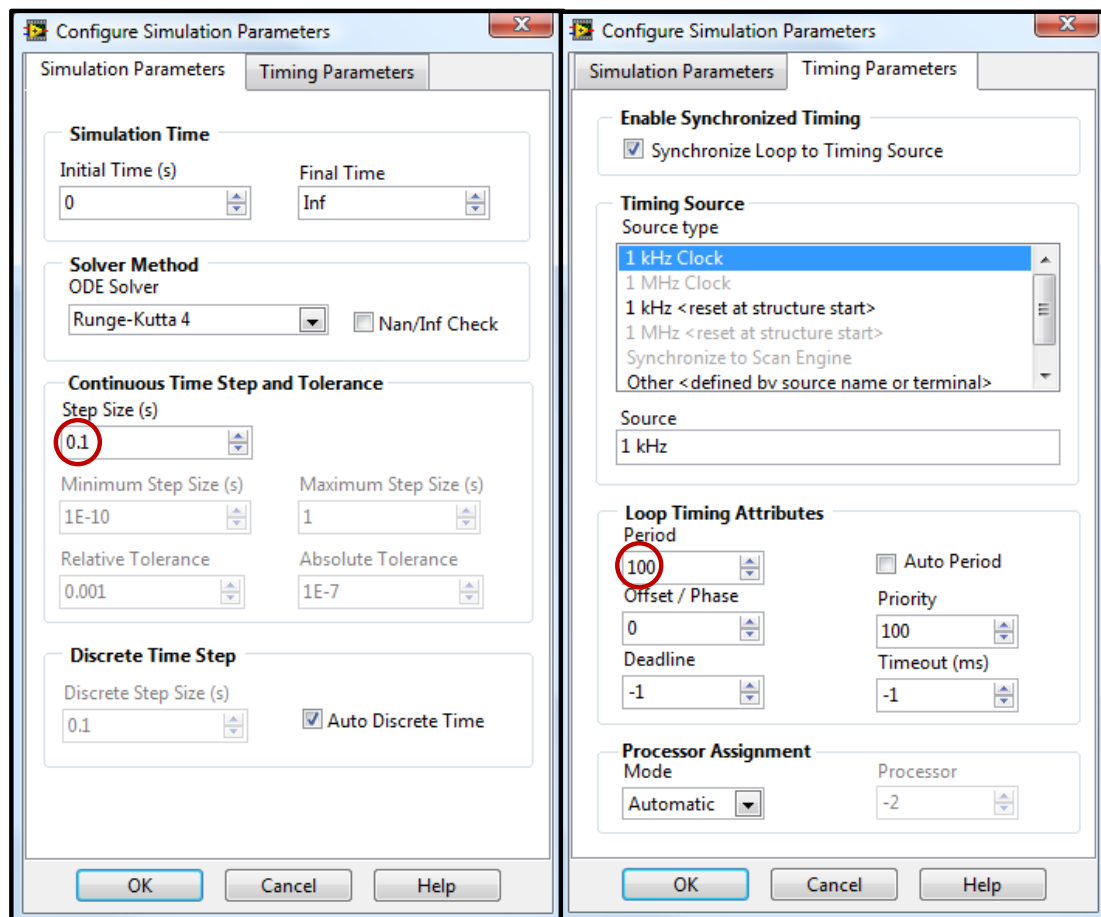


Figure 4-23. Simulation parameters configuration window

The continuous transfer functions for the elements of the DO scheme, as well as the low pass filter on the conductivity signal are converted to discrete transfer functions to enable synchronisation of the hardware and software operations. The following VI available in the ‘Control Design & Simulation’ palette is used to obtain the discrete transfer functions:

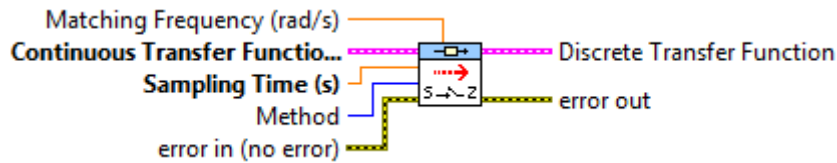


Figure 4-24. CD Convert Continuous to Discrete VI

The Tustin (Bilinear) method is chosen to carry out the conversion, in which case the Laplace operator ‘s’ is approximated as:

$$s \rightarrow \frac{2(z-1)}{T_s(z+1)} \quad (4-2)$$

where,  $T_s$  is the sampling interval.

### 4.2.3 Conductivity Signal Conditioning

Using the USB6008 DAQ device for the conductivity signal eliminated the large spikes in the process signal which were observed when the USB6211 device was used. However, the signal still contained some measurement noise which may have a detrimental impact on the control performance. The simplest way to reduce the degree of variations in the signal is to add a low-pass filter to the acquired data to attenuate the high frequency components (noise) of the signal. In the present study a first order low-pass filter with a time constant of 0.375 seconds (two thirds of the sampling interval) is selected to smooth out the measurement noise to some extent. Increasing the filter time constant enhances the noise reduction capability of the filter at the expense of larger lags introduced in the input signal, which may lead to deterioration of the control performance. The filter is implemented in LabVIEW on the path of the incoming conductivity signal. Further enhancement of the filter design, and perhaps hardware filter considerations, are outside the scope of the current work.

### 4.2.4 Implementation of pH Control Loop in Simulink

The experimentally determined process model obtained via open loop step tests is used to study and specify suitable control schemas for pH control by means of simulations. The nominal control loop contains a PI controller, whilst, the addition of a pH characteriser and a disturbance observer scheme to improve the control performance are also investigated in detail.

pH control simulations are often based on the knowledge of titration characteristics of the system. A titration curve is a plot of pH values versus the corresponding ratio of the acid and base present in the system. Hence to simulate the pH process it is crucial to have an accurate representation of the titration characteristics. In the present work, the titration curve of 0.1M solutions of hydrochloric acid and sodium hydroxide are obtained by conducting a standard titration experiment. The experimentally determined titration curve is then implemented in Simulink using a ‘Lookup Table’ block, shown in Figure 4-25, where the input data are the volumetric ratios of the base to acid streams, whilst the output data are the corresponding pH values.

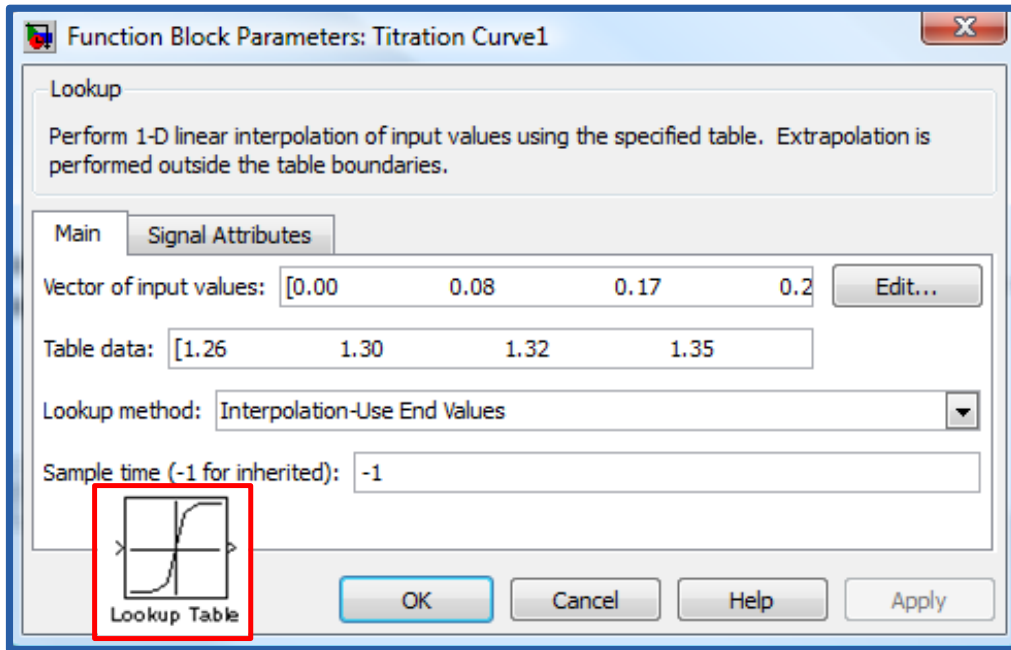


Figure 4-25. Lookup Table block

The nominal set up of a feedback pH control loop is illustrated in Figure 4-26. The ‘PID Controller’ block (Simulink Extras > Additional Linear) calculates an output based on the value of the error for each execution of the loop. The error is based on the difference between the specified pH setpoint and the pH measurement downstream of the process. The control objective in the pH control runs is to maintain the effluent pH at the neutral point of 7 pH. Therefore, if the value of error is positive, implying that the effluent pH is below 7, then the controller increases the base flowrate from the nominal value by generating a positive controller output. Conversely, if the error is negative the controller reduces the base flow rate from the baseline to regulate the effluent pH. Changes in the acid stream flowrate are introduced to model process disturbances, whilst during the normal operation the acid flow is constant.

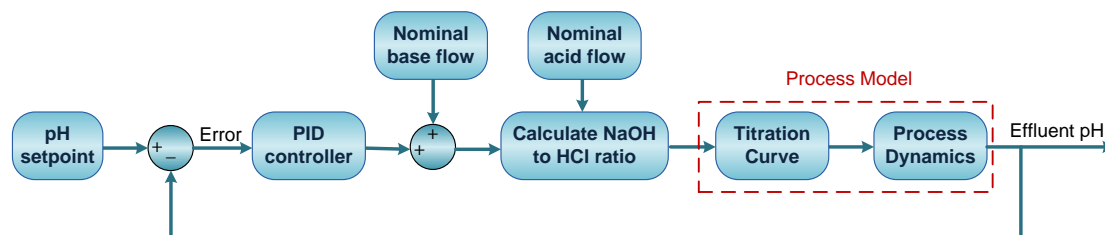


Figure 4-26. pH control loop

For each loop execution the ratio of the base to acid flowrates are calculated using a ‘Function’ block (Simulink > User-defined Functions). This value is then fed to the titration curve which is implemented in a Lookup Table block. If the value matches an experimental data point in the block’s input, then the output generated (effluent pH) is the corresponding element in the output vector of the block. However, if the calculated ratio does not match any of the experimental data in the input vector of the Lookup Table block, then the block performs linear interpolation between the two appropriate experimental data points to determine an output value. If the block input is less than the first or greater than the last experimental data point in the input vector, then the block uses the first or last values of pH in

the output vector. Selection of the 'Interpolation-Use End Values' lookup method ensures that the pH values generated by the simulation are logical and do not go beyond the acceptable pH range. Finally, the experimentally determined process dynamics which combine the base stream pump, the SDR, the pH sensor and transmitter dynamics are implemented in a 'Transfer Function' block (Simulink > Continuous).

Two points regarding the setup of the above control loop should be emphasized here. First, the input-output model of the process determined by the open loop tests describes the system behaviour using a first order model which also includes the titration characteristics. However, as an experimental titration curve is included in the simulations, the gain of the process implemented in the process dynamics transfer function is set to one. Otherwise, the process gain is included in the simulation loop twice which leads to incorrect results. The second point is that transfer functions operate on the basis of deviation from a steady state value as opposed to an absolute value. For instance, the output of the titration curve block in Figure 4-26 is the actual value of the effluent pH corresponding to the ratio of base to acid present in the system. Therefore, this value should first be converted to deviation from setpoint before being passed through the transfer function block describing the process dynamics.

The nominal pH control loop is adjusted accordingly to include a characteriser and a disturbance observer in the control loop. Similar to the titration curve, the pH characteriser is also implemented in a Lookup Table block. A high order, variable step ODE solver namely ODE45 (Darmand-Prince) is used to solve the simulation models. The control loops are subjected to various disturbance rejection, setpoint tracking and robustness tests to evaluate the performances of the selected control schemes. The results and discussion of the simulated pH control tests are presented in the next chapter.

### ***4.2.5 pH Control Experiments***

Sodium hydroxide pellets (98+%) and hydrochloric acid (37% v/v) supplied by VWR International are used for the pH control experiments to make up 0.1M feed solutions. 4 grams of sodium hydroxide pellets are weighed and dissolved in each litre of water using a magnetic stirrer before the feed solution is charged into the feed vessel. Also, 8.4ml of the concentrated acid is measured and added to each litre of water under a fume cupboard prior to transferring the dilute acidic feed solution to the feed vessel.

After charging the feed vessels the flow of nitrogen through the rotary union is started to prevent contact and subsequent damage of the non-contact bearings within the unit. If the nitrogen pressure falls below 3.4 bar the SDR control system stops the disc rotation via an interlock. The disc and the reactor wall temperatures are set to 25°C via the temperature control units. The system generally reaches steady state within ten minutes. The disc rotational speed is then set via the SDR software to the nominal value of 750 rpm. The stopcock valves on the feed vessels are opened and the peristaltic and gear pumps are started to deliver the acid and base solutions to the SDR at a flow of approximately 5 ml/s.



The open loop step tests are carried out to obtain input-output model of the system. The tests are performed by introducing step changes in flowrate of the base stream, in an open-loop configuration, whilst the corresponding effect on the effluent pH is measured and recorded. Throughout the test, the flowrate of the acid stream is kept constant. Both upwards and downwards steps, by adjusting the gear pump speed by 20 rpm (0.1 ml/s), are implemented to capture any direction-dependent characteristics that might prevail in the system.

The feedback control experiments are started by clicking the run button in the LabVIEW program which closes the loop. The controller performance is assessed in terms of setpoint tracking and disturbance rejection. For the disturbance rejection runs, the acid stream flowrate is increased by 20% from the baseline of 5 ml/s. The flowrate is then brought back to the baseline before a 20% reduction is introduced. For the setpoint tracking runs, changes in the pH setpoint are introduced in order to assess the ability of the controller to follow the specified desired value. Wherein step changes with magnitude of 2 and 5.2 pH units are implemented from the steady state value of pH 7 in both directions. The values of the process variable together with the setpoint and the controller output are compiled to an Excel file at each execution of the loop.

At the end of each run the pumps are stopped and the feed stream valves are closed. The system is then flushed with water to minimise the risk of corrosion on the stainless steel equipment. The disc and the nitrogen flow are subsequently halted and the temperature control units are switched off.

#### ***4.2.6 Conductivity Control Experiments using the Rotational Speed***

Barium chloride dihydrate (99+%) and sodium sulphate anhydrous (99+%) supplied by Fisher Scientific are used to make up 0.01M feed solutions for the conductivity control experiments. 14.2 grams of sodium sulphate and 24.4 grams of barium chloride are used for each litre of the solvent. The measured quantities of the salts are dissolved in de-ionised water using a magnetic stirrer before the feed solutions are charged into the feed vessels.

The nitrogen flow to the rotary union is then started, while the disc and the reactor housing walls are set to 25°C. The valves on the feed vessels are opened and the aqueous solutions of barium chloride and sodium sulphate are pumped to the SDR at constant flowrates of 5 ml/s.

The open loop tests involve introducing step changes in the disc rotational speed and recording the output response of the system, namely the effluent stream conductivity. The disc rotational speed is increased from a baseline speed of 900 rpm to 1600 rpm, which is then brought back to the original level before a drop to 200 rpm is implemented. The changes in the conductivity of the product stream as a result of the variations in the disc rotational speed lead to determination of the input-output model of the precipitation process.

Similar to the pH control experiments, the feedback control loop is closed by executing the LabVIEW program. The control schemes are evaluated in terms of setpoint tracking to explore the potential of achieving a control task by means of manipulating the disc rotational

speed. The values of the process variable, controller output and the setpoint are transferred to an Excel file for each iteration of the control loop.

Upon completion of each run, the feed stream pumps are switched off and the disc is brought to a halt. The nitrogen flowrate to the rotary union and the temperature control units are then shut down. The system is then thoroughly flushed with water and the disc surface and the conductivity probe are wiped clean to remove any residual precipitated particles.

### 4.2.7 Thermal Imaging Experiments

The surface temperatures of the thin liquid films produced on the rotating disc are analysed using the infrared thermal imaging camera for a range of operating conditions. The processing fluids examined by the IR camera include water, Therminol SP, water and glycerol as well as aqueous solutions of HCl and NaOH. The acid and base solutions are made up to concentrations of 0.1M and 0.5M; whilst, the water and glycerol solutions are made up by mixing equal volumetric amounts of the two substances.

Glycerol is added to water to investigate the effect of viscosity on heat transfer and the hydrodynamics of thin liquid films. A synthetic oil (Therminol SP) which has different properties (boiling point, heat capacity, emissivity, etc.) compared to water is also used as processing fluid. The aqueous feeds containing 0.1M or 0.5M concentrations of hydrochloric acid and sodium hydroxide are studied to evaluate the potential effects of the heat of reaction.

The operating conditions for the thermographic runs are displayed in Table 4-3. For the cases of water and Therminol SP, two feed arrangements discussed in Section 4.1.2 are applied. Higher flowrates are used for the cases involving the distributor system in order to achieve continuous flow of the liquid through the annulus gap. It was observed that at lower flowrates, the liquid exiting the annular space merged with the fluid jet from the circular tube (see Figure 4-8) before the two feed streams came in contact with the disc.

Table 4-3 Operating conditions

Working Fluid	Feed arrangement*	$T_d$ [°C]	Q [ml/s]	N [rpm]
Water	1	25, 50, 70	5, 10, 15	500, 1250, 2000
Water	2	25, 50, 70	10, 15, 20	500, 1250, 2000
Water/Glycerol mixture	1	25, 70	5, 10	500, 2000
Therminol SP	1	25, 70, 100	1, 5, 10, 15, 20	500, 1250, 2000
Therminol SP	2	50, 70, 100	10, 15, 20	500, 1250, 2000
HCl and NaOH solutions (0.1 and 0.5M)	1	25, 70	5, 10	500, 2000

\*1. Single point injections, 2. Distributor system

The start-up and shut-down procedures are the same as those described in the previous sections. In brief, the feed vessels are first charged with the processing fluids and the disc and reactor wall temperatures are set to the desired values. The flow of nitrogen to the rotary union is started before the disc is set in motion at a desired rotational speed. When the system reaches steady state a single snap shot of the liquid film is taken by the IR camera for subsequent offline analysis. At the end of each experiment, the temperature control units, the disc, the nitrogen flow and the feed pumps are shut down. The system is then flushed with

warm water to remove any residue of the processing fluids from the equipment. In order to obtain accurate measurements of an object's temperature a number of input parameters need to be specified in the camera software, as discussed next.

#### 4.2.7.1 Evaluation of the IR Camera Input Parameters

The following object parameters must be supplied to the camera used in this study in order to compensate for the effect of a number of different radiation sources:

1. The emissivity of the object
2. The reflected apparent temperature
3. The distance between the object and the camera
4. The relative humidity
5. Temperature of the atmosphere

The object's emissivity is often the most important input parameter to be evaluated. The true emissivity of the liquid film on a rotating disc could not be measured in this study and had to be estimated from relevant information available in the literature. The challenge in evaluating the emissivity of thin liquid films on a rotating surface is the fact that emissivity is a function of film thickness [155, 156]. Based on the Nusselt theory of thin film flow, the film thickness decreases with increasing disc radius (Equation 2-3), as illustrated graphically in Figure 4-27 and Figure 4-28 for a number of flowrates and rotational speeds (viscosities evaluated at 43 °C). This relationship implies that the emissivity of the liquid film varies depending on the radial position on the disc.

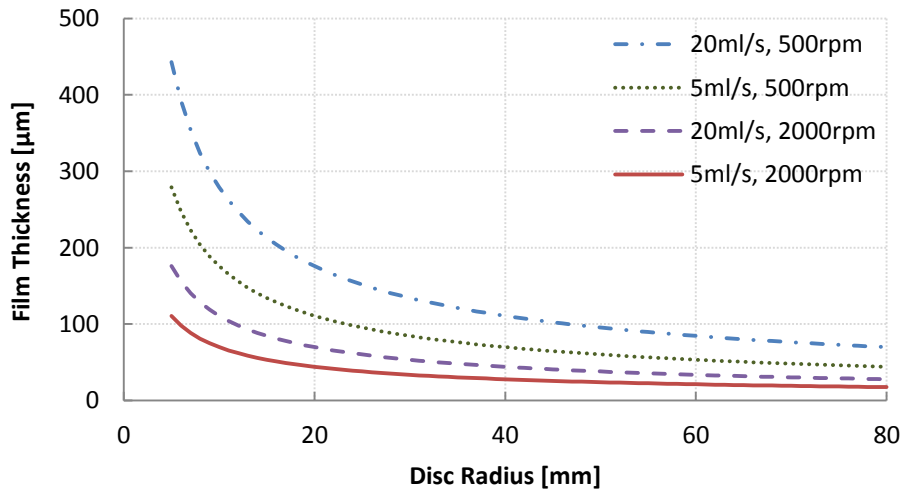


Figure 4-27. Water film thickness profile

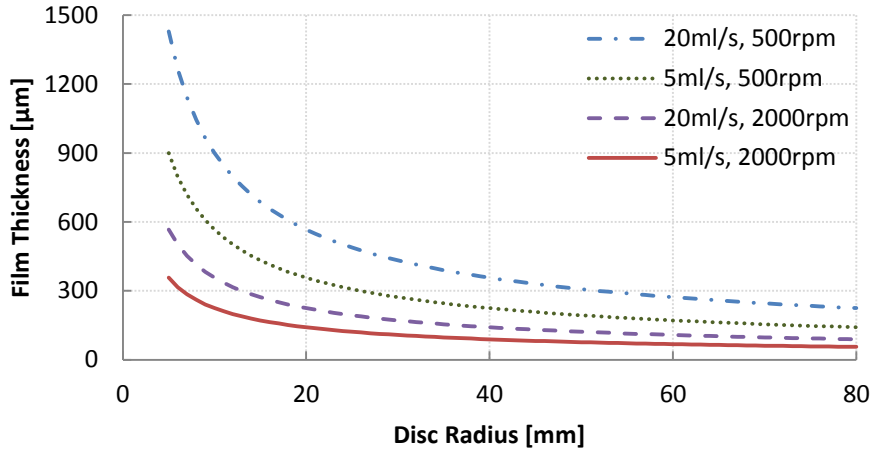


Figure 4-28. Therminol SP film thickness profile

For runs with water, the minimum film thickness was kept above 20  $\mu\text{m}$ . Assuming that the data presented in Figure 4-29 is applicable to the operating conditions in this study, the emissivity of the water films should not be far from the typical value of 0.96 [171]; this value was used for runs with water and water-glycerol.

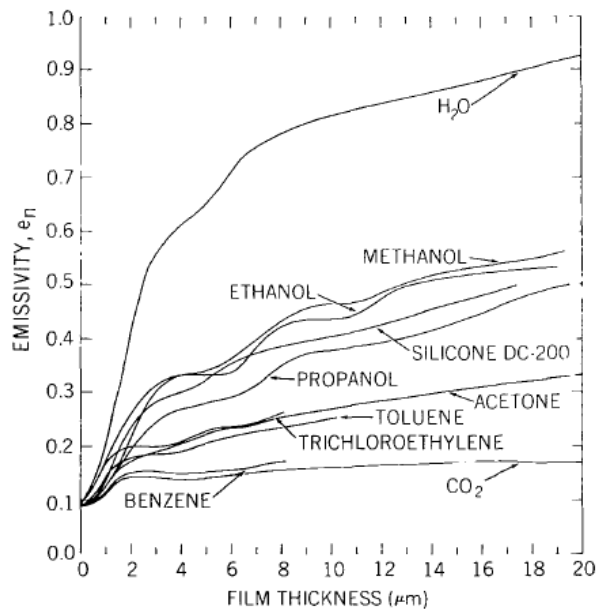


Figure 4-29. Emissivity as a function of film thickness on polished stainless steel surface at 77K [156]

However, no data regarding the emissivity of Therminol SP (mixture of synthesis hydrocarbons) were available. The closest information that could be adopted was the emissivity of lubricating oil on Ni base at 20°C, presented in Table 4-4 .

Table 4-4. Emissivity of lubricating oil [171]

Film Thickness[ $\mu\text{m}$ ]	Emissivity
25	0.27
50	0.46
125	0.72
Thick coating	0.82

Figure 4-30 illustrates the effect of the minimum and maximum emissivity values taken from Table 4-4 on temperature measurements across a thin film of Therminol SP for a typical run. It can be seen that the emissivity values significantly influence the temperature measurements, thus accurate measurements are only possible if the emissivity can be determined accurately.

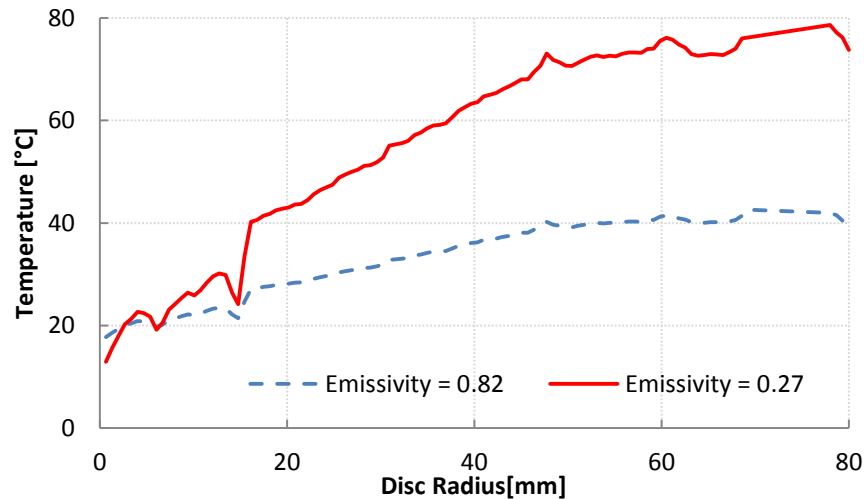


Figure 4-30. Effect of emissivity on temperature measurement,  $T_d=70^\circ\text{C}$

The best way for calculating the temperature profiles across the disc in this study might be to divide each thermogram into a number of small segments and evaluate the corresponding film thickness and emissivity within each segment. A simpler method is to use the value of emissivity corresponding to the estimated average film thickness for each run. The temperature measurements obtained using these two methods for a typical run are illustrated in Figure 4-31. Using emissivity values corresponding to small segments across the disc is more accurate; however, the difference between the two methods is relatively small. Hence, for simplicity it was decided to use the emissivity values corresponding to the predicted average film thickness for each run.

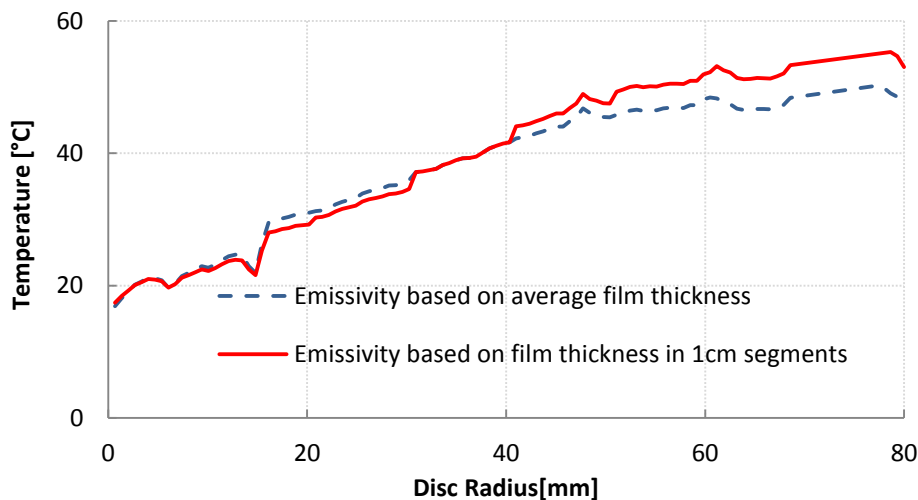


Figure 4-31. Methods of evaluating emissivity

The underlying limitation, however, is that accurate estimation of film thickness may not be possible as film thickness is a function of kinematic viscosity which is in turn a function of temperature (an unknown parameter). The dependence of viscosity on temperature is especially relevant to relatively viscous process liquids such as Therminol SP used in this study. Furthermore, the presence of surface waves and disturbances due to bringing the liquid up to the disc angular velocity leads to very complex fluid dynamics on the rotating disc, not accounted for in Nusselt model of thin film hydrodynamics, which applies to a smooth film. All of these effects make prediction of the true film thickness very difficult across the whole of the disc surface. Consequently, the emissivity values and the resulting temperature measurements are associated with a degree of uncertainty. A simulation investigation of errors in infrared thermography [159] revealed that overestimation of emissivity by 30% leads to  $-(1 - 4)\%$  error in the measured temperature; whilst underestimation of the emissivity by 30% results in  $+(2 - 7)\%$  error in the measured temperature for emissivity range of 0.4 to 0.98 and object temperature range of 300 to 400K.

The reflected apparent temperature was measured to be 20°C using the procedure described in the camera's user manual [153]. In the present experimental setup the distance between the object and the camera lens is 0.4 m. For short distances and normal humidity, the relative humidity can generally be left at a default value of 50%, whilst, the temperature of the atmosphere was monitored over the run period and an average value of 20°C was measured.

### **4.3 Summary**

This chapter began by presenting the apparatus used to carry out the current investigations. The individual components of the SDR unit along with the auxiliary equipment such as pumps and temperature control units, as well as sensors and transmitters were described in detail. The software simulation packages used in the control studies were also outlined.

A detailed description of the procedures adopted to conduct the present work was also provided in this chapter. This included software implementation of the feedback control loops, experimental procedures and the evaluation of input parameters to obtain the thermographic measurements. The experimental conditions such feed concentrations and flowrates, disc rotational speed and temperatures were also outlined. The results and discussion of the experimental and simulations studies concerning pH and conductivity control in a SDR, as well as the thermographic analysis of thin liquid films are presented in the next three chapters.

## Chapter 5. pH Control

The control studies in the present work are carried out in two phases: (1) pH control (2) conductivity control using the disc rotational speed. The results of the latter investigation are presented and discussed in the next chapter. Here, the focus is on pH control where the objective is to neutralise an acidic process stream (dilute hydrochloric acid) by adjusting the flowrate of a basic reagent stream (dilute sodium hydroxide). To control the pH of the effluent stream at a desired value, the controller manipulates the flowrate of the base stream based on the feedback signal sent from the pH transmitter, as illustrated in Figure 5-1.

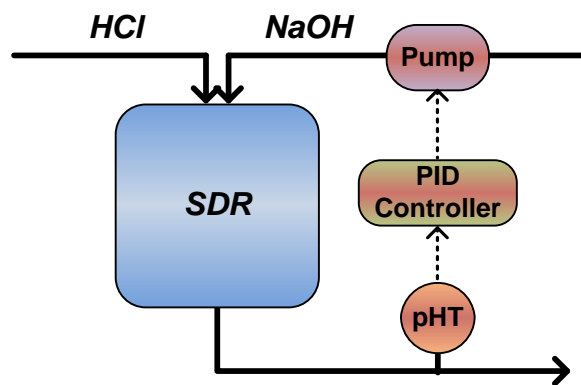


Figure 5-1 Schematic of pH control loop

The control investigations involve both simulation and experimental studies. An appropriate model of the process is first determined experimentally via open loop step tests. The model is then used to study the interactions between different parameters and also to identify suitable control schemas via simulation. Selected control strategies are then implemented online to enable the experimental study of pH control in the SDR unit. The apparatus used to carry out both simulation and experimental studies, along with the applied procedures were outlined in the previous chapter. The present chapter provides the results and discussion of the pH control investigations.

### 5.1 Process Model

The process model for the case of pH control consists of the pH titration curve in series with a first order dynamic model of the system.

#### 5.1.1 Titration Curve

The laboratory generated titration curve of the system is presented in Figure 5-2. As expected for a strong acid/strong base system, the titration curve depicts a highly nonlinear behaviour, with great sensitivity around the equivalence point. As the process gain is equal to the slope of the titration curve, it can be seen that different operating regions with very high and very low gains prevail in the system. The steep section of the titration curve, between 2

and 12 pH, shows that the effluent pH changes significantly with a small change in the reagent concentration. The relatively flat portions of the curve in the acidic and basic regions, on the other hand, indicate the reduced sensitivity of the system to reagent addition.

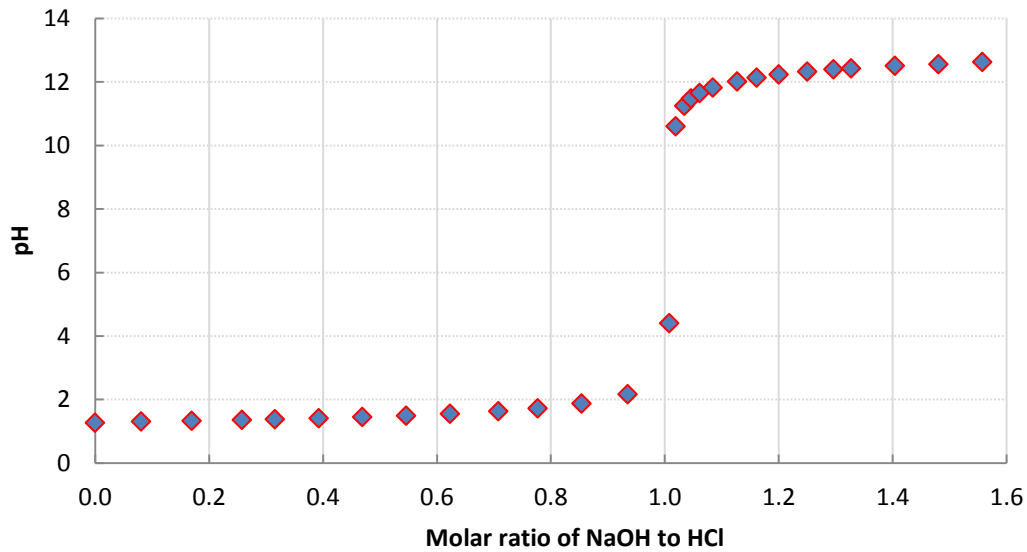


Figure 5-2 Laboratory generated titration curve

The titration curve may also be generated using a mathematical model of the system. A relatively simple technique known as ‘interval-halving search method’ is described by McMillan [24]. This method can be adopted to model the pH of strong acid/strong base systems, based on the charge balance equation, presented below:

$$C_B - C_A + 10^{(-pH)} - 10^{(pH-pK_w)} = 0 \quad (5-1)$$

$C_B$  and  $C_A$  are concentrations of base and acid respectively. Strong acids and bases are completely ionized; hence, ion concentrations are equal to the acid and base concentrations. The charge balance equation applied to the HCl/NaOH system, states that the sum of  $\text{Na}^+$ ,  $\text{Cl}^-$ ,  $\text{H}^+$  and  $\text{OH}^-$  ion concentration must equal zero. In the interval-halving search method, excess charge is calculated for the pH value at the midpoint of the pH search interval. If the charge is negative the upper pH search limit is decreased to the midpoint pH; and if the charge is positive the lower pH search limit is increased to the midpoint pH. The interval-halving continues until the interval is less than a specified tolerance error. However, this method of generating the titration curve is computationally demanding, hence, the data points from the laboratory generated titration curve are used to model the pH characteristics.

### 5.1.2 Dynamic Model of the Process

The process model, which combines the dynamics of the reagent pump, SDR and pH probe as well as the titration characteristics, is determined by input-output tests. The process model allows analysis of the dynamics and interactions within the system, and hence provides a platform for the specification and testing of control schemas via simulation. The input-output data describing the variation in the effluent pH as a result of input step changes in the base stream flowrate are illustrated in Figure 5-3.



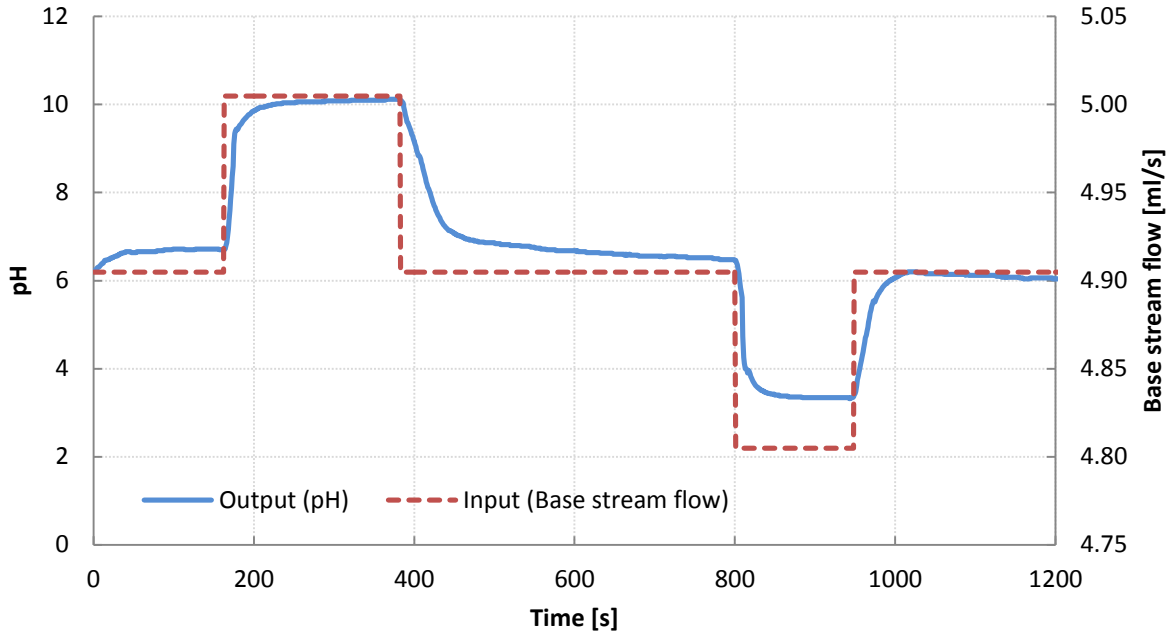


Figure 5-3. Input-output data

The input-output data show that the pH response is asymmetric, even though the input step changes are symmetrical. It can be seen that the pH responses are different depending on the initial state of the system when the step change is applied, and also on the direction of the step change. For instance, the process gain is higher when base flow is increased compared to when it is decreased. In addition, pH responds faster to changes that are introduced when the output is close the equivalence point. The input-output data are imported into MATLAB/Simulink and subsequently used to determine a transfer function which describes the process model. The process model parameters, namely process gain and time constant are adjusted to achieve the best fit between the experimental data and that produced by the model. The first order transfer function obtained is presented below:

$$G_p = \frac{k_p}{\tau_p s + 1} = \frac{34}{18s + 1} \quad (5-2)$$

Where,  $k_p$  is the process gain with units of pH/(ml/s base) and  $\tau_p$  is the process time constant with units of seconds. In the open loop step tests, the step changes in the flowrate of the base stream were introduced by manually adjusting the speed of the reagent stream pump. The corresponding flowrates were then subsequently calculated using the pump calibration data. Since the exact value of the base flowrate could not be measured and recorded against the same sample clock used for the effluent pH measurements, it is not possible to accurately measure the actual value of the time delay. Therefore, a delay free model is fitted to the experimental data. Figure 5-4 shows the output pH responses obtained from the input-output tests along with those produced by the model, which show a reasonable agreement.

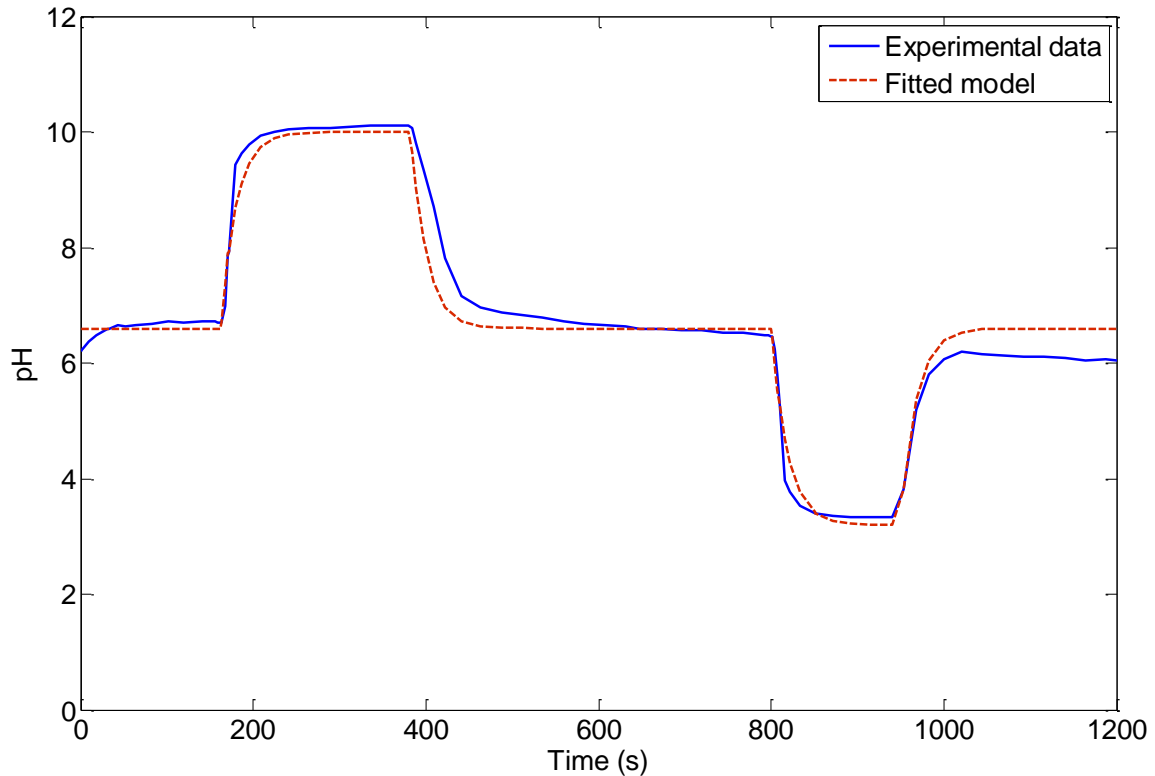


Figure 5-4. Process model and experimental pH responses

The rather large value of the process gain (34) reflects the steepness of the slope of the titration curve between 2 and 12 pH, whereby small changes in the input result in large deviations in the output. The time constant combines the dynamics of the actuator, SDR, pH probe and transmitter. In order to preserve the nonlinear characteristics of the pH process, the titration curve is included in the simulations, and thus the process gain of the first order model is set to 1, as shown by the following block diagram:

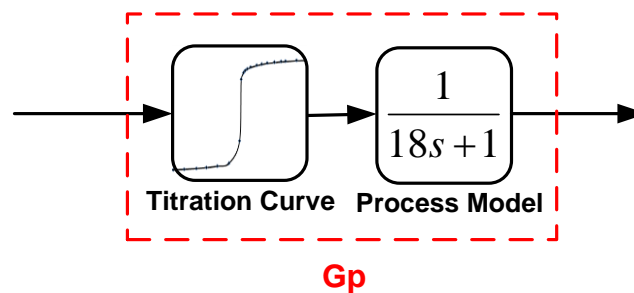


Figure 5-5. Implementation of the process model

As discussed previously the value of the time delay in the system could not be accurately measured, thus a delay free process model was developed. However, a delay term to account for transport/measurement time delays in the system will be included in the simulation studies. Two rather arbitrary values of time delay (1 and 5 seconds) are tested to evaluate the potential impact of the time delay on the controller's performance. These values of the time delay are also used in the direct synthesis formula to obtain the appropriate controller tuning parameters.

## 5.2 Simulation Studies

The simulation studies are carried out based on the process model presented in the previous section along with two values of the time delay. Applying the direct synthesis method to the first order process model yields a PI controller. The aim of the simulation studies is to investigate the performances of the linear PI controller along with two nonlinear compensation methods for the task of pH control. The influence of time delay on control performance is also investigated in detail. The results are discussed in the subsequent sections.

### 5.2.1 Control Strategies

The control strategies investigated here employ a feedback control structure in which the controller's action is based on the difference between the setpoint and the pH of the effluent stream, as illustrated in Figure 5-6. A major shortcoming of feedback control is that a corrective action is taken only after the controlled variable deviates from the setpoint, as a result of a load disturbance in the influent and/or reagent stream, or when there is a change in setpoint. Furthermore, the performance of a feedback controller in terms of disturbance rejection and setpoint tracking is adversely affected by the loop dead time, which is equal to the sum of transportation and measurement delays, actuator dead time, mixing time, etc.

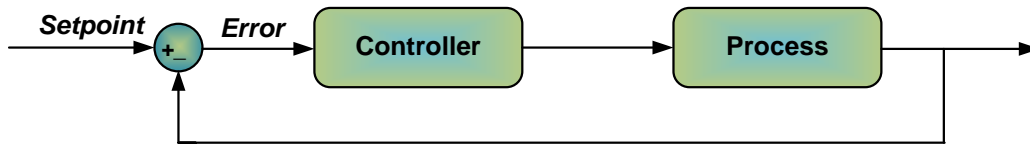


Figure 5-6. Feedback control scheme block diagram

To avoid instability in a feedback loop the product of the controller and process gains should be less than one at the ultimate period of the system [24]. Therefore, the controller gain must be decreased to maintain stability when operating at the steep region of the titration curve, where the process gain is high. However, this small value of the controller gain results in sluggish responses when operating at the flat portions of the titration curves (acidic and basic regions).

The direct synthesis method is used to obtain the controller parameters, which leads to a PI controller based on the first order model of the process. The only tuning parameter in the direct synthesis method is the closed loop time constant,  $\lambda$ . Small values of  $\lambda$  result in large controller gains which provide fast responses. However, if the value of  $\lambda$  is too small the closed loop might become unstable. In the present study for pH control, a suitable closed loop time constant was determined by trial and error. It was found that a value equal to one-tenth of the process time constant, i.e. 1.8 seconds, provides a good balance between fast control and stability. Therefore, the tuning parameters of the PI controller based on the direct synthesis method are as follows:

Table 5-1. PI controller tuning parameters (direct synthesis)

	$\theta = 1\text{ s}$	$\theta = 5\text{ s}$
Kc [ml.s <sup>-1</sup> base/pH]	0.189	0.078
Ti [s]	18	18

pH control is often regarded as a challenging task due to the non-linear and time-varying nature of the process. Therefore, controllers that are both nonlinear and adaptive may be required to achieve satisfactory performance [90]. However, the objective of the present study is to apply controllers based on the most commonly used PI/PID algorithms to perform the control task. However, the additions of a pH characteriser as well as a disturbance observer scheme, as nonlinear compensation methods, are also investigated in the present study to assess the degree to which these techniques can help mitigate the effects of nonlinearity. Thus, the control strategies considered here are as follows:

1. PI controller
2. PI controller plus pH characteriser (PI+C)
3. PI controller plus disturbance observer (PI+DO)
4. PI controller plus pH characteriser and disturbance observer (PI+C+DO)

The block diagrams of the above control schemes implemented in Simulink are presented in Appendix E. The tuning parameters presented in Table 5-1 are initially used for all control algorithms to provide a basis for performance comparison purposes. Note, however, the controller for each scenario can be fine-tuned to obtain the best achievable control performance.

The pH characteriser is the titration curve rotated, as shown in Figure 5-7. The X-axis of the characteriser is the measured pH and the Y-axis is the normalised molar ratio of base to acid, obtained from the titration data presented in Figure 5-2.

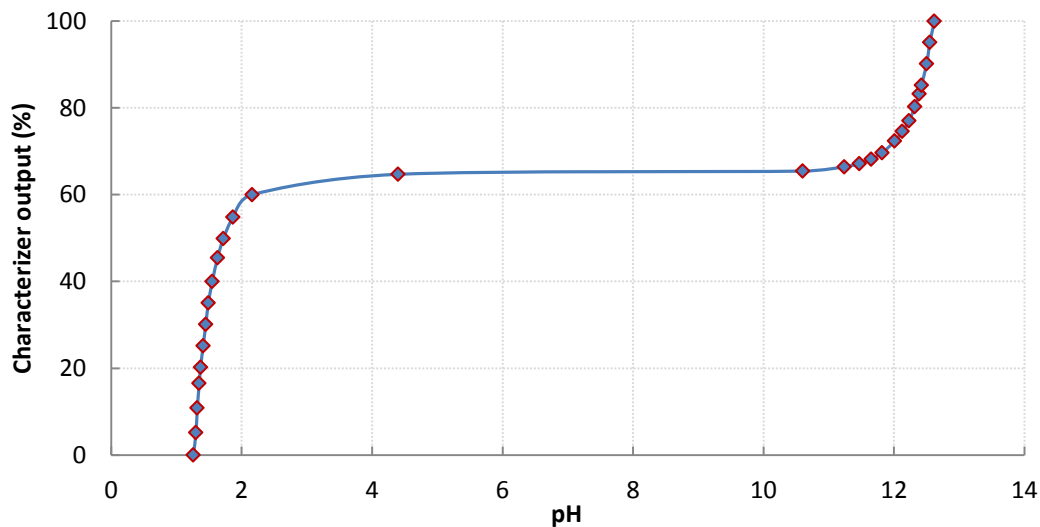


Figure 5-7. pH Characteriser

The disturbance observer approach uses the inverse of the nominal plant model to estimate disturbances and cancel them subsequently. In the present work the effectiveness of

DOs in dealing with the nonlinearities encountered in pH control is investigated. As outlined in Chapter 2, the general structure of a disturbance observer is as follows:

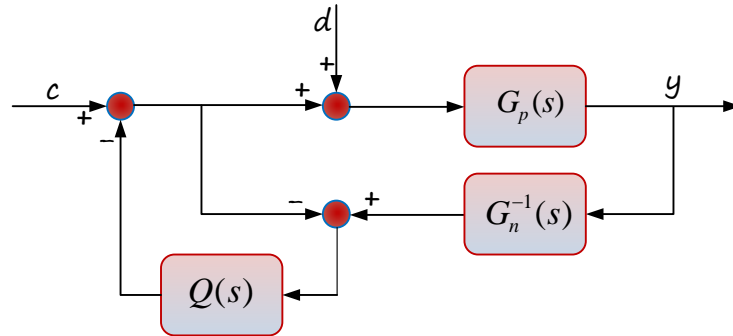


Figure 5-8. Disturbance Observer: delay-free

The DO structure can also be represented in the equivalent format shown in Figure 5-9, which is more practical to implement [19].

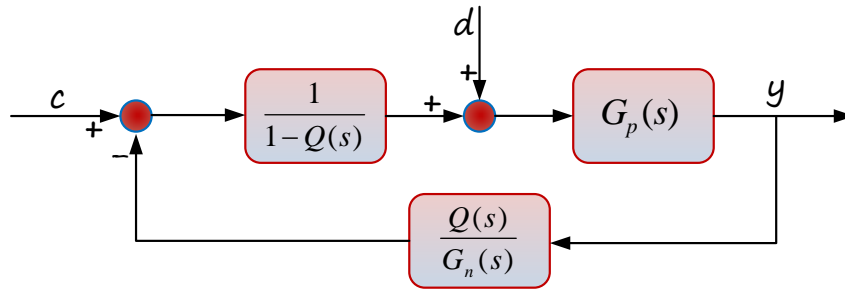


Figure 5-9. Disturbance Observer (practical representation): delay-free

The delay-free plant nominal model  $G_n$  in this study is equal to the process model as presented below,

$$G_n = \frac{34}{18s + 1} \tag{5-3}$$

Jones and Tham [20] discuss two approaches for incorporating the time delay in the DO design. In the first method the nominal plant model  $G_n$  remains delay free and the time delay term,  $G_\theta$ , delays the control signal before it is used in the DO loop, as illustrated in Figure 5-10.

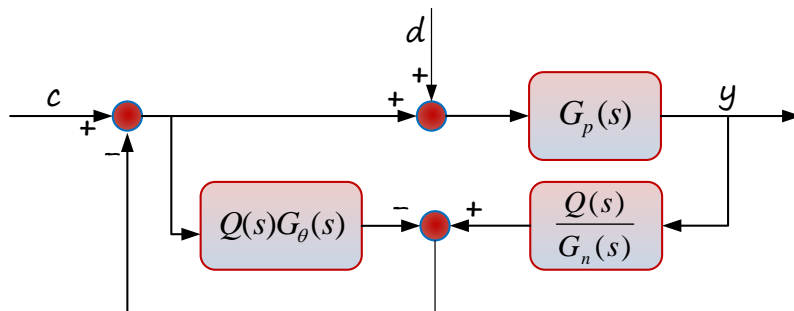


Figure 5-10. Disturbance observer: time-delay implementation 1

The second implementation, shown in Figure 5-11, involves including a low order approximation (e.g. Pade method) of the time delay term into the nominal plant model. Previous investigations [20] showed that the first implementation provides the best disturbance rejection performance in a noise free environment, whilst the second approach

has superior noise attenuation characteristics. The nominal plant model used in the second implementation which includes a delay term is given by the following expression for the current process:

$$\tilde{G}_n = G_n \tilde{G}_\theta = \frac{34}{(18s+1)(\theta s+1)} \quad (5-4)$$

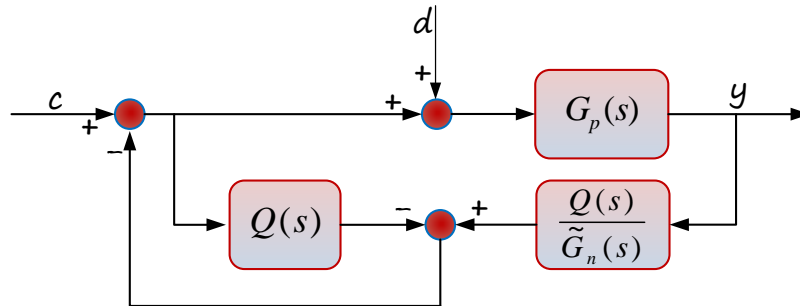


Figure 5-11. Disturbance observer: time-delay implementation 2

So far, three DO structures have been outlined, the first structure does not account for the time delay in the design, whilst the remaining two implement a delay term in the DO design. These structures will be referred to as DO1 (Figure 5-9), DO2 (Figure 5-10) and DO3 (Figure 5-11). In the DO design a low-pass filter is selected such that  $Q / G_n$  is realisable. For DO1 and DO2 the relative degree of the filter needs to be at least 1; whilst, DO3 requires a minimum relative degree of 2 for the filter design. The following equation based on Binomial coefficients [20] maybe used to design the low pass filter  $Q$ :

$$Q = \frac{1 + \sum_{k=1}^{N-m} a_k (\tau_f s)^k}{1 + \sum_{k=1}^N a_k (\tau_f s)^k} \quad (5-5)$$

where,  $m$  = relative degree of  $G_n$

$\tau_f$  = filter time constant

$a_k$  = Binomial coefficients

The above equation leads to filter designs with a first order numerator; however, a simpler filter design with a zero order numerator may also be used. These alternative designs are presented in Table 5-2 for the three DO structures considered here. An analysis of the different DO schemes described above, including the choice of filter, is carried out to determine an optimal design for the pH control task under investigation, as outlined in the next section.

Table 5-2. DO filter design

	High order filter	Low order filter
DO1 and DO2	$\frac{2\tau_f s + 1}{\tau_f^2 s^2 + 2\tau_f s + 1}$	$\frac{1}{\tau_f s + 1}$
DO3	$\frac{3\tau_f s + 1}{\tau_f^3 s^3 + 3\tau_f^2 s^2 + 3\tau_f s + 1}$	$\frac{1}{\tau_f^2 s^2 + 2\tau_f s + 1}$

### 5.2.2 Optimal Disturbance Observer Design

Two filter designs (high or low order) are considered for DO1, DO2 and DO3 schemes, as presented in Table 5-2. A series of simulation runs are carried out to assess the disturbance rejection performance of the pH control loops, which include various DO designs, for two values of time delay (1 and 5 seconds). The disturbances are modelled as 20% increase and subsequently 20% decrease in flowrate of the acid stream from its steady state value. The controllers are tuned using the parameters presented in Table 5-1. The simulation results are used to specify the most appropriate DO design for the pH control system.

The disturbance rejection performances of the control loops including DO1, DO2 and DO3 schemes with a high or a low order filter are presented in Figure 5-12, Figure 5-13 and Figure 5-14 respectively. For these initial runs the time delay is modelled as 1 second and the filter time constants are selected as 18 seconds. The corresponding IAE values for each case are quoted in the Figure captions. In all cases, the high order filters result in larger overshoots in the pH response, in comparison to the responses achieved using the low order filter designs. Furthermore, for DO1 and DO2 designs, the high order filters lead to small amplitude constant oscillations in the pH response following a 20% reduction in the acid stream flow rate (the second disturbance).

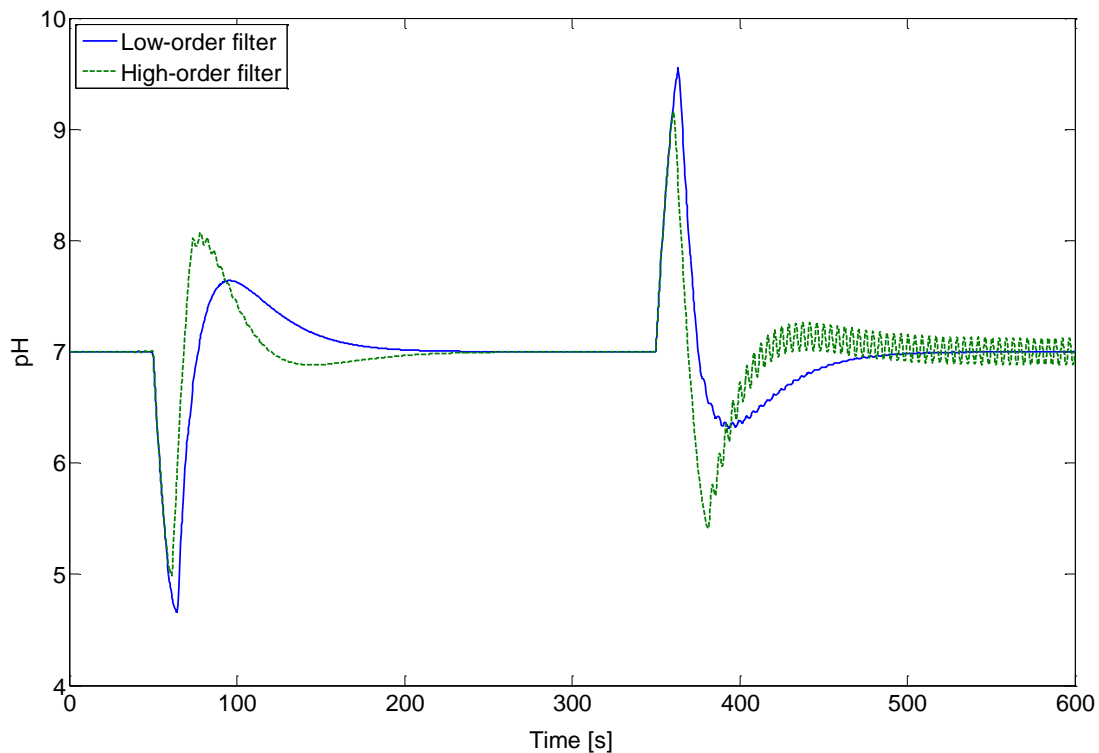


Figure 5-12. DO1 scheme,  $\theta = 1\text{s}$ ,  $\tau_f = 18\text{s}$   
[IAE: low order filter = 135.1, high order filter = 126.3]

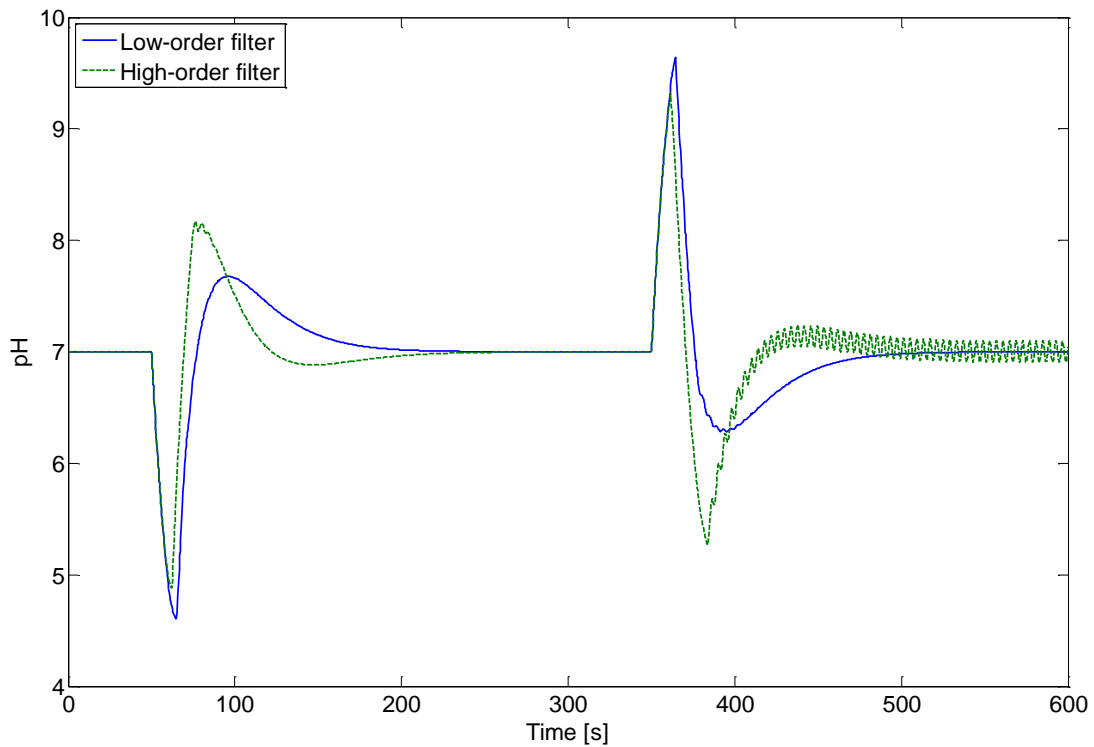


Figure 5-13. DO2 scheme,  $\theta = 1\text{s}$ ,  $\tau_f = 18\text{s}$   
 [IAE: low order filter = 142.7, high order filter = 132.5]

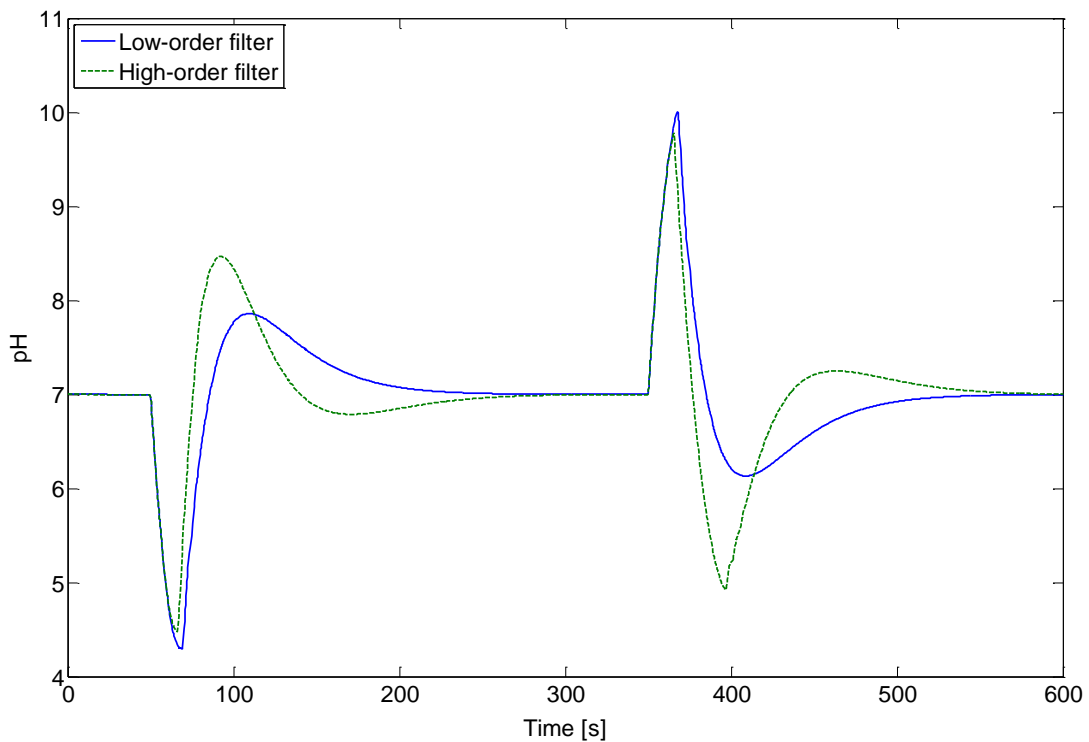


Figure 5-14. DO3 scheme,  $\theta = 1\text{s}$ ,  $\tau_f = 18\text{s}$   
 [IAE: low order filter = 214.8, high order filter = 221.7]

Despite the larger overshoots and low amplitude oscillations observed for a high order filter design applied to DO1 and DO2 schemes, because of faster disturbance rejection, the resulting IAE values are marginally lower for the high order filter cases (see Figure 5-12 and Figure 5-13). For the DO3 scheme the low order filter provides superior performance



compared to the high order filter both in terms of IAE values and the overshoot magnitude, as shown in Figure 5-14. However, the differences in the IAE values for the low and high order filters in each case are not significant. Therefore, the low order filter designs are selected for the current investigations based on the observations that they result in smaller overshoots and cause no oscillations in the pH output response in presence of the process disturbances.

So far, for a given filter time constant and time delay, it has been shown that the DOs with a low order filter give better performances compared to those achieved when a high order filter was used. The disturbance rejection performances of the three DO schemes with a low order filter ( $\tau_f = 18\text{s}$ ) for a time delay value of 1 and 5 seconds are presented in Figure 5-15 and Figure 5-16 respectively. A comparison of the two figures shows that the performances of the control algorithms deteriorate significantly as the value of the delay term is increased from 1 to 5 seconds. In particular, for all cases a time delay of 5 seconds drives the system into sustained oscillations or limit cycles. The results show that the disturbance rejection performances of the three DO implementations are not vastly different in terms of the pH output response and the IAE values. As DO1 results in the lowest value of IAE for both of the time delay cases, it is selected as the most favourable choice.

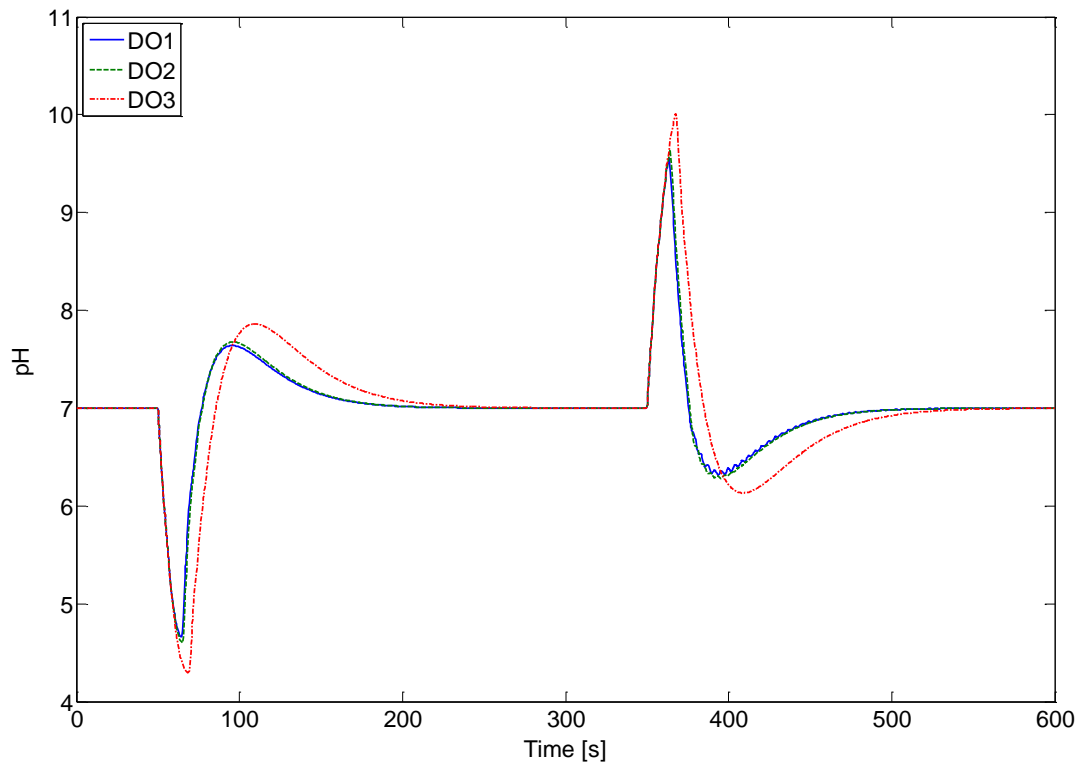


Figure 5-15. All DO cases with low order filters,  $\theta = 1\text{s}$ ,  $\tau_f = 18\text{s}$   
[IAE: DO1 = 135.1, DO2 = 142.7, DO3 = 214.8]

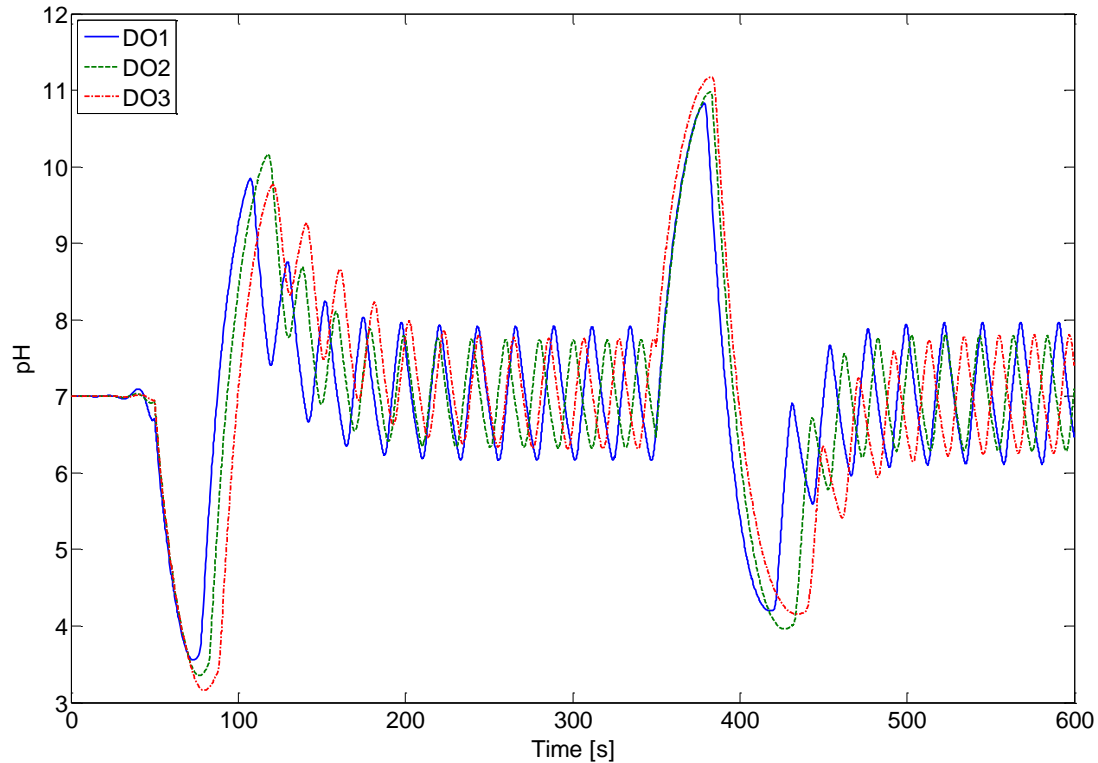


Figure 5-16. All DO cases with low order filters,  $\theta = 5\text{s}$ ,  $\tau_f = 18\text{s}$   
 [IAE: DO1 = 526, DO2 = 559.3, DO3 = 634.7]

Based on the presented results the DO1 scheme with a first order low pass filter is identified as the most appropriate disturbance observer design. The only remaining parameter that needs to be specified in the DO design is the filter time constant  $\tau_f$ . So far a time constant equal to the process time constant (18s) has been used for benchmarking. Here, two extra filter time constants ( $\tau_f = 0.5 \tau_p$  and  $0.1 \tau_p$ ) are also tested to determine the best value. As shown in Figure 5-17 for the 1s delay case, the disturbance rejection performance in terms of IAE is enhanced by reducing the value of the filter time constant. However, the amount of constant oscillations or limit cycles is increased when the smaller filter time constants are used. In essence by reducing the filter time constant tighter control is achieved at the expense of reducing the stability margins.

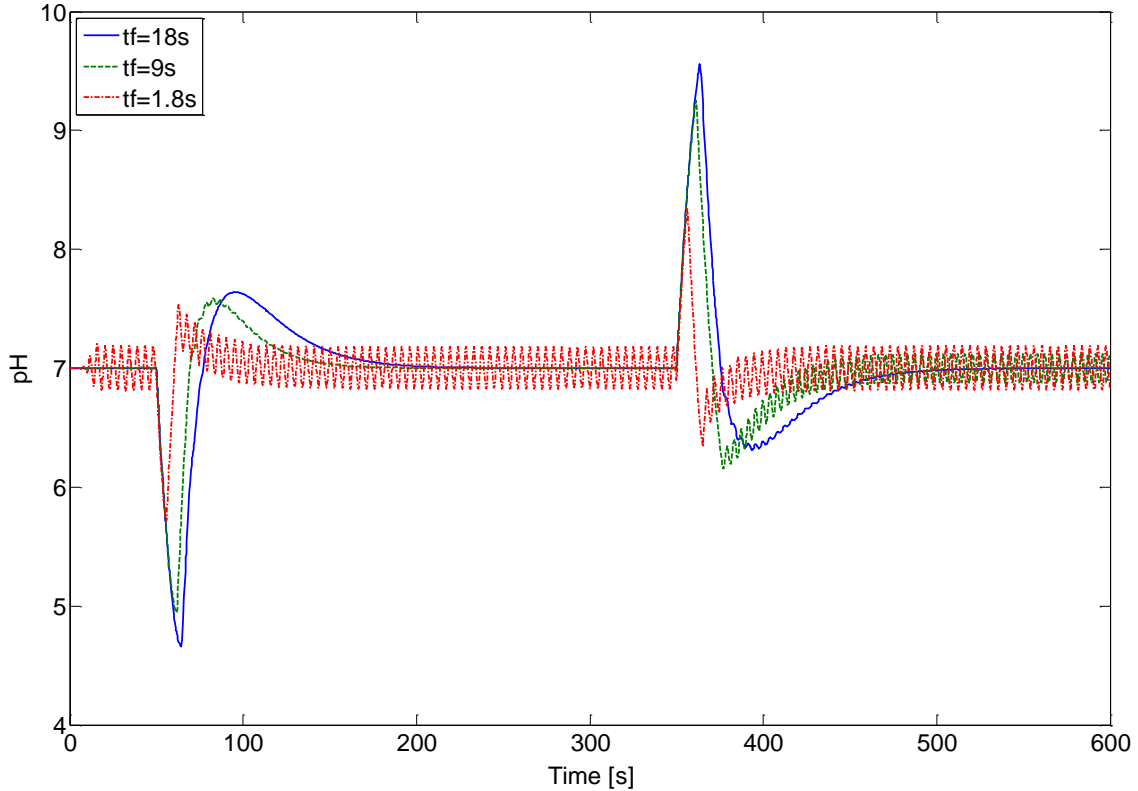


Figure 5-17. DO1 with low order filter,  $\theta = 1$ s  
 [IAE:  $\tau_f(18s) = 135.1$ ,  $\tau_f(9s) = 104.4$ ,  $\tau_f(1.8s) = 80.19$ ]

For the 5s delay case presented in Figure 5-18, limit cycles are observed for all cases and the highest value of IAE is achieved when the smallest filter time constant is implemented. Therefore, based on the simulation results presented here a filter time constant equal to the process time constant (18s) is selected as the best value (between the three values tested) since it provides the least amount of oscillations. In summary, the delay free implementation of the DO scheme (DO1, Figure 5-9) with a first order low pass filter and a time constant of 18 seconds are selected for the subsequent simulation analysis of the DO applied to the pH control task.

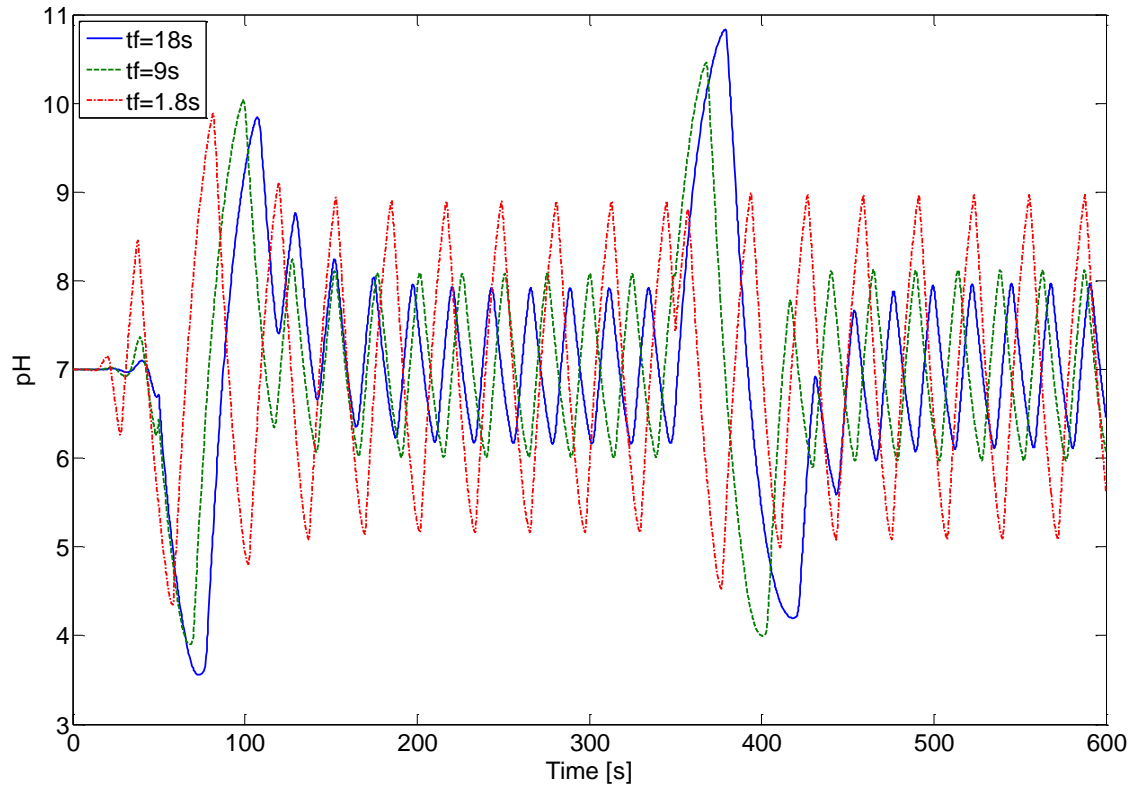


Figure 5-18. DO1 with low order filter,  $\theta = 5s$   
 [IAE:  $\tau_f(18s) = 526$ ,  $\tau_f(9s) = 496$ ,  $\tau_f(1.8s) = 636.8$ ]

### 5.2.3 Performance Evaluation

The performance of each control scheme is assessed for disturbance rejection, setpoint tracking and robustness. In a neutralisation process disturbances can occur in flowrate and/or concentration of either or both inlet streams. In this study, changes in flowrate of the influent (acid) stream is chosen as an example of input disturbances to evaluate the disturbance rejection capabilities of the control schemes. The acid flow is first increased from its steady state value by 20%, then it is returned to its initial baseline before a 20% reduction in flow is implemented. For the setpoint tracking runs, the setpoint is increased from the nominal value of 7 to 12.2 pH. The setpoint is then returned to 7 before a step to 1.8 pH is implemented.

Robustness is the controller's ability to achieve satisfactory performance despite the presence of modelling mismatches and uncertainties. Two main sources of uncertainty are identified in the control schemes considered here. The first source of modelling mismatch might arise from the characteriser not being an exact inversion of the real titration characteristics. A characteriser with a slightly different slope, as shown in Figure 5-19, is implemented to assess the robustness of the control schemes involving a characteriser. This is a plausible scenario for a real process as the presence of impurities, weak acids and bases may cause a change in the buffering capacity of the system and consequently change the slope of the titration curve.

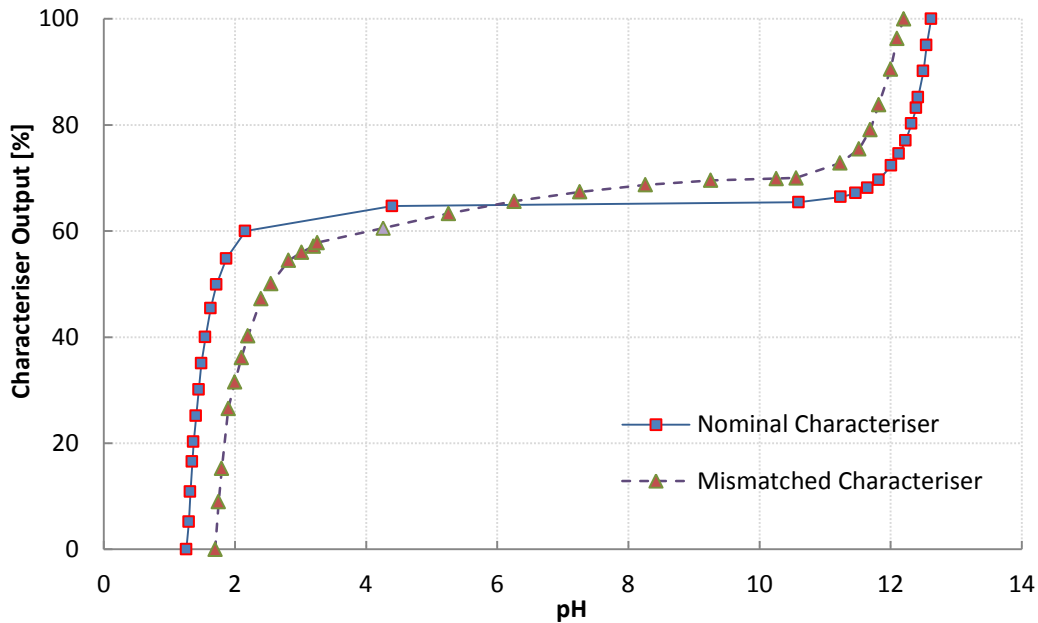


Figure 5-19. Characteriser mismatch

The second source of modelling disparity can appear in the DO design, where the nominal plant model does not exactly match the real process dynamics.  $\pm 20\%$  change in both gain and time constant of the nominal plant model are implemented to evaluate the effects of modelling mismatches in the DO design. The robustness of the control strategies are presented for the case of disturbance rejection. The setpoint tracking robustness is not presented here as the outcome was found to be similar to that of the disturbance rejection runs.

The performances of each control scheme in terms of disturbance rejection, setpoint tracking and robustness are assessed primarily by visual inspection of the controlled variable over time. The desired response should follow the typical behaviour of a FOPDT with minimised overshoots, oscillations, settling time and offset. Setpoint tracking and disturbance rejection performances are also assessed by the IAE criteria so as to enable a quantitative analysis and comparison of the tested control schemes.

#### 5.2.4 Disturbance Rejection Performances

The disturbance rejection performances of the four control strategies are illustrated in Figure 5-20 for the 1 second time delay case, using the direct synthesis tuning parameters (see Table 5-1). The results show that despite the large initial deviation from the setpoint, the PI controller provides adequate performance in rejecting the disturbances. The addition of a pH characteriser results in larger initial deviations from the setpoint and a more sluggish transient response. It is noted that the least initial process upsets as a result of the disturbances are obtained when the DO structure is coupled with the PI controller. The differences between the initial deviations from the setpoint for the cases of PI and PI plus DO are rather small (less than 1 pH unit), nevertheless, the results demonstrate the ability of the DO scheme to estimate and subsequently reject disturbances. The control scheme including both the characteriser and the DO results in poorer disturbance rejection compared to the PI only case as large overshoots are present, in addition to a slow performance.

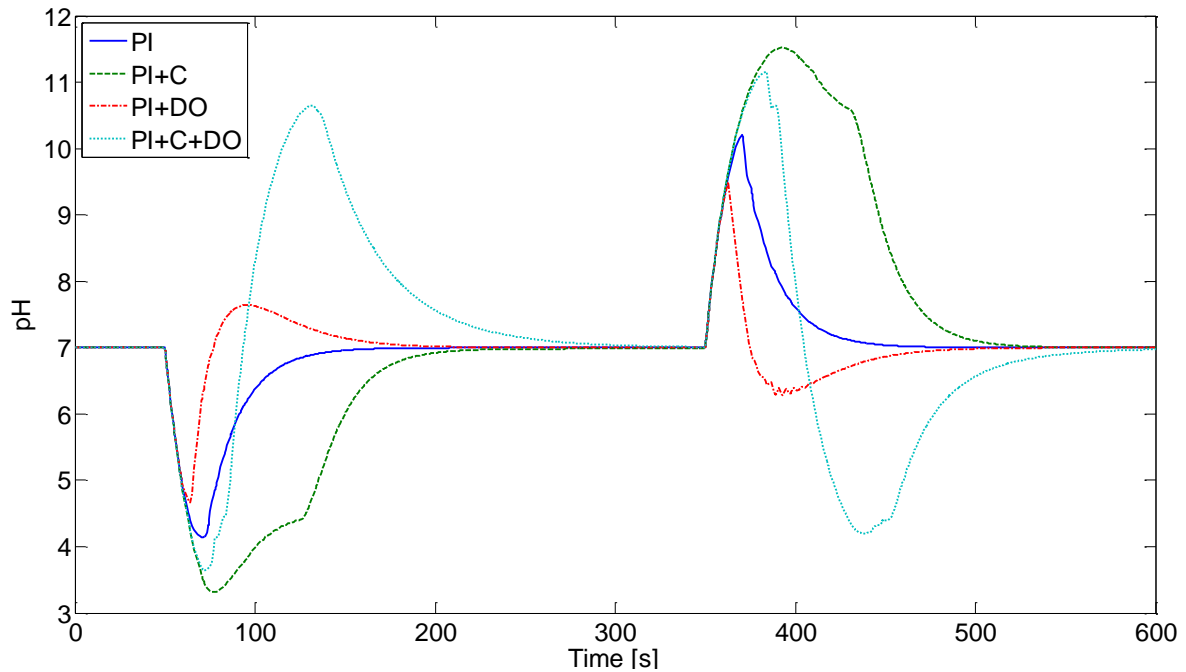


Figure 5-20. Disturbance rejection performance [ $\theta = 1$ s, direct synthesis]

The direct synthesis tuning parameters used here are based on the process model obtained by the input-output tests. Thus any uncertainties in the process model directly influence the resulting performance of the tuning parameters. Furthermore, the controller gain may be fine tuned by adjusting the closed loop time constant  $\lambda$  in the direct synthesis formula. Using the same tuning parameters for all control schemes provides a benchmark for initial comparisons. However, the PI controllers may be manually tuned for each control strategy to improve the resulting performances. As illustrated in Figure 5-21, the sluggish control performances and the overshoots observed in Figure 5-20 are eliminated by fine tuning the PI controllers for each scheme.

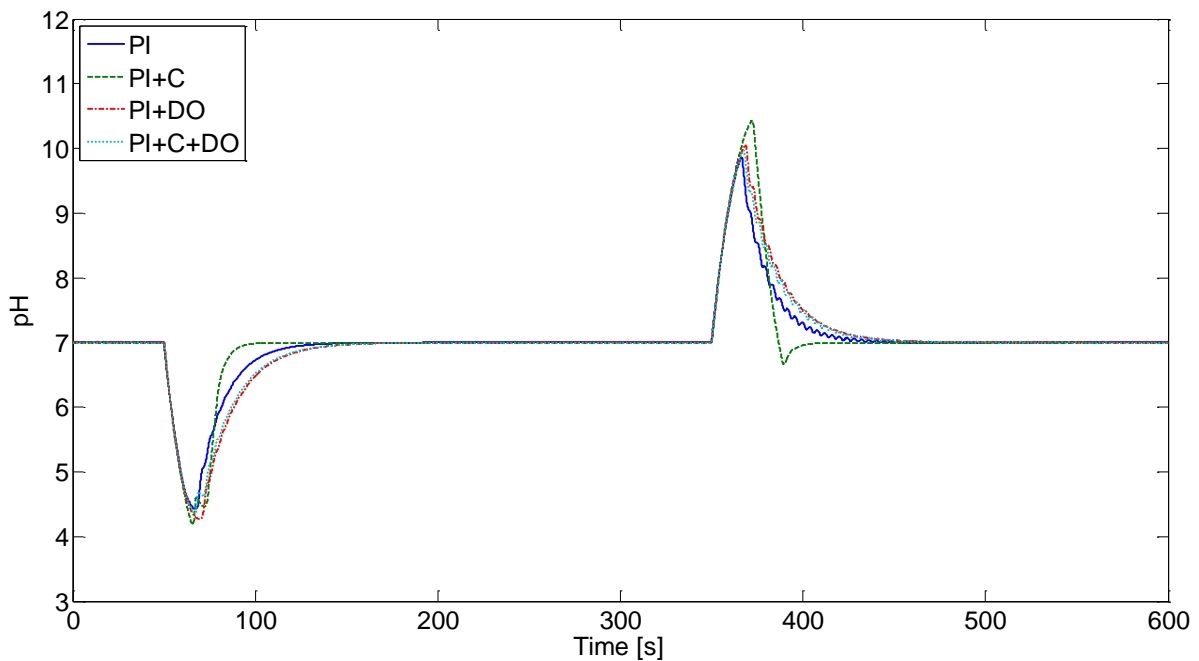


Figure 5-21. Disturbance rejection performance [ $\theta = 1$ s, manual tuning]

The controller settings after fine tuning, along with the corresponding IAE values for the case of 1 second time delay are presented in Table 5-3. It can be noted that when the direct synthesis tuning parameters are used, the cases including a characteriser result in the worst control performance in terms of IAE; whilst, the PI plus DO case yields the best performance. However, upon fine tuning the PI controllers the disturbance rejection performances of the four control schemes become more comparable, resulting in very similar IAE values. The inclusion of the nonlinear compensation methods (characteriser and DO) in the control scheme alters the dynamics of the closed loop, thus the controllers need to be tuned accordingly. An interesting point to note is that using a P only controller for the cases including the DO does not lead to any offsets in the process variable. The fact that the DO scheme is capable of removing offsets makes the process of controller tuning easier, since a P controller with only one tuning parameter may be adopted. In the presented results (time delay of 1s) the closed loop responses are not adversely affected by the nonlinearity of the pH system and the PI controller is able to achieve the control task without the aid of any additional schemes.

Table 5-3. Disturbance rejection IAE values ( $\theta = 1s$ )

Control scheme	Direct synthesis ( $\lambda=1.8s$ )		IAE (direct synthesis)	Manual tuning		IAE (manual tuning)
	Kc	Ti		Kc	Ti	
PI	0.189	18	194.6	0.22	14.7	136.5
PI+C	0.189	18	654.2	0.80	6.4	134.4
PI+DO	0.189	18	135.1	0.18	-	175.6
PI+C+DO	0.189	18	644.6	1.6	-	166.8

However, as the time delay is increased the performances of the PI controllers, with the initial direct synthesis parameters, deteriorate significantly compared to the case of 1s time delay, as presented in Figure 5-22. For the PI only case, in addition to a large initial deviation from the setpoint, the controlled pH cycles between  $7 \pm 1$  pH. The addition of the pH characteriser in the control scheme suppresses the limit cycles observed for the PI case at the expense of a considerably more sluggish response. In contrast, the DO scheme is unsuccessful in eliminating the limit cycles, whilst large overshoots are also present. The case including the characteriser and the DO also provides a poor performance as large overshoots and slow disturbance rejection capability prevail.

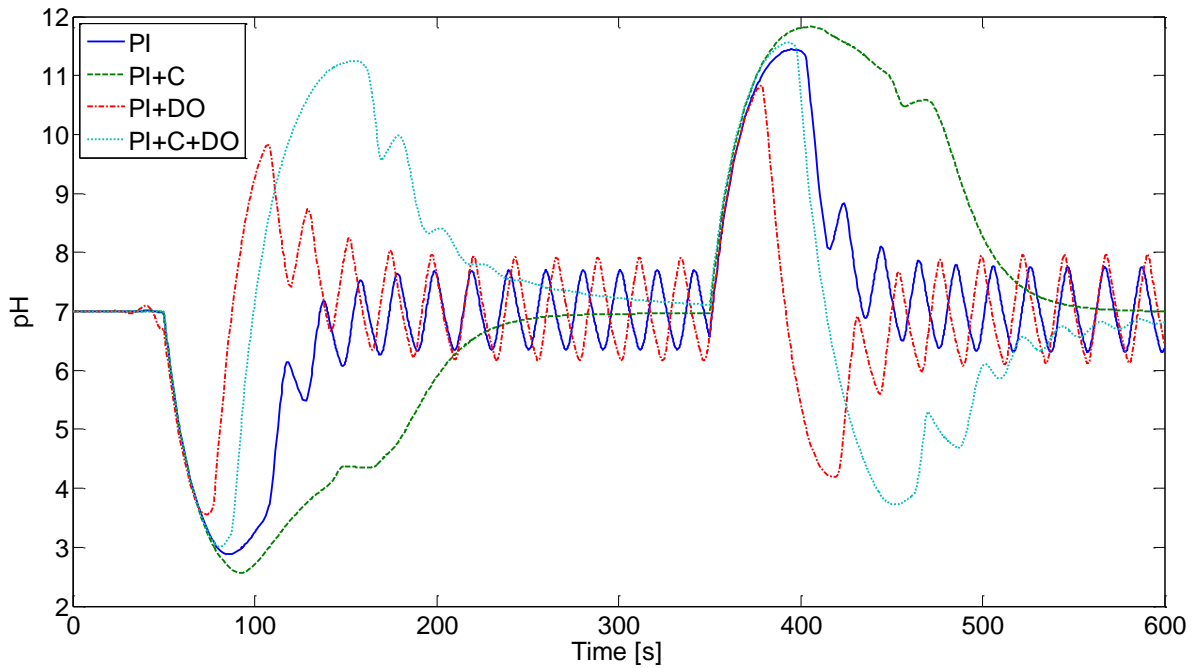


Figure 5-22. Disturbance rejection performance [ $\theta = 5s$ , direct synthesis]

However, the fine tuned PI controllers provide improved disturbance rejection performances, as shown in Figure 5-23. It can be seen that the initially observed overshoots and sluggish transient responses are diminished. However, the DO scheme is still unable to suppress the limit cycles present in the output pH response. The performance of the DO scheme in suppressing limit cycles may be improved by further tuning of the filter time constant. As discussed in Section 5.2.2 a larger filter time constant reduces the oscillations observed in the process variable.

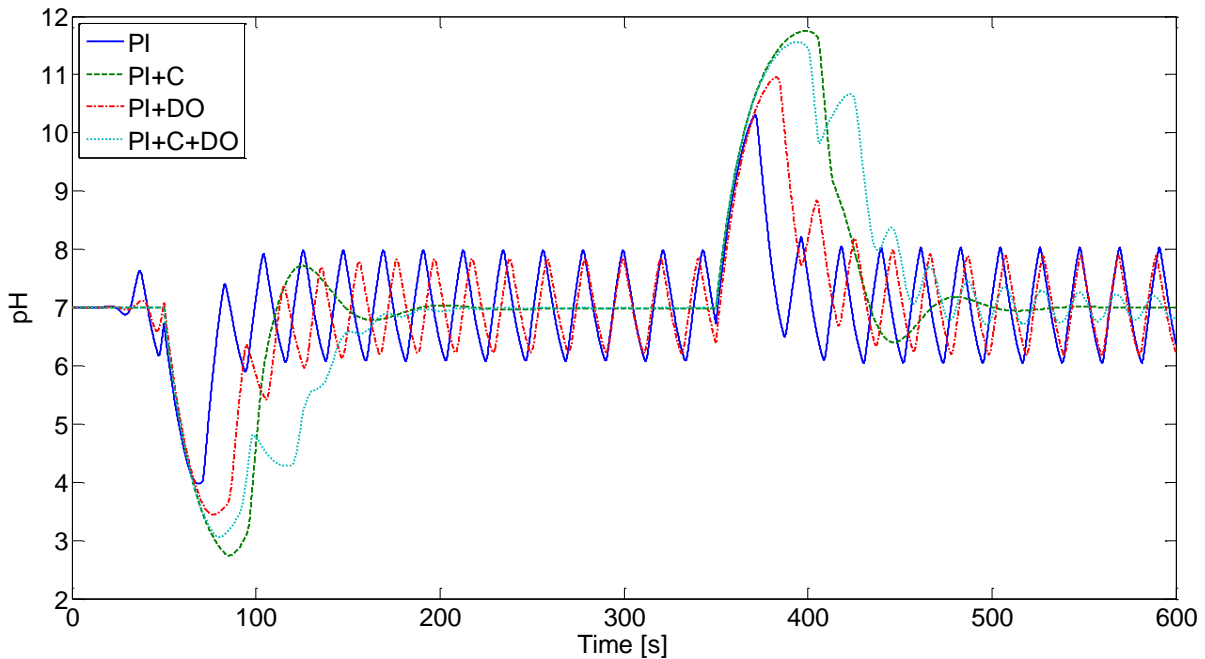


Figure 5-23. Disturbance rejection performance [ $\theta = 5s$ , manual tuning]

The controller tuning parameters as well as the resulting IAE values are presented in Table 5-4 for the cases of disturbance rejection in presence of 5 seconds time delay. When



the direct synthesis parameters are used, the observed pattern is very similar to the case of the smaller time delay; whereby the schemes including the characteriser lead to inferior disturbance rejection performances in terms of IAE, whilst, the addition of the DO results in the best performance. The results show again that adjusting the control parameters leads to significant reduction of the IAE values and thus improvement of the control performance. Similar to the 1s time delay case a P controller is used for manual tuning of the cases including the DO scheme without any offsets.

Table 5-4. Disturbance rejection IAE values ( $\theta = 5s$ )

Control scheme	Direct synthesis ( $\lambda=1.8s$ )		IAE (direct synthesis)	Manual tuning		IAE (manual tuning)
	Kc	Ti		Kc	Ti	
	PI	0.078		18	608.7	
PI+C	0.078	18	1024	0.06	6	459.0
PI+DO	0.078	18	525.9	0.10	-	462.2
PI+C+DO	0.078	18	915.1	0.12	-	575.7

### 5.2.5 Setpoint Tracking Performances

The setpoint tracking performances of the four control schemes in presence of 1 second time delay, using the direct synthesis tuning parameters, are presented in Figure 5-24. It can be observed that the PI controller provides satisfactory setpoint tracking performance with the initial tuning parameters, without the nonlinear compensation schemes. The addition of the characteriser results in a more sluggish transient response when the setpoint value is returned to 7 pH from the acidic and basic regions. The PI plus DO scheme provides a poor setpoint tracking performance as offsets are present in the basic and acidic regions and large overshoots occur when the setpoint is returned to the baseline of 7 pH. It is noted that the PI plus DO scheme provides a poor setpoint tracking performance, since offsets are evident when the setpoint is at 12.2 or 1.8 pH. The case including both the characteriser and the DO yields a better setpoint tracking performance compared to that achieved by the PI plus DO scheme.

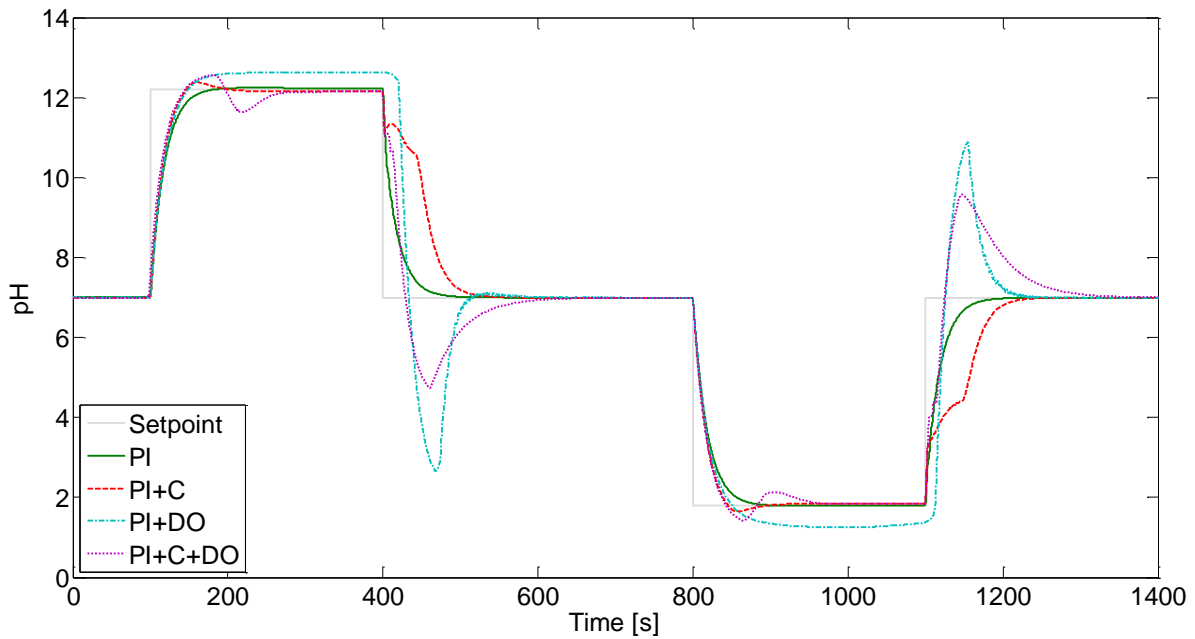


Figure 5-24. Setpoint tracking performance [ $\theta = 1$ s, direct synthesis]

Similar to the disturbance rejection runs, the performances of the control schemes are improved by fine tuning the PI controllers for each case, as presented in Figure 5-25. The results show that when the value of the time delay is 1 second, there are no limit cycles in the effluent pH response and the setpoint tracking performances of all control schemes are almost equivalent, provided that the PI controllers are tuned accordingly.

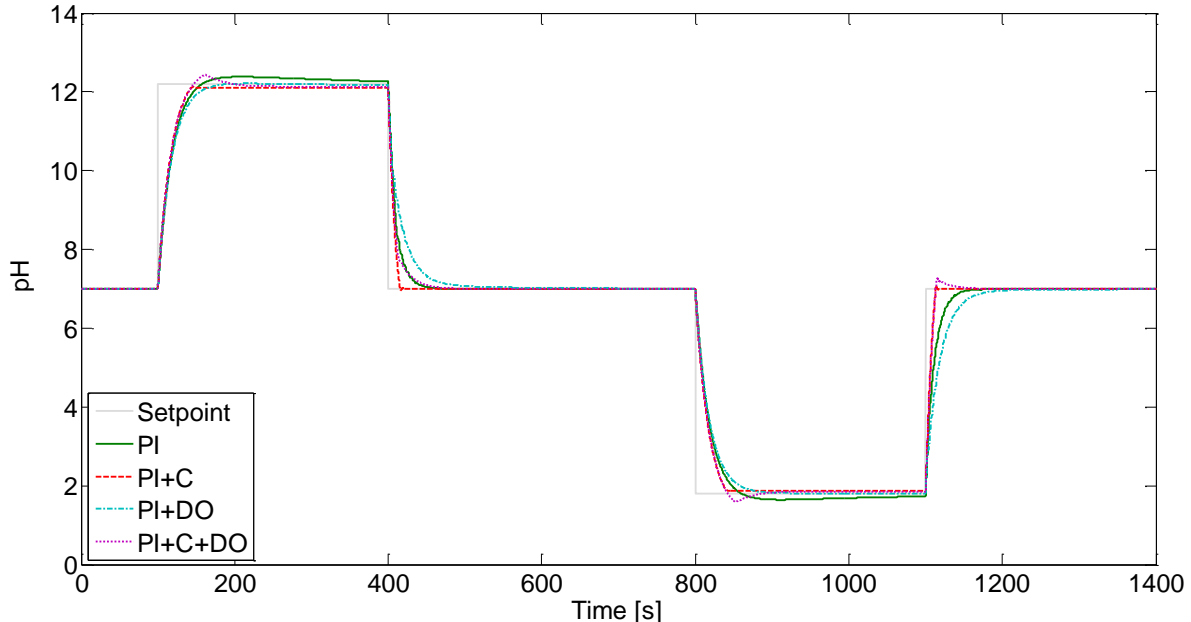


Figure 5-25. Setpoint tracking performance [ $\theta = 1$ s, manual tuning]

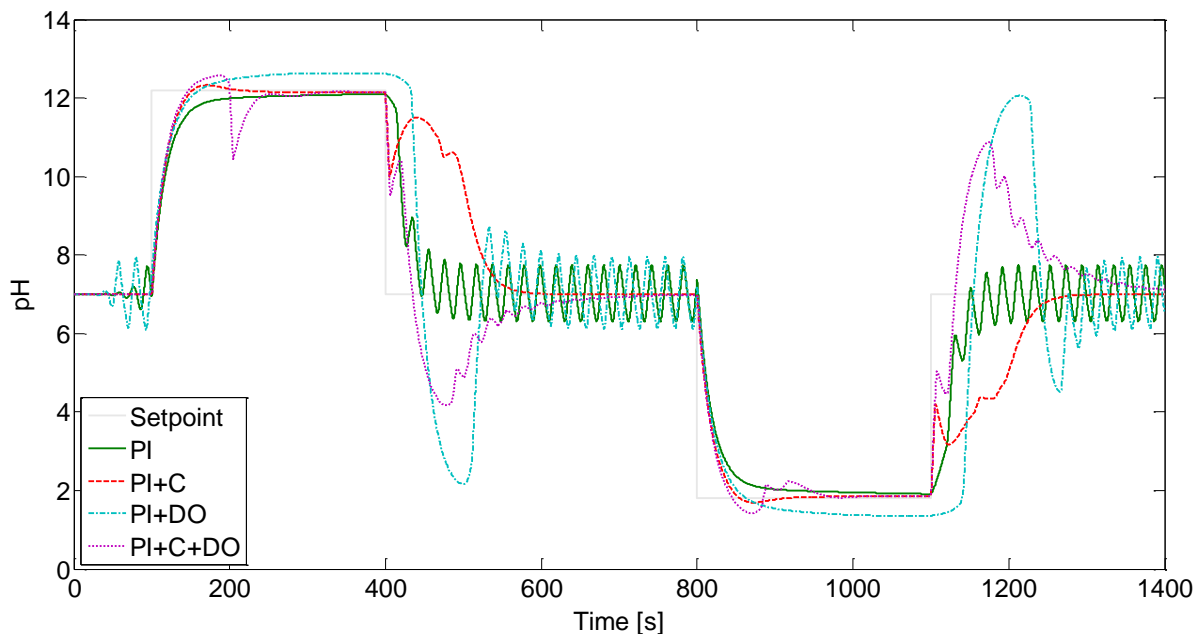
Table 5-5 presents the tuning parameters and the corresponding IAE values for setpoint tracking using different control schemes in the presence of a 1 second time delay. When the initial tuning parameters via the direct synthesis method are used, the PI only case provides the best setpoint tracking in terms of IAE values, whilst the poorest performance is obtained when the DO is included in the feedback control scheme. The control performances are significantly improved for the cases including the characteriser and/or the disturbance

observer by means of tailoring the PI tuning parameters for each scheme. In order to eliminate the offsets initially observed for the PI plus DO scheme, the integral term is increased by almost seven folds. Whilst turning off integral action and only using the proportional term improves the performance of the cases involving a characteriser, without causing any offsets.

Table 5-5. Setpoint tracking IAE values ( $\theta = 1s$ )

Control scheme	Direct synthesis ( $\lambda=1.8s$ )		IAE (direct synthesis)	Manual tuning		IAE (manual tuning)
	Kc	Ti		Kc	Ti	
	PI	0.189		18	382.0	
PI+C	0.189	18	656.9	1.00	-	265.8
PI+DO	0.189	18	949.3	0.18	120.0	394.9
PI+C+DO	0.189	18	684.3	0.55	-	279.3

Figure 5-26 presents the setpoint tracking performances of the four control schemes, using the direct synthesis tuning parameters, in presence of a 5 seconds time delay. The general performance trends of the four control schemes are similar to that observed for the 1 second time delay case, wherein the PI controller provides the best performance in terms of the IAE. However, in presence of a larger time delay the process variable limit cycles around the setpoint of 7 pH, for the cases of PI and PI plus DO. Similar to the case of 1s time delay, the PI plus DO provides the poorest setpoint tracking performance as offsets are present in the acidic and basic regions and large overshoots occur when the setpoint is returned to 7 pH.

Figure 5-26. Setpoint tracking performance [ $\theta = 5s$ , direct synthesis]

The sluggish transient responses and the overshoots attained when the initial direct synthesis tuning parameters are used can be eliminated by fine tuning the PI controllers as presented in Figure 5-27. Nevertheless, the limit cycles around the equivalence point, which are a direct consequence of the system nonlinearity coupled with large time delays, still

remain for all cases, apart from the PI plus characteriser control scheme. As mentioned previously, the performance of the DO scheme in terms of suppression of the limit cycles may be improved by tuning the filter time constant.

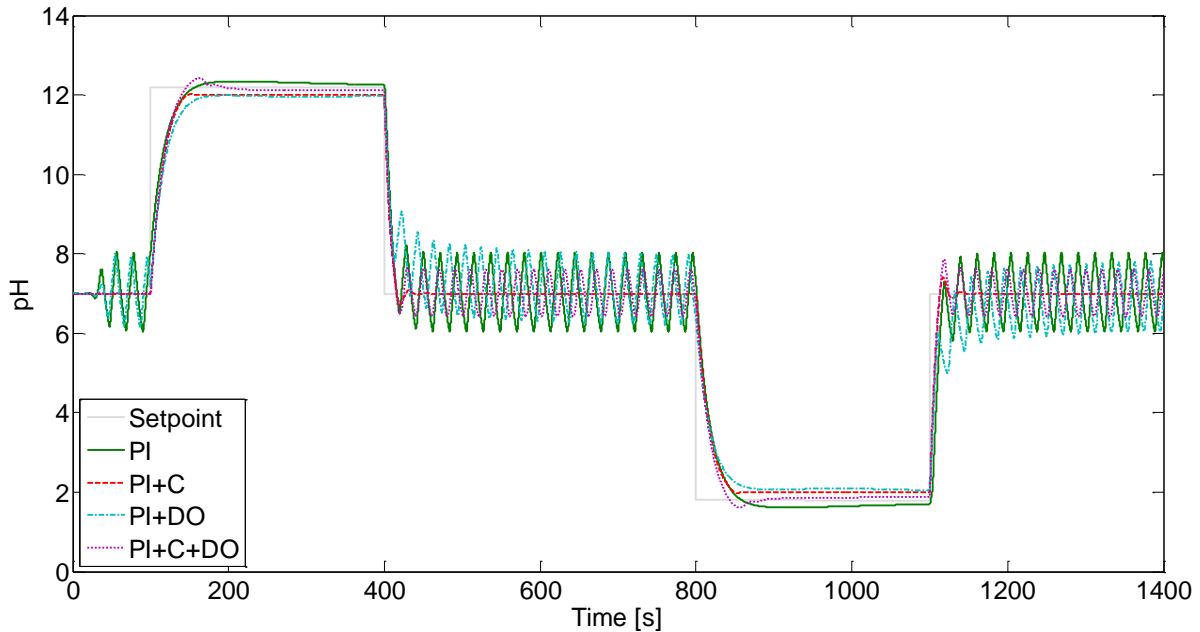


Figure 5-27. Setpoint tracking performance [ $\theta = 5\text{s}$ , manual tuning]

The resulting IAE values for the two tuning methods, presented in Table 5-6, once again show that the control performances in terms of IAE are vastly improved by adjusting the control parameters to match the characteristics of each control scheme. Upon fine tuning the controllers the PI plus characteriser scheme provides the lowest IAE value and thus the best control performance. Again it is noted that a large integral time constant is required to remove the offsets observed for the case of PI plus DO, whilst, the P only controllers result in satisfactory control performance with no offsets when a pH characteriser is included in the control loop. These findings are in contrast with the disturbance rejection results wherein satisfactory control performance was achieved without the integral action for the cases including the DO. To ensure good disturbance rejection and setpoint tracking performances are achieved a balance between the values of the controller parameters used for the respective runs should be found.

Table 5-6. Setpoint tracking IAE values ( $\theta = 5\text{s}$ )

Control scheme	Direct synthesis ( $\lambda=1.8\text{s}$ )		IAE (direct synthesis)	Manual tuning		IAE (manual tuning)
	Kc	Ti		Kc	Ti	
PI	0.078	18	921.5	0.18	12	794.8
PI+C	0.078	18	1099	0.20	-	425.1
PI+DO	0.078	18	1812	0.12	150	874.2
PI+C+DO	0.078	18	1077	0.20	-	588.3

### 5.2.6 Robustness Assessment

As previously discussed, the main sources of modelling mismatch are identified as the inaccurate estimation of the pH characteriser and the nominal plant model in the DO design. The robustness of the control schemes which involve a pH characteriser and/or disturbance observer are assessed in this section. The disturbance rejection performances of the selected control schemes using the nominal models are compared to those achieved in presences of modelling uncertainties to evaluate the robustness of the examined control schemes. Note that the setpoint tracking robustness is not discussed here as the outcome was found to be similar to the case of disturbance rejection. The controller tuning parameters are those obtained initially by the direct synthesis method for the case of 1 second time delay (see Table 5-1).

The disturbance rejection robustness of the PI plus characteriser scheme is illustrated in Figure 5-28. The results show that the modelling mismatch in the characteriser introduces some oscillations in the controlled pH. The observed limit cycles may be attributed to the fact that the characteriser does not accurately invert the titration characteristics, resulting in deterioration of the nonlinear compensation capability of the system. Nonetheless, the controller is still capable of rejecting the disturbances, despite the presence of modelling mismatches. It is interesting to note that the control performance using the mismatched characteriser is less sluggish and the initial deviations from the setpoint are smaller, compared to the performances achieved when the nominal model of the characteriser is used. This occurrence is attributed to the PI controller tuning parameters being more suitable for the mismatched characteriser.

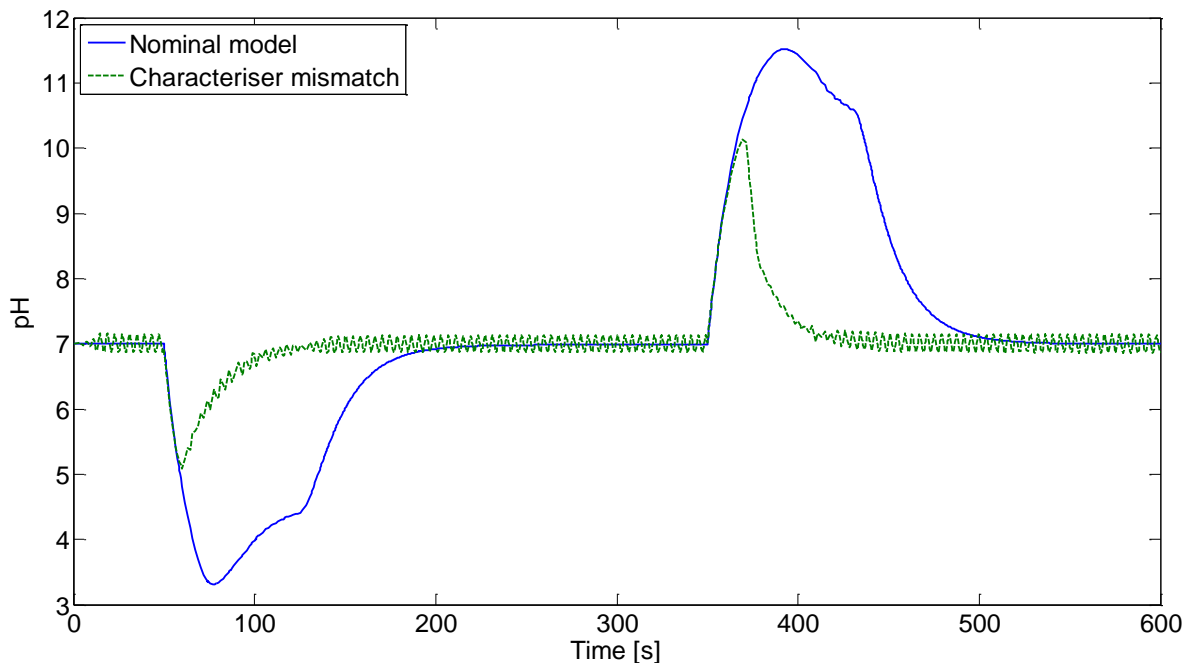


Figure 5-28. PI plus characteriser robustness

The disturbance rejection of the PI controller plus DO scheme is presented in Figure 5-29 for the nominal model along with the cases including mismatched models of the nominal plant. It is evident that the disturbance observer scheme is highly robust despite the existence

of modelling uncertainties, as the pH responses of the mismatched cases are almost identical to that achieved when the nominal model is used.

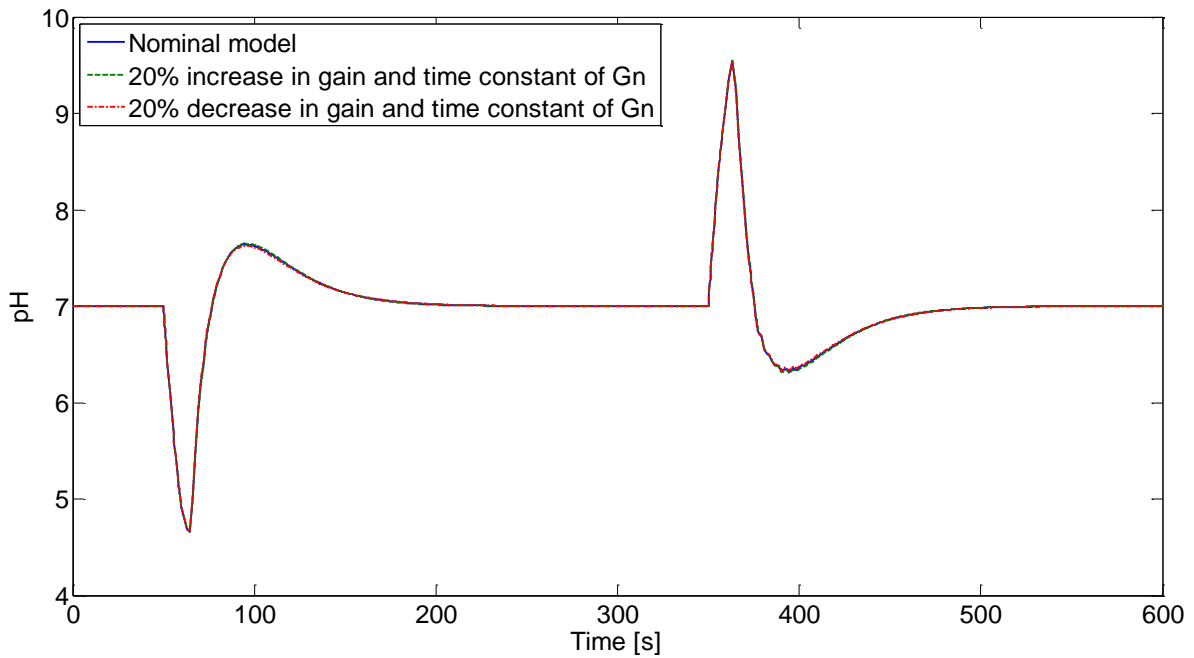


Figure 5-29. PI plus disturbance observer robustness

The disturbance rejection robustness performance of the PI controller plus characteriser and DO scheme is presented in Figure 5-30. The presence of modelling mismatches in the nominal plant model and the characteriser leads to appearance of limit cycles in the pH response. However, as observed for the PI plus characteriser case, the performances of the control scheme in terms of initial deviations from the setpoint and the magnitude of the overshoots are enhanced, when modelling mismatches are present.

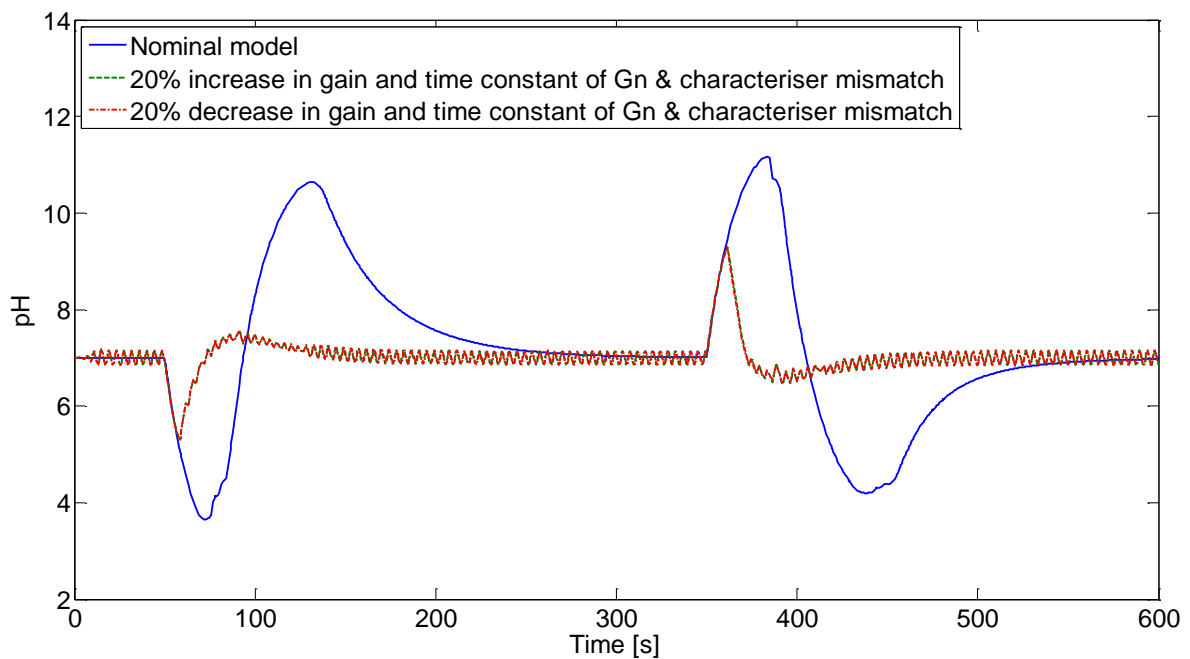


Figure 5-30. PI plus characteriser and disturbance observer robustness

## ***5.3 Experimental pH Control***

The simulation results presented earlier in this chapter provide an insight into the effectiveness of the control schemes considered here to control the effluent pH in a SDR. It was shown that a PI controller provides adequate disturbance rejection and setpoint tracking performances in presence of small time delays. However, as the value of the time delay is increased the control performance deteriorates and the effluent pH limit cycles around the neutral point. The pH characteriser provided the best nonlinear compensation by suppressing the limit cycles, in presence of a 5 seconds time delay. However, the performance of the disturbance observer in terms of nonlinear compensation was not striking with a filter time constant of 18s, according to the simulation results.

The underlying objective of the present work is to assess whether a given control task in a SDR can be achieved using the most common PI/PID controllers together with the commercially available sensors and actuators. Therefore, the PI scheme is applied to the experimental set up in order to confirm the outcome of the simulation results. It was also decided to implement the DO scheme online to further evaluate the nonlinear compensation potentials of the scheme, and also to verify the simulation results. Therefore, the two control schemes which are tested experimentally are the PI and the PI plus DO. The following sections outline the experimental implementation of the selected control strategies along with tuning of the PI controller and selection of the DO filter time constant. The experimental results of feedback pH control in a SDR are then presented and discussed.

### ***5.3.1 Control Loop Setup***

The detailed description of the control loop elements which include hardware and software components are provided in the previous chapter. The control loop is a RCP (Rapid Control Prototyping) configuration, in which a software controller is used to control a hardware plant, as shown in Figure 5-31. The signal from the pH transmitter is acquired by a data acquisition device and sent to the controller. The controller output signal is then sent to the base stream pump via the data acquisition device to maintain the effluent pH at the desired setpoint. The programs developed in the LabVIEW environment to implement a PI/PID as well as a PI/PID plus disturbance observer scheme are presented in Appendix F.

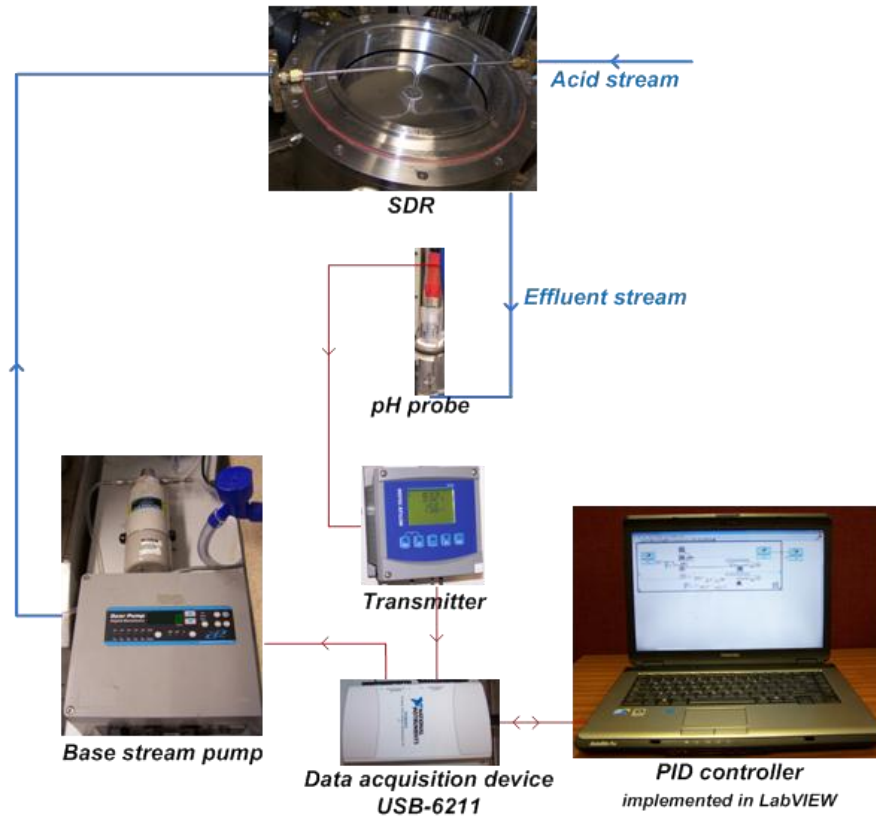


Figure 5-31. pH control loop elements

### 5.3.2 Controller Tuning

The process model parameters obtained from input-output tests (also used in the simulation runs) were initially used to tune the controller for the online pH control experiments. However, as discussed in this section, the controller needed to be fine tuned to improve the performance. In order to obtain appropriate tuning parameters for the controller, the acid flow is started first whilst the controller is in manual mode and the base flowrate is set to zero. The control loop is then closed and the controller attempts to bring the process variable (PV) to the desired setpoint (SP) of 7 pH and maintain it at that level. This approach tests the controller's ability to bring the system to steady state at start up. Furthermore, the controllers attempt to start the base flow and neutralise the process stream is analogous to rejecting a disturbance caused by an increase in flowrate or concentration of the process stream. The pH control process studied here is a challenging task which entails controlling a highly nonlinear system using a linear controller. Therefore the criterion for tuning the controller is defined as the controller's ability to maintain the process variable at steady state value of 7 pH with the minimum amount of oscillations.

Initially, the controller tuning parameters are obtained using the direct synthesis method for a time delay of 1 second. However, as discussed in the previous chapter appropriate conversion of the units must be performed first. The PID controller block in LabVIEW has units of '%CO/%PV' for the gain, and 'minutes' for the integral and derivative time constants. In strict terms, the percentage units of the controller gain do not cancel each other out as they relate to different quantities, namely the percentage ranges of the process variable and the



controller output. However, in practice, the units of the controller gain are often omitted for simplicity, without suggesting that the parameter is dimensionless. Therefore the units of the process gain and time constant need to be modified before the direct synthesis equation is used. The maximum flow that the base pump can deliver is 18 ml/s, therefore the process gain is equal to:

$$k_p = 34 \left( \frac{\text{pH}}{\text{ml/s Base}} \right) \times \frac{18(\text{ml/s})}{14(\text{pH})} \times \frac{100(\%PV)}{100(\%CO)} = 43.7 \frac{\%PV}{\%CO}$$

Applying the direct synthesis method ( $\lambda=1.8\text{s}$ ) leads to a controller gain of 0.15 %CO/%PV and an integral time of 0.3 minutes, whilst the derivative time is set to zero. Figure 5-32, shows the closed loop response of the system using the above parameters.

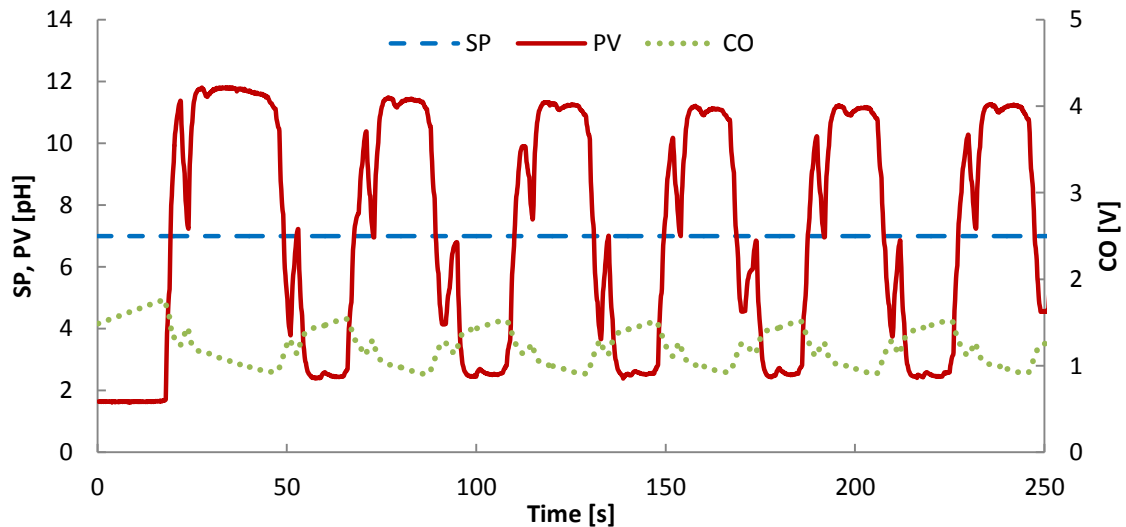


Figure 5-32. Controller tuning [ $K_c = 0.15$ ,  $T_i = 0.3$  min,  $T_d = 0$ ]  
[SP: setpoint, PV: process variable, CO: controller output]

It can be seen that the initial controller settings yield unsatisfactory performance, as the process variable oscillates between 2 and 12 pH. The direct synthesis approach is a model based tuning method whose performance is directly related to the accuracy of the process model used. The presence of limit cycles in the controlled variable might be a consequence of using too large a controller gain. The proportional gain makes changes to the controller output based on the setpoint tracking error ( $SP - PV$ ). When operating in the steep region of the titration curve, very small changes in the reagent flow could cause large deviations in the process variable. Therefore, the rather large changes in the controller output plotted in Figure 5-32 are likely to make the system unstable and cause sustained oscillations in the process variable. Referring back to the direct synthesis formula (Appendix B),  $K_c$  is inversely proportional to the process gain and time delay. Therefore, if the time delay and/or the process gain are underestimated, the direct synthesis method leads to a proportional gain which is too large for that process. Additionally,  $K_c$  is also inversely proportional to the tuning parameter  $\lambda$ , which is chosen to be 1.8 s for the initial runs. The oscillations around the setpoint are expected to dampen if larger values of  $\lambda$  and therefore smaller proportional gains are used. However, a smaller controller gain results in a more sluggish performance at the acidic and basic operating regions (flat portions of the titration curve). Figure 5-33 shows the

significantly improved performance of the controller when a tenfold smaller proportional gain (0.015) is used.

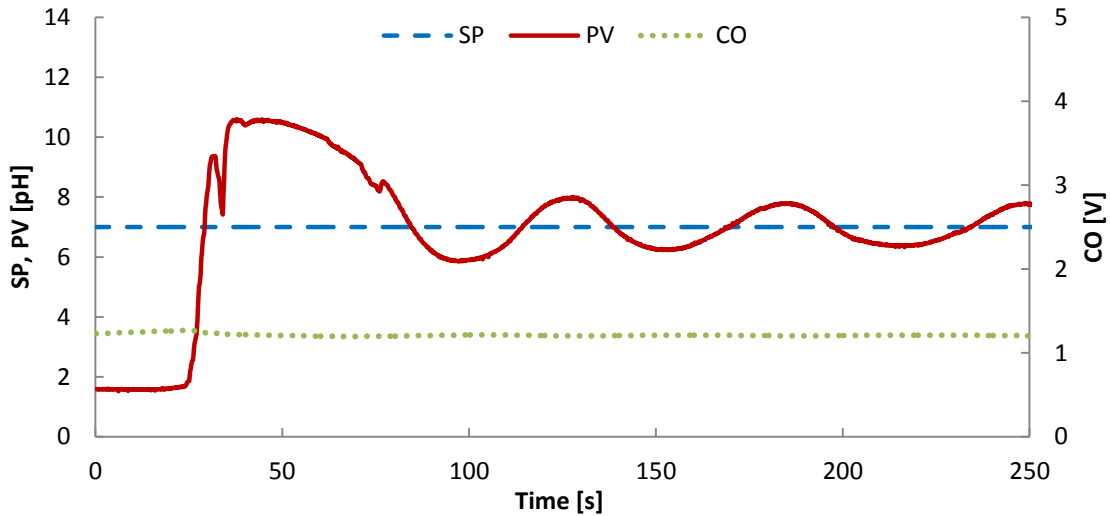


Figure 5-33. Controller tuning [ $K_c = 0.015$ ,  $T_i = 0.3$  min,  $T_d = 0$ ]

Another widely used tuning approach is the Ziegler-Nichols method [172] which is performed by turning off both integral and derivative actions, whilst the proportional gain is increased in small increments until sustained oscillations in the process variable are observed. The controller gain which causes the constant oscillations is referred to as the ultimate gain  $K_u$  and the period of the oscillations is called the ultimate period  $T_u$ . The PI and PID controller settings can be determined from the ultimate gain and period according to Table 5-7. For the present process the ultimate gain is found to be 0.05 %CO/%PV, whilst the ultimate period has a value of 0.85 minutes. The corresponding PI and PID controller performances are presented in Figure 5-34 and Figure 5-35.

Table 5-7. Ziegler-Nichols tuning method

	$K_c$	$T_i$	$T_d$
PI	$0.45 K_u$	$T_u/1.2$	-
PID	$0.60 K_u$	$0.5 T_u$	$T_u/8$

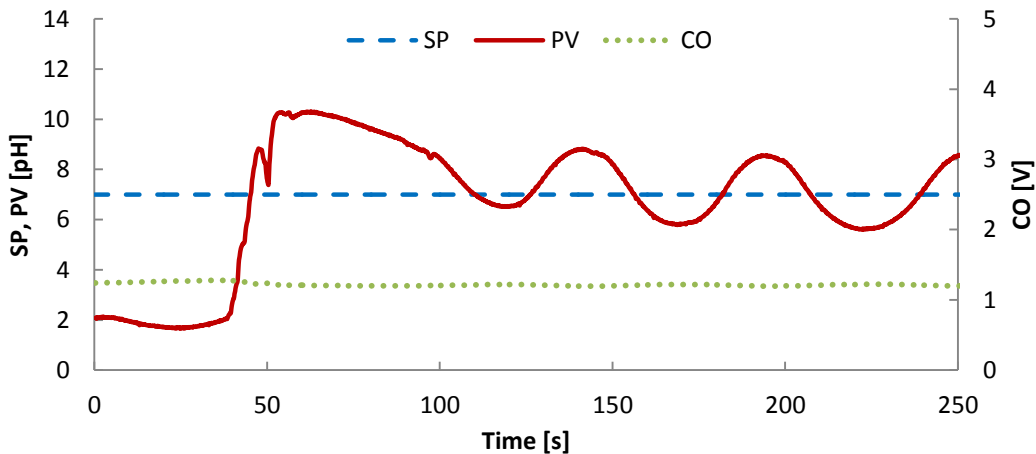


Figure 5-34. Controller tuning [ $K_c = 0.023$ ,  $T_i = 0.708$  min,  $T_d = 0$ ]

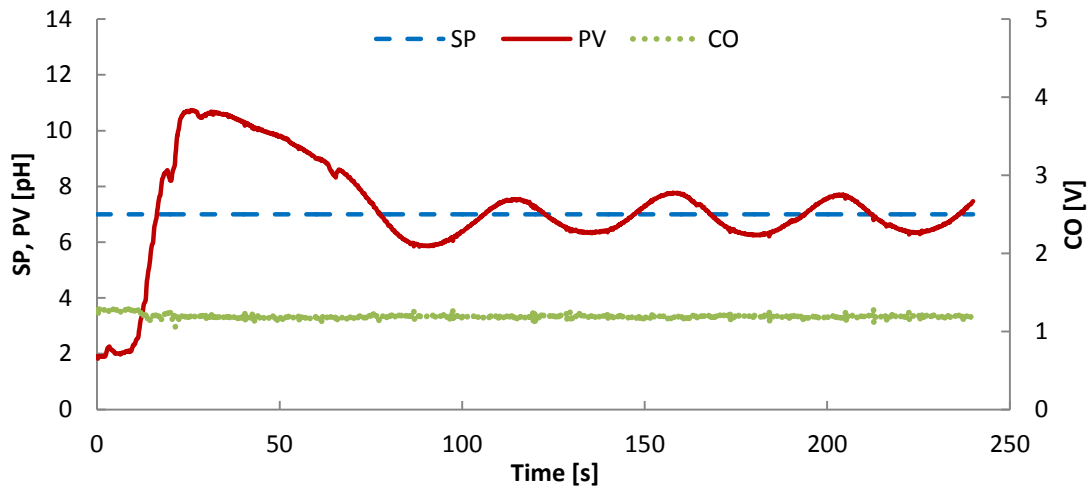


Figure 5-35. Controller tuning [ $K_c = 0.03$ ,  $T_i = 0.43$  min,  $T_d = 0.11$  min]

It is known that the derivative term of a PID controller makes the system more sensitive to noise; however, a higher gain can be used without approaching the stability margins. The results of the Ziegler-Nichols tuning presented above show that the PID controller performs better than the PI controller, since the amplitude of limit cycles in the process variable is smaller. Nevertheless, the controlled variable still limit cycles within  $\pm 0.7$  pH of the setpoint. Although, this level of low amplitude oscillation might be acceptable for the current task, the PID controller can be fine tuned by reducing the proportional gain from 0.03 to 0.025, as presented in Figure 5-36. These controller settings are selected as the final values of the PID controller parameters and are used for the subsequent runs.

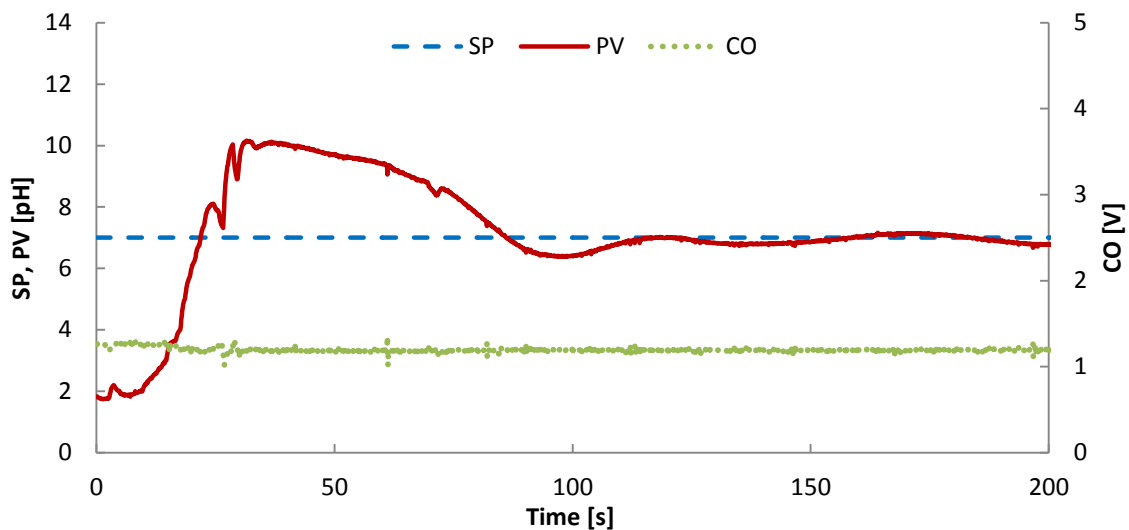


Figure 5-36. Controller tuning [ $K_c = 0.025$ ,  $T_i = 0.43$  min,  $T_d = 0.11$  min]

### 5.3.3 Selection of DO Filter Time Constant

The simulation studies showed that a smaller DO filter time constant results in a more rapid response at the expense of more oscillations in the process variable. The results of applying filter time constants of 1.8, 18 and 180 seconds are presented in Figure 5-37 to

Figure 5-39, whilst the PID settings are those determined in the previous section. The experimental results are in agreement with the simulation runs, whereby a larger filter time constant provides a more stable response. In the present study, for online implementation of the DO scheme, a filter time constant of 180s is selected. It should be noted that a larger filter time constant eliminates the observed limit cycles in the output pH at the expense of a more sluggish response with a larger rise time.

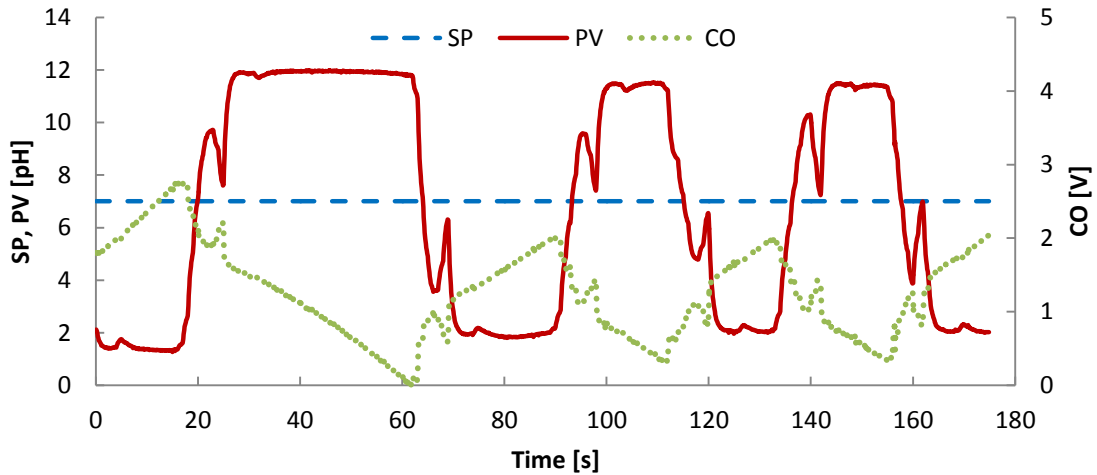


Figure 5-37. DO filter time constant selection [ $\tau_f = 1.8\text{s}$ ]

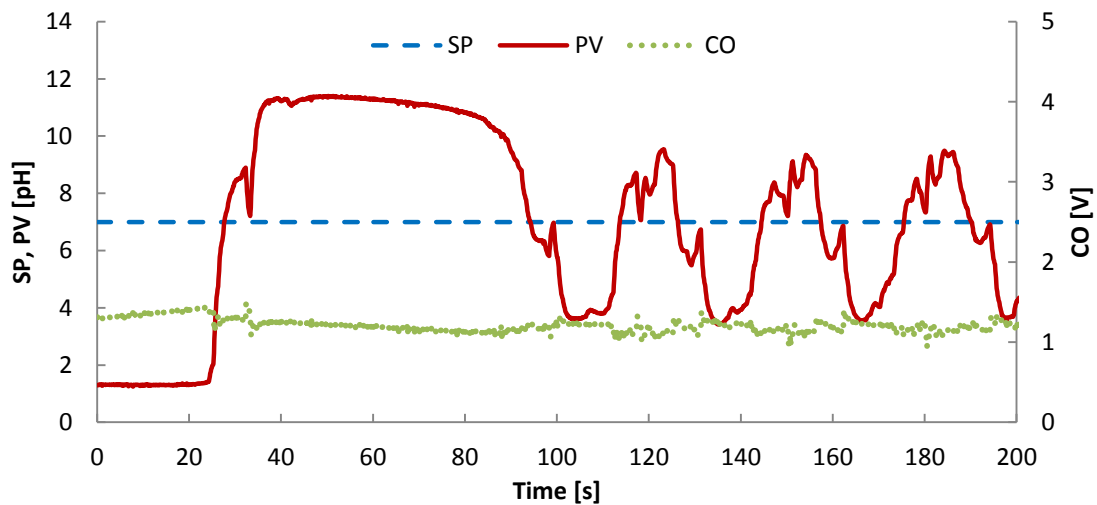


Figure 5-38. DO filter time constant selection [ $\tau_f = 18\text{s}$ ]

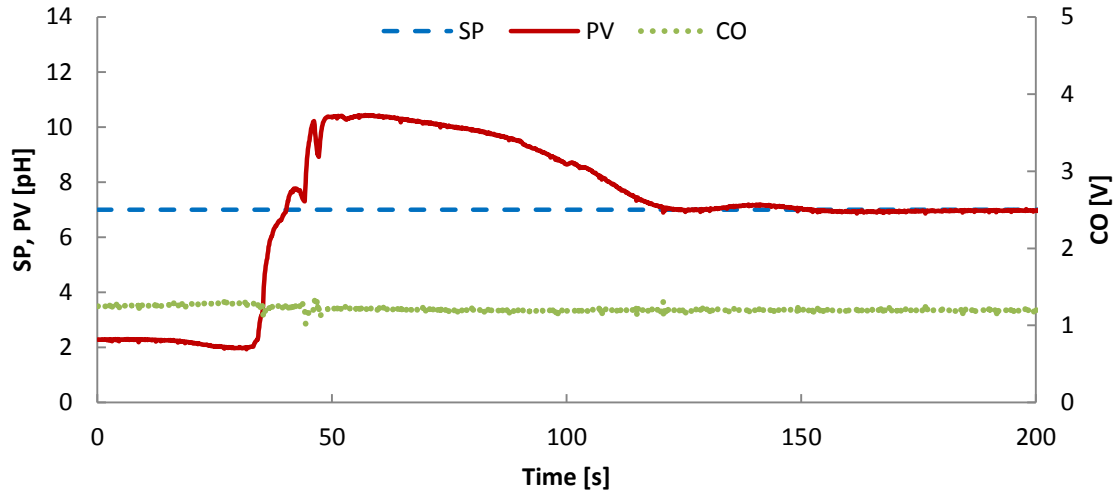


Figure 5-39. DO filter time constant selection [ $\tau_f = 180\text{s}$ ]

### 5.3.4 Performance Evaluation

The previous sections described how appropriate PID controller settings along with a suitable DO filter time constant were obtained. These parameters are used to evaluate the control performance in terms of disturbance rejection and setpoint tracking for the PID and PID plus DO control schemes. The disturbances in the acid flowrate are applied by manual adjustment of the acid stream pump speed, whilst, the changes in the setpoint are implemented by adjusting the user specified value of the setpoint on the front panel of the LabVIEW code. The repeatability of the obtained data is also assessed by carrying out a number of duplicate closed loop tests. In all the pH control tests, the disc speed is maintained at a constant value of 750 rpm. However, variations in the disc speed may occur as a result of equipment malfunction or external disturbances. The disc rotational speed and the feed flowrates have a significant effect on hydrodynamics of thin liquids films and thus may influence the processes carried out in SDRs. Therefore, some control runs are repeated at a different disc speed of 1500 rpm to investigate the potential impact of the rotational speed on pH control. The controller performances are evaluated by visual inspection of the resulting output responses (effluent pH) as well as the calculated IAE values.

### 5.3.5 Disturbance Rejection Performance

The disturbance rejection performances of the PID and PID plus DO schemes are presented in Figure 5-40 and Figure 5-41 respectively. The influent (acid stream) flow is calculated from the known speed of the peristaltic pump, using the calibration data presented in Chapter 4. The reagent (base stream) flow is calculated from the controller output voltage signal and the gear pump calibration data. The process variable (effluent pH) is measured by the pH probe and the setpoint (SP) is the user specified desired value of the controlled variable. The IAE values for each run are given in the figure captions. In both schemes the controller is able to recover from the imposed disturbances and the process variable is brought back to the set point. However, large delays in the process response are evident for

both cases. The large lags are mainly attributed to the pure time delay and slow response time of the pH probe.

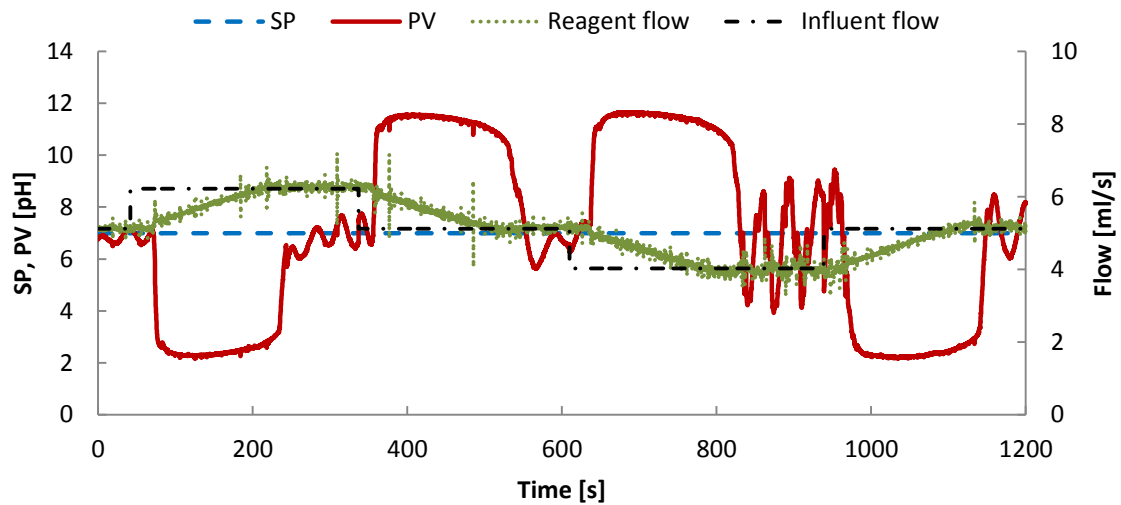


Figure 5-40. PID controller disturbance rejection performance  
[IAE = 3,442]

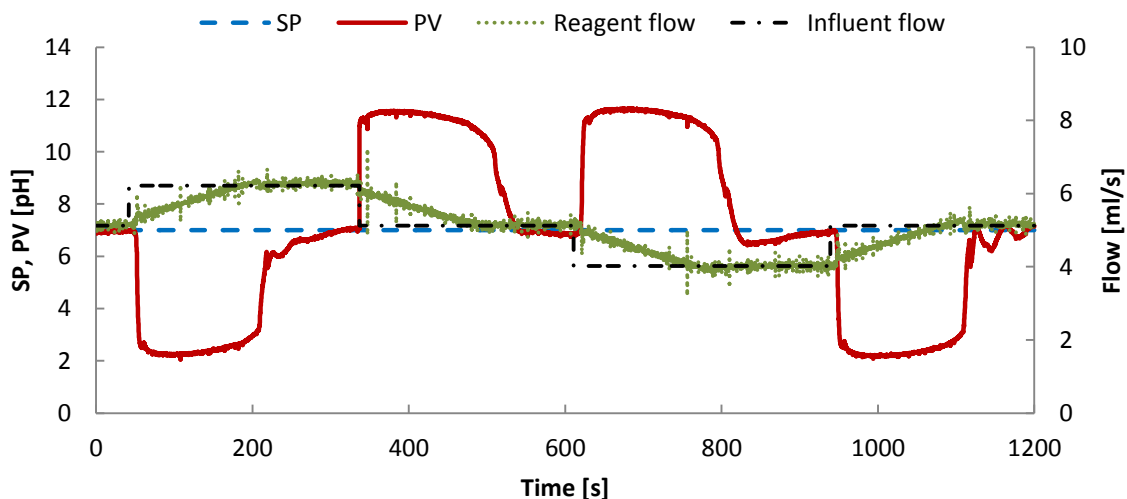


Figure 5-41. PID controller and disturbance observer disturbance rejection performance  
[IAE = 3,152]

For the PID control scheme without the DO, the process variable oscillates around the setpoint value, with the largest oscillations occurring when the acid flow is reduced by 20% from its steady state value. The large oscillations are indications of the onset of unstable behaviour which are also observed in the repeat runs (see Figure 5-45 and Figure 5-47). This may be caused by unsuitable controller tuning parameters, since a single set of values is used to cover a wide spectrum of operating conditions. The large oscillations are observed when the influent flowrate and consequently the reagent flowrate are reduced by 20% from their steady state values. This marginally alters the liquid residence time on the disc as well as the degree of mixing within the reacting media. This might imply that the process enters a different operating region in terms of the film hydrodynamics, hence, may require a new set of tuning parameters to match the new characteristics. This gives rise to the postulation that

more advanced control schemes are required for satisfactory control of SDRs, as the unit may cross the boundaries of various operating regions based on the hydrodynamics of the thin processing films. A more sophisticated control scheme will be able to formulate suitable control parameters for multiple operating regions of the SDR at various flowrates (and/or rotational speeds).

Including the DO scheme suppresses the limit cycles and provides a superior disturbance rejection performance, as shown in Figure 5-41, also reflected by a smaller value of IAE. However, the scheme including the DO seems to be more sluggish compared to the PID scheme. Since including the DO scheme reduces the undesired effects of the system nonlinearity, larger controller gains may be used to achieve faster responses without approaching the stability margins of the system. The same controller tuning parameters are used for both schemes to provide a benchmark for comparison and investigation of the impact of including the DO scheme, independent of the influence of controller tuning parameters. Thus, further enhancement of the performance of the PID plus DO scheme by fine tuning the controller is not considered here.

The experimental results demonstrate the ability of the DO scheme to suppress the effluent pH limit cycles. It should be noted that DO filter time constant implemented in LabVIEW for the experimental runs is 10 times larger than that used for the simulation runs (180s versus 18s). This explains the ability of the DO scheme to suppress the limit cycles in the experimental runs, but not in the simulation runs for 5s time delay (Figure 5-23). This explanation is substantiated by the runs presented in Section 5.3.3, whereby, the constant oscillations observed when a filter time constant of 18s is used are eliminated by increasing the filter time constant to 180 seconds. Furthermore, the time delays in the simulation runs were chosen arbitrarily and may be different to the actual value of time delay present in the system, leading to discrepancies between the simulation and experimental results.

### ***5.3.6 Setpoint Tracking Performance***

The setpoint tracking performance of the PID controller, involving large (5.2 pH units) step changes in the setpoint, is presented in Figure 5-42. It is evident that the controller's setpoint tracking is sluggish when the system enters the acidic and basic operating regions. This behaviour is expected as the controller is tuned for stability when operating in the steep region of the titration curve. As discussed previously, the controller's gain is inversely proportional to the process gain which is in turn determined by the slope of the titration curve. Therefore, using a single set of tuning parameters obtained at the steep region of the titration curve (near the equivalence point) results in sluggish response at the flat portions of the titration curve (acidic and basic regions).

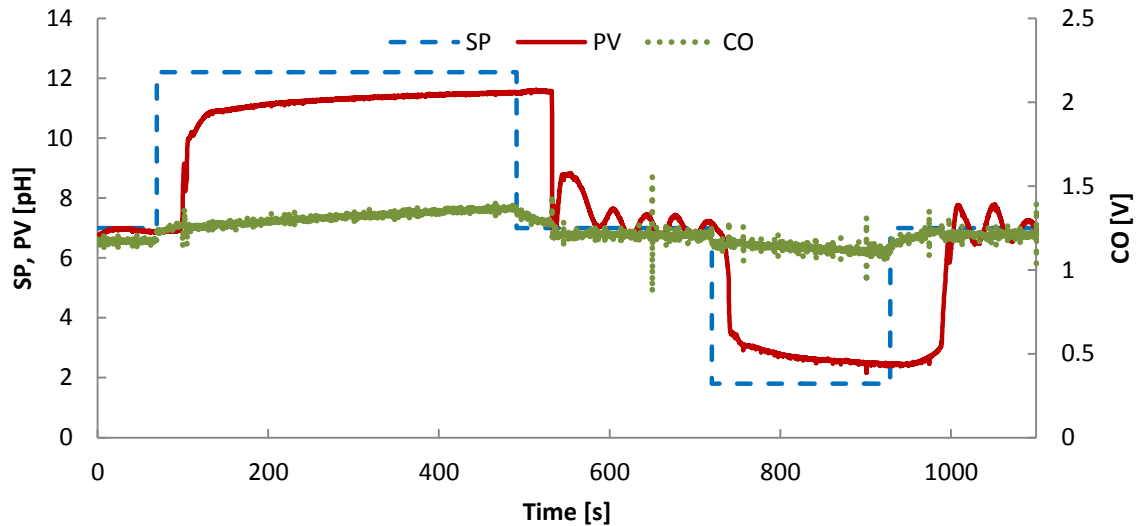


Figure 5-42. PID controller setpoint tracking performance [IAE = 1,439]

Smaller step changes (2 pH units) in the setpoint, whereby the controller is still operating in the steep region of the titration curve, are also considered. The resulting setpoint tracking performances of the PID controller with and without the DO are presented in Figure 5-43 and Figure 5-44. It can be seen that in both cases the controller provides adequate performance by coercing the process variable to follow the setpoint. The addition of the DO marginally improves the controller's performance, indicated by the smaller value of IAE; however, there are still some oscillations in the process variable when the setpoint is reduced to 5 pH and then back to 7 pH in both cases.

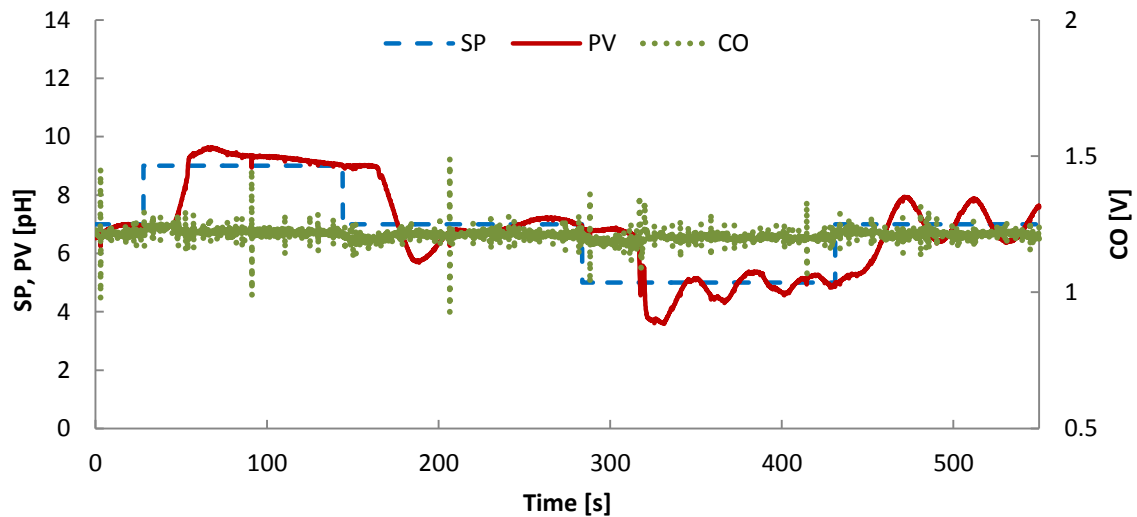


Figure 5-43. PID controller setpoint tracking performance [IAE = 357]



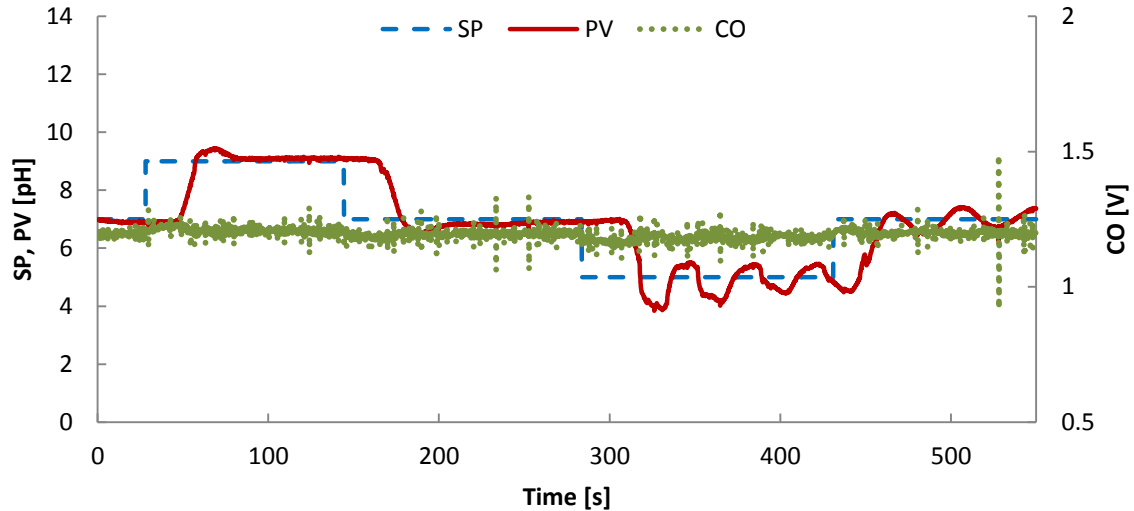


Figure 5-44. PID controller and disturbance observer setpoint tracking performance [IAE = 327]

The large time delays observed in the disturbance rejection runs are also evident in the setpoint tracking runs presented above, which are attributed to the pH probe characteristics. The presented experimental results are in good agreement with the simulation results when large time delays prevail in the system.

The disturbance rejection and setpoint tracking results show that successful control of the pH process in a SDR is achieved by means of commercially available instrumentation. However, with the current set up it is impossible to draw definite conclusions regarding the control aspects of the SDRs itself. This is because the sensor is positioned downstream of the SDR and has a considerably larger time constant compared to that of the SDR. This method of monitoring the process variable includes some undesired ‘tail effects’ which may not be associated with the SDR itself. A more accurate investigation into control characteristics of SDRs and the influence of the liquid film hydrodynamics can be carried out if sensors with adequately fast response times are incorporated within the disc itself. If this can be achieved, a more effective control based on real-time measurements of the process variable on the disc may be achieved; whereby the detrimental effects of the current setup are avoided. Burns and Jachuck [68] report obtaining real-time measurements of the liquid film conductivity using concentric electrodes embedded on the disc at radial intervals of 1cm. This design allows isolation of the SDR characteristics from the undesired end effects. However, despite the theoretical appeal of the described approach, its practical implementation may be hindered by the technical and operational difficulties of incorporating the sensors on the rotating disc, particularly in presence of very thin liquid films.

### 5.3.7 Repeatability Assessment

The disturbance rejection runs presented in section 5.3.5 are repeated to assess the reproducibility of the results. The repeat runs presented in Figure 5-45 and Figure 5-46, show a reasonable agreement with the results obtained previously. However, it should be noted that as the pH control of a strong acid/strong base system around the neutral point is extremely sensitive, minor variations in the experimental conditions, such as the changes in the feed

concentration from batch to batch, would have noticeable impacts on the control outcome. Additionally, the dynamics of the pH probe might vary over time depending on how well the sensor is maintained; this could also lead to some discrepancies between the repeat runs.

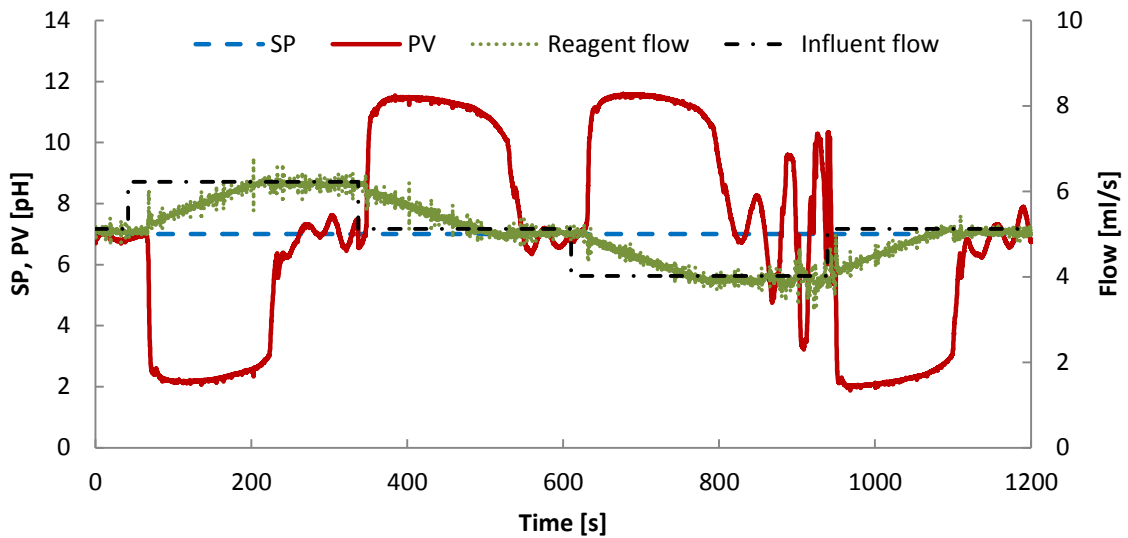


Figure 5-45. PID controller repeat run  
[IAE = 3,260]

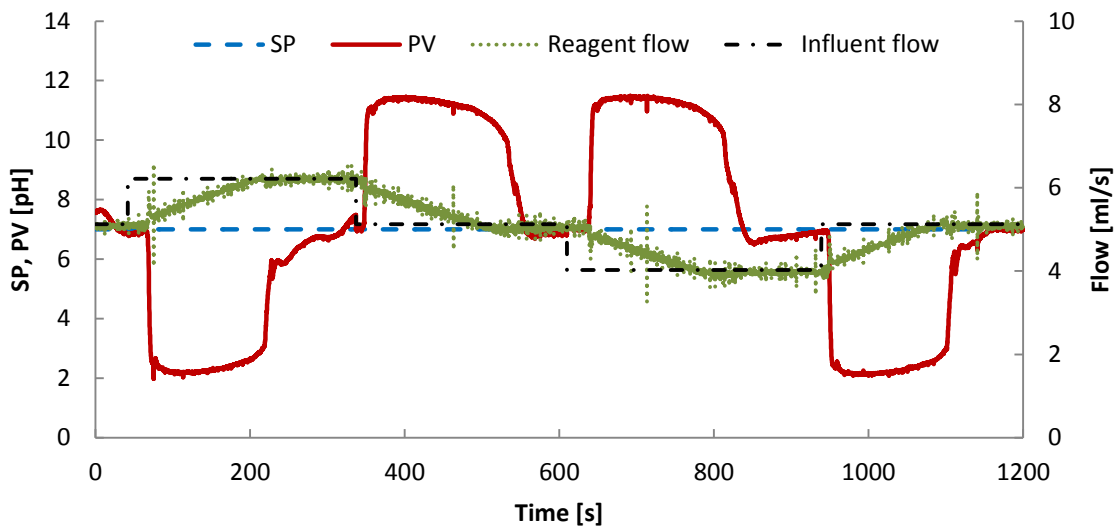


Figure 5-46. PID controller and disturbance observer repeat run  
[IAE = 3,110]

As discussed previously, pH control of a strong acid/strong base system is notoriously difficult using a linear PID controller. The process gain around the neutral point is very large due to the steep slope of the titration curve, thus the controller gain has to be set low to maintain the closed loop stability. A small controller gain results in a very slow process response at the acidic and basic regions where the titration curve is relatively flat. The large delays and slow responses observed in the presented results are attributed to the difficulties of pH control and should not be associated with the SDR which has very fast dynamics.

### 5.3.8 Effect of Rotational Speed

All the results presented so far were obtained at a constant disc rotational speed of 750 rpm. At different rotational speeds the liquid residence time on the disc as well as the exerted shear rate and thus the mixing intensity of the liquid film will vary. Depending on whether a particular reaction is mixing or kinetics limited, the variations in the mixing intensity and residence time could affect the rate of reaction. The residence time on the disc is influenced by the disc rotational speed and feed flowrate, which in turn will affect the system dynamics. Thus, it might be possible that the controller's performance fluctuates at different rotational speeds. This could also be the case when the disc rotational speed is constant but the flow of one or both feed streams are changed. The disturbance rejection of the PID controller with and without the DO scheme are tested at a higher rotational speed of 1500 rpm, as shown in Figure 5-47 and Figure 5-48. The results are comparable to those obtained at 750 rpm, whereby the small variations between the data are believed to be within the expected variability of the different runs.

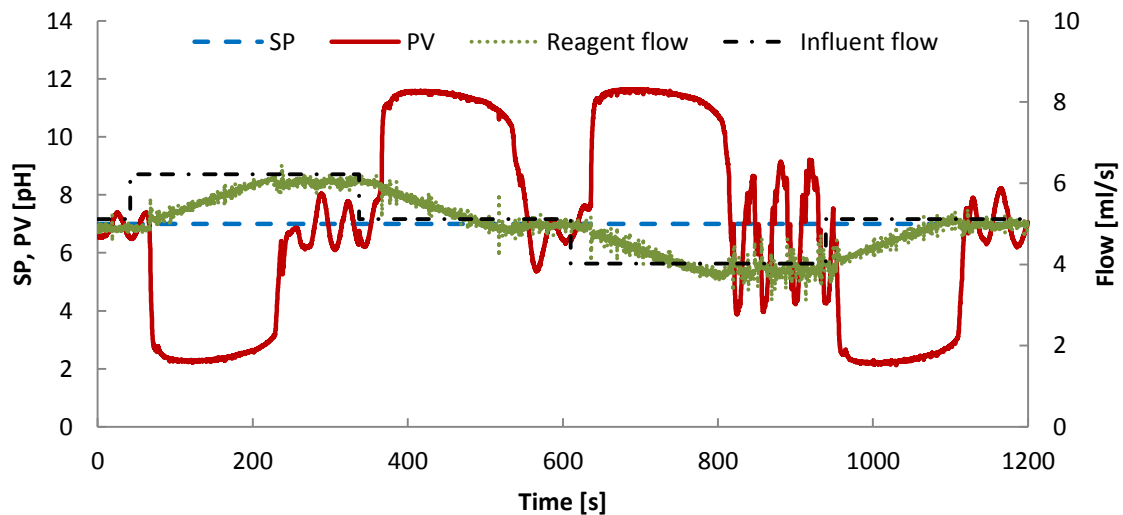


Figure 5-47. PID controller disturbance rejection, disc speed = 1500 rpm  
[IAE = 3,371]

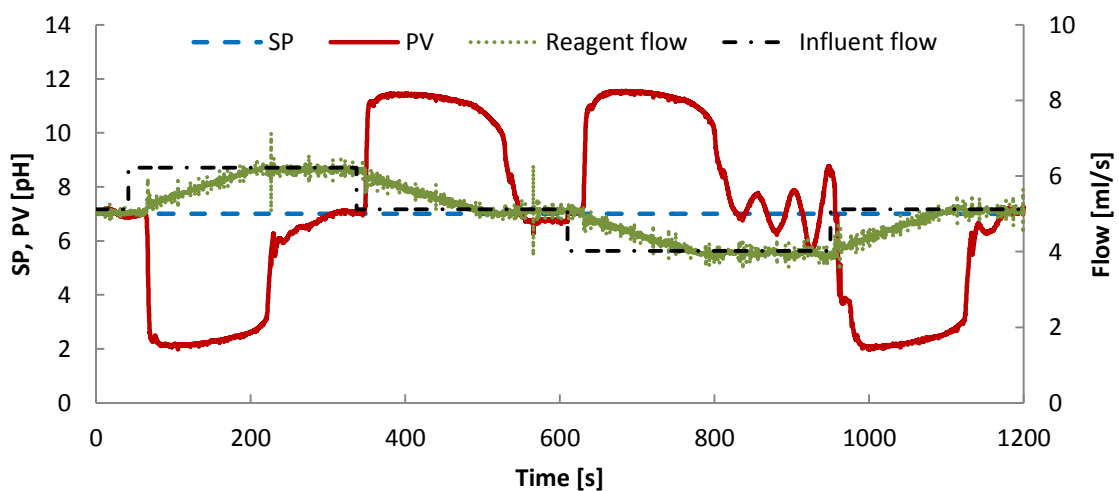


Figure 5-48. PID controller and DO disturbance rejection, disc speed = 1500 rpm  
[IAE = 3,160]

The liquid residence time on the disc is decreased as the rotational speed is increased at constant flow rate; consequently the reactor time constant is reduced. However, in the present setup the dynamics of the pH probe are dominant. This is reflected by the large process time constant of 18 seconds obtained via the open loop tests, whilst the time constant (residence time) of the SDR within the experimental conditions is less than one second. Therefore, the minor changes in the SDR dynamics due to the changes in the rotational speed (or feed flowrate) are not likely to have any significant impact on the controller's performance for the case of pH control. The potential effects of the disc rotational speed on control of process in SDRs are extensively discussed in the next chapter.

## 5.4 Summary

This chapter presented the results of the simulations and experimental assessment of pH control in a SDR. The chapter began by presenting the input-output data which led to the determination of a process model in form of a first order transfer function. The experimentally determined titration curve and the corresponding pH characteriser were also presented. The titration characteristics and the process model were used to develop simulations of the pH control process in the SDR.

The simulation results showed that a PI controller obtained based on the first order process model provides satisfactory setpoint tracking and disturbance rejection performances, when time delays in the closed loop are small. However, the control performance deteriorated as the value of the time delay was increased, whereby the output pH began to oscillate around the setpoint. Amongst the two simulated nonlinear compensation methods, the characteriser provided a superior performance in terms of its ability to suppress the effluent pH limit cycles. However, it was of research interest to further investigate the potentials of applying DOs to mitigate the undesired effects of the pH nonlinearity.

For the online runs it was found that superior control performance is achieved when the derivative action is used. Thus a PID controller with and without the disturbance observer was used to experimentally assess the pH control performance in a SDR. The experimental results confirmed that the challenging task of pH control may be achieved in a SDR using a PID controller coupled with a common pH probe and a variable speed pump. Given the challenges involved, it may be concluded that the obtained control performances are satisfactory. However, the control transient responses were very sluggish and the effluent pH limit cycled around the setpoint when a PID controller was used.

The addition of the DO scheme resulted in improved control performances in terms of IAE compared to the case of PI/PID only, for both simulation and experimental studies. Furthermore, in both simulation and experimental pH control studies it was found that superior suppression of limit cycles is achieved as the value of the filter time constant in the DO design is increased. The experimental pH control results using a PID controller were more analogous to simulation studies with a larger time delay of 5 second, emphasizing again that large time delays in the system lead to significant deterioration of the control performance.

It was envisaged that a more sophisticated SDR design, with embedded sensors on the disc may be required to isolate the control characteristics of the SDR from the pH probe and the undesirable end effects of the current set up. This chapter presented the first part of the control studies in a SDR. The second part of the investigations, concerning the use of the disc rotational speed as the manipulated variable, is presented in the next chapter.

# Chapter 6. Control using Disc Rotational Speed

The previous chapter presented the results of pH control in a SDR obtained via simulation and experimental studies. In spinning disc reactors the rotational speed of the disc offers an extra degree of freedom in design, operation and control of such devices. Adjusting the disc rotational speed alters the liquid residence time on the disc as well as the mixing intensity and the shear stress exerted on the liquid film. These could in turn have an impact on, for example, selectivity, conversion, crystal size distribution, etc. Achieving a control task by manipulating the rotational speed of the disc is a new concept which can offer great potentials. The feasibility and practicality of such a scheme will be investigated in this section via experimental tests. The precipitation of barium sulphate from barium chloride and sodium sulphate is used as an example process to facilitate the proposed investigations. The feed solutions are pumped to the SDR where the precipitation reaction takes place and the conductivity of the effluent stream is controlled by manipulating the disc rotational speed, as illustrated in Figure 6-1.

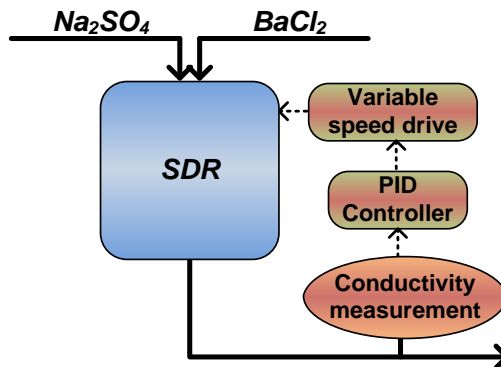


Figure 6-1. Schematic of conductivity control loop

This chapter begins by presenting the input-output model of the system obtained from step response tests. The input-output data define the characteristics of the process in terms of gain, time constant and delay, which will in turn provide a platform for obtaining controller tuning parameters via the direct synthesis method. The experimental results of the conductivity control using the disc speed are then presented and discussed.

## 6.1 Input-Output Model

The input-output data relating the conductivity of the effluent stream to the disc rotational speed are presented in Figure 6-2. It can be seen that an increase in the disc speed from the baseline of 900 rpm results in a small ( $\sim 5\mu\text{S}/\text{cm}$ ) reduction in the effluent stream conductivity. In contrast, a reduction in the disc speed from the baseline results in a much larger ( $\sim 26\mu\text{S}/\text{cm}$ ) increase in the conductivity level. The observed nonlinearity in the output response is expected due to complex interaction of micromixing and residence time with the disc

rotational speed, as discussed in detail later in this chapter. Note that the system has a negative gain as the process output varies in a different direction than the input. This implies that increasing the disc rotational speed enhances the rate of precipitation causing a reduction in the net ion concentration, represented by a drop in the conductivity level. Furthermore, the responses to the first two step changes (900 to 1600rpm and vice versa) are sluggish with no observable pure time delays. In contrast, the output responses to the second two step changes in the input (900 to 200 rpm and vice versa) exhibit larger time delays but the final values are reached faster.

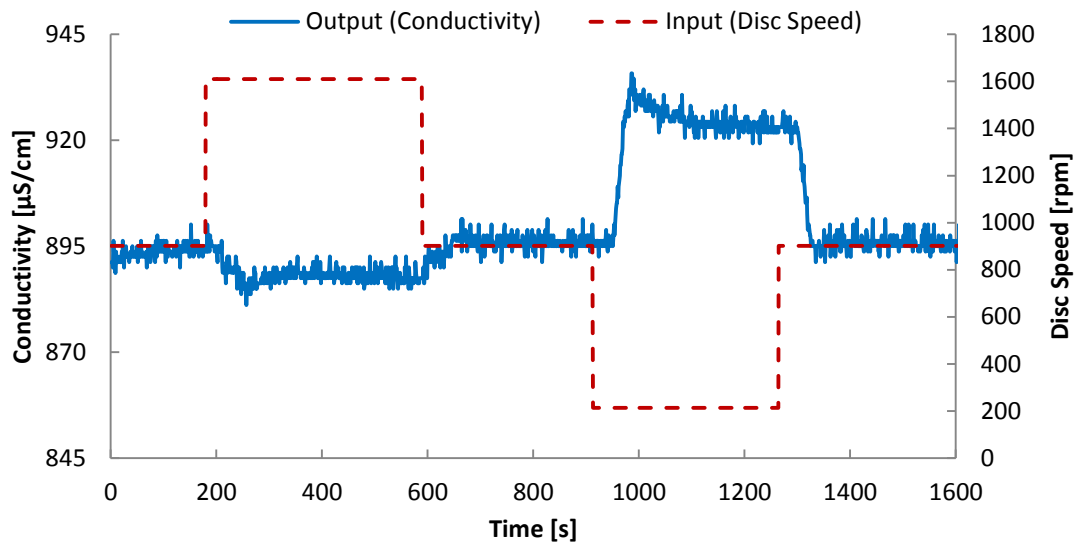


Figure 6-2. Input-output data

It should be noted that the voltage signal sent to the disc speed control unit and the conductivity measurements are both recorded using the same software timing. Therefore, in contrast to the pH control process model, here it is possible to estimate the time delay present in the system using the obtained input-output data. However, fitting the above data to a model which accurately represents the overall system behaviour is literally impossible due to the degree of nonlinearity and asymmetry of the output response. Therefore, a first order plus delay model is fitted to the two sets of step changes separately. The experimental data along with the fitted model for the two segments of the test are presented in Figure 6-3 and Figure 6-4. The values of the process model parameters are given in the figure captions.

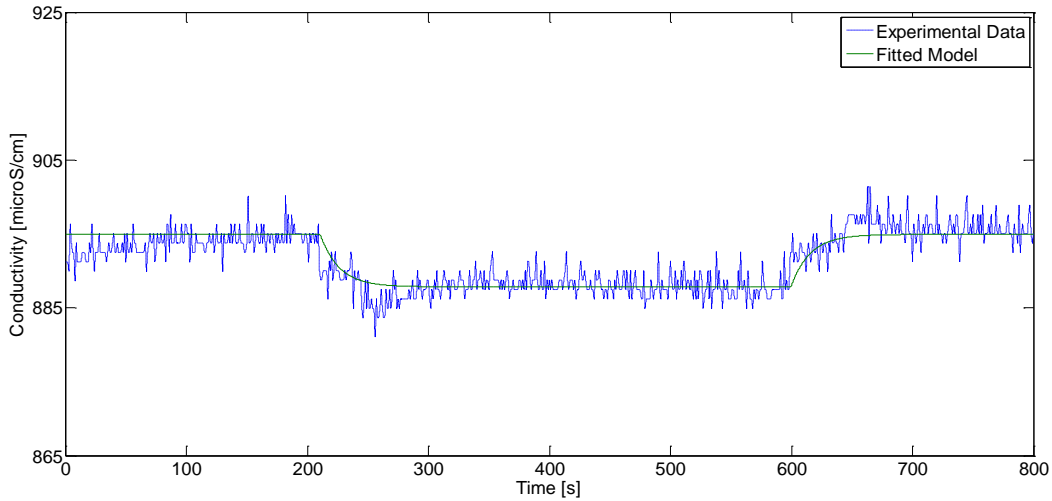


Figure 6-3. Modelled and experimental data for the first two steps  
 [k = -0.01 (μS/cm)/rpm, τ = 16s, θ = 1s]

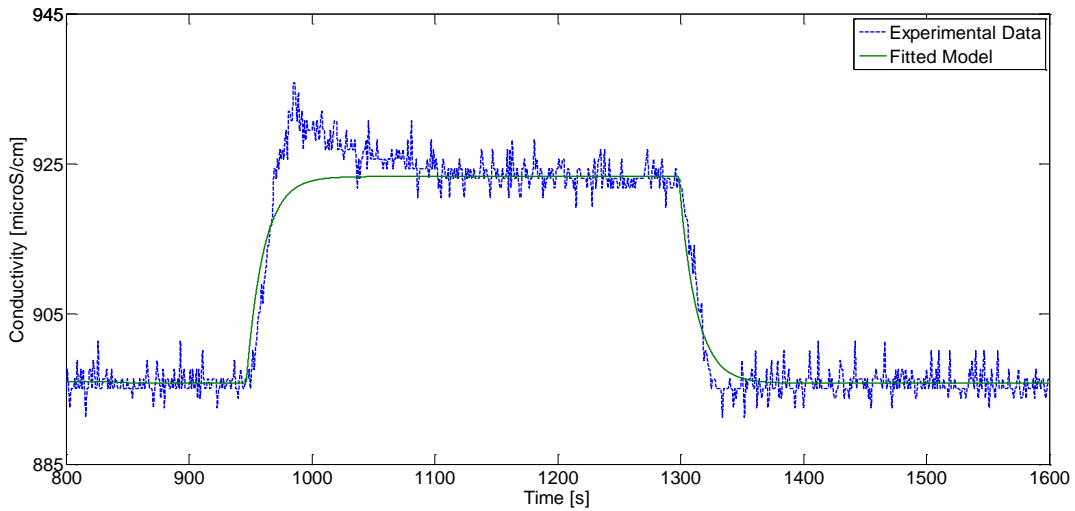


Figure 6-4. Modelled and experimental data for the second two steps  
 [k = -0.04 (μS/cm)/rpm, τ = 14s, θ = 35s]

The overall process model, which is only a rough approximation of the process behaviour, is derived by taking an arithmetic average of the process gains, time constants and time delays obtained for the two sets of data. The averaged process model is presented below:

$$G_p = \frac{k_p}{\tau_p s + 1} e^{-\theta s} = \frac{-0.025}{15s + 1} e^{-18s} \quad (6-1)$$

Where  $k_p$  has units of (μS/cm)/rpm, whilst  $\tau_p$  and  $\theta$  are in seconds. The data produced by the average model are compared to the experimental values in Figure 6-5. As expected, the agreement between the model and the experimental data is poor. Nevertheless, the average model may be used to obtain the initial controller tuning parameters using the direct synthesis method.



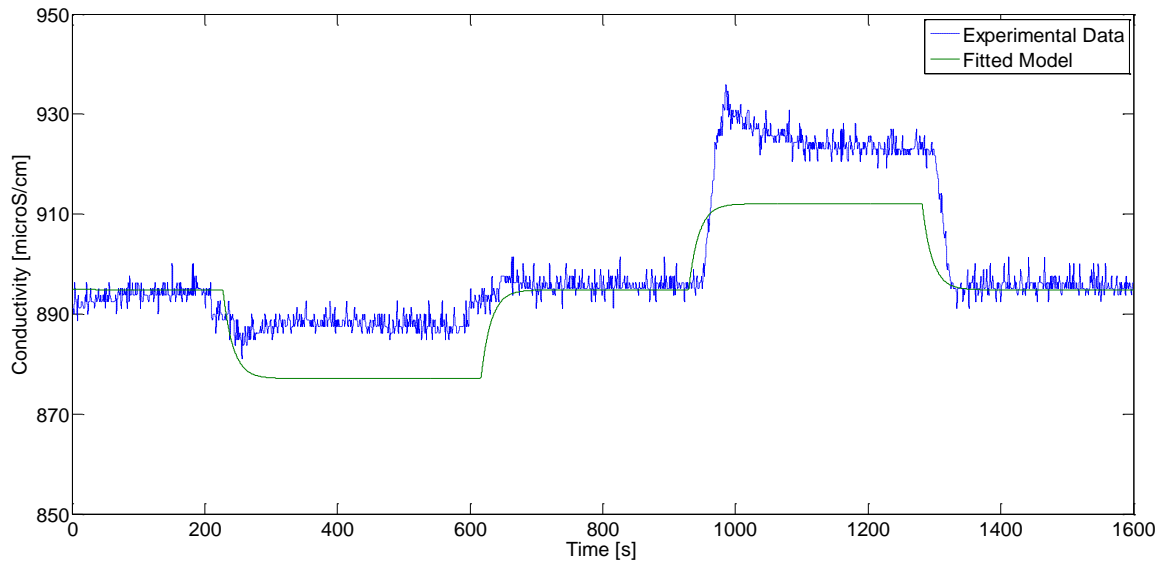


Figure 6-5. Modelled and experimental data  
 $[k = -0.025 \text{ (}\mu\text{S/cm)/rpm, } \tau = 15\text{s, } \theta = 18\text{s}]$

## 6.2 Control Loop Setup

The hardware and software components of the control loop, presented in Figure 6-6, were described in Chapter 4. Similar to the pH control loop, the setup is a RCP configuration in which a software controller is used to control a hardware process. The conductivity signal is transmitted from the sensor to the data acquisition device before being used by the software controller to generate an appropriate control command. The controller output signal is then transferred to the SDR variable speed drive via the same data acquisition device to manipulate the rotational speed of the disc, and thus achieve the control objective. Two control strategies involving a PI controller with and without a disturbance observer are implemented and tested. The LabVIEW block diagrams of the two feedback control schemes are presented in Appendix G.

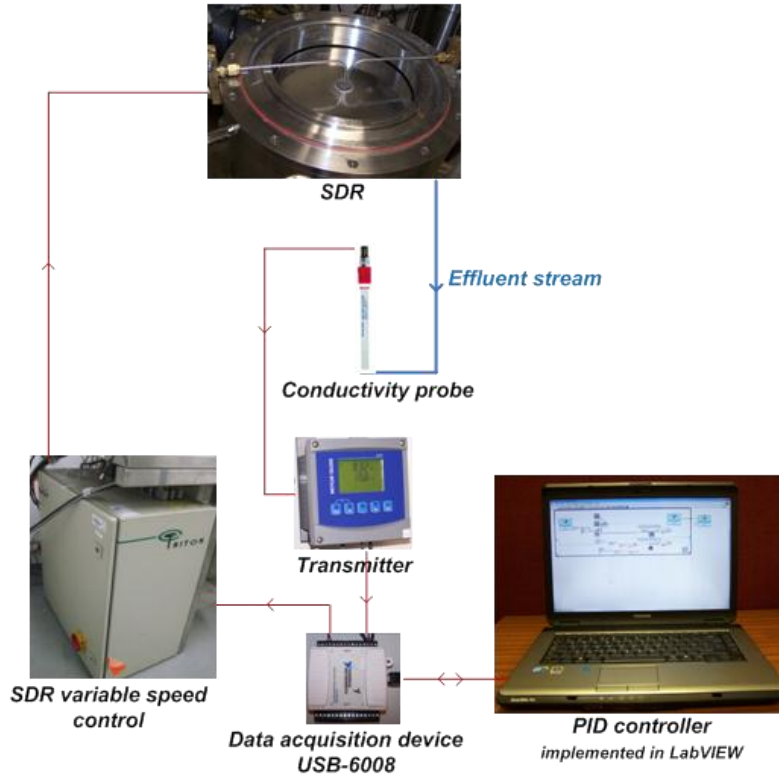


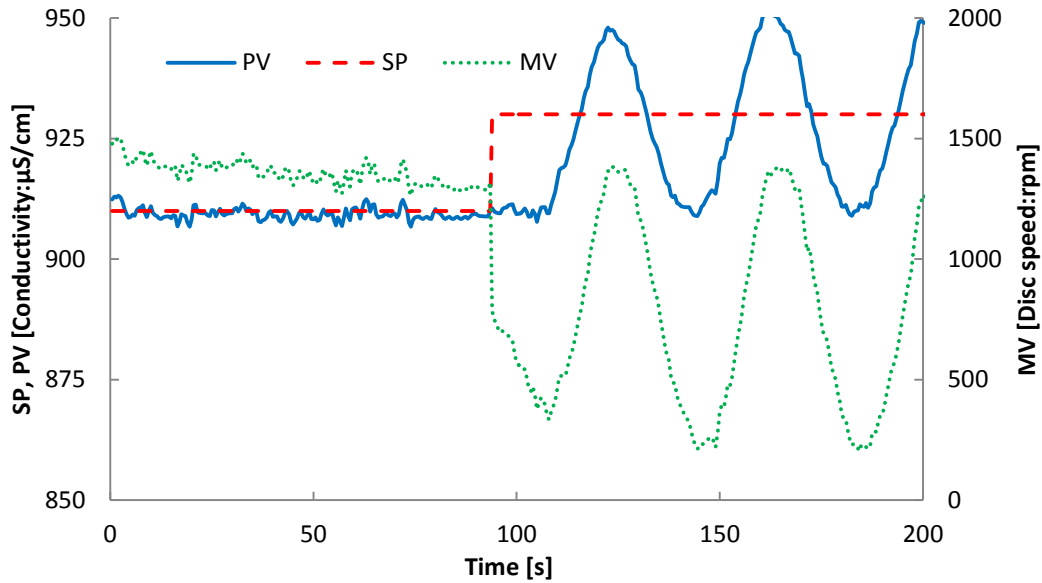
Figure 6-6. Conductivity control loop elements

### 6.3 Controller Tuning

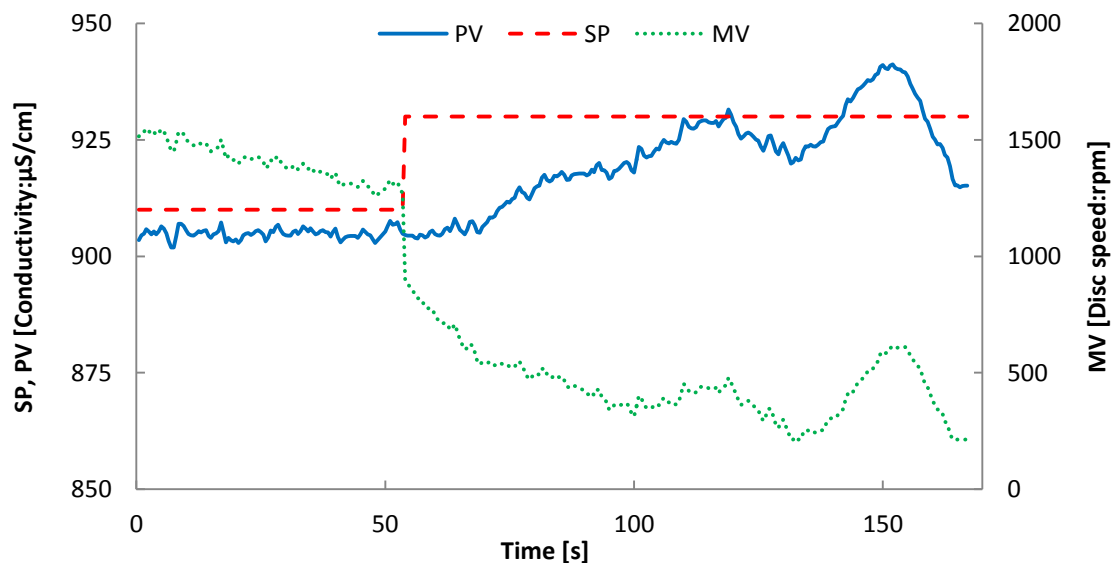
To fine tune the PID controller the flow of the two reacting streams are started and the control loop is closed. Then a step change in the setpoint is introduced and the controller tuning parameters are adjusted to obtain a steady response in the process variable. The SDR is operated within a range of 200-2000 rpm, whilst the transmitter output range is limited to 0-2000  $\mu\text{S}/\text{cm}$ . Therefore, the units of the process gain may be converted to the appropriate format to obtain the controller gain, as follows:

$$k_p = -0.025 \left( \frac{\mu\text{S}/\text{cm}}{\text{rpm}} \right) \times \frac{2000 - 200(\text{rpm})}{2000 - 0(\mu\text{S}/\text{cm})} \times \frac{100(\%PV)}{100(\%CO)} = -0.0225 \frac{\%PV}{\%CO} \quad (6-2)$$

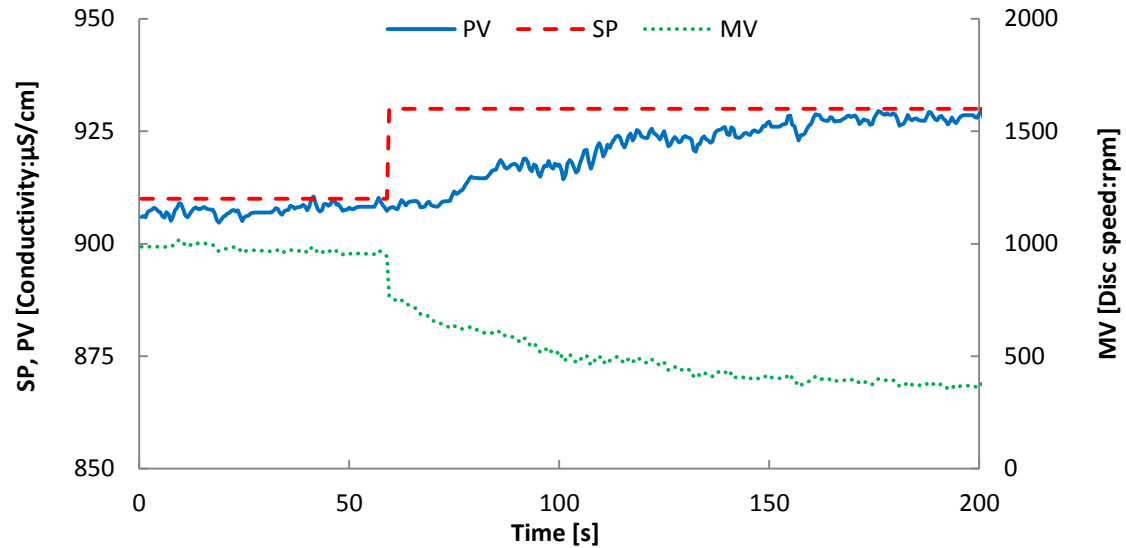
Applying the direct synthesis method to the averaged First Order Plus Dead Time (FOPDT) process model results in a PI controller with a gain of -34 %CO/%PV and an integral time of 0.25 minutes (taking the closed loop time constant,  $\lambda$ , as one-tenth of the process time constant). The output response when the above parameters are used is presented in Figure 6-7.

Figure 6-7. PI controller tuning [ $K_c = -34$ ,  $T_i = 0.25$  min]

It can be seen that the controller's attempt to drive the process variable towards the setpoint leads to sustained oscillations in the effluent conductivity level. This is attributed to the large variations in the manipulated variable (disc speed) caused by a too large controller gain. The oscillations are significantly reduced if the magnitude of the controller gain is reduced to  $-20$ , as shown in Figure 6-8.

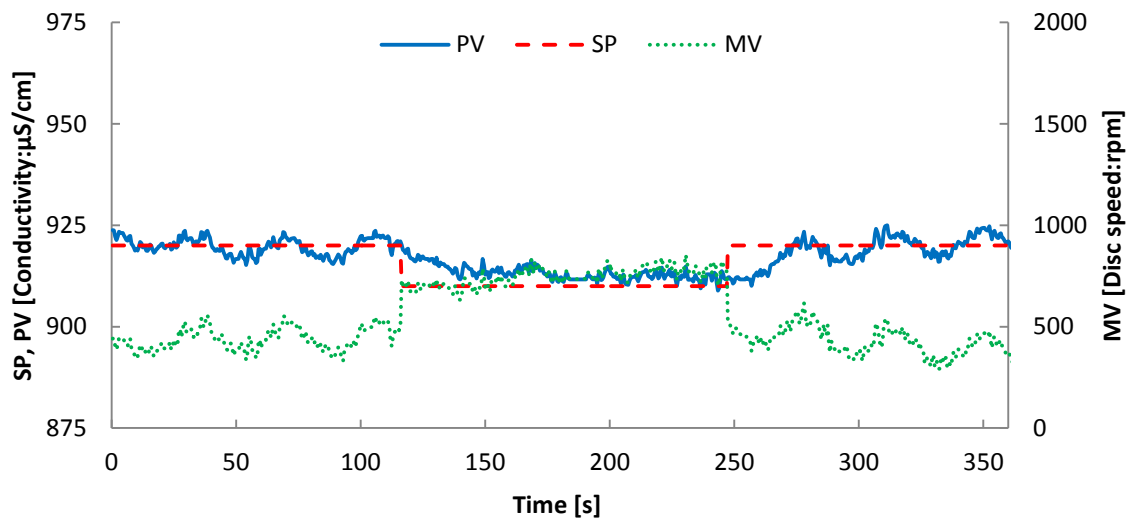
Figure 6-8. PI controller tuning [ $K_c = -20$ ,  $T_i = 0.25$  min]

A steadier response is achieved by a further change of the controller gain to  $-10$  as presented in Figure 6-9. However, it is observed that the oscillations in the controlled variable are eliminated, at the expense of a more sluggish response. Nevertheless, the performance is satisfactory for the purpose of the current study. The derivative action is not considered here as the process signal is noisy and a PI controller is more suitable than a PID. Therefore, the controller gain of  $-10$  and integral time of  $0.25$  minutes are used for the subsequent runs.

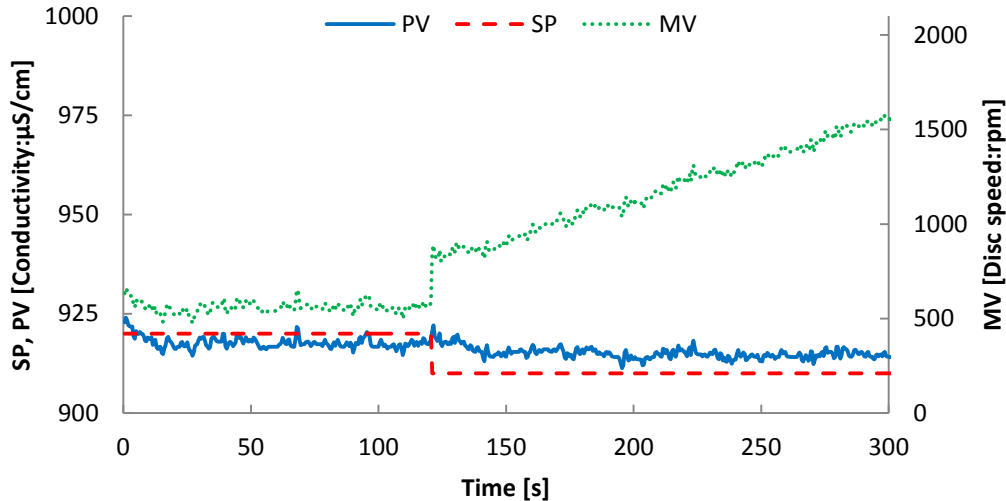
Figure 6-9. PI controller tuning [ $K_c = -10$ ,  $T_i = 0.25$  min]

## 6.4 Selection of DO Filter Time Constant

For the pH control experiments, the DO filter time constant was set to 180 seconds and it was observed that smaller values led to constant oscillations in the controlled variable. For the DO scheme applied to the conductivity control task, two values of the filter time constant, namely 90s and 180s are assessed, while the PI controller parameters are those obtained in the previous section. As shown in Figure 6-10, a filter time constant of 90s results in low amplitude limit cycles in the process variable when the setpoint is at 920  $\mu\text{S}/\text{cm}$ .

Figure 6-10. DO filter time constant selection [ $\tau_f = 90\text{s}$ ]

It is found that the oscillations in the process variable are minimised when a larger filter time constant of 180 seconds is used, as shown in Figure 6-11. Therefore, the filter time constant of 180 seconds is also selected as the optimal value for the conductivity control experiments. The potential reasons leading to the offset evident in Figure 6-11 are discussed in Section 6.7.

Figure 6-11. DO filter time constant selection [ $\tau_f = 180\text{s}$ ]

## 6.5 Setpoint Tracking Performance

The setpoint tracking performance of the PI controller is presented in Figure 6-12. The results are encouraging as they show that the disc rotational speed can successfully be used as the manipulated variable to achieve a given control task in SDRs. These findings present a vastly appealing potential for adopting an innovative approach to process control for SDRs and other similar intensified technologies which offer extra degrees of freedom in their design and operation. However, from a strictly control point of view, the setpoint tracking performance could still be improved; firstly by improving the signal conditioning of the incoming signal to suppress the measurement noise, and secondly by devoting more effort to fine tune the controller further. One striking point in the presented data is that the controller is unable to force the process variable to follow the final step change in the setpoint. This occurrence is an indication of the presence of system constraints, as will be discussed further in Section 6.7.

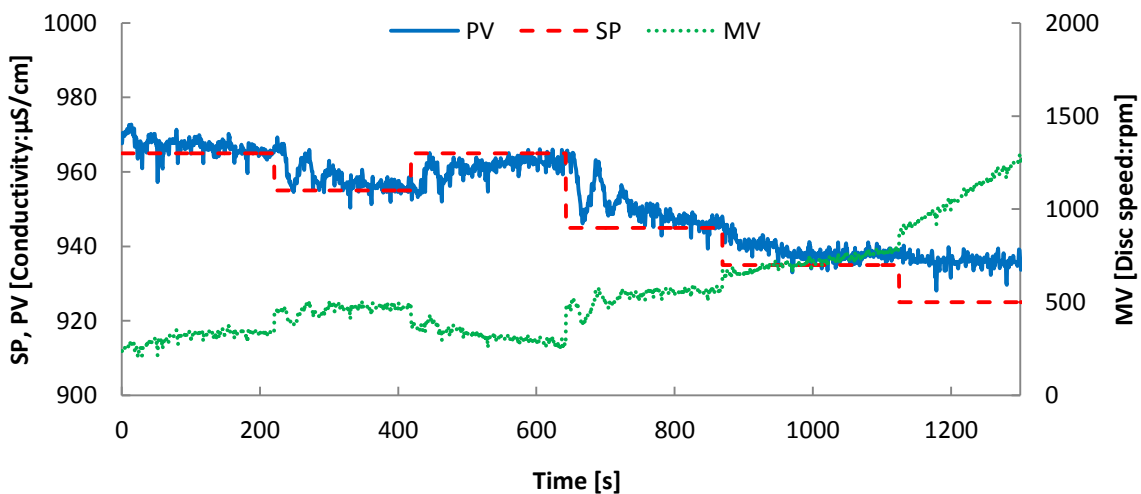


Figure 6-12. PI controller setpoint tracking performance

The setpoint tracking performance of the PI controller plus DO is presented in Figure 6-13. It is observed that the addition of the DO leads to an over-damped response compared

to that achieved without the DO scheme. The oscillations observed in Figure 6-12 are also no longer present. Overall, the results show that the addition of the DO scheme improves the control performance by reducing the oscillations in the process variable. However, to achieve an optimum performance, the PI controller settings need to be fine-tuned with the DO present, as discussed in the Chapter 5 for the case of pH control. The previously observed system constraint is also evident here where the controller is unable to coerce the process variable to follow the penultimate step change in the setpoint, despite the drastic increase in the manipulated variable.

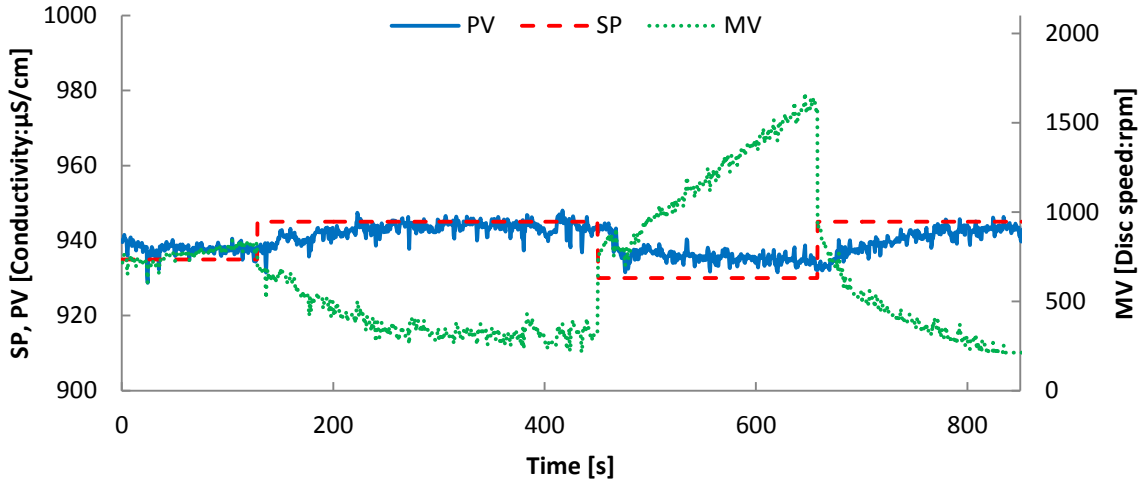


Figure 6-13. PI controller plus disturbance observer setpoint tracking performance

The closed loop data presented so far indicate that there are strong potentials for using the disc rotational speed as a manipulated variable, in addition to the more conventional methods of achieving a control task. However, it was observed that there are performance envelopes for the proposed scheme, outside which the control objective may not be achievable. It is worthwhile to investigate the potential causes of this system limitation as discussed in Section 6.7, following a discussion on the repeatability of the experimental data.

## 6.6 Repeatability Assessment

The conductivity data obtained at constant disc speed of 900 rpm during three different open loop runs are displayed in Figure 6-14. Despite constant operating conditions in terms of the disc speed, disc temperature, feed flowrate and feed concentration, the conductivity levels of the effluent stream are notably different.

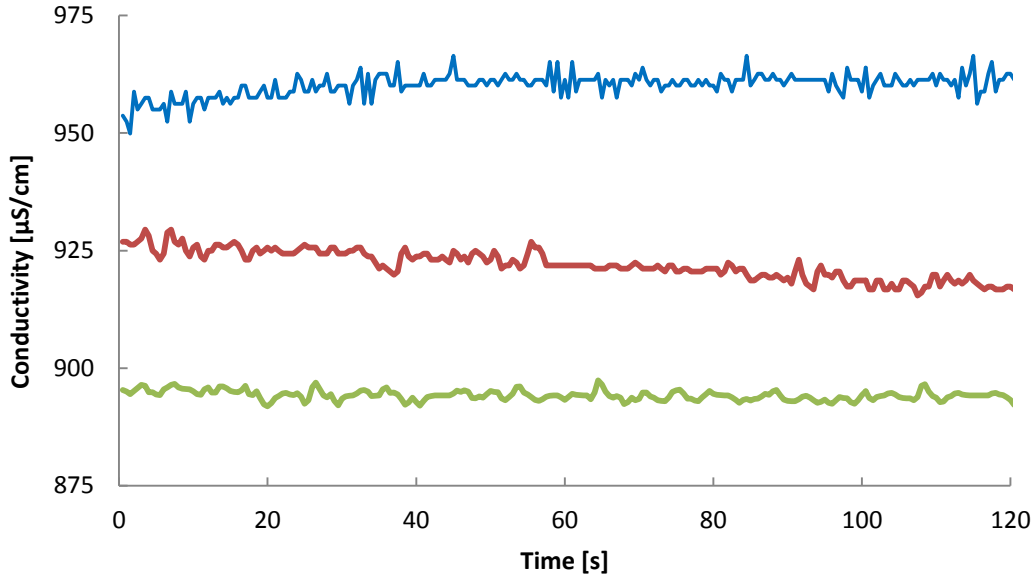


Figure 6-14. Time-varying characteristics of the conductivity signal  
[Output responses of three open loop runs with the same operating conditions]

The average and standard deviation of the plotted data points in Figure 6-14 are 925 and 27  $\mu\text{S/cm}$  respectively. This variation of around 3% may be attributed to the experimental errors associated with the feed solution preparation. The relationships between conductivity and concentration for barium chloride and sodium sulphate solutions, based on the data available in the literature [173], are presented in Figure 6-15. The large slopes of the data sets imply that small changes in the molar concentration of the feed streams would result in large changes in the conductivity values.

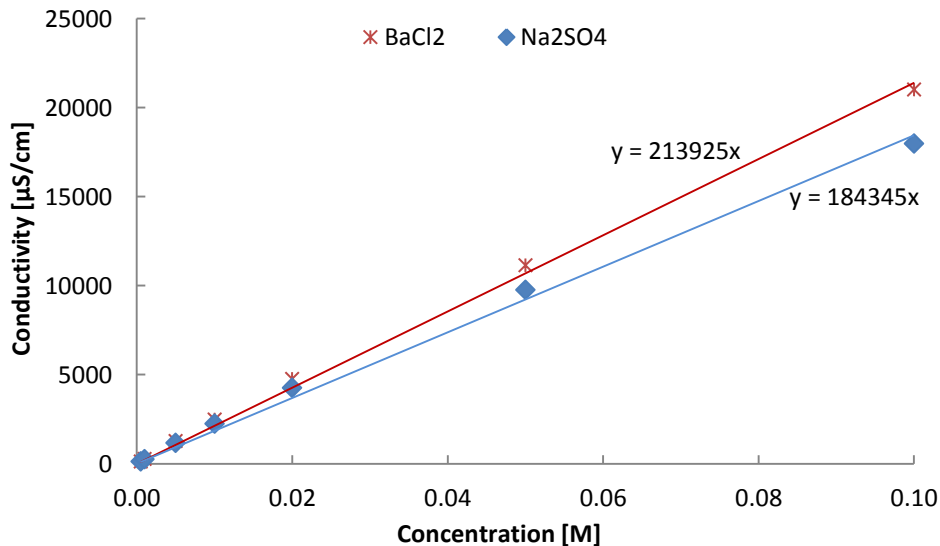


Figure 6-15. Conductivity versus concentration (at 25°C)

Based on the above correlations, the theoretical variations in the conductivity level of each feed stream caused by errors in the feed concentration may be calculated. As shown in Figure 6-16 a variation of 27  $\mu\text{S/cm}$  could be due to a variation of less than 2% in one of the feed streams.

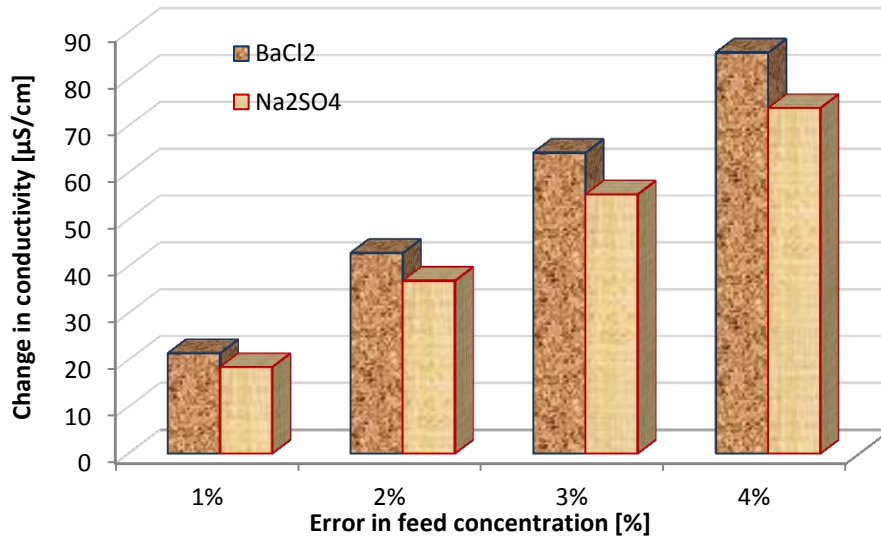


Figure 6-16. Changes in conductivity due to variation of feed molar concentration

Another factor which may result in the drifting of the conductivity data is the build up of the precipitate on the conductivity probe, despite regular cleaning. The particle build up on the probe may impair the accuracy of the conductivity measurements over time leading to time varying characteristics, as well as large measurement delays. Furthermore, as soon as the reagent streams come in contact on the disc, a thin layer of barium sulphate precipitates starts to build up on the disc surface, as shown in Figure 6-17. It is possible that the presence of a layer of crystals on the disc may alter the course of precipitation, by inducing secondary nucleation for instance, and thus lead to reduced repeatability.

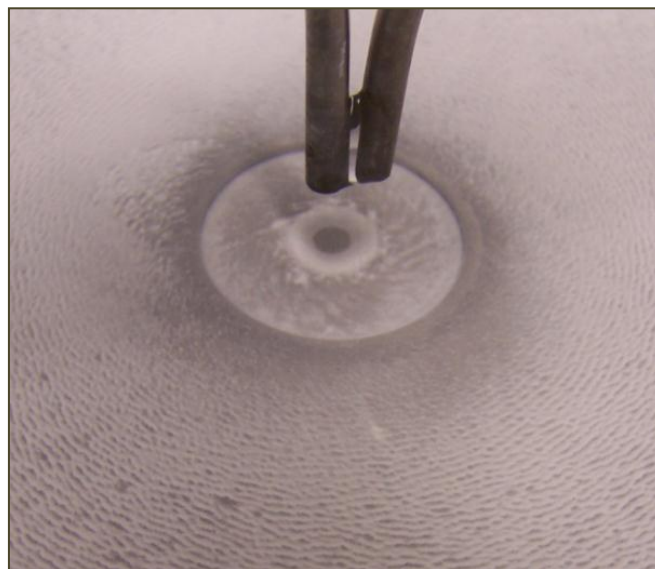


Figure 6-17. Barium sulphate particles build up on the disc

To establish whether the cleanliness of the disc and/or conductivity probe has any influence on the course of precipitation, two sets of open loop experiments are carried out. The first set involves continuous operation wherein the disc rotational speed is stepped from 200 to 1800 rpm at constant feed flowrates. The magnitude of each step is 400 rpm, introduced at 120 seconds time intervals. The second set comprises of a series of runs



corresponding to the same disc rotational speeds, however the system is flushed and the disc/probe surfaces are wiped clean before each step increase in the disc rotational speed. The conductivity values over the final 60 seconds period at each disc speed for the first and second experiments (referred to as continuous and stage-wise respectively) are illustrated in Figure 6-18. The results show that the build up of the precipitates over time in the system seems to enhance the rate of precipitation as the effluent conductivity level is lower for the continuous run compared to that of the stage-wise trials, towards the end of the test where the amount of particle accumulation in the system has increased.

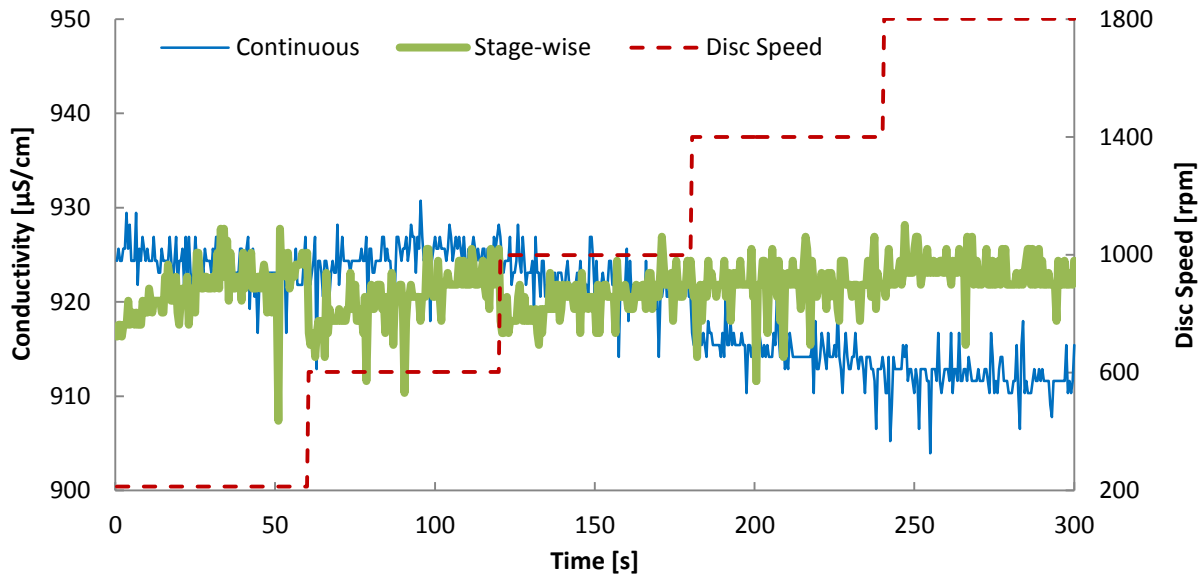


Figure 6-18. Effect of disc/probe cleanliness on effluent conductivity [0.01M feed]

The same behaviour was also observed for higher feed concentrations as presented in Figure 6-19. The presented data show that for continuous operation the precipitation mechanism may change over time due to the build-up of the crystals in the system. This behaviour implies that more sophisticated controllers may be required to cope with the time varying characteristics of the system. Alternatively, provisions could be put in place to minimise the build-up of barium sulphate particles in the system. Oxley et al. [57] also reported a similar issue arisen by adhesion of crystallised material to the stainless steel disc which led to sever encrustation. The problem was overcome by coating the disc with a thin layer of PTFE.

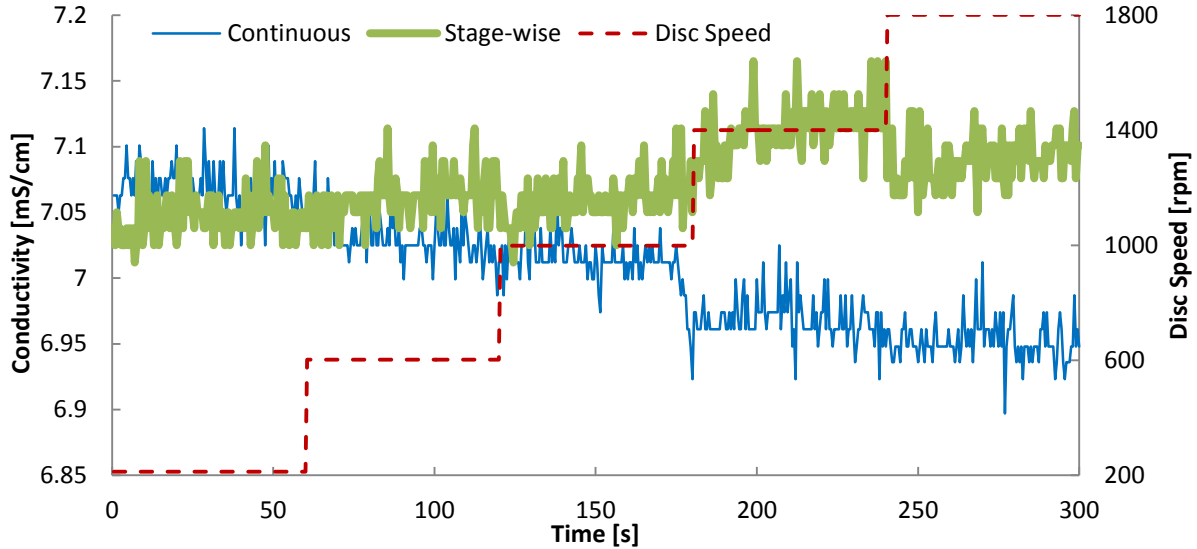


Figure 6-19. Effect of disc/probe cleanliness on effluent conductivity [0.1M feed]

In this section the potential contributory factors for the observed variations in the experimental data were discussed. It is worth noting that even very small degrees of variation in the process output may have a significant impact on the control performance for the present system. The average process gain estimated from the input-output tests is very small ( $-0.025$  ( $\mu\text{S}/\text{cm}$ )/rpm) implying that large changes in the disc speed are needed to cause small changes in the effluent conductivity. Based on the averaged process gain, the standard deviation of  $27\mu\text{S}/\text{cm}$  corresponds to a change in the disc speed of 1080 rpm, which is 60% of the controller output range. Therefore, achieving a consistent control performance for the selected experimental conditions is likely to be a challenging task.

## 6.7 Analysis of Results

It is known that the disc rotational speed has a strong influence on the hydrodynamics of thin liquid films. The results presented earlier in this chapter demonstrated that the conductivity of the effluent stream in the barium sulphate precipitation shows measureable sensitivity to the disc rotational speed. Furthermore, the setpoint tracking results confirmed that the disc speed may be used as a manipulated variable to achieve a given control task. However, the results showed signs of system constraints or performance envelopes beyond which the process variable is independent of the manipulated variable, leading to the failure of such a control approach. In this section, the effect of the rotational speed on the course of reaction for the selected process is studied further in order to shed some light on the observed phenomenon.

### 6.7.1 System Constraint

Figure 6-20 presents the average conductivity data at various rotational speeds abstracted from the closed loop run presented in Figure 6-12. It is evident that the conductivity is more sensitive to the rotational speed up to the disc speeds of approximately 800 rpm. However, beyond this point the conductivity of the effluent stream becomes virtually insensitive to

changes in the rotational speed. This is also readily observable in Figure 6-12, where the controller increased the disc rotational speed from around 800 rpm to 1300 rpm in the failed attempt to bring the process variable to the setpoint, following the final step change. These findings agree rather well with the results of Cafiero et al. [26] who reported that the crystal production rate continuously increased on increasing the rotational speed up to a certain point beyond which no significant change was observed.

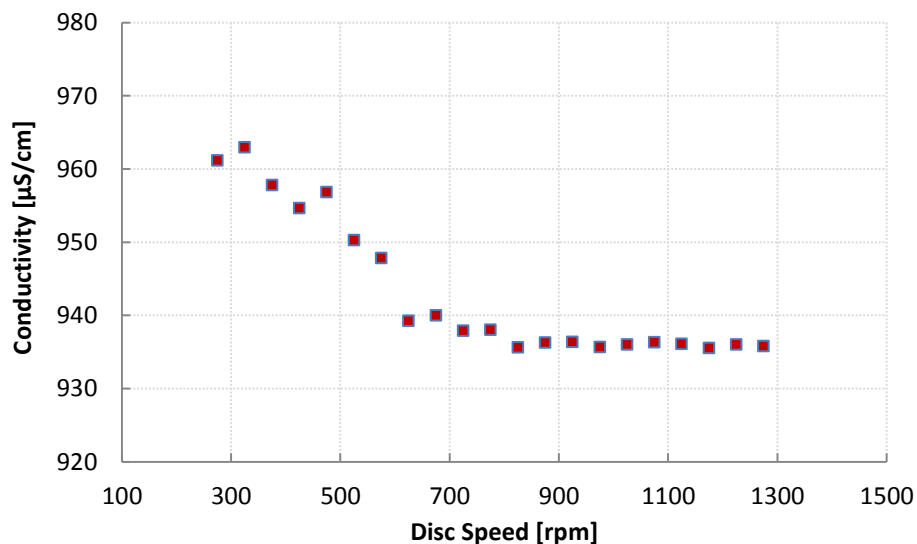


Figure 6-20. Conductivity versus disc rotational speed

This occurrence is considered as a system constraint in terms of controller design, where the process variable is nonresponsive to the controller's command. Such behaviour, however, is not specific to the precipitation reaction considered here, and can be regarded as a characteristic feature of SDRs. Keeping all the other operating conditions constant, as the rotational speed is increased the liquid residence time on the disc is reduced. Therefore, conversion should steadily decline with increasing rotational speed if a reaction is kinetically limited. However, if the reaction is very fast but mixing limited, conversion should increase with increasing rotational speed as the film thickness is reduced, the shear rate exerted on the liquid film is increased and more turbulence is induced in the film via surface waves, all of which lead to enhanced mixing. If the mixing and reaction time are similar for a given reaction, then the reaction rate may be controlled by both mixing and the reaction kinetics. Thus an optimum rotational speed might exist which provides a balance between good mixing and sufficient residence time to give the highest yield. A trade-off rotational speed was indeed observed in previous experimental studies [56, 70].

It is also worth noting that similar opposing effects between mixing and residence time may also prevail by adjusting the feed flowrates in SDRs [49]. Therefore, regardless of whether the disc rotational speed or the feed flowrate is used to control a reaction, the cut-off points where enhanced mixing is counteracted by reduced residence time needs to be defined. These characteristics of SDRs give rise to the postulation that perhaps advanced control algorithms are required to account for such complex interactions of the film hydrodynamics with the manipulated variables, particularly in the presence of process disturbances.

As discussed previously, the disc rotational speed is one of the key factors which dictates the residence time and the mixing characteristics of the liquid films in SDRs. The effects of residence time and mixing on the selected precipitation process are analysed by comparing the respective time scales as discussed in the following sections.

### 6.7.2 Effect of Mixing

Typically, the enhanced mixing conditions in SDRs are achieved in presence of thin highly sheared liquid films which exhibit numerous waves or surface instabilities. Figure 6-21 presents the film thickness profile at various disc rotational speeds for the experimental conditions adopted here (see Equation 2-3). It can be seen that the film thickness profile starts to even out at higher rotational speeds. Thus, for the current system, it might be that the mixing intensity is not greatly enhanced beyond an optimum disc speed, as the influence on the film thickness is reduced. Another factor that might be at play here is that beyond the optimum disc rotational speed, extremely thin films with smooth surfaces may prevail [15]. Therefore, further reduction in the film thickness may be counter-balanced by the reduction of the surface waves, leading to no net enhancement of the mixing conditions. To elaborate on this point the surface characteristics of thin liquid films will be investigated further in the next chapter.

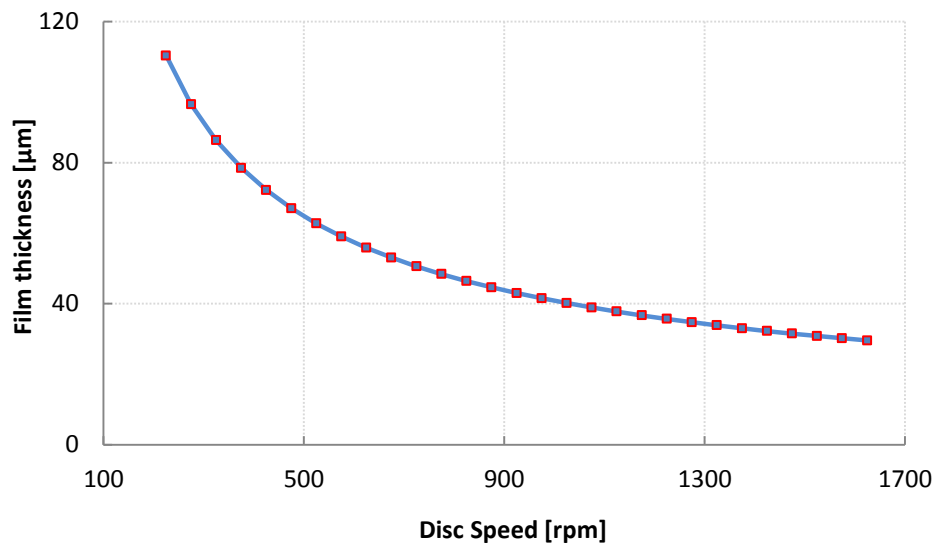


Figure 6-21. Film thickness at various disc rotational speeds  
[Evaluated at the outer disc radius, flowrate: 10ml/s, kinematic viscosity:  $10^{-6}\text{m}^2/\text{s}$ ]

The disc rotational speed has a direct influence on micromixing which in turn is known to have a significant effect on the course of reaction, if the micromixing time constant is comparable or larger than the reaction time [174]. Therefore, in addition to the potential effects of the film thickness and surface waves, beyond a certain rotational speed the micromixing time might become so short that it has little or no influence on the rate of reaction, i.e. reaction is not mixing limited. In this section, the micromixing times corresponding to the experimental conditions are calculated in order to explain the observed trends of the experimental data.

Baldyga et al. [120] developed the following expression for calculation of the micromixing time constant for molecular diffusion accelerated by deformation:

$$t_{micro} \cong 2 \left( \frac{\nu}{\varepsilon} \right)^{0.5} \operatorname{arcsinh}(0.05Sc) \quad (6-3)$$

where,  $t_{micro}$  = micromixing time constant [s]

$\nu$  = kinematic viscosity [ $\text{m}^2/\text{s}$ ]

$\varepsilon$  = energy dissipation rate [ $\text{m}^2/\text{s}^3$ ]

$Sc$  = Schmidt number ( $= \frac{\nu}{D_{AB}}$ , where  $D_{AB}$  = diffusion coefficient [ $\text{m}^2/\text{s}$ ])

For Schmidt numbers smaller than 4000, the micromixing time constant is controller by engulfment and may be approximated as [120]:

$$t_{micro} \cong 17.3 \left( \frac{\nu}{\varepsilon} \right)^{0.5} \quad (6-4)$$

The kinematic viscosity of water at 25°C is  $8.9 \times 10^{-7} \text{ m}^2/\text{s}$ , while the diffusion coefficient of barium sulphate in water using the Scheibel equation [175] is estimated to be  $1.49 \times 10^{-9} \text{ m}^2/\text{s}$  (see Appendix H). Thus, the resulting Schmidt number for the present system is equal to 597, implying that micromixing is controlled by engulfment and therefore Equation 6-4 should be used to calculate the micromixing time constant.

It is worth mentioning that the actual value of the diffusion coefficient obtained in SDRs may be higher than the value estimated here, due to the enhanced diffusion/mass transfer within the thin highly sheared liquid films. The experimental data presented by Guo et al. [176] show that the diffusion coefficient for a barium sulphate in water system increases exponentially with increasing ultrasonic energy input. The centrifugal field exerted on the processing films in SDRs is expected to have a similar enhancement effect on mass transfer as that of the ultrasound energy. Thus, the diffusion coefficient is expected to increase with increasing disc rotational speed. This however, does not affect the calculations presented here as a larger diffusion coefficient results in even a smaller Schmidt number which does not invalidate the expression used here for calculation of the micromixing time constant.

The only parameter that needs to be estimated for determining the micromixing time is the energy dissipation rate. Khan [177] measured the power required to drive the rotor assembly in a SDR system, with and without the flow of liquid on the disc. The difference between the two measured power dissipation values was taken to be equal to the kinetic energy given to the liquid to flow on the disc in addition to the frictional losses as the film crosses the disc surface. Khan [177] also derived theoretical expressions for the two components of the power dissipation, as presented below in Equations 6-5 and 6-7, and showed that the theoretical predictions are in reasonable agreement with his experimental data.

$$i) P_K = \frac{Q\rho}{2} \left[ (r^2\omega^2 + u^2)_o - (r^2\omega^2 + u^2)_i \right] \quad (6-5)$$

$$\text{where, } u = \left( \frac{Q^2\omega^2}{12\pi^2 r\nu} \right)^{1/3} \quad (6-6)$$

$$\text{ii) } P_F = \frac{Q\rho\omega^2}{2}(r_o^2 - r_i^2) \quad (6-7)$$

where,  $P_k$  = kinetic power dissipation [W]

$P_F$  = friction power dissipation [W]

$Q$  = volumetric flowrate [ $\text{m}^3/\text{s}$ ]

$\rho$  = liquid density [ $\text{kg}/\text{m}^3$ ]

$r$  = disc radius [m]

$\omega$  = angular velocity [rad/s]

$u$  = average velocity of liquid solution [m/s]

$\nu$  = kinematic viscosity [ $\text{m}^2/\text{s}$ ]

In turbulent flow theory, the kinetic energy is the primary energy component which contributes to mixing. Therefore, the kinetic power dissipation is used here to calculate the power dissipation rate required for estimation of the micromixing time. This approach was also adopted by previous researchers [26, 178]. The power dissipation rate,  $\varepsilon$ , has units of  $\text{m}^2/\text{s}^3$  or equivalently W/kg which may be calculated by dividing the kinetic power dissipation by mass of the processing fluid as presented below:

$$\varepsilon = \frac{P_K}{Q\rho t_{res}} = \frac{1}{2t_{res}} [(r^2\omega^2 + u^2)_o - (r^2\omega^2 + u^2)_i] \quad (6-8)$$

where,  $t_{res}$  is the fluid residence time on the disc. As presented in Figure 6-22, the micromixing time constants for total flowrate of 10 ml/s and rotational speeds of 200 to 1600 rpm ranges from 8.3 – 0.4 ms respectively.

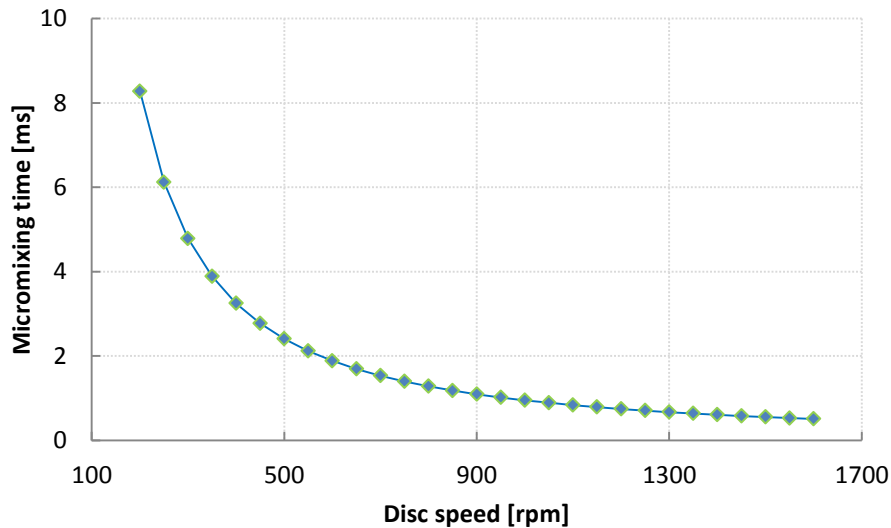


Figure 6-22. Influence of disc speed on micromixing time constant

To evaluate the effect of micromixing on the course of precipitation, the micromixing time constants are commonly compared to the induction time [26, 132]. The induction period is defined as the elapsed time between creation of supersaturation and the formation of first particle of detectable size [107]. Carosso and Pelizzetti [122] experimentally determined the following correlation for the induction time of barium sulphate precipitation:

$$\log t_{ind} = 15.5(\log S)^{-2} - 4.2 \quad (6-9)$$

where, S denotes supersaturation ratio calculated from the following expression:

$$S = \gamma \left( \frac{C_{Ba} C_{SO_4}}{K_{sp}} \right)^{1/2} \quad (6-10)$$

Where,  $\gamma$  = activity coefficient

$C$  = concentration [mol/dm<sup>3</sup>]

$K_{sp}$  = solubility product [mol<sup>2</sup>/dm<sup>6</sup>]

Carosso and Pelizzetti [122] used the light transmittance as a mean to measure the induction time for barium sulphate particles, over feed concentrations of  $8 \times 10^{-4}$  to  $8 \times 10^{-3}$  M. Extrapolating beyond the aforementioned experimental concentration range, introduces some degrees of uncertainty in the calculated induction time. Nevertheless, the above correlation (also used more recently [26, 132]) is used here to determine the induction period.

For the experimental conditions adopted here (0.01M initial concentrations), following Bromley's method [179], the activity coefficient is calculated as 0.4068 (see Appendix I). As presented in Table 6-1, the induction time for the experimental conditions adopted here (13.02 ms) is larger than the calculated micromixing times (8.3 – 0.4 ms for 200-1600 rpm). Therefore, micromixing is not likely to have a significant influence on the course of reaction for the experimental conditions considered here. However, as the feed concentration is increased the induction time is reduced (see Table 6-1), and thus micromixing becomes more controlling.

Table 6-1. Induction times

$C_{\text{feed}}$ [M]	$\gamma$	S	Induction time [ms]
0.01	0.4068	388	13.02
0.1	0.15	1430	2.28
1	0.0389	3709	1.04

### 6.7.3 Effect of Residence Time

The insensitivity of the measured conductivity values to the disc rotational speed beyond 800 rpm could be caused by insufficient fluid residence time in the system. The residence time can have a potential impact on the course of reaction only if it is shorter than the reaction time. In this section, an attempt is made to quantify the reaction time characteristics of the barium sulphate precipitation process, which will in turn allow the determination of the potential effects of the residence time.

The theoretical fluid residence times in the SDR corresponding to the experimental conditions investigated here, are plotted in Figure 6-23 (see Equation 2-4). Note that the conductivity probe is situated downstream of the SDR, thus the fluid residence time within the system before a measurement is made, tends to be longer than the values presented here, because of the transport lags.

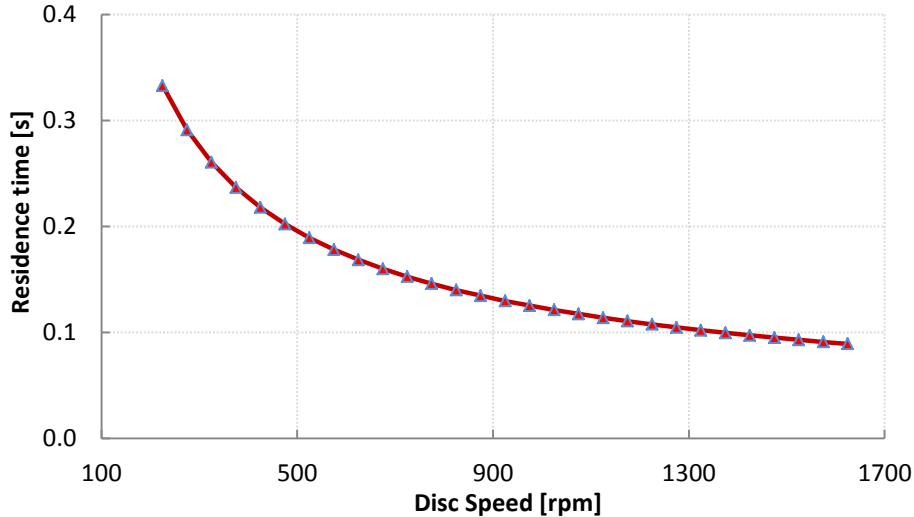


Figure 6-23. Residence time at various disc rotational speeds  
[flowrate:10ml/s, kinematic viscosity: $10^{-6}\text{m}^2/\text{s}$ ]

The reaction time required to achieve a specific conversion may be used to evaluate the potential effects of residence time on the course of precipitation. Öncül et al. [118] developed a direct solution of the barium sulphate moment equations, which predicts the concentration profiles of the chemical species within a homogeneous reaction zone, with respect to time. The analytical solution is zero-dimensional in space and may be used to estimate the characteristic time scales of the reaction. The resulting ordinary differential equation is fourth order and still too complex to be solved analytically (see Appendix J).

In the present study, the model developed by Öncül et al. [118] is solved in Simulink enabling the estimation of semi-analytical concentration profiles of the chemical species. The numerical simulations were found to be very stiff, therefore a fixed step ODE solver with an appropriate step size must be used. The fixed step size should be selected in proportion to the value of the supersaturation ratio,  $S$ . For large values of  $S$  which result in very fast reaction rates, extremely small time step increments are required to ensure accurate results are obtained. The concentration profiles for the reacting ions and the product, using activity coefficient of 0.4068, are presented in Figure 6-24.

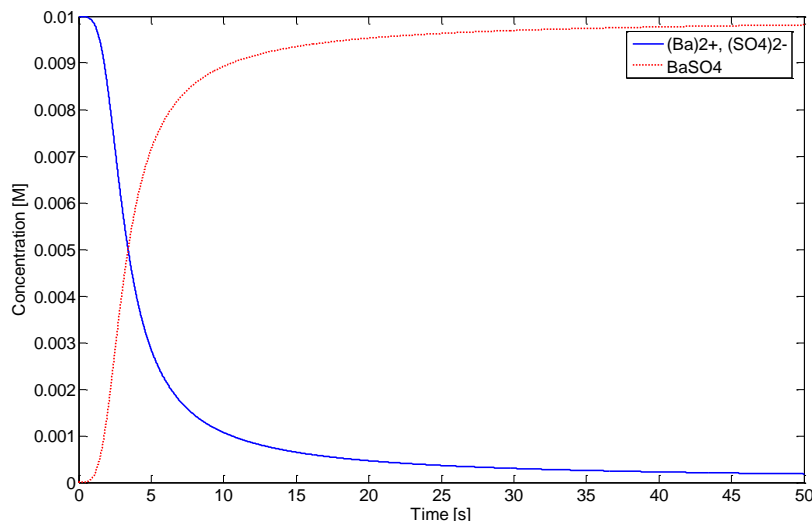


Figure 6-24. Concentration versus time



The concentration curves show that the reaction rate for the initial conditions applied here is rather slow. Thus, it takes more than 18 seconds to reach a 95% conversion, indicating that the residence time on the disc could potentially impact the chemical conversion for the current experimental conditions, as the residence time on the disc is shorter than the reaction characteristic times.

Table 6-2. Chemical conversion times

$C_{\text{feed}}$ [M]	$\gamma$	S	Time at 50% conversion	Time at 95% conversion
0.01	0.4068	388	3.41s	18.49s
0.1	0.15	1430	0.2s	1.2s
1	0.0389	3709	5.4ms	30.5ms

However, as outlined in Table 6-2, increasing the initial feed concentrations results in drastic reductions of the reaction time constants. It can be seen that for initial feed concentration of 1M, the time required to achieve a 95% conversion is reduced to 30.5ms. The reaction times for feed concentrations of 1M are clearly much shorter than the residence times on the disc. Therefore, at higher initial concentrations which result in larger supersaturation ratios, the reaction rates are extremely fast, and thus, independent of the residence times on the disc. For successful control of such processes, the controller should take appropriate actions based on the operating region and whether the process is controlled by residence time or mixing, or a combination of both. Disturbances in the feed flowrate or concentrations as well as changes in the disc speed or temperature could potentially result in moving from one operating region to another. Therefore, advanced control algorithms may be required to account for such complex behaviour.

The general trend of the conductivity versus disc rotational speed data presented in this chapter indicates that the rate of reaction is increased with increasing disc rotational speed, characterised by a drop in the effluent conductivity level. However, there are also indications that, beyond a certain point, the reaction becomes insensitive to the disc speed. Assuming that the general kinetic model and the correlation for the induction time used here to analyse the results are accurate and applicable to the SDR, the following remarks can be made. The micromixing time is shorter than the induction time for the tested conditions. Therefore, the process is not likely to be affected by micromixing. Therefore, the observed enhancement in the reaction rate with increasing rotational speed may be attributed to the enhanced mixing intensity due to the formation of surface waves (mesomixing). The effect of disc rotational speed on surface characteristics of thin liquid films and thus the corresponding impact on heat transfer performance will be investigated in the next chapter. On the other hand, the residence times on the disc are shorter than the reaction time for the tested feed concentration. Hence, it is possible that kinetic limitations, controlled by the residence time, could also have an influence on the extent of reaction. Therefore, the insensitivity of the conductivity data to the disc speed beyond a certain value may well be due to insufficient residence time on the disc

and/or the reduction of surface waves as very thin liquid films with no surface waves might prevail.

## 6.8 Summary

This chapter presented the experimental results on achieving a feedback control task by exploiting the disc rotational speed as the manipulated variable. The example process used to carry out the investigations was precipitation of barium sulphate from aqueous solutions of barium chloride and sodium sulphate, whereby the conductivity of the effluent stream was the controlled variable. The input-output model of the system, which exhibited nonlinear behaviour and large time delays, was used to obtain the initial controller parameters via the direct synthesis method. The PI controller settings were fine-tuned and an optimum DO filter time constant was obtained experimentally.

The setpoint tracking performances of the control loops with and without DO were adequate to demonstrate the potential of using the disc rotational speed as the manipulated variable. The addition of the DO scheme improved the control performance by suppressing the dampening oscillations observed without the DO in place. There is scope for further improvement of the control performance by reducing the measurement noise in the conductivity signal and by fine tuning the controller parameters further.

The repeatability analysis of the conductivity versus disc rotational speed showed that even minor variations in the feed concentration can potentially lead to significant consequences. Since the process gain of the system is very small, small changes in the feed concentration may lead to failure of the control task due to the saturation of the controller output in an attempt to compensate for such variations (disturbances). The effect of precipitate build up in the system on control of the process and reproducibility of the data was also discussed.

Analysis of the experimental data led to the conclusion that the rate of the precipitation reaction increases with increasing disc rotational speed, represented by reduction of the effluent stream conductivity, due to the enhanced mesomixing within the liquid film. However, beyond a certain disc speed, the reaction rate becomes insensitive to the disc rotations speed. This is attributed to insufficient residence time on the disc and/or the reduction of the degree of mesomixing within the liquid films as very thin films without waves may be produced.

The above concluding statements are only relevant for the dilute (0.01M) feed solutions used here; at higher concentrations it is predicted that the kinetic limitations are overcome as the reaction proceeds at a faster rate and thus the residence time is unlikely to limit the extent of the reaction. Meanwhile, as the reaction times are extremely fast, micromixing becomes the dominant mechanism. This in theory, should lead to a steady increase in conversion, as the micromixing time reduces with increasing disc speed.

To achieve a given control task in SDRs, it is essential to first develop a comprehensive understanding of the relationship between the manipulated variable and the controlled parameter. It is also required to account for the interaction of different operating parameters

which define the hydrodynamics of the thin liquid films. Depending on the complexity of the system more advanced control schemes may have to be employed to achieve a satisfactory control performance.

Based on the results presented in this chapter it is envisaged that extremely thin liquid films with a smooth surface may be formed beyond a certain disc speed. Furthermore, it is also known that the actual temperature profiles across the thin liquid films could significantly influence the rate of reaction for many processes, and hence the intensification capability of the SDRs. Therefore, the temperature profiles across the liquid films as well as the presence of surface instabilities and the flow regimes may need to be accounted for in the control algorithm to achieve the best performance. The results of the investigations into temperature profiles of thin liquid films as well as film hydrodynamics using an infrared camera are presented in the next chapter.

## ***Chapter 7. Thermographic Studies***

The literature available on the complex thin film flow characteristics, including both experimental and modelling studies, is plentiful e.g. [10-14, 62]. The heat transfer from a rotating surface to thin liquid films has also been studied previously [15, 16, 177]. This chapter makes a new contribution to the subject by employing a novel approach involving an Infrared (IR) camera to study the hydrodynamics and heat transfer characteristics of thin liquid films. The adopted method is particularly interesting as the interdependency of thin film flow regime and the heat transfer capability from the disc to the liquid film is highlighted visually in images that reveal striking characteristics of the film.

It is known that the film hydrodynamic and thus the heat/mass transfer characteristics are strongly dependent on the liquid flowrate, disc rotational speed and physical properties of the processing fluids. Furthermore, the surface characteristics of the rotating disc and the feed distribution design are also expected to have a strong influence on the thin film flow and the formation of surface instabilities. Thus, the film hydrodynamic characteristics may be considered unique to the SDR design and operating conditions. The film flow regime together with the type and intensity of surface waves are important considerations in most applications of thin film flow. Hence, it is essential to characterise the process intensifying features of thin film flow for a particular SDR and for the process under investigation.

Boiarkina et al. [59] carried out such investigations and showed that the wave regimes do not impact the rate of reaction in the photocatalytic degradation of methylene blue in a SDR. However, the authors reported a distinct shift in the reaction order, and thus conversion, at specific operating regions. This effect was attributed to the presence of mass transfer limitations at some operating regions (feed flowrates: 5, 10, 20 ml/s, disc rotational speeds: 50, 100, 200 rpm) which resulted in lower conversions and pseudo-second order reaction rate. On the other hand, the mass transfer limitations were thought to have been removed at other operating regions (feed flowrate = 15 ml/s, disc rotational speeds = 100, 200 rpm), wherein higher conversions matching a pseudo first order reaction kinetics were observed. In the present work, concerning a neutralisation and a precipitation reaction, it was also observed that the process behaviour varies in different operating regions, as presented and discussed in Chapters 5 and 6. Thermographic analysis of the liquid films may provide explanations for the previously observed process behaviours in terms of the physical effects brought about by the film dynamics within the operation envelope.

This chapter presents the results and discussion of the thermographic investigations. The design of experiments which includes a range of operating conditions for four types of processing fluids was outlined in Chapter 4. The accuracy of the thermographic measurements is directly dependent on how accurately the input parameters were estimated, of which the object's emissivity is the most important factor. The evaluation of the input parameters and the corresponding levels of uncertainty were also discussed in Chapter 4.

The liquid film hydrodynamics at various operating conditions are studied by means of visual inspection of the IR images. The thermograms also provide a platform for qualitative analysis of the liquid film temperature profiles. Furthermore, the liquid film temperatures across the disc may be obtained using the ‘line’ tool in the ThermaCAM software drawn from the disc centre to the disc periphery, which enables quantitative analysis of temperature profiles across the liquid films. The effect of flowrate, disc rotational speed, disc temperature, feed configuration, film viscosity and heat of reaction are investigated in the present study.

Finally the measured temperature profiles by the IR camera are compared to a theoretical model. The physical properties required to estimate the theoretical temperature profile are evaluated at an average temperature calculated on the basis of  $\frac{1}{2}$  (disc temperature + liquid feed temperature). The physical properties of Therminol SP are provided by the manufacturer, as shown in Appendix K, whilst the physical properties of water were obtained from NIST Chemistry WebBook [180]. The main effect plots presented in this chapter include the results of the experimental data using the full factorial design of experiments outlined in Table 4-3.

## 7.1 Effect of Flowrate and Rotational Speed

This section presents the results and discussion of the investigations into the effects of feed flowrate and disc rotational speed on film hydrodynamics and temperature profiles. The tests are carried out for two processing fluids (water and Therminol SP) which have different properties, as shown in Table 7-1.

Table 7-1. Physical properties at 40°C and 1bar

	Water	Therminol SP
Boiling point [°C]	100	351
Density [kg/m <sup>3</sup> ]	992	858
Viscosity [Pa.s]	0.00065	0.0163
Heat capacity [kJ/kg.K]	4.179	1.978
Thermal conductivity [W/m.K]	0.631	0.126
Surface tension [mN/m]	69.6	-

### 7.1.1 Water Films

The thermographic images of water films at various operating conditions, when the disc is at 70°C, are presented in Figure 7-1. The cold feed is heated as the fluid moves towards the disc edges under the action of centrifugal force. As shown in the colour scale bar, black and blue indicate cooler regions of the film while red and orange represent areas with more heat. It should be noted that a thermogram depicts an image of the object based on the amount of infrared radiation received by the camera from various points of the object surface. Therefore, the film flow patterns and the surface waves are only visible in the thermograms if there are variations in the surface temperature of the film as a result of the underlying hydrodynamic characteristics.

The thermograms show that at low rotational speeds, a significant number of large amplitude irregular waves are present on the surface, which decay as the film moves towards

the disc edges. It should be borne in mind that fine wavelets may still exist at radial positions close to the disc edges; whereby the surface temperature variations between the peaks and troughs of the waves are below the precision of thermal imager. At a constant flowrate, as the rotational speed is increased, the surface waves start to shrink towards the disc centre, whereby an increasingly smooth film is formed. The water film was observed to have no waves at the lowest flowrate and the highest disc speed, corresponding to the lowest film thickness. It is expected that thin liquid films which exhibit numerous surface waves provide the best condition for heat and mass transfer [15, 16]. However, the thermograms indicate that the most efficient heat transfer from the disc to the liquid film transpires for the thinnest films with minimal apparent surface waves.

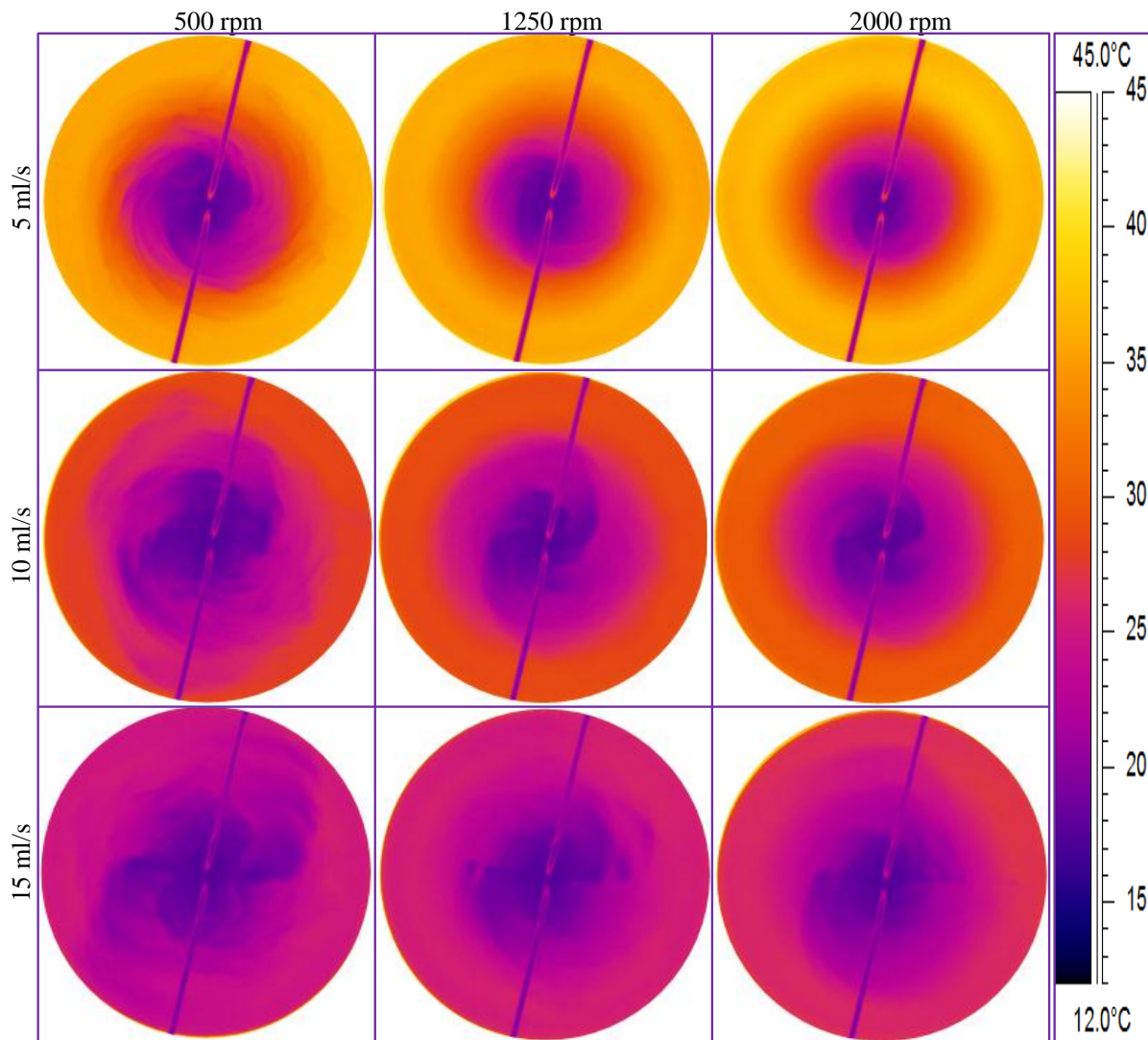


Figure 7-1. Thermograms of water films at various operating conditions  
[Disc temperature = 70° C, feed temperature = 15° C]

The heat and mass transfer coefficients in SDRs may be affected by mixing at two different scales. Theoretically, for the case of heat transfer, it is expected that enhanced mixing (at any scale) within the liquid film leads to augmented transfer of heat from the disc surface to the liquid film. Therefore, even though mesomixing seems to subside at higher rotational speeds, as smooth films are formed, micromixing is expected to increase which

may compensate for the absence of surface waves. Furthermore, the fact that thinner films with reduced conduction paths are produced at higher rotational speeds may make up for the reduced meso scale mixing, and thus lead to an enhancement in heat transfer from the disc to the liquid film.

The reduction in film thickness also means that the diffusion path is reduced, and thus enhanced mass transfer performance should be attained. However, as the rotational speed is increased the surface waves are diminished which implies that mesomixing becomes less significant compared to micromixing. Depending on the kinetics of a given process, this could have a complex impact on the course of reaction, as discussed for precipitation of barium sulphate in the previous chapter.

A faint spiral profile superimposed on the irregular surface waves is also apparent at some operating conditions, most strongly at the lowest flowrate and the lowest rotational speed. This flow pattern which unwinds in the direction of rotation is indicative of the retarding Coriolis forces [61, 181] on the film. The Coriolis force is directed at right angles to both the axis of rotation and the local velocity vector, opposing the displacement of fluid elements in the direction of rotation [182]. In essence, the leading balance on the azimuthal direction is between the viscous and Coriolis forces [183] which can lead to angular slip of the fluid on the disc. According to Emslie [184] the Coriolis force is negligible if the kinematic viscosity of the fluid is greater than the angular velocity multiplied by the square of the film thickness:

$$\nu \gg \omega \delta^2 \quad (7-1)$$

Therefore, the effect of the Coriolis forces, which leads to a spiral flow pattern, becomes less significant as thinner films are produced. At conditions where the spiral flow pattern is strong, it appears that some degree of radial mixing occurs between adjacent annular elements of the processing fluid, resulting in jagged temperature boundaries. This behaviour is more analogous to a stirred tank reactor where backmixing within the fluid elements takes place. However, as the disc rotational speed is increased (particularly at lower flowrates), well defined concentric fluid elements with sharper temperature boundaries are formed which suggests a transition to plug flow regime.

The wave patterns seem to be strongly influenced by the entrance effect of the two liquid jets, particularly at higher flowrates. At film flow of 15 ml/s (2 jets of 7.5ml/s) there is a straight line pattern originating between the feed nozzles, where the two fluid streams come in contact on the disc. This phenomenon is attributed to the high kinetic energy of the impinging jets at high velocities which prevents the liquid feeds from coupling with the rotating disc. The length of the observed streak is reduced at higher rotational speeds. Nevertheless, these flowrates seem to be too high for the current setup, wherein the inlet effects perturb the formation of a uniform film for a large section of the disc.

The thermograms illustrate that increasing the disc rotational speed at a constant flow rate results in a reduction of the cold central region, indicating better disc/film heat transfer performance. This is attributed primarily to reduced film thicknesses and thus reduced conduction paths at high rotational speed and low flowrates. In contrast, increasing the

flowrate at constant disc speed has the opposite effect. The thermograms presented in Figure 7-1 are captured when the disc temperature is at 70°C. The same trials are carried out for disc temperatures of 25 and 50°C. The main effect plots of flowrate and disc rotational speed using the liquid film temperatures at the disc periphery obtained from 27 experimental trials are presented in Figure 7-2. As observed in the thermograms, low liquid flowrates and high disc speeds both enhance the rate of heat transfer from the disc to the liquid film, denoted by the higher final liquid film temperatures. However, the influence of flowrate on the liquid film temperatures is evidently stronger than of the disc speed, for the smooth disc used in the present work.

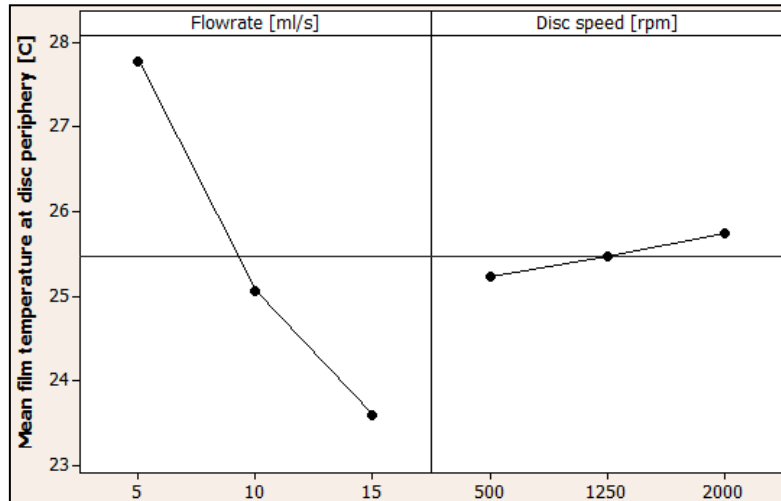


Figure 7-2. Effect of feed flowrate and disc speed on water film temperatures

As previously discussed, the heat transfer from the disc to the liquid film is likely to be influenced by the film thickness and also by the presence of surface waves and film instabilities. The theoretical film thicknesses for the experimental conditions may be calculated using the Nusselt theory. However, this approach assumes a stable liquid film with no shear at the gas-liquid interface and thus no surface waves. It has been shown that the actual film thickness typically tends to be larger than that predicted by the Nusselt model [11, 62] due to the presence of surface waves. Nevertheless, the Nusselt model provides a reasonable basis for studying the liquid film hydrodynamics (see Chapter 2) and is adopted for the analysis of the results in the present chapter.

Figure 7-3 presents the final liquid film temperatures versus the values of film thickness calculated based on the Nusselt model (Equation 2-3). It can be seen that generally higher film temperatures are attained at lower film thicknesses, particularly at higher disc temperatures. However, the experimental data do not fit a consistent trend and the degree of variation in data increases with increasing disc temperature. For instance when the disc is at 70°C, film thicknesses of 18 and 44 $\mu\text{m}$  both result in the same final film temperature. This implies that there are other factors at play which contribute to heat transfer enhancement from the disc to the liquid film.



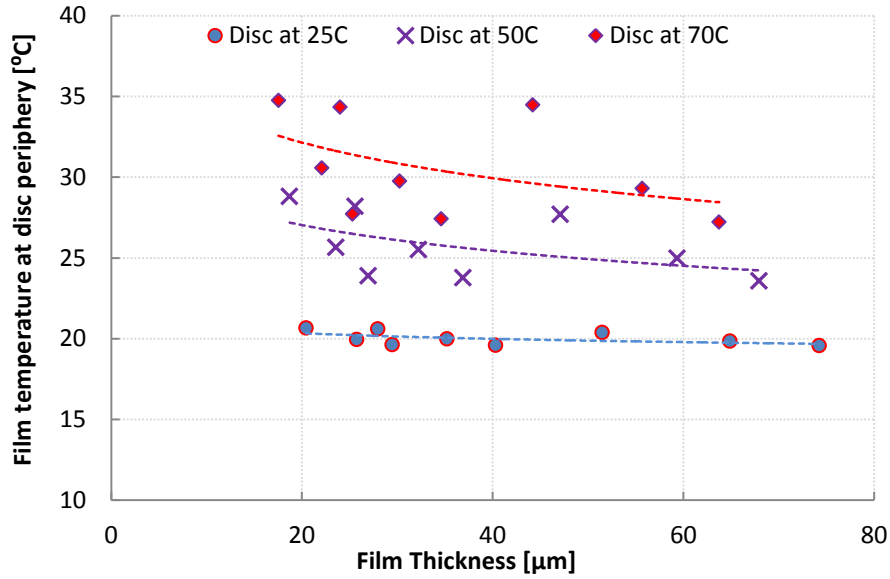


Figure 7-3. Effect of film thickness on water film temperatures

A possible reason for the inconsistency of the experimental film temperature data with respect to the estimated film thickness may be the fact that surface waves are not accounted for in the Nusselt model. Another parameter which could counteract the reduced film thickness is the residence time on the disc. Longer contact time between the liquid film and the disc is expected to increase the amount of heat transferred from the disc to the liquid films. This is confirmed by the general trend observed for the experimental data presented in Figure 7-4. Note that the residence times are also calculated based on the simplified Nusselt model of a fully developed laminar flow (Equation 2-4). As expected, the experimental data do not follow a regular pattern with respect to residence time either, as a result of interactions between different factors and the complex hydrodynamics of thin liquid films.

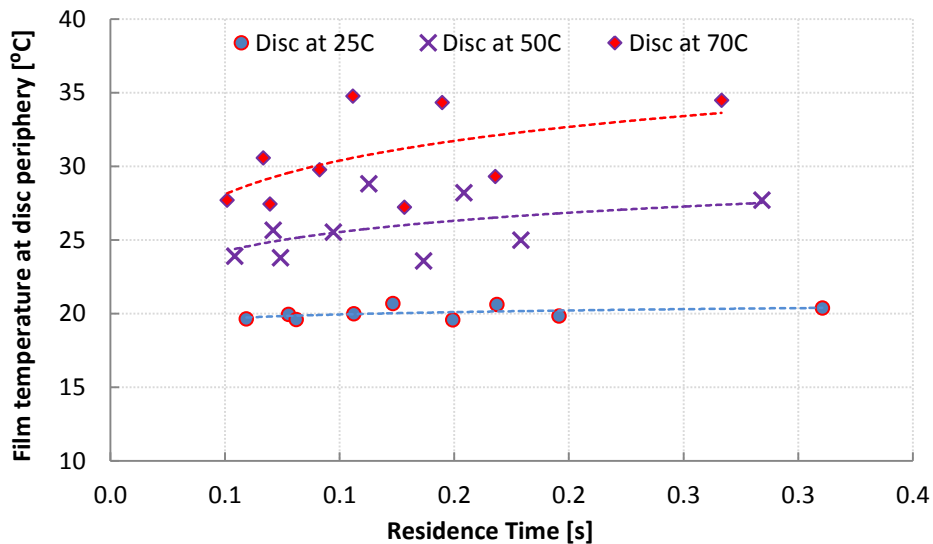


Figure 7-4. Effect of residence time on water film temperatures

Small film thicknesses and long residence times are required to ensure effective transfer of heat from the disc to the liquid film. From the following theoretical relationships it is

evident that changes in the fluid flowrate and disc rotational speed alter both parameters of interest (film thickness and residence time) for effective heat transfer.

$$\delta \propto \frac{Q^{1/3}}{\omega^{2/3}} \quad (7-2)$$

$$t_{res} \propto \left( \frac{1}{\omega Q} \right)^{2/3} \quad (7-3)$$

Where,  $\delta$  = film thickness [m]  
 $Q$  = volumetric flowrate [m<sup>3</sup>/s]  
 $\omega$  = angular velocity [rad/s]  
 $t_{res}$  = average film residence time [s]

Aoune and Ramshaw [16] used the Fourier number (presented below) to assess the extent to which the liquid film is involved in the disc/film heat transfer process. They suggested that the Fourier number,  $F$ , must be greater than 1 to ensure effective penetration and thus effective film involvement.

$$F = \frac{Dt}{\delta^2} \quad (7-4)$$

Where,  $D$  = thermal diffusivity [m<sup>2</sup>/s]  
 $t$  = film surface residence time [s]

The film thickness is evaluated at the mid-radial point, whilst the film surface residence time is taken as two thirds of the average film residence time ( $t_{res}$ ). The thermal diffusivity,  $D$ , can be calculated from the following expression:

$$D = \frac{k}{\rho C_p} \quad (7-5)$$

Where,  $k$  = thermal conductivity [W/mK]  
 $\rho$  = liquid density [kg/m<sup>3</sup>]  
 $C_p$  = heat capacity [J/kgK]

Since the Fourier number accounts for both film thickness and residence time on the disc, it is a more suitable parameter for indirect assessment of the impact of flowrate and rotational speed on the film temperatures. The dependency of the Fourier number on flowrate and disc rotational speed is outlined by the following expression, which is in good agreement with the experimental data presented in Figure 7-2; wherein, the feed flowrate has a stronger effect on the film temperature, and thus the effectiveness of heat transfer from the disc.

$$F \propto \left( \frac{\omega^2}{Q^4} \right)^{1/3} \quad (7-6)$$

The final film temperatures against the values of Fourier number corresponding to each experimental condition are presented in Figure 7-5. The value of Fourier number for a given fluid is increased by extending the liquid's residence time on the disc and/or by producing thinner films. Lower liquid flowrates result in longer residence times and thinner films, which both contribute to larger Fourier numbers and higher heat transfer efficiency from the disc to

the liquid film. However, increasing the rotational speed leads to thinner films on the disc at the expense of reduced residence times. Nevertheless, as the Fourier number is more strongly dependent on the film thickness than the residence time, it can be stated that lower flowrates and higher disc rotational speed contribute to larger Fourier numbers and in turn more effective heat penetration through the liquid film.

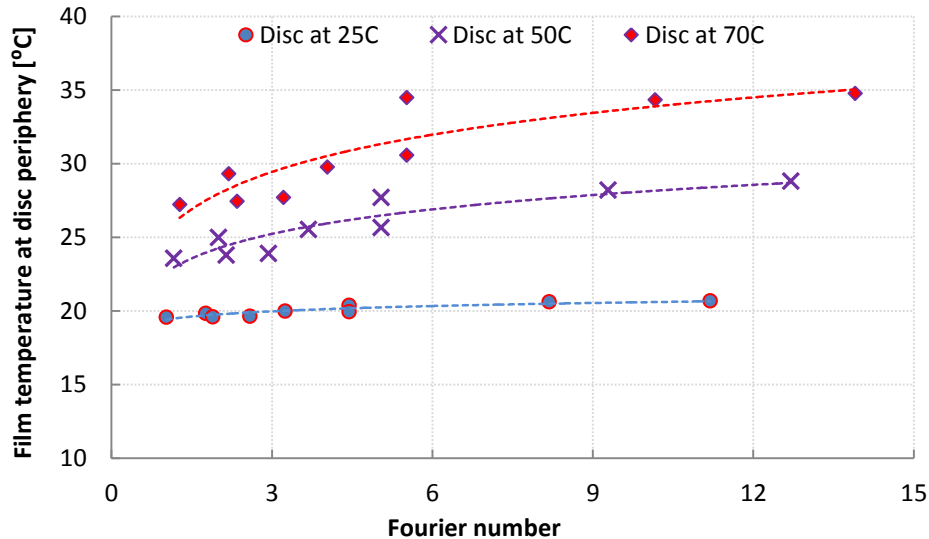


Figure 7-5. Water film temperatures versus Fourier number

The experimental data follow a more consistent trend with increasing Fourier number compared to the cases of film thickness and residence time considered separately. However, some data points still do not fit the general trend closely. This discrepancy may be greatly reduced if the wave induced intensification aspects of the thin film flow could be quantified and included in the calculations. This is, unfortunately, outside the scope of the present study.

### 7.1.2 Therminol SP Films

It was envisaged that some heat might be lost from the water films due to evaporation since the SDR could not be enclosed for the thermal imaging runs. Therefore, it was decided to repeat the trials with a processing fluid which has a higher boiling point to minimise the possibility of heat loss via evaporation. Therefore, the trials were repeated using Therminol SP as the processing fluid. However, as presented in Table 7-1 the two processing fluids have different physical and thermal properties. Furthermore, there is a larger degree of uncertainty associated with emissivity of Therminol SP films than water, as discussed in Chapter 4. Therefore, the differences in the measured temperatures could not be isolated to the effect of heat of evaporation. Nevertheless, repeating the runs with oil as processing fluid serves as a platform for comparison of the trends observed for water films. The thermograms of thin oil films when the disc temperature is maintained at 70°C are presented in Figure 7-6. Generally, higher film temperatures are achieved when Therminol SP is used as the processing fluid compared to water for the same conditions. The potential underlying reasons for this are discussed in Section 7.6.

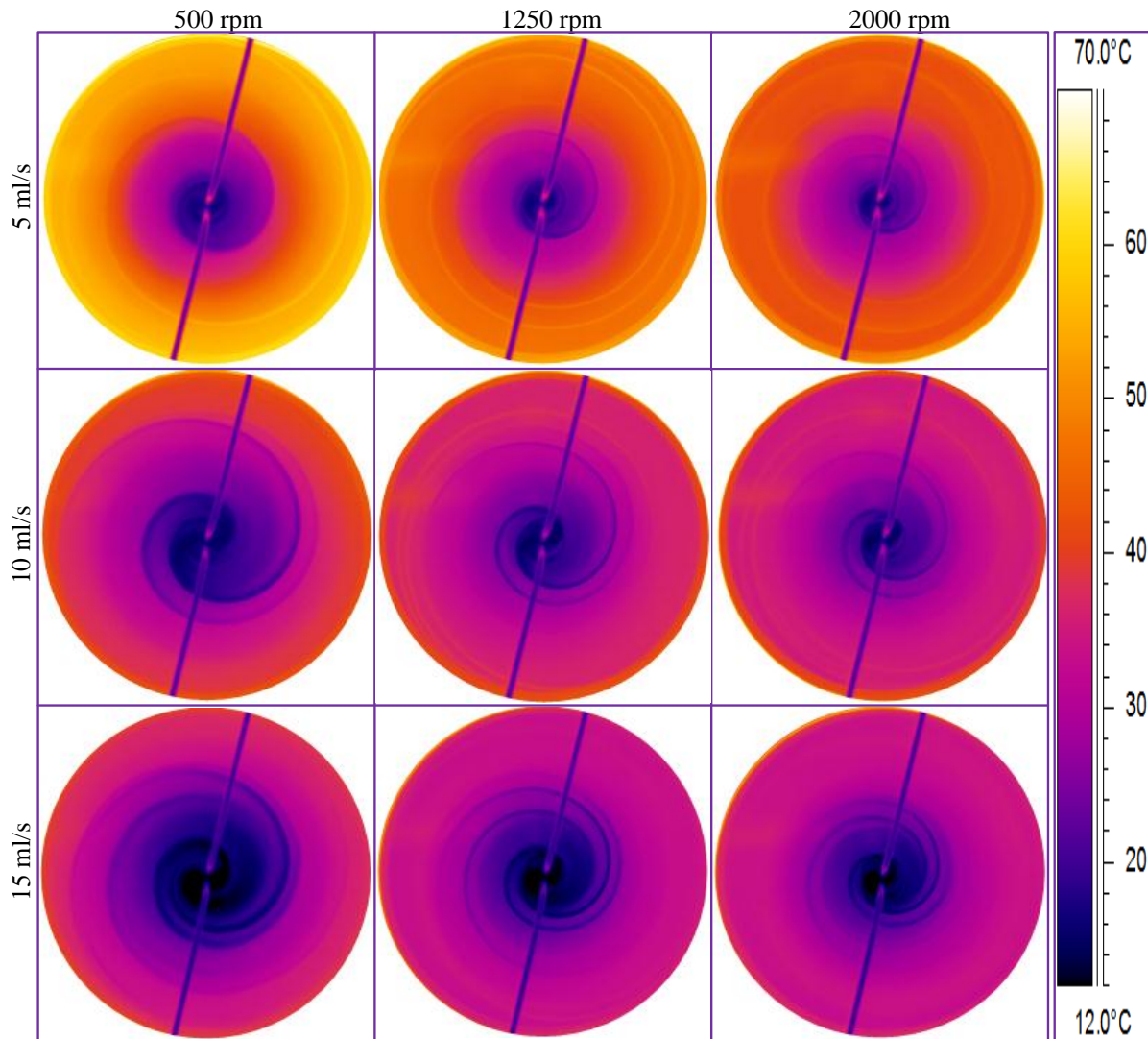


Figure 7-6. Thermograms of Therminol films at various operating conditions  
[Disc temperature = 70° C, feed temperature = 15° C]

It is observed that the flow regimes and wave patterns significantly differ from those observed for water films, whereby the more radial flow path is replaced by spiral fronts which unwind in the direction of disc rotation. The stark differences in the flow and wave characteristics are mainly attributed to the differences in the viscosity of the two processing fluids. This is confirmed by studying the effect of film viscosity by means of adding glycerol to water, as will be discussed in the next section. The surface of the spiral flow path appears to be at a markedly lower temperature compared to the neighbouring segments of the film.

The thermograms show that the cold central region of the film is contracted by increasing the disc rotational speed and reducing the fluid flowrate which leads to enhanced heat transfer from the disc to the liquid, similar to that observed for water films. For the Therminol films, 5 flowrates ranging between 1-20 ml/s were examined at 3 rotational speeds of 500, 1250 and 2000 rpm, whilst the disc temperature was set to 25, 70 or 100°C. The main effect plots of flowrate and disc speed across the spectrum of the experimental conditions (Figure 7-7) show that the effect of film flowrate on the measured temperatures is much stronger than that of the disc speed, a finding which was also applicable to the water system. However, for the case of

water films, the film temperature increased slightly with increasing disc speed. Conversely, the Therminol film temperature slightly decreases with increasing disc rotational speed. Nevertheless, the differences between the average data points at various rotational speeds are very small and thus the film temperature could be considered insensitive to the disc rotational speed.

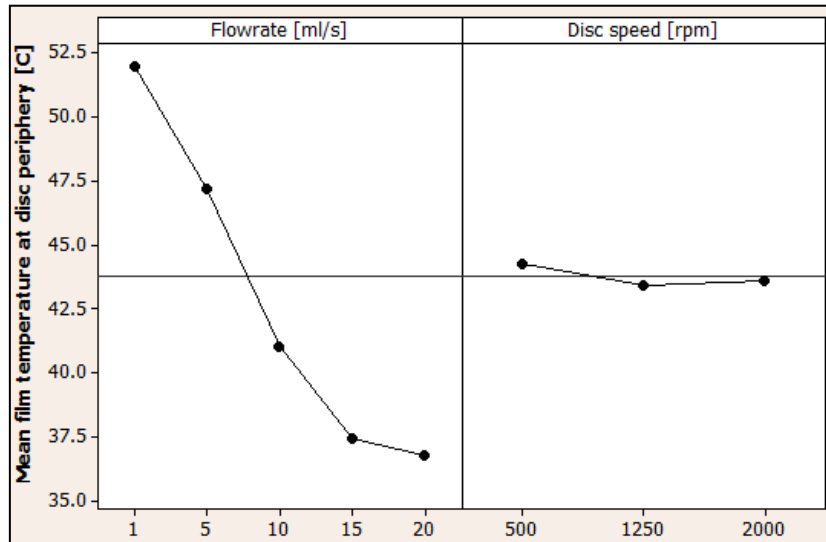


Figure 7-7. Effect of feed flowrate and disc speed on Therminol film temperatures

The measured film temperatures are analysed using the same approach adopted for water films, discussed in the previous section. Plotting the film temperatures at the disc periphery against the calculated film thicknesses (Figure 7-8) and residence times (Figure 7-9) reveals similar trends to those observed for water films. Thus, thinner films and longer residence times lead to the most efficient heat transfer from the disc to the liquid film and thus the highest final film temperatures. However, as observed for the water films, the data points deviate significantly from the general trends when film thickness and residence time are considered separately, due to the counteraction of the two parameters when flowrate and disc speed are adjusted.

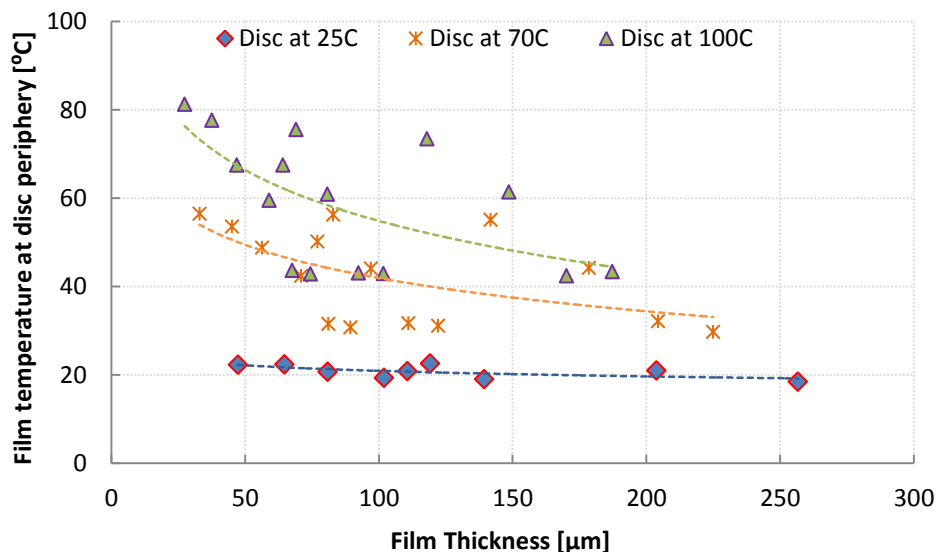


Figure 7-8. Effect of film thickness on Therminol film temperatures

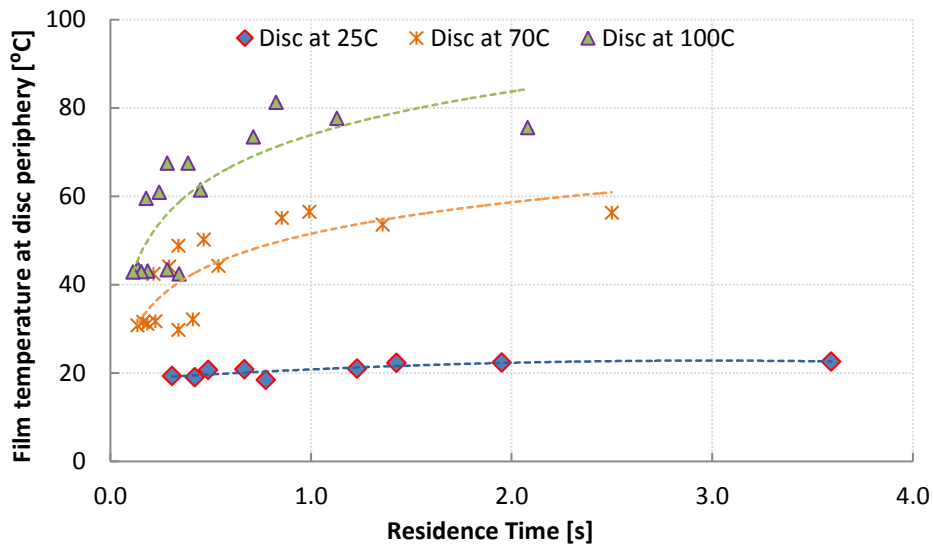


Figure 7-9. Effect of residence time on Therminol film temperatures

Figure 7-10 illustrates the relationship between the measured film temperatures and the calculated Fourier number. As expected, typically higher film temperatures are attained at larger Fourier numbers. However, similar to the case of water films, there are some data points which fall outside the general trend, implying that other factors such as the contribution of surface waves may need to be accounted for.

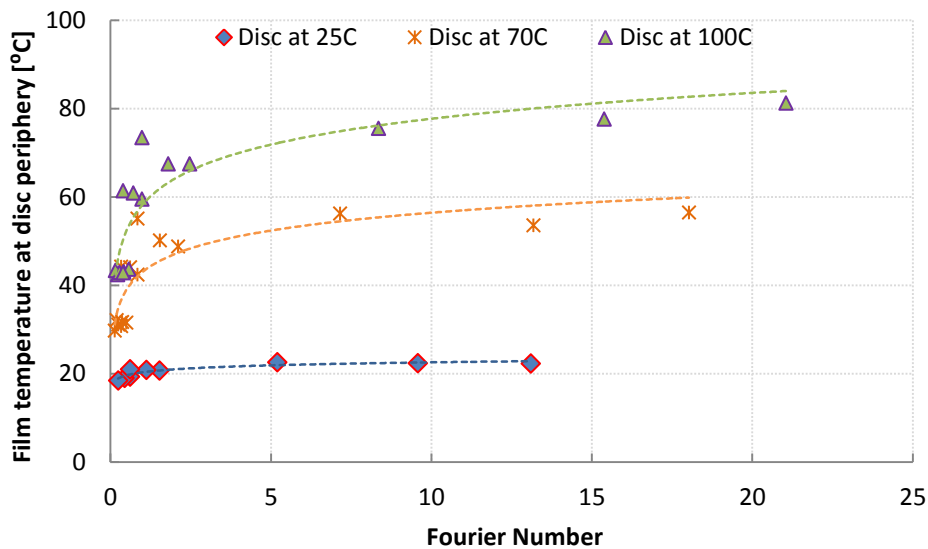


Figure 7-10. Therminol film temperatures versus Fourier number

## 7.2 Effect of Viscosity

A comparison between the thermograms of water and Therminol presented in the previous section led to the postulation that the stark differences observed in the flow patterns and wave characteristics are due to the viscosity of the processing films. Thus, it was decided to investigate the effect of viscosity by adding glycerol to water (50/50 volume ratio) to enable a comparison of the resulting flow regimes with that of pure water. Glycerol has a

density of  $1.26 \text{ g/cm}^3$ , thus mixing equal volumetric amounts of water and glycerol leads to a 56% glycerol by weight solution. The viscosity values for water [173] and 56 Wt.% aqueous solution of glycerol [185] at various temperatures are presented in Figure 7-11. Note that the values for the glycerol and water mixture were obtained by linear interpolation of the literature data available for 50 and 60 Wt. % glycerol solutions.

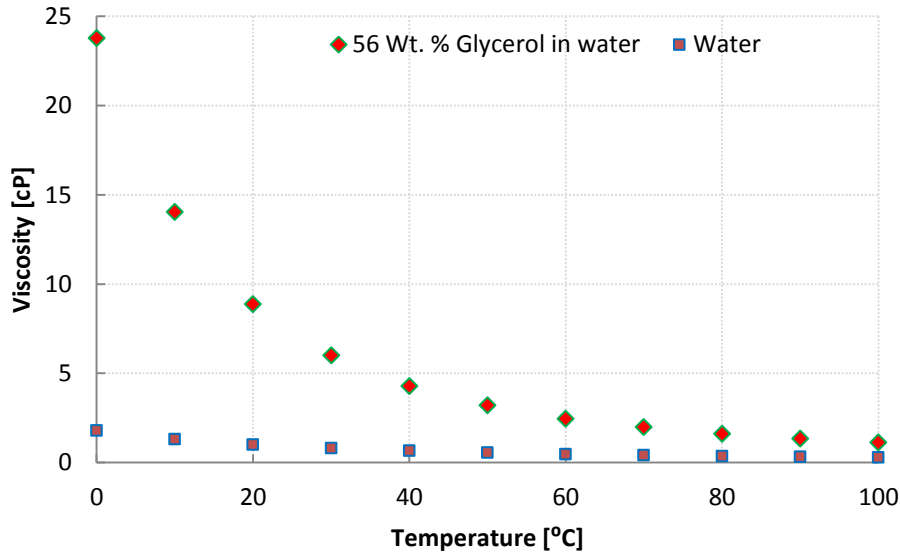


Figure 7-11. Viscosity versus temperature data

Figure 7-11 shows that the viscosity of the tested glycerol solution at  $20^\circ\text{C}$  is higher than that of water by a factor of 8, however, the difference between the data sets are reduced as the fluid temperature is increased. The addition of glycerol to water enables investigations of the effect of viscosity on the film flow regime. However, the surface tension of the processing film, which is also known to have a strong influence on film hydrodynamics [11], is also altered by the addition of glycerol. The values of surface tension for a 56 Wt. % glycerol solution are obtained by linear interpolation of the literature data [185] for 39.31 and 61.44 Wt.% mixtures. Comparing the resulting values with that of pure water [173] (see Figure 7-12) shows that the magnitude of surface tension is reduced by 5% at  $30^\circ\text{C}$  by addition of glycerol to water. Based on the pattern of the presented data, larger reductions in the surface tension are expected at the feed temperature of approximately  $15^\circ\text{C}$ .

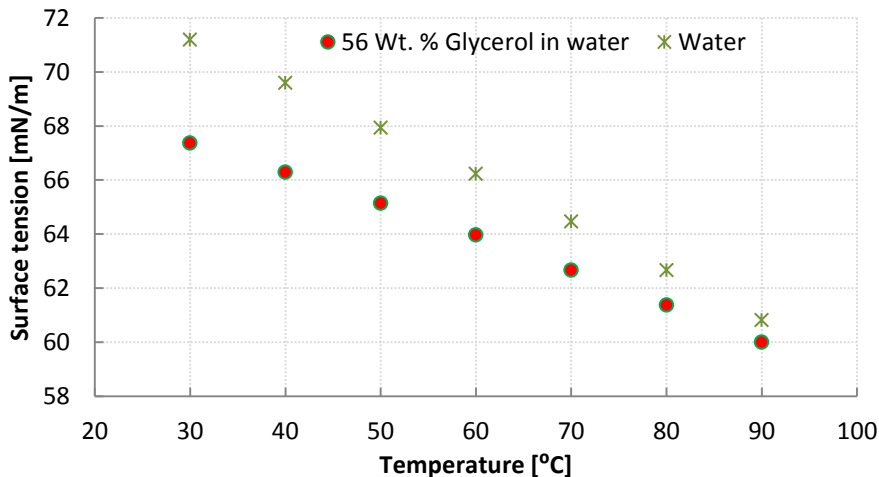


Figure 7-12. Surface tension versus temperature data

The experimental work of Charwat et al. [11] suggested that thin water films become completely stable and exhibit no surface waves, if the apparent surface tension is reduced below 57 mN/m by means of surface active agents. The threshold value of surface tension, below which the film surface instabilities are completely suppressed, may be different from the quoted empirical value for the present experimental setup and conditions. However, considering that changes in the surface tension properties, as a result of the addition of glycerol, are relatively small and the surface tension is above the available guideline of 57 mN/m, it is safe to assume that the impact of surface tension on film hydrodynamics are negligible for the present system. Therefore, the changes in the flow regimes when pure water and aqueous glycerol processing fluids are used may be attributed solely to differences in film viscosity. For the runs presented in this section, the glycerol/water mixture was delivered to the disc centre using only one feed tube. This was to eliminate the perturbations resulting from the collision of two liquid jets on the disc and to isolate the effect of viscosity on thin film flow.

The thermograms obtained for water and water plus glycerol processing films are presented in Figure 7-13, at two levels of flowrate and disc rotational speed, whilst the disc temperature is set to 70°C. From the thermal images, it is evident that the large amplitude irregular surface waves which are observed for pure water disappear when glycerol is added to the feed. This effect is due to the viscous dampening of surface waves which leads to smoother films being generated. Furthermore, the water films seem to follow a radial flow path from the disc centre towards the disc edges which is in sharp contrast with the spiral flow pattern observed for the case of water and glycerol. As discussed previously, waves on the surface of thin films have been shown to enhance heat transfer in fluids on a rotating disc [15] due to their ability to provide better mixing and greater temperature uniformity in both the axial and radial direction depending on the nature of the waves [11]. In the present work, the absence of the irregular waves on the surface of the viscous fluid is thus seen to result in a clear demarcation in temperature between sections of the film as it spirals out towards the edges, indicating almost no radial mixing occurs. This is in sharp contrast to the relatively greater uniformity in temperatures observed with water.



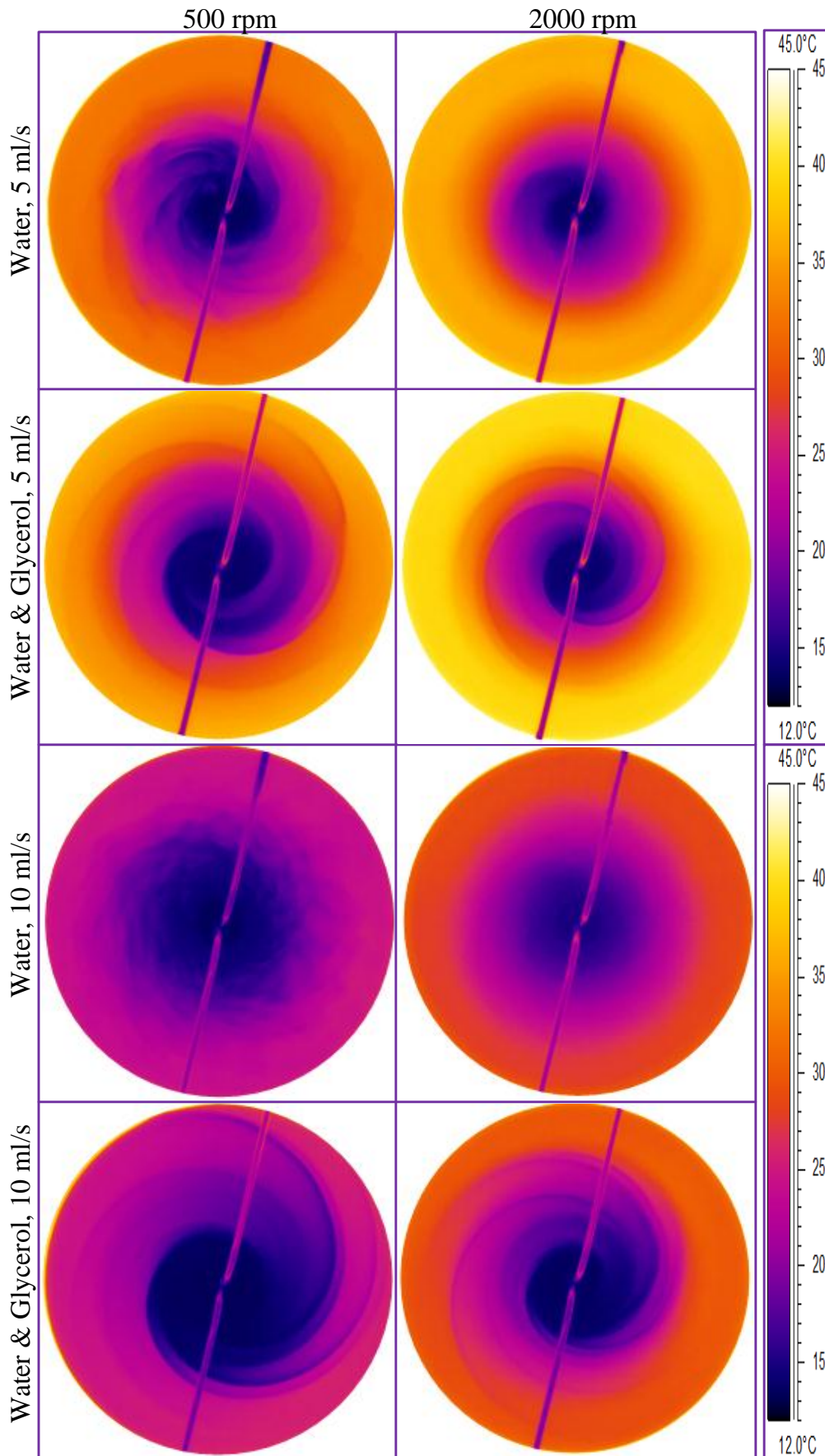


Figure 7-13. Thermograms of water vs. water & Glycerol films  
 [Disc temperature = 70° C, feed temperature = 15° C]

### 7.3 Effect of Disc Temperature

The mean film temperatures measured at the disc periphery across a range of flowrates and disc speeds are plotted against the disc setpoint temperatures for water and Therminol films in Figure 7-14 and Figure 7-15 respectively. The average film temperatures for the case of water and glycerol solutions are not significantly different from that of the water, and thus are not presented here. As expected the disc temperature has a strong effect on the final film temperature in both cases as it governs the driving force for heat transfer from the disc to the liquid films. However, it is noted that the film temperatures are significantly lower than the disc temperatures.

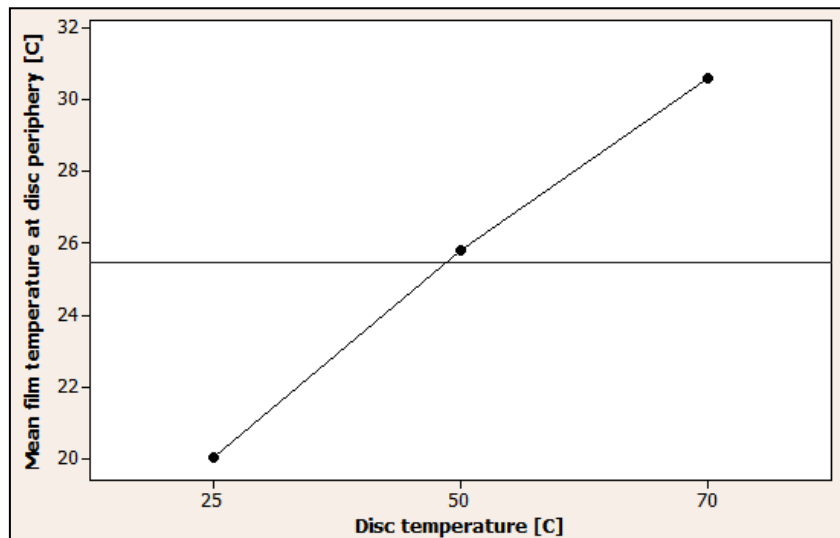


Figure 7-14. Effect of disc temperature on water film temperatures

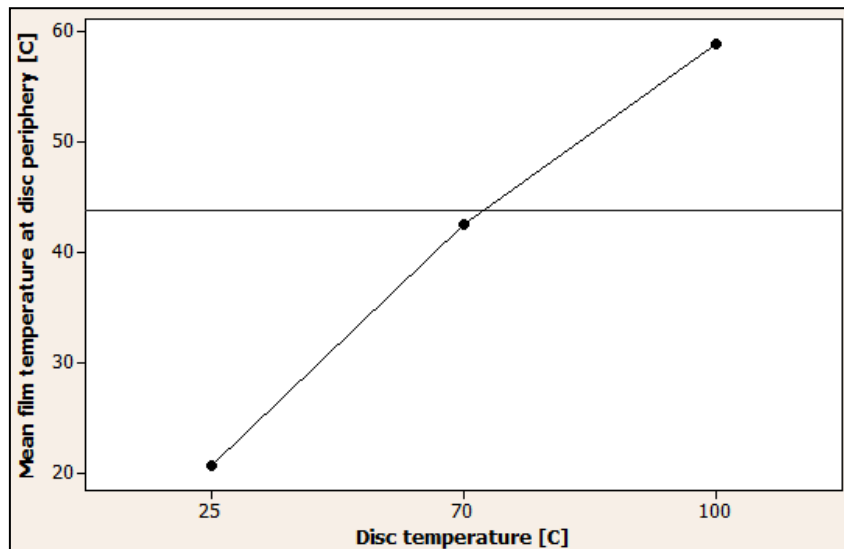


Figure 7-15. Effect of disc temperature on Therminol film temperatures

Note that the film temperature measurements ought to be interpreted with some caution in quantitative analysis of the results, as the data may not accurately reflect the heat transfer capability of the SDR. This is because, as discussed in Chapter 4, the SDR system could not be enclosed, thus the surrounding air was not in equilibrium with the processing fluid. This could result in heat losses from the film to the surrounding air via convection and/or

evaporation. Furthermore, the emissivities of the processing films with varying thicknesses were estimated based on the information available in the literature and the Nusselt model of thin film flow. Therefore, any uncertainties in the estimated object emissivity as well as the rest of the input parameters would directly affect the accuracy of the infrared measurements. Nevertheless, the obtained data provide an effective means for studying the trends and interactions of the operating conditions with the liquid film temperatures. Aside from the impact of uncertainties in the thermographic measurements and the heat losses from the system, the differences between the final temperature of the film and that of the disc are attributed to the operating parameters. The heat transfer from the disc to a given fluid is a strong function of the film flowrate and disc rotational speed, whereby thin films and long residence times are required for effective penetration of heat from the disc through the liquid film, as discussed in the previous sections.

The heat transfer efficiencies averaged across the experimental conditions at a set disc temperature for water and Therminol films are presented in Figure 7-16. Here, the efficiency is defined as the final liquid film temperature divided by the disc temperature. It is noted that the heat transfer efficiency drops for both processing fluids as the disc temperature is increased. It is expected that the rate of heat transfer is increased with increasing disc temperature, since the driving force governed by the difference in temperature of the feed ( $\sim 15^{\circ}\text{C}$ ) and that of the disc becomes larger. However, as the liquid film is heated to higher temperatures the driving force for convective heat loss to the surrounding air is also increased. In addition to the potential for higher heat loss from the liquid film, it is likely that the fluid residence time on the disc is simply too short for the sufficient transfer of heat from the disc to the liquid film required to heat the cold film up to the disc temperature, despite the faster rate of heat transfer.

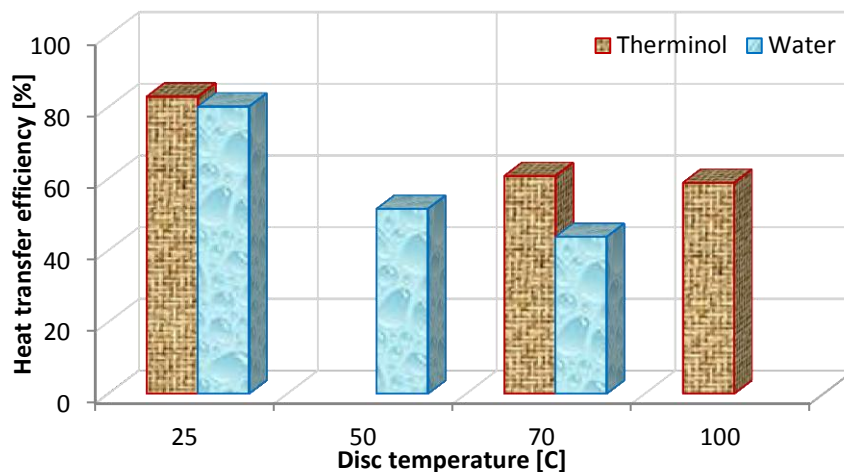


Figure 7-16. Heat transfer efficiency versus disc temperature

## 7.4 Effect of Feed Configuration

As outlined in Chapter 4, two different designs of the feed arrangement (single point injection and distributor system) are employed to deliver the processing fluid to the disc centre and investigate the potential effects of the nozzle design on film hydrodynamics and

temperature profiles. The thermograms of water films obtained at various operating conditions using the two feed configurations are presented in Figure 7-17.

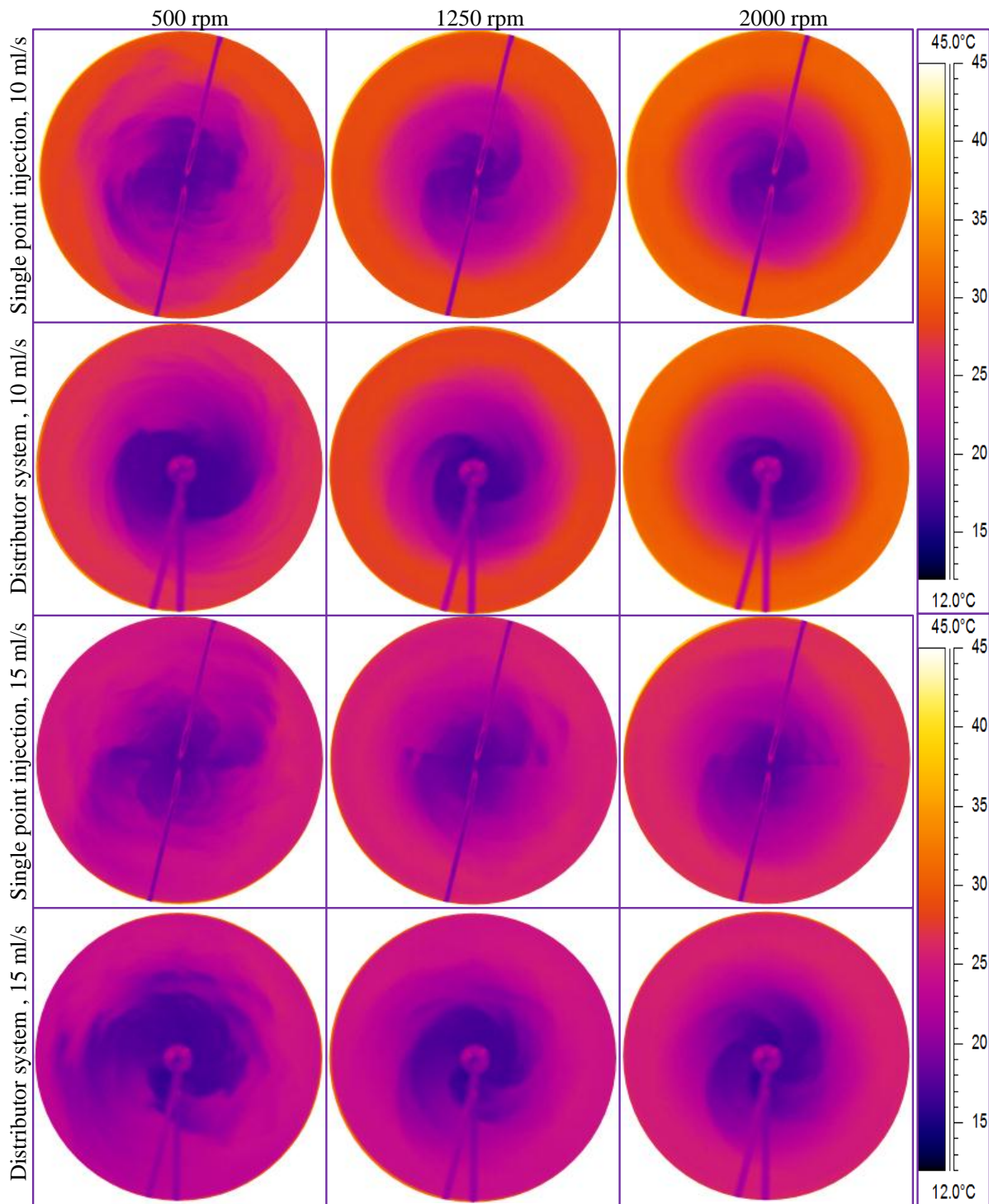


Figure 7-17. Thermograms of water films for two different feed configurations  
[Disc temperature = 70° C, feed temperature = 15° C]

It was found that the distributor system functioned more efficiently at higher flowrates; whereby, below a certain flow rate the liquid flowing through the 0.1 mm annular gap started to merge in with the second stream flowing through the circular pipe inside the annulus, see (Figure 4-8). The thermograms show that the two feed configurations examined here do not

significantly influence the liquid film temperatures. However, the two designs result in slightly different flow patterns and wave characteristics, emphasising the fact that film hydrodynamics may be considered unique to each particular SDR and feed distributor designs. The central cold regions of the film seem to be slightly larger for the case of the distributor system. However, the straight wall of liquid which is formed as a result of collision of the two feed streams at high flowrates (observed with the single point injections) is eliminated by the distributor design. The corresponding thermograms obtained using Therminol as the processing fluid, are presented in Figure 7-18.

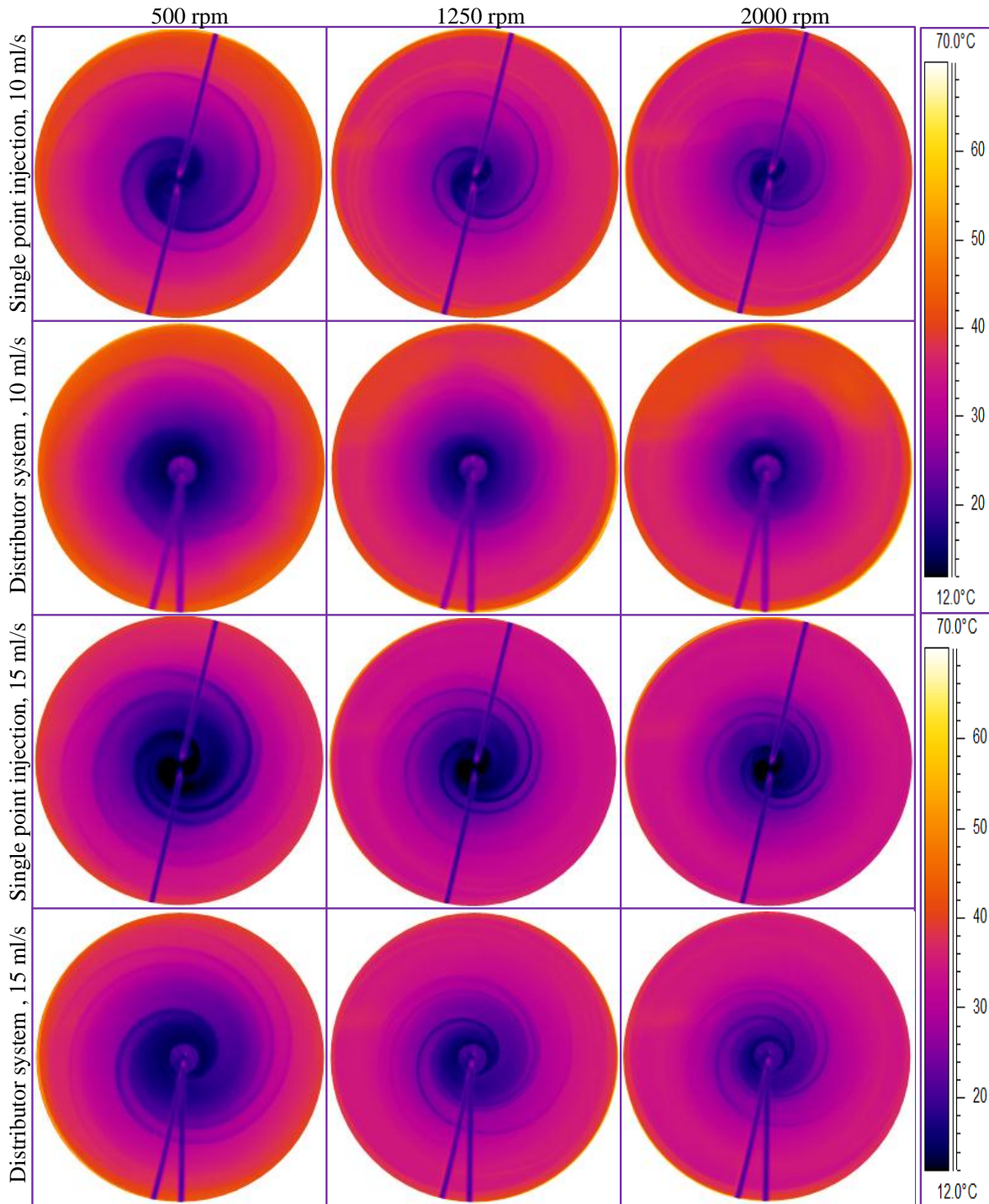


Figure 7-18. Thermograms of Therminol films for two different feed configurations [Disc temperature = 70° C, feed temperature = 15° C]

Once again the two feeding system designs do not lead to a significant difference in the final film temperatures. However, it is evident that the distributor system provides a superior degree of mixing within the Therminol films. The spiral fronts which seem to have a much cooler surface than the rest of the liquid film are more blended in, when the distributor system is used, particularly at flow rate of 10 ml/s. At the higher flowrate of 15ml/s the cold spiral fronts are still visible when the distributor is used; however, the temperature differences between the peak and troughs of the spiral fronts seem to be less pronounced compared to that observed for the case of single point injections.

Overall, the distribution of one of the liquid feeds through an annulus gap seems to provide better mixing conditions within the film, compared to the case of two separate tubular feed pipes. Nevertheless, the improvements in mixing do not yield a notable enhancement in transfer of heat from the disc to the liquid film. The major drawback of the current design of the distributor system is that larger flowrates are required to obtain a continuous flow of liquid through the annulus gap and to prevent the fusion of the two feed streams before they hit the disc. The results confirm that the nozzle design may have a significant impact on the film hydrodynamics and the wave characteristics. A larger variation of the feed delivery system designs, including various tube diameters and different feeding positions should be tested to characterise the effect of nozzle design on thin film flow.

## ***7.5 Effect of Heat of Reaction***

SDRs are commonly regarded as reactor technologies highly suited for carrying out exothermic reactions due to their enhanced heat transfer characteristics. An example neutralisation reaction was carried out to assess the effect of heat of reaction on film temperatures using the IR camera. Aqueous solutions of hydrochloric acid and sodium hydroxide at two concentrations (0.1 and 0.5M) were pumped to the SDR, whilst snapshots of the liquid films were taken by the thermal imager to investigate the effect of heat of reaction on the film temperatures at various operating conditions.

The experimental data were obtained at two levels of feed flowrate, disc temperature and rotational speed. The mean liquid temperatures measured at the disc periphery across the range of the operating conditions are presented in Figure 7-19. It is observed that on average, the films produced from 0.1M solutions of acid and base are approximately 4°C hotter than the water films corresponding to the same operating conditions. On the other hand, the films resulting from 0.5M concentrations of acid and base only show an average 0.5°C increase in the final film temperature compared to the case of 0.1M feed concentration. The amount of heat released by the reaction is a linear function of the feed concentrations. Therefore, at adiabatic conditions the increase in temperature of the liquid films should be proportionate to the feed concentrations. However, the present runs were not conducted under adiabatic conditions as the disc temperature was controlled by an external heat transfer unit and the liquid films were exposed to relatively cold air. The heat transfer to/from the liquid films could explain the observation that the film temperatures do not increase linearly with the feed concentrations.

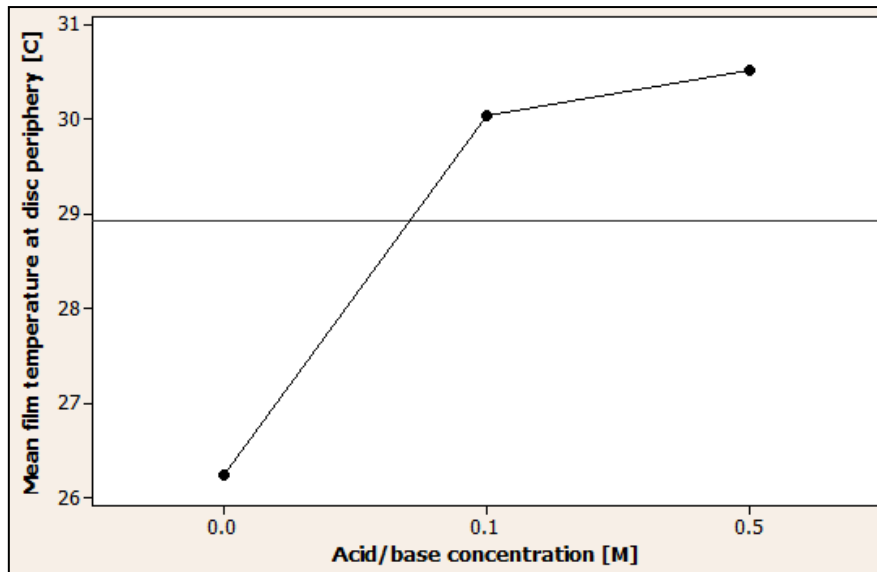


Figure 7-19. Effect of heat of reaction on film temperature

In order to obtain isothermal conditions across the reaction mixture, the heat equivalent to the heat of reaction at the operating temperature must be transferred to or from the system. If the disc and the feed streams are at the same temperature, then upon mixing of the reactants and release of the reaction exotherm, the film temperature is expected to rise above the disc temperature. In that case, the excess heat is absorbed by the disc or lost to the surrounding air.

In the current SDR design, the disc temperature controller adjusts the amount of heat input to the system based on the feedback signal of the thermocouples immersed in the heat transfer fluid flowing underneath the disc. Therefore, the controller maintains the temperature of the heat transfer fluid not the processing film. Hence, the variations in the film temperature as a result of the reaction endotherm/exotherm are unlikely to be picked up by the temperature control system, as the mass of the processing fluid is much smaller than that of the disc and the heat transfer fluid. If the feed streams are at a lower temperature than that of the disc, as is the case here, the liquid film temperature rises due to the heat input from the disc, and also as a result of the reaction exotherm.

For the current SDR design it is unlikely that strictly isothermal conditions can be achieved, particularly in presence of process disturbances. To effectively control the film temperature at a given setpoint with or without the heat of reaction, a more elaborate control scheme is required in which the actual film temperature is used in the feedback temperature control loop, as opposed to the temperature measurements obtained from the disc or the heat transfer fluid flowing underneath the disc. However, direct measurements of the film temperature may not be practical especially in presence of very thin liquid films by means of the commercially available temperature sensors. Therefore, more costly and sophisticated control schemes coupled with unconventional temperature sensors may be required to achieve tight control of the liquid film temperatures.

## 7.6 Comparison with a Theoretical Model

The following mathematical model was developed by Boodhoo [61] to predict the temperature profile in thin liquid films across a rotating disc:

$$T = T_d - \frac{(T_d - T_i)}{\exp\left\{\frac{\pi h}{m C_p} (r^2 - r_i^2)\right\}} \quad (7-7)$$

where,  $C_p$  = specific heat capacity [J/(kg K)]

$h$  = heat transfer coefficient [W/(m<sup>2</sup>K)]

$m$  = liquid mass flowrate [kg/s]

$r$  = radial distance from the disc centre [m]

$r_i$  = radial distance of the inlet from the disc centre [m]

$T$  = film temperature at radial distance  $r$  [K]

$T_d$  = disc temperature (assumed constant) [K]

$T_i$  = inlet film temperature [K]

The derivation of the above equation is based on a constant film heat transfer coefficient,  $h$ , averaged across the disc surface. Further, it is assumed that heat transfer occurs by convection from disc to the liquid film in a direction perpendicular to the disc surface. The temperature variations across the film height are also neglected in the derivation of the model based on the assumption that thin, perfectly mixed liquid films are formed on the disc.

The accuracy of the temperature profile determined from the theoretical model is highly dependent on the value of the film heat transfer coefficient used. A number of previous studies have experimentally determined the average and local heat transfer coefficients on a spinning disk under various operating conditions. Jachuck and Ramshaw [15] measured the average film heat transfer coefficients from a brass disc to thin water films to be between 6 and 11.2 kW/m<sup>2</sup>K for a smooth disc of diameter 360 mm over a range of flowrates and rotational speeds. The results indicated that the heat transfer coefficient depends on both liquid film thickness and surface waves in the liquid film. Generally a thin film with numerous surface ripples should provide the best conditions for heat transfer. Increasing the disc rotational speed produces thinner films; however, beyond a particular value, extremely thin liquid films without any surface waves are produced, which may result in a drop of heat transfer coefficient. Additionally, the results showed that increasing the fluid flowrate generally leads to an increase in the heat transfer coefficients for the range of parameters studied, which is attributed to more waves being formed at higher flowrates which induce more efficient mixing. However, as film thickness increases with increasing flowrate, beyond a certain flowrate the heat transfer coefficient starts to fall. Therefore, to achieve the best heat transfer performance a compromise between film thickness and surface waves may be necessary, which can be achieved by manipulating the rotational speed and feed flowrate.

As discussed in Chapter 2, Aoune and Ramshaw [16] provided a theoretical estimation of the local heat transfer coefficient on the basis of the simple Nusselt theory which is expressed as:



$$h = \frac{5k}{3\delta} \quad (7-8)$$

where,  $k$  and  $\delta$  are thermal conductivity and film thickness respectively. The Nusselt theory has been developed for smooth films and therefore does not take the effect of surface waves into account. Thus it should result in conservative values for water-like liquids which may exhibit numerous surface waves. However, the agreement between the experimental data provided by Aoune and Ramshaw [16] and those predicted based on the Nusselt theory is rather poor. The comparison indicates that the measured local heat transfer coefficients are higher than the Nusselt predictions near the disc centre and at the disc periphery, whilst the Nusselt model over-predicts the heat transfer coefficient for the rest of the disc surface (see Figure 2-5). Comparing the theoretical values of heat transfer coefficient obtained from the above equation with the experimental data reported by Jachuck and Ramshaw [15] also shows an over-prediction of the heat transfer coefficient by the Nusselt model for most cases on a smooth disc. However, at higher viscosities where lower heat transfer performance is obtained, the measured and predicted data show better agreement [16].

In the present work, the average value of heat transfer coefficient across the whole disc surface is initially evaluated using the Nusselt model. However, as the evidence from previous work suggests that the Nusselt model over-predicts the heat transfer coefficient for a large portion of the disc, particularly for water-like fluids at positions away from the disc centre and the disc periphery [16], the theoretical temperature profiles are also estimated based on fractions of the originally calculated heat transfer coefficient. This approach illustrates the contribution of the heat transfer coefficient to the calculated temperature profiles.

Figure 7-20 and Figure 7-21 show the typical temperature profiles of thin water films across the disc, both measured by the IR thermal imager and predicted from the mathematical model, using three different values of the average film heat transfer coefficient. Where,  $x$  denotes the fraction which is used in estimation of the heat transfer coefficient based on the Nusselt theory:

$$h = x \cdot \frac{5k}{3\delta} \quad (7-9)$$

As can be seen, the temperature profiles obtained from the thermographic measurements are significantly lower than those predicted by the theoretical expression if heat transfer coefficient is calculated based on the Nusselt theory ( $x=1$ ). However, the theoretical temperatures match the experimental data more closely when a smaller fraction of the heat transfer coefficient is used to allow for the potential over-estimation of heat transfer coefficient by the Nusselt model.

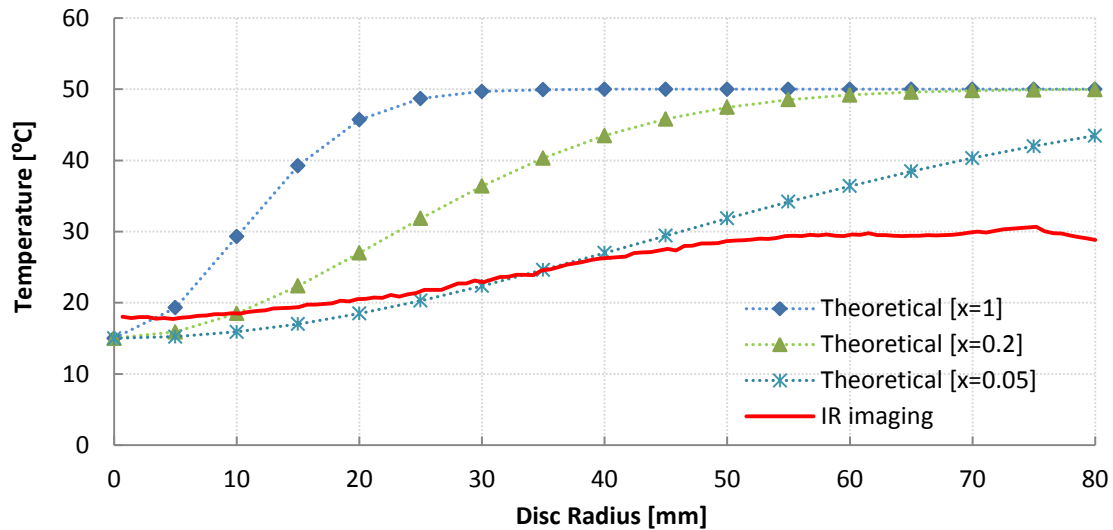


Figure 7-20. Water film temperature profiles  
 $[Q = 5 \text{ ml/s}, N = 2000 \text{ rpm}, T_d = 50^\circ\text{C}, \text{emissivity} = 0.96]$

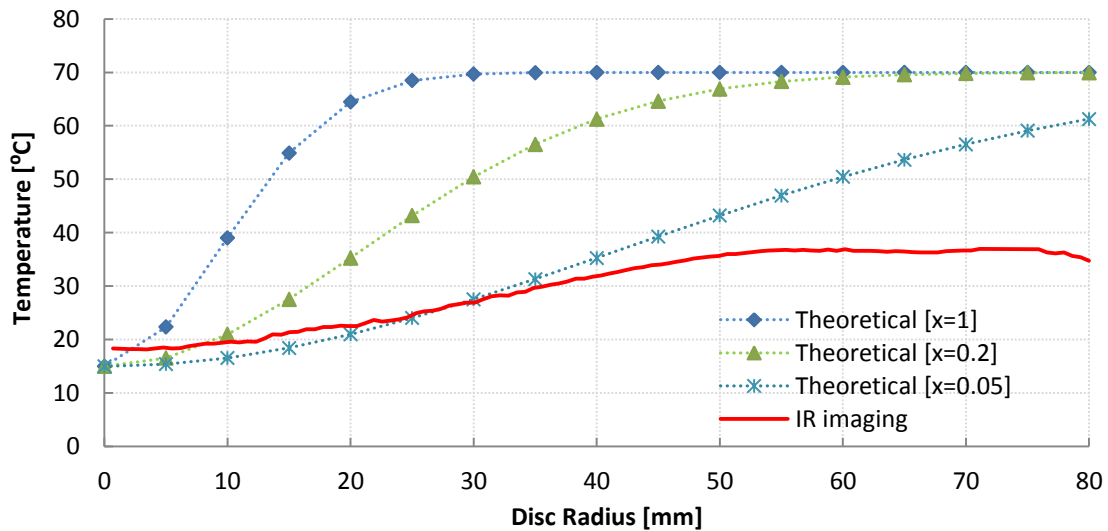


Figure 7-21. Water film temperature profiles  
 $[Q = 5 \text{ ml/s}, N = 2000 \text{ rpm}, T_d = 70^\circ\text{C}, \text{emissivity} = 0.96]$

There are other possible reasons which could account for the mismatch between the thermal imaging temperature data and the predicted temperature profiles. For instance, one of the main assumptions in deriving the temperature profile model is that heat losses to the surroundings are negligible. However, as in this practical setup the liquid film was exposed to relatively cold air at  $20^\circ\text{C}$  and a saturated environment in equilibrium with the liquid film did not exist, the validity of this assumption needs to be verified. Wagner [186] derived an expression for calculating the heat transfer coefficient from a rotating disc to ambient air in case of a laminar boundary layer. Assuming that the same expression is applicable for the case of heat transfer from a liquid film to the surrounding air, the convective heat loss may be estimated. The heat loss due to convection using this approach was found to be less than 3% of the total heat input, which can be considered negligible. This agrees well with Quinn and Cetegen's [65] analysis which revealed that the heat loss due to convection into the air above

the disc was at most 1% of the overall heater power. Furthermore, the assumption of negligible heat loss to the surroundings could also be undermined due to potential evaporation from the liquid film. Quinn and Cetegen [65] have shown that evaporative cooling from the liquid film surface on a rotating disc only has a moderate effect on the Nusselt number magnitude. Nevertheless, this effect should be accounted for in the theoretical model in order to enable a closer comparison between theory and experimental data.

Another assumption in deriving the theoretical model is that the thickness of the film is so small and mixing within the film is so intense that temperature variations across the height of the film are negligible. If this assumption is not valid, the surface of the liquid film which is measured by the IR camera is expected to be at a lower temperature than the liquid layer in contact with the disc. The assumption of constant heat transfer coefficient across the disc is also not strictly correct. Heat transfer coefficient is a function of liquid film thickness which varies across the disc. Using different values of heat transfer coefficient at various radial positions leads to a more complex mathematical model.

The rather large discrepancy between the theoretical and measured film temperatures could be attributed to a combination of factors such as underlying assumptions of the model not being valid in practice, as discussed above, and also errors in measured temperatures due to incorrect emissivity values. Valid comparison between the IR thermographic measurements and a theoretical model may only be possible if uncertainties in evaluation of emissivity of thin films with varying thickness could be removed and also a more vigorous mathematical model is developed which accounts for convective and evaporative heat losses as well as variation of temperature in the axial direction. More importantly, the value of the heat transfer coefficient used to calculate the theoretical temperature profiles needs to be evaluated based on a more accurate model or an empirical correlation.

Figure 7-22 and Figure 7-23 show the theoretical and thermographic temperature profiles in thin oil films across the rotating disc for two typical runs. It can be observed that near the disc centre where the film thickness is high, temperatures estimated by the IR camera are higher than those predicted by the mathematical model. Conversely, towards the disc periphery where the liquid film gets thinner temperatures are under-estimated by the IR camera compared to the theoretical values. This trend was also observed for the water films but the cross-over point was closer to the disc centre.

Since Therminol SP has a high boiling point of 351°C at atmospheric pressure, it is unlikely that any significant amounts of heat could have been lost due to evaporation. This could be one of the contributory factors leading to the observation that the measured film temperatures in Figure 7-22 approach the theoretical profile more closely compared to the case of water (Figure 7-20), under identical conditions of operation of the disc. Furthermore, the heat capacity of Therminol is smaller than that of water by twofold, thus the same heat input should yield a temperature rise twice larger than observed with water (for the same mass of processing fluid). Nevertheless, a discrepancy of 20°C between the theoretical temperatures near the disc edges (based on the Nusselt model prediction of heat transfer coefficient) and the experimentally determined temperatures still remains.

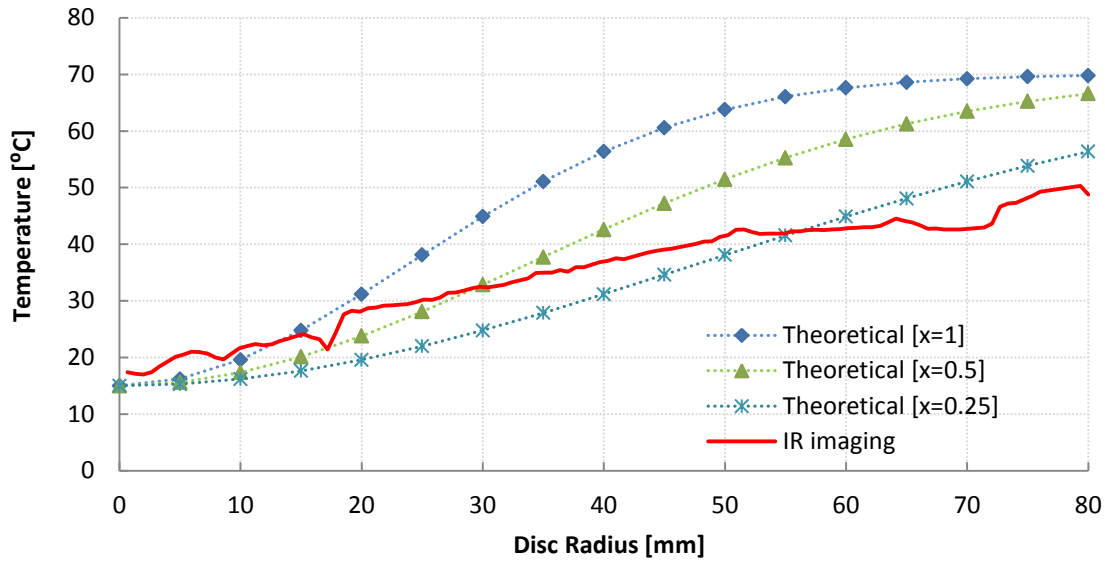


Figure 7-22. Therminol film temperature profiles  
 $[Q = 5 \text{ ml/s}, N = 2000 \text{ rpm}, T_d = 70^\circ\text{C}, \text{emissivity} = 0.65]$

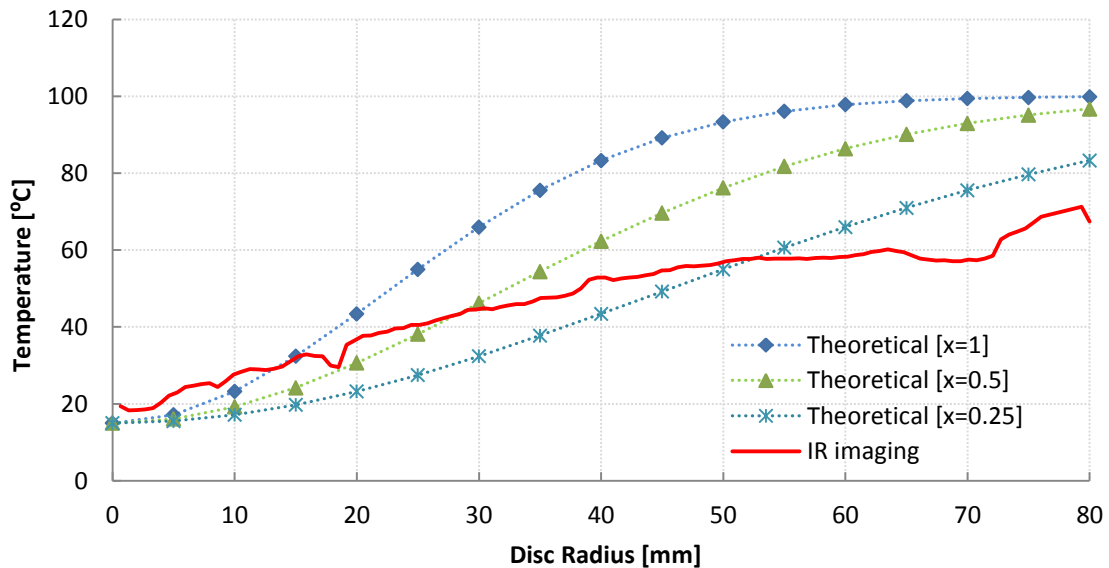


Figure 7-23. Therminol film temperature profiles  
 $[Q = 5 \text{ ml/s}, N = 2000 \text{ rpm}, T_d = 100^\circ\text{C}, \text{emissivity} = 0.59]$

If it can be assumed that the difference between the theoretical and experimental profiles are solely due to the over-prediction of the heat transfer coefficient values, whilst other factors such as uncertainty in the emissivity can be ignored, the experimental data for water films imply that the heat transfer coefficient is over-estimated by at least an order of magnitude using the Nusselt theory. However, the magnitudes of potential over-estimations of the heat transfer coefficient for oil films seem to be much lower than that observed for water films. The observation that at higher viscosities the measured heat transfer performance is in closer agreement with that predicted by the Nusselt model is also reported by Aoune and Ramshasw [16].

## **7.7 Summary**

The thermographic analysis of thin liquid films on a rotating surface across a range of operating conditions provides a useful insight into the flow regimes, hydrodynamic characteristics and the corresponding impact on heat transfer. These parameters strongly influence the intensification aspects of SDRs and may need to be accounted for in the control algorithm to achieve the best performance. The water films exhibit large amplitude surface waves particularly near the disc centre and at low rotational speeds. The sharp temperature boundaries observed at low flowrates and high rotational speeds are indicative of a plug flow regime, where radial dispersion is negligible, whilst some degrees of radial mixing prevailed at lower disc speeds.

More viscous processing fluids (Therminol and aqueous glycerol solution) show vastly different characteristics in terms of film flow path on the rotating disc and the presence of surface waves. The observed differences are attributed to Coriolis forces and viscous dampening of surface wavelets respectively. The results also show that the disc/film heat transfer performance is enhanced as the film thickness is reduced and the fluid residence time on the disc is increased (larger Fourier numbers) at higher disc speeds and/or lower flowrates.

The two tested feed arrangements result in slightly different wave patterns and mixing efficiencies. The effect of heat of reaction on the liquid film temperatures are also investigated by means of thermographic measurements. It is envisaged that a more elaborate temperature control scheme which is based on the actual temperature measurements of the liquid film is required to achieve tight temperature control of the reaction media; whilst, isothermal operation with the current design particularly due to the contributions of the heat of reaction and process disturbances is highly unlikely.

A comparison between a Nusselt-based theoretical temperature profile and the IR temperature measurements show that there are large differences, especially when water is used as the process fluid. This could be due to several factors, the most probable one being the overestimation of the average film heat transfer coefficient using the Nusselt theory of condensation. Furthermore, the temperature measurements obtained in this study are associated with some levels of uncertainty as the true emissivity of the liquid film on the rotating disc, and its dependency on film thickness could not be measured. Additionally, as the liquid film was not in equilibrium with the surrounding environment, the measured temperatures do not reflect the actual disc/film heat transfer capabilities.

It is well established that SDRs provide enhanced heat transfer capabilities attributed to reduced conduction path of thin liquid films and also the presence of numerous surface ripples which promote intense mixing within the film. However, the results presented here suggest that a cold liquid feed flowing onto the centre of the disc may not get up to the disc temperature before it reaches the disc periphery, depending on the operating conditions. Care must be taken when selecting the disc rotational speed and liquid flowrate to ensure effective penetration of heat from the disc through the liquid film, indicated by a high Fourier number, is occurring. Furthermore, the operating conditions should be defined such that the desired thin film flow regime and wave characteristics, which are directly related to intensification

aspects of SDRs, are obtained. The results show that a thermal imager may be employed to provide guidance for specification of the desired operating window, and thus contribute to optimal operation and control of such devices. The thermographic technique may also be adopted as a useful tool in design of SDRs leading to specification of optimum feed distribution system, disc size, disc surface geometry, etc.

## ***Chapter 8. Conclusions and Recommendations***

The previous chapters presented the results and discussion of the simulation/experimental studies concerning control and operation of a spinning disc reactor. The conclusions that may be drawn in light of the present research are summarised in this chapter. The present work has unveiled both challenges and opportunities for control and operation of SDRs. However, some areas deserve more research attention in order to uphold this promising reactor technology as a viable commercial alternative to conventional systems. It is hoped that the conclusions and recommendations for future developments presented in this chapter will promote more research interest in the field of process control for intensified equipment, which in turn should pave the way for greater industrial acceptance of such technologies.

### ***8.1 Conclusions***

The control and operation of a SDR has been studied by means of simulations and experimental investigations. Two processes, namely neutralisation and precipitation, have been used to facilitate the control investigations. Furthermore, thermographic measurements of thin liquid films have been used to study the thin film flow regimes and temperature profiles across the disc, both of which influence the operation and control of SDRs. The conclusions that may be drawn from the present work are listed below:

1. The miniaturised intensified units, such as SDRs, have very fast dynamics, comparable to or possibly faster than those of the commercially available sensors and actuators. Therefore, the instrumentation dynamics should be considered if model based tuning methods are used for controller design. However, including the instrumentation dynamics in a model based controller design results in non-standard high order controllers, which may be impractical for industrial implementation. In order to achieve the control objectives using the most commonly used PI/PID controllers a model reduction technique may be applied either to the process or the controller transfer function. The model order reduction techniques outlined in the present work (barring the frequency response method) provide similar control performances in terms of setpoint tracking and disturbance rejection.
2. The potential impacts of equipment size reduction on control was studied by simulating example conventional and intensified systems, whereby the time constant of the former system was 100 folds larger than that of the latter. It was found that a superior control performance in terms of IAE is achieved for the simulated intensified system, implying a faster and more efficient control performance. However, better performances for the intensified system were achieved at the expense of larger overshoots and greater system susceptibility to load disturbances.

3. The frequency responses of the open loop simulated systems indicated that low volume intensified systems have tighter stability margins compared to their conventional counterparts. This implies that reducing the process time constant brings the closed loop system closer to instability; therefore, more care is required in control and operation of intensified units.
4. The simulation results of pH control in a SDR showed that a PI controller results in satisfactory setpoint tracking and disturbance rejection performances, provided that the time delays in the closed loop are small (1s). However, the control performance deteriorated as the value of the time delay was increased (5s), whereby the output pH began to oscillate around the setpoint. Two methods of nonlinear compensation (disturbance observer and pH characteriser) were also studied by means of simulation. Both methods showed interesting potentials in suppressing the undesired effects of pH system nonlinearities.
5. A PID controller with and without the disturbance observer was used to experimentally assess the pH control performance in a SDR. The experimental results confirmed that the challenging task of pH control may be achieved in a SDR using a PID controller coupled with a common pH probe and a variable speed pump. In both schemes the controller was able to track the setpoint and recover from the imposed disturbances. However, the control transient responses were very sluggish and the effluent pH limit cycled around the setpoint when a PID controller without the DO was used. Further, large delays in the process responses were evident, mainly attributed to the pure time delay and slow response time of the pH probe.
6. The largest amplitude oscillations in the effluent pH, which were indicative of the onset of unstable behaviour, occurred consistently at specific acid and base flowrates. This implies that the process entered a different operating region from the steady state conditions, and thus a new set of tuning parameters were required to match the new process characteristics. This suggests that more advanced control schemes are required for satisfactory control of SDRs, as the unit may cross the boundaries of various operating regions based on the hydrodynamics of the thin processing films. A more sophisticated control scheme will be able to formulate suitable control parameters for multiple operating regions of the SDR at various flowrates and/or rotational speeds.
7. With the current set up it is difficult to draw definite conclusions regarding the control aspects of the SDRs. This is because the sensor is positioned downstream of the SDR and has a considerably larger time constant compared to that of the SDR. This method of monitoring the process variable includes some undesired 'tail effects' which may not be associated with the SDR itself.
8. The setpoint tracking performances of the control loops, implemented to control the conductivity of the effluent stream for the process of barium sulphate precipitation,



adequately demonstrated the potential of using the disc rotational speed as the manipulated variable. The addition of the DO scheme improved the control performance by suppressing the dampening oscillations observed without the DO in place.

9. Analysis of the experimental data for feed concentrations of 0.01M and disc rotational speed of 200-2000 rpm led to the conclusion that the rate of the precipitation reaction increases with increasing disc rotational speed, represented by reduction of the effluent stream conductivity, due to the production of thinner films and the enhanced mesomixing within the film (at constant feed flowrates). However, beyond a certain disc speed the reaction rate became insensitive to the disc rotations speed, which is attributed to insufficient residence time on the disc and/or the reduction of the degree of mesomixing within the liquid films, as very thin films with smooth surfaces were produced.
10. However, the above concluding statement is only relevant for the dilute (0.01M) feed solutions used here. At higher concentrations, the kinetic limitations are overcome and thus the residence time is unlikely to have any effect on the course of reaction. Meanwhile, as the reaction and induction times are extremely fast, micromixing becomes the dominant mixing mechanism. This in theory should lead to a steady increase in conversion, as the micromixing time reduces with increasing disc speed.
11. To achieve a given control task in SDRs, it is essential to first develop a comprehensive understanding of the relationship between the manipulated variable (e.g. feed flowrate, disc rotational speed) and the controlled parameter (e.g. concentration, particle size). It is also required to account for the interaction of different operating parameters which define the hydrodynamics of the thin films. Depending on the complexity of the system, it may be unavoidable to resort to more advanced control schemes to achieve a satisfactory performance.
12. The thermographic analysis of thin liquid films on a rotating surface across a range of operating conditions provided an insight into the flow regimes, hydrodynamic characteristics and the corresponding impact on heat transfer from the disc to the liquid film. The water films exhibited large amplitude surface waves particularly near the disc centre and at low rotational speeds. The sharp temperature boundaries observed at low flowrates and high rotational speeds were indicative of a plug flow regime; whilst some degrees of radial mixing prevailed at lower disc speeds. More viscous processing fluids (Therminol and aqueous glycerol solution) showed vastly different characteristics in terms of film flow and nature of the surface waves. The observed differences are attributed to Coriolis forces and viscous dampening of surface wavelets respectively.
13. The thermographic analysis also showed that the disc/film heat transfer performance is enhanced as the film thickness is reduced and the fluid residence time on the disc is increased at higher disc speeds and/or lower flowrates. These conditions give rise to larger Fourier numbers, indicating that perhaps heat transfer correlations are best developed based on this dimensionless number.

14. The effect of heat of reaction on the liquid film temperatures was also investigated by means of thermographic measurements. It was envisaged that a more elaborate temperature control scheme, which is based on the actual temperature measurements of the liquid film, is required to achieve tight temperature control of the reaction media. Based on these observations, it is predicted that isothermal operation with the current design particularly in presence of heat of reaction and process disturbances is highly unlikely.
15. A comparison between a Nusselt-based theoretical temperature profile and the IR temperature measurements showed large discrepancies, especially when water is used as the process fluid. This could be due to several factors, the most probable ones being the overestimation of the average film heat transfer coefficient using the Nusselt theory of condensation and incorrect emissivity value for the IR measurements, which is strongly dependent on fluid film thickness.
16. It is well established that SDRs provide enhanced heat transfer capabilities attributed to reduced conduction path of thin liquid films and also the presence of numerous surface ripples which promote intense mixing within the film. However, the thermographic analysis showed that a cold liquid feed flowing onto the centre of the disc may not get up the disc temperature before it reaches the disc periphery, depending on the operating conditions. Emphasizing that the disc rotational speed and liquid flowrate need to be selected such that effective penetration of heat from the disc through the liquid film is facilitated. A thermal imager may also be used to define the operating conditions which entail the desired thin film flow regime and wave characteristics, which are directly related to intensification aspects of SDRs, and therefore enable more effective operation and control of such devices.

## ***8.2 Recommendations for Future Work***

The present research is one of the very few thorough investigations into control and operation of SDRs to this date. Some of the findings of the present work are also applicable to other low volume intensified units. However, the control and operation of PI equipment need to be more actively investigated if such technologies are to be implemented in industry. Based on the challenges and opportunities unveiled in the present work, the following areas are identified for further research:

1. In the present study, control strategies were considered for two example processes carried out in a SDR. However, the control strategies were merely passive regulatory systems which were devised based on the available SDR design and the conventional sensors/actuators. Therefore, the control performance is inevitably limited by the SDR design and the performance characteristics of the available instrumentation. The measurement and transport time delays in the present control loop setup are much greater than the dynamics of the SDR, and thus, present a significant limitation on control of such devices. Therefore, intensified sensors with faster dynamics and smaller volumes

may need to be developed to achieve an optimum control performance. Additionally, process control and the conceptual design of intensified equipment should ideally be considered simultaneously. There should be provisions made for embedding the new generation of sensors on the disc surface to achieve real-time measurement of the process variable within the processing films, as opposed to placing the conventional sensors downstream of the SDRs. Particularly, as non-invasive measurement techniques which do not disturb the stability of thin film flow on the disc are generally preferred. These recommendations are rather long term and call for the development of more elaborate sensors and equipment design. Such large leaps in instrumentation and equipment design require a lot of research endeavours and capital investments, which may put the industrial acceptance of intensified equipment on hold for a while longer.

2. The results demonstrated a vastly appealing potential for exploiting the disc rotational speed as an extra degree of freedom in control system design for SDRs. It is recommended that this concept is investigated further for a wider range of processes and operating conditions. Additional experimental work is required to demonstrate the feasibility and relative merits of using the disc speed as the manipulated variable, as opposed to the conventional methods of achieving a control task, for instance by adjusting the feed flowrate.
3. The implementation of a disturbance observer was shown to improve the control performance by reducing the limit cycles and mitigating the undesired effects of the system nonlinearity. The same PID parameters were used for the schemes with and without the DO, to study the effect of disturbance observer scheme independent of the tuning parameters of the outer loop controller. However, the PID controller settings may be refined to obtain the best achievable performance when the DO is included in the control loop. The preliminary assessment of the DO presented some promising potentials and deserves further in depth investigations.
4. Previous research has shown that the Nusselt theory of a stable flow often provides inaccurate estimations of thin film hydrodynamics in terms of the film thickness, residence time on the disc, radial velocity, etc. However, this model is the simplest and most widely used representation of thin film flow. Various empirical and mathematical models are also available in the literature. However, the mathematical models seem notoriously complex and difficult to implement, whilst, the empirical correlations are limited to the particular SDR design and the range of the operating conditions they have been developed for. The film hydrodynamics is the underlying factor for heat and mass transfer processes within the processing fluid, and thus the intensification features of SDRs. Therefore, the accurate prediction of the thin film flow and surface wave characteristics forms the foundations of successful operation and control of such devices. Therefore, the SDR technology could benefit enormously if empirical models of the film hydrodynamics which covered a wider spectrum of SDR designs and operating conditions, or a more accurate version of the Nusselt theory which accounts for the surface instabilities could be developed.

5. The thermographic studies provided an interesting insight into the flow regimes and wave characteristics of thin liquid films. Furthermore, the analysis shed more light on the heat transfer performance from the disc to a cold film of liquid at various operating conditions. However, the accuracy of the measurements for quantitative analysis of the film temperature profiles was hindered by a number of factors. Firstly, the SDR was not enclosed, thus the processing films were not in equilibrium with the air boundary layer. Future investigations could benefit from enclosing the SDR system with an IR transparent material in order to reduce the amount of heat loss from the processing film. Another factor which may have influenced the accuracy of the thermographic measurements is the accuracy of the liquid film emissivity. In the present study, the values of emissivity were estimated based on the information available in the literature for liquid films of varying thickness. The actual measurements of the liquid film emissivity at various film thicknesses present an interesting research opportunity, which could in turn remove the uncertainties of IR measurements encountered in the present work. Furthermore, various disc designs with surface irregularities along with different feed nozzle designs and feed locations may also be studied by means of the thermographic techniques to portray a more comprehensive picture of thin film flow in SDRs. Therefore, the thermographic techniques may serve as a useful tool in design of SDRs. Further investigations may also lead to the development of a robust empirical model of the temperature profiles across the disc.
  
6. To achieve effective operation and control of SDRs first the hydrodynamic characteristics of thin liquid films need to be defined. Then the corresponding impacts of film hydrodynamics on a specific process need to be characterised. The often complex relationship between the controlled variables and the manipulated variables forms the basis of devising a successful control scheme for SDRs. Depending on the complexity of the process and the interactions of the input and output parameters, advanced control schemas based on internal model control, neural networks, fuzzy logics, etc., may be employed for control of processes in SDRs. The future developments of control strategies for SDRs would benefit from exploring more sophisticated control schemes and comparing their relative merits with those of the basic PID algorithm adopted in this study.

## Nomenclature

		<i>Units</i>
$C$	Concentration	mol/L
$c$	Controller output	
$C_p$	Specific heat capacity	J/kgK
$D$	Thermal diffusivity	$\text{m}^2/\text{s}$
$d$	Disturbance	
$D_{AB}$	Diffusion coefficient of solute	$\text{m}^2/\text{s}$
$e$	Error	
$F$	Fourier number	
$g$	Acceleration due to gravity	$\text{m}/\text{s}^2$
$G(s)$	Transfer Function	
$G^*(s)$	Reduced order transfer function	
$G_m$	Gain margin	
$h$	Film heat transfer coefficient	$\text{W}/\text{m}^2\text{K}$
$j$	Complex operator	
$k$	Thermal conductivity	$\text{W}/\text{mK}$
$k$	Steady state gain	
$K_c$	Controller gain	
$K_{sp}$	Solubility product	$\text{mol}^2/\text{dm}^6$
$m$	Mass flowrate	kg/s
$N$	Rotational speed	rpm
$P_F$	Frictional power dissipation	W
$P_K$	Kinetic power dissipation	W
$Q$	Volumetric flowrate	$\text{m}^3/\text{s}$
$Q(s)$	Filter transfer function	
$r$	Radial distance from the disc centre	m
$Re$	Reynolds number	
$s$	Laplace transform variable	$\text{s}^{-1}$
$S$	Supersaturation	
$Sc$	Schmidt number	
$t$	Time	s
$T$	Temperature	K
$t$	Film surface residence time	s
$T_0$	Numerator time constant	s
$T_D$	Derivative time constant	s or min

$T_D^2$	Second order derivative time constant	s or min
$T_I$	Integral time constant	s or min
$t_{ind}$	Induction time	s
$t_{micro}$	Micromixing time	s
$t_{res}$	Mean fluid residence time	s
$T_s$	Sampling period	s
$u$	Average solution velocity	m/s
$U(s)$	Setpoint	
$v$	Velocity	m/s
$Y(s)$	Process output	
$z$	Vertical distance along the z-axis	m
$z$	Discrete Laplace transform operator	

**Greek Characters**

$\alpha$	Activity	
$\alpha_k$	Binomial coefficient	
$\gamma$	Shear rate	$s^{-1}$
$\gamma$	Activity coefficient	
$\delta$	Film thickness	m
$\varepsilon$	Energy dissipation rate	$m^2/s^3$
$\theta$	Time delay	s
$\lambda$	Closed-loop time constant	s
$\nu$	Kinematic viscosity	$m^2/s$
$\rho$	Density	$kg/m^3$
$\tau$	Time constant	s
$\phi$	Phase shift	degree
$\phi_m$	Phase margin	degree
$\omega$	Angular velocity ( $2\pi N/60$ )	rad/s
$\omega$	Frequency of oscillations	rad/s
$\omega_c$	Corner frequency	rad/s

**Subscripts**

$a$	Actuator
$c$	Controller
$d$	Disc, delay
$f$	Filter
$i$	Inlet/inner

$m$	Measurement
$n$	Nominal
$o$	Outlet/outer
$p$	Process
$r$	Radial direction in cylindrical co-ordinates
$\theta$	Angular direction in cylindrical co-ordinates

**Acronyms**

A/D	Analog to Digital
ADE	Application Development Environment
AR	Amplitude Ratio
ATR	Attenuated Total Reflection
C	Characteriser
CFD	Computational Fluid Dynamics
CO	Controller Output
COSHH	Control of Substances Hazardous to Health
CSD	Crystal Size Distribution
CSTR	Continuous Stirred Tank Reactor
D/A	Digital to Analog
DAQ	Data Acquisition
DO	Disturbance Observer
DWC	Dividing Wall Column
EGU	Engineering Units
FIFO	First In First Out
FLIR	Forward Looking Infrared
FOPDT	First Order Plus Dead Time
FTIR	Fourier Transform Infrared
IAE	Integral of Absolute Error
ID	Internal Diameter
IMC	Internal Model Control
IR	Infrared
LabVIEW	Laboratory Virtual Instrumentation Engineering Workbench
MatLab	Matrix Laboratory
MIMO	Multiple Input Multiple Output
ODE	Ordinary Differential Equation
P	Proportional (controller)
PI	Proportional-Integral (controller)
<i>PI</i>	Process Intensification
PID	Proportional-Integral-Derivative (controller)

PIDD <sup>2</sup>	Proportional-Integral-Derivative-Derivative <sup>2</sup> (controller)
PRC	Process Reaction Curve
PV	Process Variable
RCP	Rapid Control Prototyping
RT	Real Time
RTOS	Real Time Operating System
SAE	Strong Acid Equivalent
SDR	Spinning Disc Reactor
SOPDT	Second Order Plus Dead Time
SP	Setpoint
VI	Virtual Instrument



## References

1. Stankiewicz, A.I. and J.A. Moulijn, 2004, *Re-engineering the chemical processing plant : process intensification*, M. Dekker: New York.
2. Keil, F.J., 2007, *Modeling of process intensification*, Wiley-VCH: Germany.
3. Reay, D.A., C. Ramshaw, and A. Harvey, 2008, *Process intensification : engineering for efficiency, sustainability and flexibility*, Butterworth-Heinemann: Oxford.
4. Harmsen, G.J. (2007) 'Reactive distillation: The front-runner of industrial process intensification - A full review of commercial applications, research, scale-up, design and operation' *Chemical Engineering and Processing*, **46**, pp.774-780.
5. Pennemann, H., V. Hessel, and H. Lowe (2004) 'Chemical microprocess technology - from laboratory-scale to production' *Chemical Engineering Science*, **59**, pp.4789-4794.
6. Sharma, N. and K. Singh (2010) 'Control of Reactive Distillation Column: A Review' *International Journal of Chemical Reactor Engineering*, **8**, pp.57.
7. Schoenmakers, H.G. and B. Bessling (2003) 'Reactive and catalytic distillation from an industrial perspective' *Chemical Engineering and Processing*, **42**, pp.145-155.
8. Nikacevic, N.M., A.E.M. Huesman, P.M.J. Van den Hof, and A.I. Stankiewicz (2012) 'Opportunities and challenges for process control in process intensification' *Chemical Engineering and Processing*, **52**, pp.1-15.
9. Stankiewicz, A.I. and J.A. Moulijn (2000) 'Process intensification: Transforming chemical engineering' *Chemical Engineering Progress*, **96**, pp.22-34.
10. Espig, H. and R. Hoyle (1965) 'Waves in a thin liquid layer on a rotating disk' *J. Fluid Mech.*, **22**, pp.671-677.
11. Charwat, A.F., R.E. Kelly, and C. Gazley (1972) 'The flow and stability of thin liquid films on a rotating disk' *J. Fluid Mech.*, **53**, pp.227-255.
12. Lenewit, G., K.G. Roesner, and R. Koehler (1999) 'Surface instabilities of thin liquid film flow on a rotating disk' *Experiments in Fluids*, **26**, pp.75-85.
13. Matar, O.K., C.J. Lawrence, and G.M. Sisoiev (2005) 'The flow of thin liquid films over spinning disks: Hydrodynamics and mass transfer' *Physics of Fluids*, **17**, pp.20.
14. Matar, O.K., G.M. Sisoiev, and C.J. Lawrence (2006) 'The flow of thin liquid films over spinning discs' *Canadian Journal of Chemical Engineering*, **84**, pp.625-642.
15. Jachuck, R.J.J. and C. Ramshaw (1994) 'Process Intensification - Heat transfer characteristics of tailored rotating surfaces ' *Heat Recovery Systems & Chp*, **14**, pp.475-491.
16. Aoune, A. and C. Ramshaw (1999) 'Process intensification: heat and mass transfer characteristics of liquid films on rotating discs' *International Journal of Heat and Mass Transfer*, **42**, pp.2543-2556.
17. Tsouris, C. and J.V. Porcelli (2003) 'Process intensification - Has its time finally come?' *Chemical Engineering Progress*, **99**, pp.50-55.
18. Ohishi, K., M. Nakao, K. Ohnishi, and K. Miyachi (1987) 'Microprocessor-controlled DC motor for load-intensive position servo system' *IEEE Transactions on Industrial Electronics*, **34**, pp.44-49.
19. Jones, R.W. and M.T. Tham (2006) 'Reducing interactions in decentralised control schemes' *2006 SICE-ICASE International Joint Conference*, Bexco.
20. Jones, R.W. and M.T. Tham (2007) 'Disturbance observer design for continuous systems with delay' *Asia-Pacific Journal of Chemical Engineering*, **2**, pp.517-525.
21. Shahruz, S.M. and S.A. Rajarama (2000) 'Suppression of limit cycles in a class of non-linear systems by disturbance observers' *Journal of Sound and Vibration*, **229**, pp.1003-1012.

22. Shahruz, S.M., C. Cloet, and M. Tomizuka (2002) 'Suppression of effects of non-linearities in a class of non-linear systems by disturbance observers' *Journal of Sound and Vibration*, **249**, pp.405-415.
23. Shinskey, F.G., 1999, *Characterizers for Control Loops*, Available from: <http://www.expertune.com/artCharact.html>, accessed: 2010.
24. McMillan, G.K., 1994, *pH measurement and control*, Instrument Society of America: Research Triangle Park, NC.
25. Baldyga, J., J.R. Bourne, and S.J. Hearn (1997) 'Interaction between chemical reactions and mixing on various scales' *Chemical Engineering Science*, **52**, pp.457-466.
26. Cafiero, L.M., G. Baffi, A. Chianese, and R.J.J. Jachuck (2002) 'Process intensification: Precipitation of barium sulfate using a spinning disk reactor' *Industrial and Engineering Chemistry Research*, **41**, pp.5240-5246.
27. Ramshaw, C. (1999) 'Process intensification and Green Chemistry' *Green Chemistry*, **1**, pp.G15-G17.
28. Van Gerven, T. and A. Stankiewicz (2009) 'Structure, Energy, Synergy, Time-The Fundamentals of Process Intensification' *Industrial & Engineering Chemistry Research*, **48**, pp.2465-2474.
29. Charpentier, J.C. (2006) 'In the frame of globalization and sustainability, process intensification, a path to the future of chemical and process engineering (molecules into money)' *Chemical Engineering Journal*, **134**, pp.84-92.
30. Stankiewicz, A. and J.A. Moulijn (2002) 'Process intensification' *Industrial & Engineering Chemistry Research*, **41**, pp.1920-1924.
31. Wang, G.Q., Z.C. Xu, and J.B. Ji (2010) 'Progress on Hige distillation-Introduction to a new device and its industrial applications' *Chemical Engineering Research & Design*, **89**, pp.1434-1442.
32. Stankiewicz, A. (2006) 'Energy matters - Alternative sources and forms of energy for intensification of chemical and biochemical processes' *Chemical Engineering Research & Design*, **84**, pp.511-521.
33. Ptasinski, K.J. and P.J.A.M. Kerkhof (1992) 'Electric field driven separations: Phenomena and applications' *Separation Science and Technology*, **27**, pp.995-1021.
34. Darabi, J., M.M. Ohadi, and S.V. Desiatoun (2000) 'Falling film and spray evaporation enhancement using an applied electric field' *Journal of Heat Transfer*, **122**, pp.741-748.
35. Kappe, C.O. and D. Dallinger (2009) 'Controlled microwave heating in modern organic synthesis: Highlights from the 2004-2008 literature' *Molecular Diversity*, **13**, pp.71-193.
36. Sun, H., F. Blatter, and H. Frei (1996) 'Cyclohexanone from cyclohexane and O<sub>2</sub> in a zeolite under visible light with complete selectivity' *Journal of the American Chemical Society*, **118**, pp.6873-6879.
37. Bahnemann, D. (2004) 'Photocatalytic water treatment: solar energy applications' *Solar Energy*, **77**, pp.445-459.
38. Chakinala, A.G., P.R. Gogate, A.E. Burgess, and D.H. Bremner (2007) 'Intensification of hydroxyl radical production in sonochemical reactors' *Ultrasonics Sonochemistry*, **14**, pp.509-514.
39. Hagenson, L.C. and L.K. Doraiswamy (1998) 'Comparison of the effects of ultrasound and mechanical agitation on a reacting solid-liquid system' *Chemical Engineering Science*, **53**, pp.131-148.

40. Thakur, R.K., C. Vial, K.D.P. Nigam, E.B. Nauman, and G. Djelveh (2003) 'Static mixers in the process industries - A review' *Chemical Engineering Research & Design*, **81**, pp.787-826.
41. Lapkin, A.A. and P.K. Plucinski, 2010, 'Engineering factors for efficient flow processes in chemical industries', in *Chemical reactions and processes under flow conditions*, The Royal Society of Chemistry: Cambridge.
42. Ashe, R. (2010) 'Shaken, not stirred' *The Chemical Engineer*, **830**, pp.39-41.
43. Jensen, K.F. (2001) 'Microreaction engineering - is small better?' *Chemical Engineering Science*, **56**, pp.293-303.
44. Mason, B.P., K.E. Price, J.L. Steinbacher, A.R. Bogdan, and D.T. McQuade (2007) 'Greener approaches to organic synthesis using microreactor technology' *Chemical Reviews*, **107**, pp.2300-2318.
45. Pennemann, H., P. Watts, S.J. Haswell, V. Hessel, and H. Lowe (2004) 'Benchmarking of microreactor applications' *Organic Process Research & Development*, **8**, pp.422-439.
46. Reay, D. (2008) 'The role of process intensification in cutting greenhouse gas emissions' *Applied Thermal Engineering*, **28**, pp.2011-2019.
47. Hessel, V. (2009) 'Novel process windows - Gate to maximizing process intensification via flow chemistry' *Chemical Engineering & Technology*, **32**, pp.1655-1681.
48. Hessel, V., P. Lob, and H. Lowe (2005) 'Development of microstructured reactors to enable organic synthesis rather than subduing chemistry' *Current Organic Chemistry*, **9**, pp.765-787.
49. Boodhoo, K.V.K., W.A.E. Dunk, M. Vicevic, R.J. Jachuck, V. Sage, D.J. Macquarrie, and J.H. Clark (2006) 'Classical cationic polymerization of styrene in a spinning disc reactor using silica-supported BF<sub>3</sub> catalyst' *Journal of Applied Polymer Science*, **101**, pp.8-19.
50. Etchells, J.C. (2004) 'Process intensification - Safety pros and cons' *Hazards XVIII Symposium*, Manchester.
51. Luyben, W.L. and D.C. Hendershot (2004) 'Dynamic disadvantages of intensification in inherently safer process design' *Industrial & Engineering Chemistry Research*, **43**, pp.384-396.
52. Klais, O., F. Westphal, W. Benaissa, and D. Carson (2009) 'Guidance on Safety/Health for Process Intensification Including MS Design Part I: Reaction Hazards' *Chemical Engineering & Technology*, **32**, pp.1831-1844.
53. Klais, O., F. Westphal, W. Benaissa, and D. Carson (2009) 'Guidance on safety/health for process intensification including MS design; Part II: Explosion hazards' *Chemical Engineering & Technology*, **32**, pp.1966-1973.
54. Ramshaw, C. and S. Cook (2005) 'Spinning around' *The Chemical Engineer*, **775**, pp.42-44.
55. Brechtelsbauer, C., N. Lewis, P. Oxley, F. Ricard, and C. Ramshaw (2001) 'Evaluation of a spinning disc reactor for continuous processing' *Organic Process Research & Development*, **5**, pp.65-68.
56. Vicevic, M., K.V.K. Boodhoo, and K. Scott (2007) 'Catalytic isomerisation of alpha-pinene oxide to campholenic aldehyde using silica-supported zinc triflate catalysts II. Performance of immobilised catalysts in a continuous spinning disc reactor' *Chemical Engineering Journal*, **133**, pp.43-57.
57. Oxley, P., C. Brechtelsbauer, F. Ricard, N. Lewis, and C. Ramshaw (2000) 'Evaluation of spinning disk reactor technology for the manufacture of pharmaceuticals' *Industrial & Engineering Chemistry Research*, **39**, pp.2175-2182.

58. Mohammadi, S. and K.V.K. Boodhoo (2012) 'Online conductivity measurement of residence time distribution of thin film flow in the spinning disc reactor' *Chemical Engineering Journal*, **207-208**, pp.885-894.
59. Boiarkina, I., S. Pedron, and D.A. Patterson (2011) 'An experimental and modelling investigation of the effect of the flow regime on the photocatalytic degradation of methylene blue on a thin film coated ultraviolet irradiated spinning disc reactor' *Applied Catalysis B-Environmental*, **110**, pp.14-24.
60. Jachuck, R.J., J. Lee, D. Kolokotsa, C. Ramshaw, P. Valachis, and S. Yanniotis (1997) 'Process intensification for energy saving' *Applied Thermal Engineering*, **17**, pp.861-867.
61. Boodhoo, K., 1999, *Process intensification : spinning disc reactor for the polymerisation of styrene*, Ph.D. thesis, Newcastle University.
62. Burns, J.R., C. Ramshaw, and R.J. Jachuck (2003) 'Measurement of liquid film thickness and the determination of spin-up radius on a rotating disc using an electrical resistance technique' *Chemical Engineering Science*, **58**, pp.2245-2253.
63. Ozar, B., B.M. Cetegen, and A. Faghri (2004) 'Experiments on heat transfer in a thin liquid film flowing over a rotating disk' *Journal of Heat Transfer-Transactions of the ASME*, **126**, pp.184-192.
64. Quinn, G. and B.M. Cetegen (2010) 'Investigation of heat transfer and bubble dynamics in a boiling thin liquid film flowing over a rotating disk' *International Journal of Thermal Sciences*, **49**, pp.643-652.
65. Quinn, G. and B.M. Cetegen (2011) 'Heat transfer in an evaporating liquid film flowing over a rotating disk' *Experimental Heat Transfer*, **24**, pp.88-107.
66. Lim, S.T., 1980, *Hydrodynamics and mass transfer processes associated with the absorption of oxygen in liquid films flowing across a rotating disc*, Ph.D. thesis, Newcastle University.
67. Moore, S.R., 1986, *Mass transfer into thin liquid films with and without chemical reaction*, Ph.D. thesis, Newcastle University.
68. Burns, J.R. and J.J. Jachuck (2005) 'Monitoring of CaCO<sub>3</sub> production on a spinning disc reactor using conductivity measurements' *AIChE Journal*, **51**, pp.1497-1507.
69. Sisoiev, G.M., O.K. Matar, and C.J. Lawrence (2005) 'Gas absorption into a wavy film flowing over a spinning disc' *Chemical Engineering Science*, **60**, pp.2051-2060.
70. Boodhoo, K.V.K. and R.J. Jachuck (2000) 'Process intensification: spinning disc reactor for styrene polymerisation' *Applied Thermal Engineering*, **20**, pp.1127-1146.
71. Boodhoo, K.V.K. and R.J. Jachuck (2000) 'Process intensification: spinning disc reactor for condensation polymerisation' *Green Chemistry*, **2**, pp.235-244.
72. Van Gerven, T., G. Mul, J. Moulijn, and A. Stankiewicz (2007) 'A review of intensification of photocatalytic processes' *Chemical Engineering and Processing*, **46**, pp.781-789.
73. Yatmaz, H.C., C. Wallis, and C.R. Howarth (2001) 'The spinning disc reactor - studies on a novel TiO<sub>2</sub> photocatalytic reactor' *Chemosphere*, **42**, pp.397-403.
74. Akhtar, M., I. Blakemore, G. Clayton, and S. Knapper (2009) 'The use of spinning disc reactor for processing ice cream base - effect of ageing in making model ice cream' *International Journal of Food Science and Technology*, **44**, pp.1139-1145.
75. Barzin, R., S.R. Abd Shukor, and A.L. Ahmad (2007) 'An overview of difficulties in controlling intensified process' *AJChE*, **7**, pp.8-15.
76. Huang, K., S.J. Wang, L. Shan, Q.X. Zhu, and J.X. Qian (2007) 'Seeking synergistic effect - A key principle in process intensification' *Separation and Purification Technology*, **57**, pp.111-120.

77. Adrian, T., H. Schoenmakers, and M. Boll (2004) 'Model predictive control of integrated unit operations: Control of a divided wall column' *Chemical Engineering and Processing*, **43**, pp.347-355.
78. Engell, S. and G. Fernholz (2003) 'Control of a reactive separation process' *Chemical Engineering and Processing*, **42**, pp.201-210.
79. Haugwitz, S., P. Hagander, and T. Noren (2005) 'Modeling and control of a novel heat exchange reactor, the Open Plate Reactor' *Control Engineering Practice*, **15**, pp.779-792.
80. Kiss, A.A. and C.S. Bildea (2011) 'A control perspective on process intensification in dividing-wall columns' *Chemical Engineering and Processing*, **50**, pp.281-292.
81. Jones, R.W. and M.T. Tham (2006) 'Control strategies for process intensified systems' *SICE-ICASE International Joint Conference*, Busan.
82. Wille, C., H.P. Gabski, T. Haller, H. Kim, L. Unverdorben, and R. Winter (2004) 'Synthesis of pigments in a three-stage microreactor pilot plant-an experimental technical report' *Chemical Engineering Journal*, **101**, pp.179-185.
83. Quiram, D.J., K.F. Jensen, M.A. Schmidt, P.L. Mills, J.F. Ryley, M.D. Wetzel, and D.J. Kraus (2007) 'Integrated microreactor system for gas-phase catalytic reactions. 3. microreactor system design and system automation' *Industrial & Engineering Chemistry Research*, **46**, pp.8319-8335.
84. Barzin, R., S.R. Abd Shukur, and A.L. Ahmad (2010) 'New spectrophotometric measurement method for process control of miniaturized intensified systems' *Sensors and Actuators B-Chemical*, **146**, pp.403-409.
85. Ferstl, W., S. Loebbecke, J. Antes, H. Krause, M. Haeberl, D. Schmalz, H. Muntermann, M. Grund, A. Steckenborn, A. Lohf, J. Hassel, T. Bayer, M. Kinzl, and I. Leipprand (2004) 'Development of an automated microreaction system with integrated sensorics for process screening and production' *Chemical Engineering Journal*, **101**, pp.431-438.
86. Wright, R.A. and C. Kravaris (1991) 'Nonlinear control of pH processes using the Strong Acid Equivalent' *Industrial & Engineering Chemistry Research*, **30**, pp.1561-1572.
87. Hurowitz, S.E., A. Bobkov, and J.B. Riggs (2000) 'pH control using advanced proportional-integral controls with the dual- injection in-line process' *Industrial and Engineering Chemistry Research*, **39**, pp.2418-2426.
88. Wright, R.A. and C. Kravaris (2001) 'On-line identification and nonlinear control of an industrial pH process' *Journal of Process Control*, **11**, pp.361-374.
89. Shinskey, F.G., 1996, *Process control systems : application, design, and tuning*, McGraw-Hill: New York.
90. Henson, M.A. and D.E. Seborg (1997) 'Adaptive input-output linearization of a pH neutralization process' *International Journal of Adaptive Control and Signal Processing*, **11**, pp.171-200.
91. Waller, K.V. and T.K. Gustafsson (1983) 'Fundamental properties of continuous pH control' *Isa Transactions*, **22**, pp.25-34.
92. Lin, J.Y. and C.C. Yu (1993) 'Automatic tuning and gain scheduling for pH control' *Chemical Engineering Science*, **48**, pp.3159-3171.
93. Alpbaz, M., H. Hapoglu, G. Ozkan, and S. Altuntas (2006) 'Application of self-tuning PID control to a reactor of limestone slurry titrated with sulfuric acid' *Chemical Engineering Journal*, **116**, pp.19-24.
94. Biagiola, S.I. and J.L. Figueroa (2002) 'State estimation in nonlinear processes. Application to pH process control' *Industrial and Engineering Chemistry Research*, **41**, pp.4777-4785.

95. Jayadeva, B., Y. Rao, M. Chidambaram, and K.P. Madhavan (1990) 'Nonlinear controller for a pH process' *Computers & Chemical Engineering*, **14**, pp.917-920.
96. Gustafsson, T.K., B.O. Skrifvars, K.V. Sandstrom, and K.V. Waller (1995) 'Modeling of pH control' *Industrial & Engineering Chemistry Research*, **34**, pp.820-827.
97. Wright, R.A., M. Soroush, and C. Kravaris (1991) 'Strong Acid Equivalent control of pH processes - An experimental study' *Industrial & Engineering Chemistry Research*, **30**, pp.2437-2444.
98. Shukla, N.V., P.B. Deshpande, V.R. Kumar, and B.D. Kulkarni (1993) 'Enhancing the robustness of internal model based nonlinear pH controller' *Chemical Engineering Science*, **48**, pp.913-920.
99. Narayanan, N.R.L., P.R. Krishnaswamy, and G.P. Rangaiah (1997) 'An adaptive internal model control strategy for pH neutralization' *Chemical Engineering Science*, **52**, pp.3067-3074.
100. Garrido, R., M. Adroer, and M. Poch (1997) 'Wastewater neutralization control based in fuzzy logic: Simulation results' *Industrial & Engineering Chemistry Research*, **36**, pp.1665-1674.
101. Chen, J.H. and T.C. Huang (2004) 'Applying neural networks to on-line updated PID controllers for nonlinear process control' *Journal of Process Control*, **14**, pp.211-230.
102. Astrom, K.J. and T. Hagglund (2001) 'The future of PID control' *Control Engineering Practice*, **9**, pp.1163-1175.
103. Brandes, B.T. (2005) 'Case study of an automatic pH control strategy for a strong acid-strong base system' *Industrial and Engineering Chemistry Research*, **44**, pp.5622-5629.
104. Umeno, T. and Y. Hori (1991) 'Robust speed control of DC servomotors using modern 2 degrees-of-freedom controller design' *IEEE Transactions on Industrial Electronics*, **38**, pp.363-368.
105. Kempf, C.J. and S. Kobayashi (1999) 'Disturbance observer and feedforward design for a high-speed direct-drive positioning table' *IEEE Transactions on Control Systems Technology*, **7**, pp.513-526.
106. Tham, M., N. Pooley, A. Ganjian, and R. Jones (2010) 'Mitigating control loop interactions: Disturbance observers versus decouplers' *International Conference on Control, Automation and Systems*, Kintex.
107. Mullin, J.M., 2001, *Crystallization*, Butterworth-Heinemann: Oxford.
108. Sohnel, O. and J. Garside, 1992, *Precipitation : basic principles and industrial applications*, Butterworth-Heinemann: Oxford.
109. Dirksen, J.A. and T.A. Ring (1991) 'Fundamentals of crystallization: Kinetic effects on particle size distribution and morphology' *Chemical Engineering Science*, **46**, pp.2389-2427.
110. Nielsen, A.E. (1958) 'Kinetics of growth in barium sulphate precipitation' *Acta Chem. Scand.*, **12**, pp.951-958.
111. Gunn, D.J. and M.S. Murthy (1972) 'Kinetics and mechanisms of precipitation' *Chemical Engineering Science*, **27**, pp.1293-&.
112. Aoun, M., E. Plasari, R. David, and J. Villermaux (1996) 'Are barium sulphate kinetics sufficiently known for testing precipitation reactor models?' *Chemical Engineering Science*, **51**, pp.2449-2458.
113. Mersmann, A., 1995, *Crystallization technology handbook*, Marcel Dekker: New York.
114. Judat, B. and M. Kind (2004) 'Morphology and internal structure of barium sulfate - derivation of a new growth mechanism' *Journal of Colloid and Interface Science*, **269**, pp.341-353.

115. Baldyga, J. and W. Orciuch (2001) 'Barium sulphate precipitation in a pipe - an experimental study and CFD modelling' *Chemical Engineering Science*, **56**, pp.2435-2444.
116. Jaworski, Z. and A.W. Nienow (2003) 'CFD modelling of continuous precipitation of barium sulphate in a stirred tank' *Chemical Engineering Journal*, **91**, pp.167-174.
117. Marchisio, D.L., A.A. Barresi, and M. Garbero (2002) 'Nucleation, growth, and agglomeration in barium sulfate turbulent precipitation' *AIChE Journal*, **48**, pp.2039-2050.
118. Oncul, A.A., K. Sundmacher, A. Seidel-Morgenstern, and D. Thevenin (2006) 'Numerical and analytical investigation of barium sulphate crystallization' *Chemical Engineering Science*, **61**, pp.652-664.
119. Oncul, A.A., B. Niemann, K. Sundmacher, and D. Thevenin (2008) 'CFD modelling of BaSO<sub>4</sub> precipitation inside microemulsion droplets in a semi-batch reactor' *Chemical Engineering Journal*, **138**, pp.498-509.
120. Baldyga, J., W. Podgorska, and R. Pohorecki (1995) 'Mixing-precipitation model with application to double feed semibatch precipitation' *Chemical Engineering Science*, **50**, pp.1281-1300.
121. Baldyga, J. and J.R. Bourne (1984) 'A fluid mechanical approach to turbulent mixing and chemical reaction part I: Inadequance of available methods' *Chemical Engineering Communications*, **28**, pp.231-241.
122. Carosso, P.A. and E. Pelizzetti (1984) 'A stopped-flow technique in fast precipitation kinetics - The case of barium sulfate' *Journal of Crystal Growth*, **68**, pp.532-536.
123. Pohorecki, R. and J. Baldyga (1983) 'The use of a new model of micromixing for determination of crystal size in precipitation' *Chemical Engineering Science*, **38**, pp.79-83.
124. Pohorecki, R. and J. Baldyga (1988) 'The effects of micromixing and the manner of reactor feeding on precipitaion in stirred tank reactors' *Chemical Engineering Science*, **43**, pp.1949-1954.
125. Baldyga, J., L. Makowski, and W. Orciuch (2007) 'Double-feed semibatch precipitation - Effects of mixing' *Chemical Engineering Research & Design*, **85**, pp.745-752.
126. Phillips, R., S. Rohani, and J. Baldyga (1999) 'Micromixing in a single-feed semi-batch precipitation process' *AIChE Journal*, **45**, pp.82-92.
127. Chen, J.F., C. Zheng, and G.T. Chen (1996) 'Interaction of macro- and micromixing on particle size distribution in reactive precipitation' *Chemical Engineering Science*, **51**, pp.1957-1966.
128. Schwarzer, H.C. and W. Peukert (2004) 'Combined experimental/numerical study on the precipitation of nanoparticles' *AIChE Journal*, **50**, pp.3234-3247.
129. Wang, Q.A., J.X. Wang, M. Li, L. Shao, J.F. Chen, L. Gu, and Y.T. An (2009) 'Large-scale preparation of barium sulphate nanoparticles in a high-throughput tube-in-tube microchannel reactor' *Chemical Engineering Journal*, **149**, pp.473-478.
130. Marchisio, D.L. and A.A. Barresi (2003) 'CFD simulation of mixing and reaction: the relevance of the micro-mixing model' *Chemical Engineering Science*, **58**, pp.3579-3587.
131. Oncul, A.A., G. Janiga, and D. Thevenin (2009) 'Comparison of various micromixing approaches for Computational Fluid Dynamics simulation of barium sulfate precipitation in tubular reactors' *Industrial & Engineering Chemistry Research*, **48**, pp.999-1007.

132. McCarthy, E.D., W.A.E. Dunk, and K.V.K. Boodhoo (2007) 'Application of an intensified narrow channel reactor to the aqueous phase precipitation of barium sulphate' *Journal of Colloid and Interface Science*, **305**, pp.72-87.
133. Matynia, A., K. Piotrowski, and J. Koralewska (2005) 'Barium sulphate crystallization kinetics in the process of barium ions precipitation by means of crystalline ammonium sulphate addition' *Chemical Engineering and Processing*, **44**, pp.485-495.
134. Wong, D.C.Y., Z. Jaworski, and A.W. Nienow (2003) 'Barium sulphate precipitation in a double-feed semi-batch stirred reactor' *Chemical Engineering Research & Design*, **81**, pp.874-880.
135. Ivanova, N.I., D.S. Rudelev, B.D. Summ, and A.A. Chalykh (2001) 'Synthesis of barium sulfate nanoparticles in water-in-oil microemulsion systems' *Colloid Journal*, **63**, pp.714-717.
136. Adityawarman, D., A. Voigt, P. Veit, and K. Sundmacher (2005) 'Precipitation of BaSO<sub>4</sub> nanoparticles in a non-ionic microemulsion: Identification of suitable control parameters' *Chemical Engineering Science*, **60**, pp.3373-3381.
137. de Caprariis, B., M. Di Rita, M. Stoller, N. Verdone, and A. Chianese (2012) 'Reaction-precipitation by a spinning disc reactor: Influence of hydrodynamics on nanoparticles production' *Chemical Engineering Science*, **76**, pp.73-80.
138. Stoller, M., L. Miranda, and A. Chianese (2009) 'Optimal feed location in A spinning disc reactor for the production Of TiO<sub>2</sub> nanoparticles' *Chemical Engineering Transactions*, **17**, pp.993-998.
139. Krishnadasan, S., J. Tovilla, R. Vilar, A.J. deMello, and J.C. deMello (2004) 'On-line analysis of CdSe nanoparticle formation in a continuous flow chip-based microreactor' *Journal of Materials Chemistry*, **14**, pp.2655-2660.
140. Wagner, J., T. Kirner, G. Mayer, J. Albert, and J.M. Kohler (2004) 'Generation of metal nanoparticles in a microchannel reactor' *Chemical Engineering Journal*, **101**, pp.251-260.
141. Braatz, R.D. (2002) 'Advanced control of crystallization processes' *Annual Reviews in Control*, **26**, pp.87-99.
142. Alatalo, H., J. Kohonen, H. Qu, H. Hatakka, S.P. Reinikainen, M. Louhi-Kultanen, and J. Kallas (2008) 'In-line monitoring of reactive crystallization process based on ATR-FTIR and Raman spectroscopy' *Journal of Chemometrics*, **22**, pp.644-652.
143. Alatalo, H., H. Hatakka, J. Kohonen, S.P. Reinikainen, and M. Louhi-kultanen (2010) 'Process control and monitoring of reactive crystallization of L-Glutamic acid' *AICHE Journal*, **56**, pp.2063-2076.
144. Heinrich, J., T. Elter, and J. Ulrich (2011) 'Data preprocessing of in situ laser-backscattering measurements' *Chemical Engineering & Technology*, **34**, pp.977-984.
145. Chianese, A. and H.J.M. Kramer, 2012, *Industrial crystallization process monitoring and control*, Wiley-VCH: Germany.
146. Hamann, C.H., A. Hamnett, and W. Vielstich, 1998, *Electrochemistry*, Wiley-VCH: New York.
147. Taguchi, K., J. Garside, and N.S. Tavaré (1996) 'Nucleation and growth kinetics of barium sulphate in batch precipitation' *Journal of Crystal Growth*, **163**, pp.318-328.
148. Stanley, S.J. (2006) 'Tomographic imaging during reactive precipitation in a stirred vessel: Mixing with chemical reaction' *Chemical Engineering Science*, **61**, pp.7850-7863.
149. Rodgers, T.L., D.R. Stephenson, M. Cooke, T.A. York, and R. Mann (2009) 'Tomographic imaging during semi-batch reactive precipitation of barium sulphate in a stirred vessel' *Chemical Engineering Research & Design*, **87**, pp.615-626.
150. Lloyd, J.M., 1975, *Thermal imaging systems*, Plenum Press: New York.



151. Williams, T.L., 2009, *Thermal imaging cameras: characteristics and performance*, Taylor and Francis: New York.
152. Vollmer, M. and K.P. Mollmann, 2010, *Infrared thermal imaging: fundamentals, research and applications*, WILEY-VCH: Germany.
153. FLIR Systems User's Manual: ThermaCAM SC640, 2007, Publ. No: 1558550, Rev: a201.
154. Kutz, M., 2006, *Mechanical Engineer's Handbook, Energy and Power*, John Wiley & Sons: New Jersey.
155. Cao, B., P. Sweeney, and G.A. Campbell (1989) 'Infrared characteristics of thin polymer film: temperature measurement of polyethylene' *Annual Technical Conference - Society of Plastics Engineers*, New York.
156. Viehmann, W. and A.G. Eubanks, 1972, *Effects of surface contamination on the Infrared emissivity and visible-light scattering of highly reflective surfaces at cryogenic temperatures*, Technical Note, Goddard Space Flight Centre.
157. Kral, J. and E.K. Matthews, 1996, *Pyrolaser & Pyrofiber Infrared Temperature Measurement with Automatic Emissivity Correction*, Available from: <http://www.pyrometer.com/paper0596.htm>, accessed: 2011.
158. Martan, J., N. Semmar, and C. Boulmer-Leborgne (2007) 'IR radiometry optical system view factor and its application to emissivity investigations of solid and liquid phases' *International Journal of Thermophysics*, **28**, pp.1342-1352.
159. Minkina, W. and S. Dudzik, 2009, *Infrared Thermography : Errors and Uncertainties*, John Wiley & Sons Ltd.: Chichester.
160. Abd Shukor, S.R. and M.T. Tham (2004) 'Performance envelopes of process intensified systems' *International Symposium on Advanced Control of Chemical Processes*, Hong Kong.
161. Smith, C.A. and A.B. Corripio, 1997, *Principles and practice of automatic process control*, J. Wiley: New York.
162. Abd Shukor, S.R., 2004, *Studying the control of intensified systems*, Ph.D. thesis, University of Newcastle upon Tyne.
163. Sung, S.W., J. Lee, and I.-B. Lee, 2009, *Process Identification and PID Control*, John Wiley & Sons Inc.: Hoboken.
164. Isaksson, A.J. and S.F. Graebe (1999) 'Analytical PID parameter expressions for higher order systems' *Automatica*, **35**, pp.1121-1130.
165. Skogestad, S. (2003) 'Simple analytic rules for model reduction and PID controller tuning' *Journal of Process Control*, **13**, pp.291-309.
166. Moler, C.B., 2004, *Numerical Computing with MATLAB*, Society for Industrial and Applied Mathematics: USA.
167. Karris, S.T., 2011, *Introduction to Simulink with engineering applications*, Orchard Publications: USA.
168. Johnson, G.W. and R. Jennings, 2006, *LabVIEW graphical programming*, McGraw-Hill: New York.
169. Travis, J. and J. Kring, 2007, *LabVIEW for everyone : graphical programming made easy and fun*, Prentice Hall: Upper Saddle River, NJ.
170. Shinnars, S.M., 1998, *Modern control system theory and design*, J. Wiley: New York.
171. Wolfe, W.L. and G.J. Zissis, 1978, *The Infrared Handbook*, Office of Naval Research:
172. Ziegler, J.G. and N.B. Nichols (1942) 'Optimum settings for automatic controllers' *Transactions of the ASME*, **64**, pp.759-768.
173. Lide, D.R., 2006, *Handbook of Chemistry and Physics*, CRC Press: Boca Raton.

174. Baldyga, J. and J.R. Bourne, 1999, *Turbulent mixing and chemical reactions*, Wiley Chichester.
175. Skelland, A.H.P., 1974, *Diffusional mass transfer*, Wiley: New York.
176. Guo, Z., A.G. Jones, and N. Li (2006) 'The effect of ultrasound on the homogeneous nucleation of BaSO<sub>4</sub> during reactive crystallization' *Chemical Engineering Science*, **61**, pp.1617-1626.
177. Khan, J.R., 1986, *Heat transfer on a rotating surface with and without phase change*, Ph.D. thesis, Newcastle University.
178. Boodhoo, K.V.K. and S.R. Al-hengari (2012) 'Micromixing characteristics in a small scale spinning disc reactor' *Chemical Engineering & Technology*, **35**, pp.1229-1237.
179. Bromley, L.A. (1973) 'Thermodynamic properties of strong electrolytes in aqueous solutions' *AICHE Journal*, **19**, pp.313-320.
180. *NIST Chemistry WebBook*, Available from: <http://webbook.nist.gov/chemistry/>, accessed: 2011.
181. Woods, W.P., 1995, *The hydrodynamics of thin liquid films flowing over a rotating disc*, Ph.D. thesis, Newcastle University.
182. Batchelor, G.K., 1967, *An Introduction to Fluid Dynamics*, Cambridge University Press: Cambridge.
183. Myers, T.G. and M. Lombe (2006) 'The importance of the Coriolis force on axisymmetric horizontal rotating thin film flows' *Chemical Engineering and Processing*, **45**, pp.90-98.
184. Emslie, A.G., F.T. Bonner, and L.G. Peck (1958) 'Flow of a viscous liquid on a rotating disk' *Journal of Applied Physics*, **29**, pp.858-862.
185. Glycerine Producers' Association, 1963, *Physical properties of glycerine and its solutions*, Glycerine Producers' Association: New York.
186. Wagner, C. (1948) 'Heat transfer from a rotating disk to ambient air' *Journal of Applied Physics*, **19**, pp.837-839.

## Appendices

### Appendix A. PID Controller

Figure A-1 illustrates the block diagram representation of a general feedback control loop. The controller objective is to make the controlled variable,  $Y$ , follow the setpoint,  $U$ , by manipulating the variable  $c$ . The error,  $e$ , is the difference between the controlled variable and the setpoint.

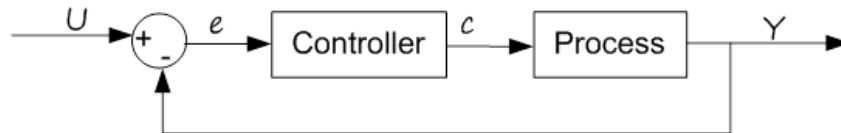


Figure A-1. Feedback control block diagram

The PID controller consists of proportional (P), integral (I) and derivative (D) elements. The P, I and D elements are proportional to the error at time  $t$ , the integral of the error up to time  $t$  and the derivative of the error at time  $t$  respectively. Hence, the PID controller action takes the present, the past and the future of the error into consideration. The ideal PID controller has the following algorithm in the continuous time domain:

$$c(t) = K_c \left( e(t) + \frac{1}{T_I} \int_0^t e(t) dt + T_D \frac{de(t)}{dt} \right) \quad (\text{A-1})$$

where,  $K_c$  = proportional gain

$T_I$  = integral time constant

$T_D$  = derivative time constant

Leading to a controller transfer function as follows:

$$G_c = K_c \left( 1 + \frac{1}{T_I s} + T_D s \right) \quad (\text{A-2})$$

## Appendix B. Controller Design by Direct Synthesis Method

Controller tuning using the direct synthesis approach [B1] for a general feedback loop, as shown in Figure B-1 is outlined in this section. Three overall process models described by third order plus delay, second order plus delay (SOPDT) and first order plus delay (FOPDT) transfer functions are considered.

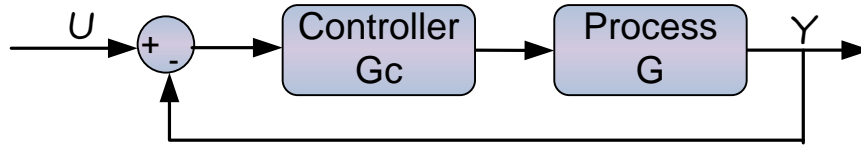


Figure B-1. Closed loop block diagram

The closed loop transfer function of the above system is,

$$\frac{Y}{U} = \frac{G_c G}{1 + G_c G} \quad (\text{B-1})$$

where  $G$  is a transfer function which describes the overall dynamics of the system. Rearranging the closed-loop equation to obtain an expression for  $G_c$  yields the synthesis equation for the controller:

$$G_c = \frac{1}{G} \left( \frac{\frac{Y}{U}}{1 - \frac{Y}{U}} \right) \quad (\text{B-2})$$

The direct synthesis method involves specifying a desired closed loop response in form of a first order plus delay transfer function, as shown below:

$$\frac{Y}{U} = \frac{e^{-\theta s}}{\lambda s + 1} \quad (\text{B-3})$$

where  $\lambda$  is a user specified closed loop time constant. For a third order plus delay model of the following form,

$$G = \frac{k}{(\tau_1 s + 1)(\tau_2 s + 1)(\tau_3 s + 1)} e^{-\theta s} \quad (\text{B-4})$$

where,  $k$  is the open loop gain and  $\tau_1$ ,  $\tau_2$  and  $\tau_3$  could represent the time constants of the process, actuator and measurement device. Approximating the delay terms using a first order Taylor series expansion:

$$e^{-\theta s} \approx 1 - \theta s \quad (\text{B-5})$$

and substituting for the overall process model and the desired closed loop response in the synthesis equation yields a controller of the form:

$$G_c = \frac{(\tau_1 s + 1)(\tau_2 s + 1)(\tau_3 s + 1)}{k(\lambda + \theta)s} \quad (\text{B-6})$$

Further expansion and rearrangement of the above terms lead to the following expression, which is equivalent to a PID<sup>2</sup> controller,

$$G_c = \frac{\tau_1 + \tau_2 + \tau_3}{k(\lambda + \theta)} \left( 1 + \frac{1}{(\tau_1 + \tau_2 + \tau_3)s} + \frac{\tau_1\tau_2 + \tau_1\tau_3 + \tau_2\tau_3}{\tau_1 + \tau_2 + \tau_3} s + \frac{\tau_1\tau_2\tau_3}{\tau_1 + \tau_2 + \tau_3} s^2 \right) \quad (\text{B-7})$$

or equally:

$$G_c = K_c \left( 1 + \frac{1}{T_I s} + T_D s + T_{D^2} s^2 \right) \quad (\text{B-8})$$

If the direct synthesis method is applied to a SOPDT overall process model of the form,

$$G = \frac{k}{(\tau_1 s + 1)(\tau_2 s + 1)} e^{-\theta s} \quad (\text{B-9})$$

a PID controller with the following parameters is achieved:

$$G_c = \frac{\tau_1 + \tau_2}{k(\lambda + \theta)} \left( 1 + \frac{1}{(\tau_1 + \tau_2)s} + \frac{\tau_1\tau_2}{\tau_1 + \tau_2} s \right) \quad (\text{B-10})$$

or equivalently:

$$G_c = K_c \left( 1 + \frac{1}{T_I s} + T_D s \right) \quad (\text{B-11})$$

Similar approach for a FOPDT overall process model of the following format,

$$G = \frac{k}{\tau s + 1} e^{-\theta s} \quad (\text{B-12})$$

yields a PI controller, as presented below:

$$G_c = \frac{\tau}{k(\lambda + \theta)} \left( 1 + \frac{1}{\tau s} \right) \quad (\text{B-13})$$

Or,

$$G_c = K_c \left( 1 + \frac{1}{T_I s} \right) \quad (\text{B-14})$$

Therefore, the direct synthesis method applied to 3<sup>rd</sup>, 2<sup>nd</sup> and 1<sup>st</sup> order overall process models leads to PID<sup>2</sup>, PID and PI control structures respectively.

### Reference

B1. Smith, C.A. and A.B. Corripio, 1997, *Principles and practice of automatic process control*, J. Wiley: New York.

### **Appendix C. Controller Model Order Reduction by Maclaurin Series Expansion**

The PID<sup>2</sup> controller equation may be rearranged in the following format,

$$G_c = \frac{f(s)}{s} = \frac{1}{s} \left( K_c T_{D^2} s^3 + K_c T_D s^2 + K_c s + \frac{K_c}{T_I} \right) \quad (C-1)$$

The first and second derivatives of the transfer function  $f(s)$  are given by,

$$f'(s) = 3K_c T_{D^2} s^2 + 2K_c T_D s + K_c \quad (C-2)$$

$$f''(s) = 6K_c T_{D^2} s + 2K_c T_D \quad (C-3)$$

Therefore, by applying the Maclaurin series expansion to the high order controller and only taking the first 3 terms into account a PID control structure is obtained:

$$G_c^* = \frac{1}{s} \left[ f(0) + f'(0)s + \frac{f''(0)}{2!} s^2 \right] = \frac{1}{s} \left[ \frac{K_c}{T_I} + K_c s + \frac{K_c T_D}{2!} s^2 \right] = K_c \left[ 1 + \frac{1}{T_I s} + T_D s \right] \quad (C-4)$$

Whilst if only the first two terms of the expansion are considered a PI controller is designed:

$$G_c^* = \frac{1}{s} [f(0) + f'(0)s] = \frac{1}{s} \left[ \frac{K_c}{T_I} + K_c s \right] = K_c \left[ 1 + \frac{1}{T_I s} \right] \quad (C-5)$$

### Appendix D. Order Reduction for Simulated Intensified & Conventional Systems

In the present study the simulated intensified system has a time constant 100 times smaller than that of the simulated conventional system. Whilst the instrumentation dynamics and time delay for both systems are identical as presented in Table D-1.

Table D-1. Control loop elements

	<i>Conventional</i>	<i>Intensified</i>
<i>Process</i>	$\frac{1}{10s+1}$	$\frac{1}{0.1s+1}$
<i>Actuator</i>	$\frac{1}{0.2s+1}$	$\frac{1}{0.2s+1}$
<i>Measurement device</i>	$\frac{1}{0.2s+1}$	$\frac{1}{0.2s+1}$
<i>Time delay</i>	$e^{-s}$	$e^{-s}$

Reduction of the above third order process models to first or second orders are outlined in the following sections.

#### D1. Step Response

The open loop responses of the simulated conventional and intensified systems are presented in Figure D-1 and Figure D-2 respectively.

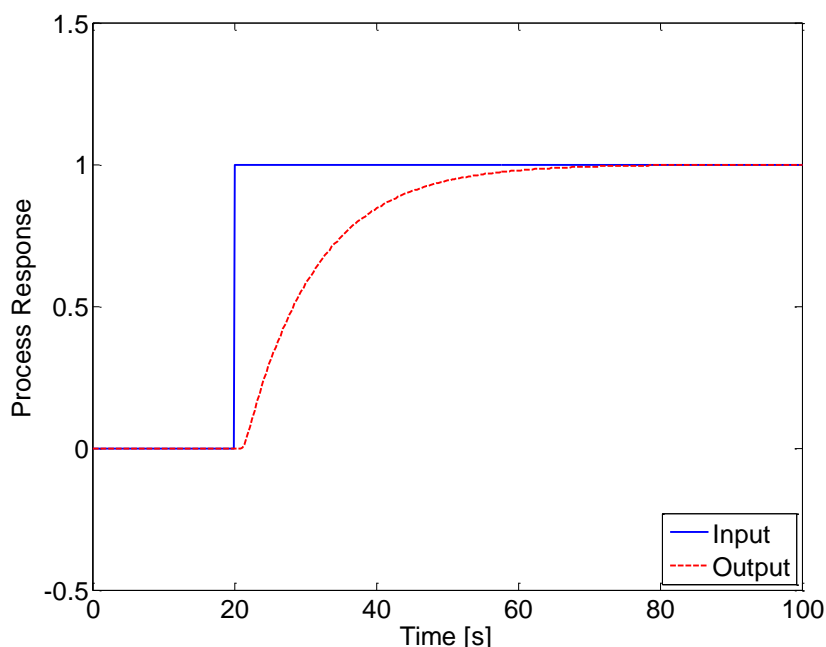


Figure D-1. Step response of the simulated conventional system

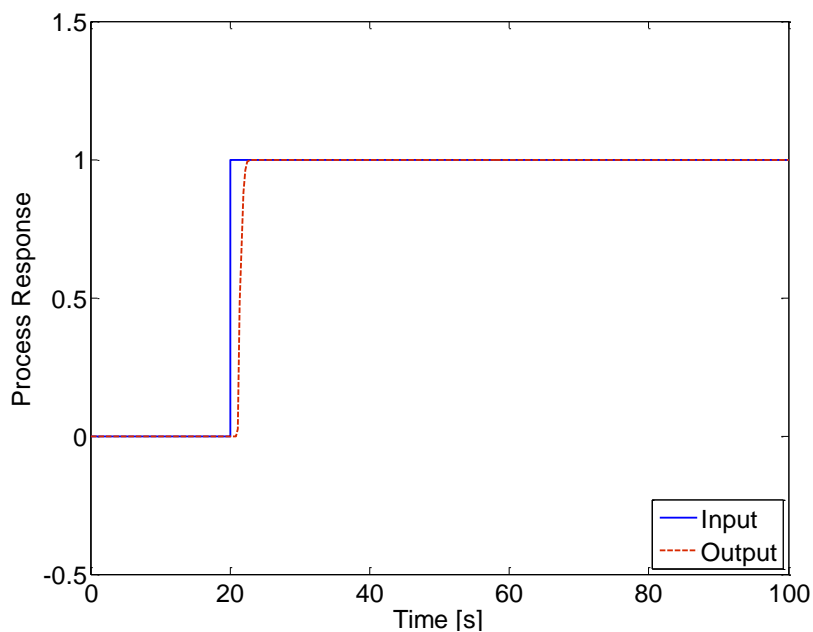


Figure D-2. Step response of the simulated intensified system

The step response of the third order conventional system yields the following first order approximation of the system:

$$G^* = \frac{1}{10.4s + 1} e^{-s} \quad (\text{D-1})$$

Similarly the reduced order approximation of the intensified system is determined as,

$$G^* = \frac{1}{0.5s + 1} e^{-s} \quad (\text{D-2})$$

## D2. Frequency Response

The overall process model for the simulated conventional system is given by,

$$G = \frac{1}{(10s + 1)(0.2s + 1)^2} e^{-s} = \frac{1}{0.4s^3 + 4.04s^2 + 10.4s + 1} e^{-s} \quad (\text{D-3})$$

The frequency response of the delay free segment of the above transfer function is presented in Figure D-3.



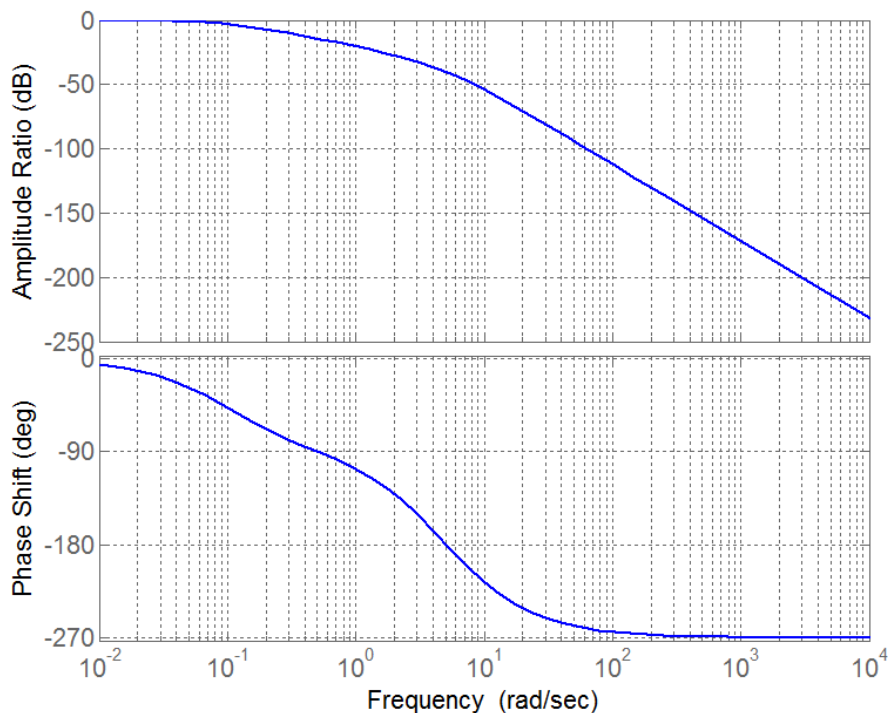


Figure D-3. Frequency response of the simulated conventional system

From the above figure the overall gain, time constant and delay may be calculated:

$$20\log k = 0 \Rightarrow k = 1$$

$$\omega_c = 1.3 \Rightarrow \tau = 0.77$$

$$\theta = -\frac{\phi(\omega_c) + 45}{57.3\omega_c} = -\frac{-115 + 45}{57.3 \times 1.3} = 0.94$$

Adding the initial delay of 1s to that estimated above yields the following FOPDT approximation of the simulated conventional system by the frequency response method:

$$G^* = \frac{1}{0.77s + 1} e^{-1.94s} \quad (\text{D-4})$$

Similarly the overall process model for the simulated intensified system is used to obtain the bode plot presented in Figure D-4.

$$G = \frac{1}{(0.1s + 1)(0.2s + 1)^2} e^{-s} = \frac{1}{0.004s^3 + 0.08s^2 + 0.5s + 1} e^{-s} \quad (\text{D-5})$$

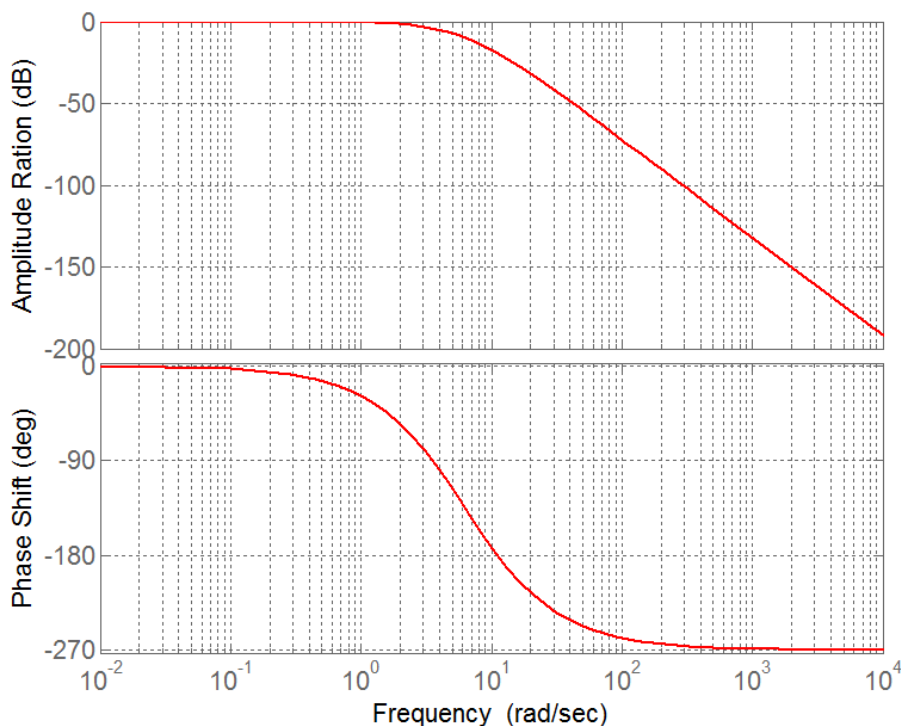


Figure D-4. Frequency response of the simulated intensified system

Therefore the overall gain, time constant and delay may be estimated as:

$$20\log k = 0 \Rightarrow k = 1$$

$$\omega_c = 6 \Rightarrow \tau = 0.17$$

$$\theta = -\frac{\phi(\omega_c) + 45}{57.3\omega_c} = -\frac{-131 + 45}{57.3 \times 6} = 0.25$$

Upon addition of the initial delay the following FOPDT model is obtained:

$$G^* = \frac{1}{0.17s + 1} e^{-1.25s} \quad (\text{D-6})$$

### D3. Isaksson and Graebe's Method

The original model for the simulated conventional system is,

$$G = \frac{B}{A} = \frac{1}{(10s + 1)(0.2s + 1)^2} e^{-s} = \frac{1}{0.4s^3 + 4.04s^2 + 10.4s + 1} e^{-s} \quad (\text{D-7})$$

By applying the Isaksson and Graebe's reduction method [D1] to the delay free segment of the model, polynomials that contain the slowest roots ( $B_1$  and  $A_1$ ) and polynomials that retain only the low order terms ( $B_2$  and  $A_2$ ) are determined:

$$B_1 = B_2 = 1$$

$$A_1 = 10s + 1$$

$$A_{2a} = 4.04s^2 + 10.4s + 1 \quad \text{Or,}$$

$$A_{2b} = 10.4s + 1$$

Note that  $A_{2a}$  leads to a second order, whilst  $A_{2b}$  results in a first order model as follows:

$$G^*(s) = \frac{\frac{1}{2}(B_1(s) + B_2(s))}{\frac{1}{2}(A_1(s) + A_2(s))} = \frac{\frac{1}{2}(1+1)}{\frac{1}{2}((10s+1) + (4.04s^2 + 10.4s + 1))} = \frac{1}{2.02s^2 + 10.2s + 1} \quad (D-8)$$

Or,

$$G^*(s) = \frac{\frac{1}{2}(1+1)}{\frac{1}{2}((10s+1) + (10.4s + 1))} = \frac{1}{10.2s + 1} \quad (D-9)$$

SOPDT and FOPDT models are then simply obtained by adding the initial delay term to the above reduced transfer functions. Following the same procedure for the simulated intensified system leads to,

$$G = \frac{B}{A} = \frac{1}{(0.1s+1)(0.2s+1)^2} e^{-s} = \frac{1}{0.004s^3 + 0.08s^2 + 0.5s + 1} e^{-s} \quad (D-10)$$

$$B_1 = B_2 = 1$$

$$A_1 = 0.2s + 1$$

$$A_{2a} = 0.08s^2 + 0.5s + 1 \quad \text{Or,}$$

$$A_{2b} = 0.5s + 1$$

$$G^*(s) = \frac{\frac{1}{2}(1+1)}{\frac{1}{2}((0.2s+1) + (0.08s^2 + 0.5s + 1))} = \frac{1}{0.04s^2 + 0.35s + 1} \quad (D-11)$$

Or,

$$G^*(s) = \frac{\frac{1}{2}(1+1)}{\frac{1}{2}((0.2s+1) + (0.5s + 1))} = \frac{1}{0.35s + 1} \quad (D-12)$$

Similarly, SOPDT and FOPDT models are obtained by adding the initial delay term to the above reduced models.

#### D4. Skogestad's Method

Applying the Skogestad's half rule [D2] to the original model of the simulated conventional systems yields the following first order plus delay model:

$$\tau = \tau_{10} + \frac{\tau_{20}}{2} = 10 + \frac{0.2}{2} = 10.1$$

$$\theta = \theta_0 + \frac{\tau_{20}}{2} + \sum_{i \geq 3} \tau_{i0} + \sum_j T_{j0} + \frac{T_s}{2} = 1 + \frac{0.2}{2} + 0.2 + 0 + 0 = 1.3$$

$$G^* = \frac{1}{10.1s+1} e^{-1.3s} \quad (\text{D-13})$$

Or alternatively the following second order plus delay model:

$$\begin{aligned} \tau_1 &= \tau_{10} = 10 \\ \tau_2 &= \tau_{20} + \frac{\tau_{30}}{2} = 0.2 + \frac{0.2}{2} = 0.3 \\ \theta &= \theta_0 + \frac{\tau_{30}}{2} + \sum_{i \geq 4} \tau_{i0} + \sum_j T_{j0} + \frac{T_s}{2} = 1 + \frac{0.2}{2} + 0 + 0 + 0 = 1.1 \\ G^* &= \frac{1}{(10s+1)(0.3s+1)} e^{-1.1s} \end{aligned} \quad (\text{D-14})$$

Note that the denominator time constants of the original model must be arranged in descending order. Following the same procedure for the simulated intensified system results in a first order plus delay model,

$$\begin{aligned} \tau &= \tau_{10} + \frac{\tau_{20}}{2} = 0.2 + \frac{0.2}{2} = 0.3 \\ \theta &= \theta_0 + \frac{\tau_{20}}{2} + \sum_{i \geq 3} \tau_{i0} + \sum_j T_{j0} + \frac{T_s}{2} = 1 + \frac{0.2}{2} + 0.1 + 0 + 0 = 1.2 \\ G^* &= \frac{1}{0.3s+1} e^{-1.2s} \end{aligned} \quad (\text{D-15})$$

Or alternatively the following second order plus delay model:

$$\begin{aligned} \tau_1 &= \tau_{10} = 0.2 \\ \tau_2 &= \tau_{20} + \frac{\tau_{30}}{2} = 0.2 + \frac{0.1}{2} = 0.25 \\ \theta &= \theta_0 + \frac{\tau_{30}}{2} + \sum_{i \geq 4} \tau_{i0} + \sum_j T_{j0} + \frac{T_s}{2} = 1 + \frac{0.1}{2} + 0 + 0 + 0 = 1.05 \\ G^* &= \frac{1}{(0.2s+1)(0.25s+1)} e^{-1.05s} \end{aligned} \quad (\text{D-16})$$

### References

- D1. Isaksson, A.J. and S.F. Graebe (1999) 'Analytical PID parameter expressions for higher order systems' *Automatica*, **35**, pp.1121-1130.  
D2. Skogestad, S. (2003) 'Simple analytic rules for model reduction and PID controller tuning' *Journal of Process Control*, **13**, pp.291-309.

### Appendix E. pH Control Loop in Simulink

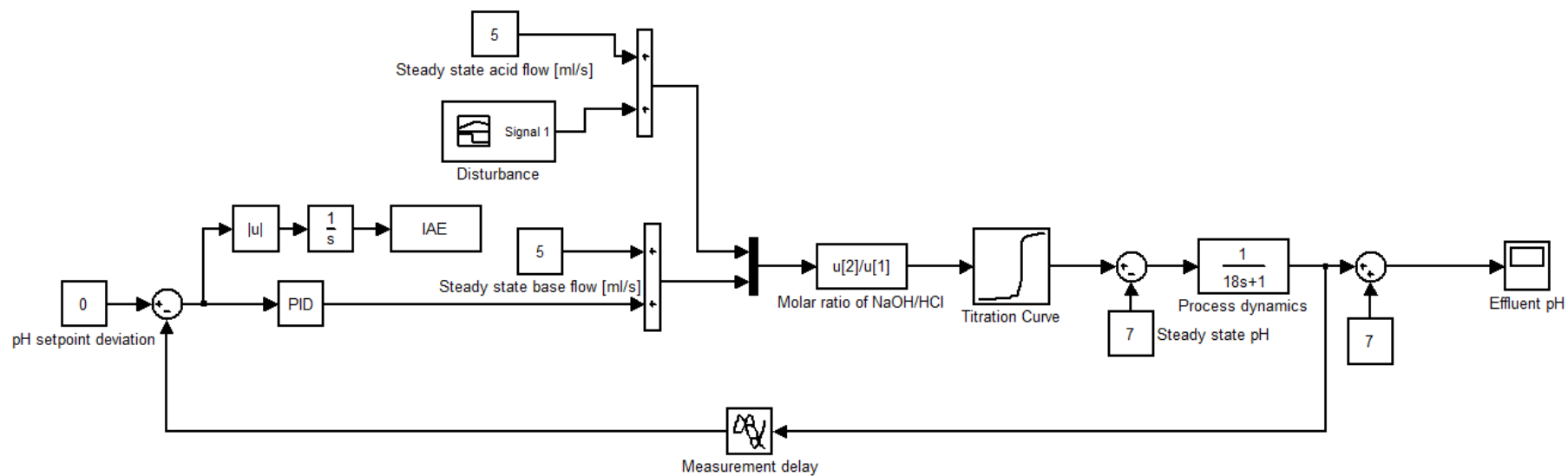


Figure E-1. Feedback control loop [PI controller]

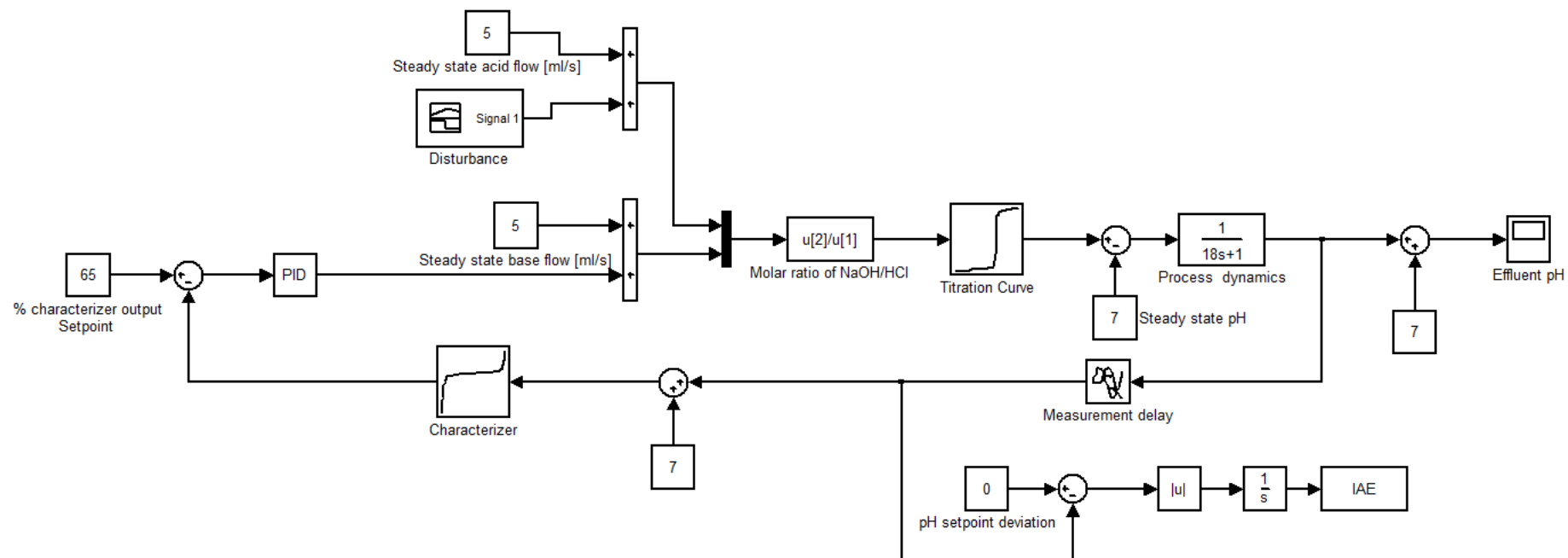


Figure E-2. Feedback control loop [PI controller plus pH characteriser]

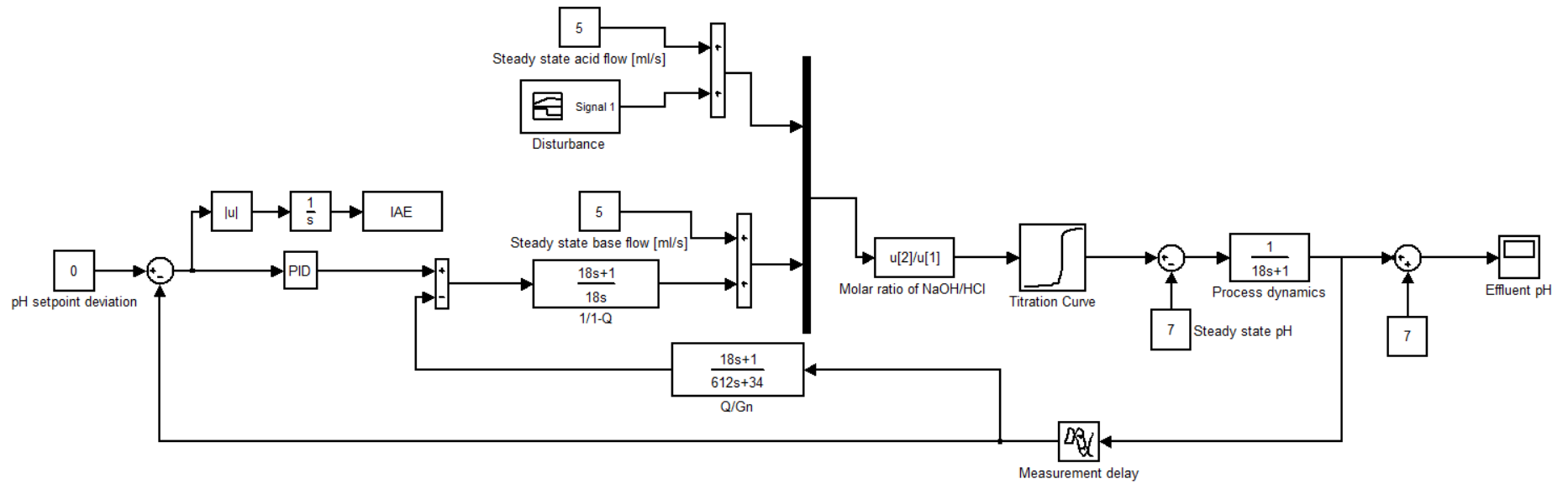


Figure E-3. Feedback control loop [PI controller plus DO]

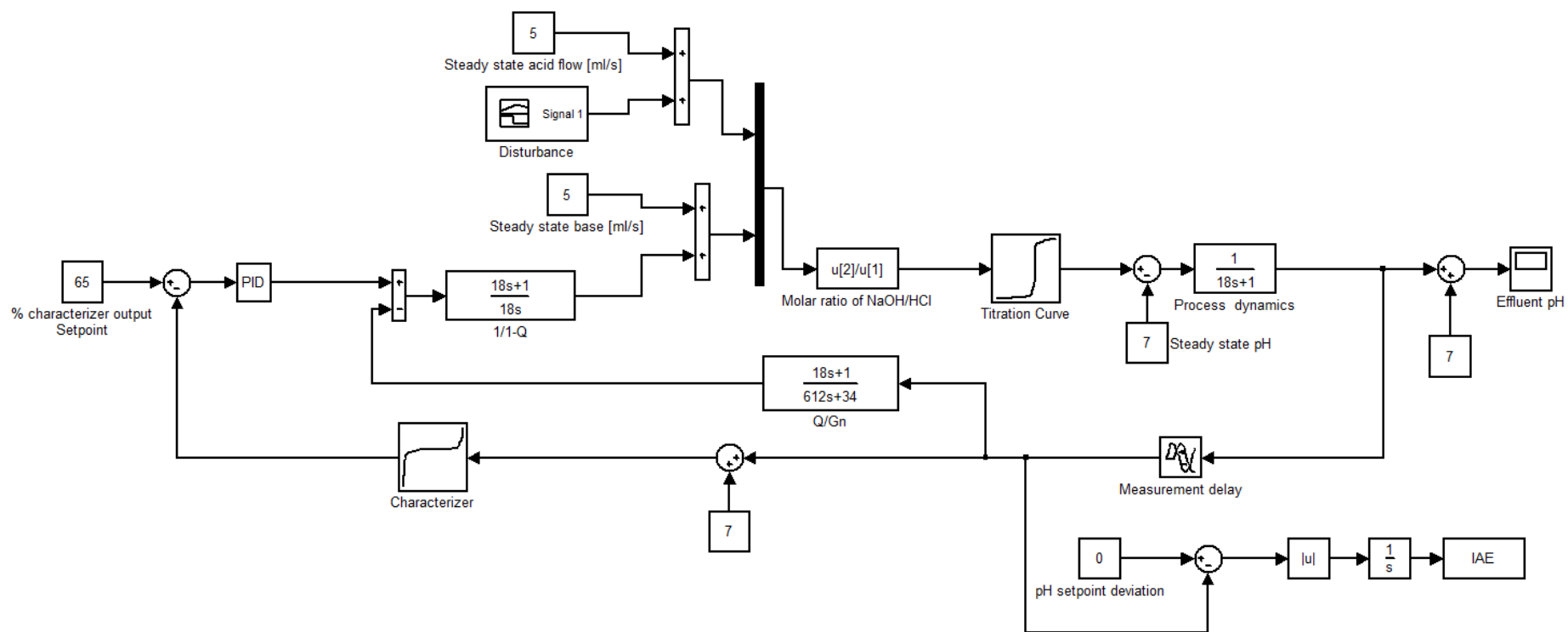


Figure E-4. Feedback control loop [PI controller plus pH characteriser and DO]



Appendix F. pH Control Loop in LabVIEW

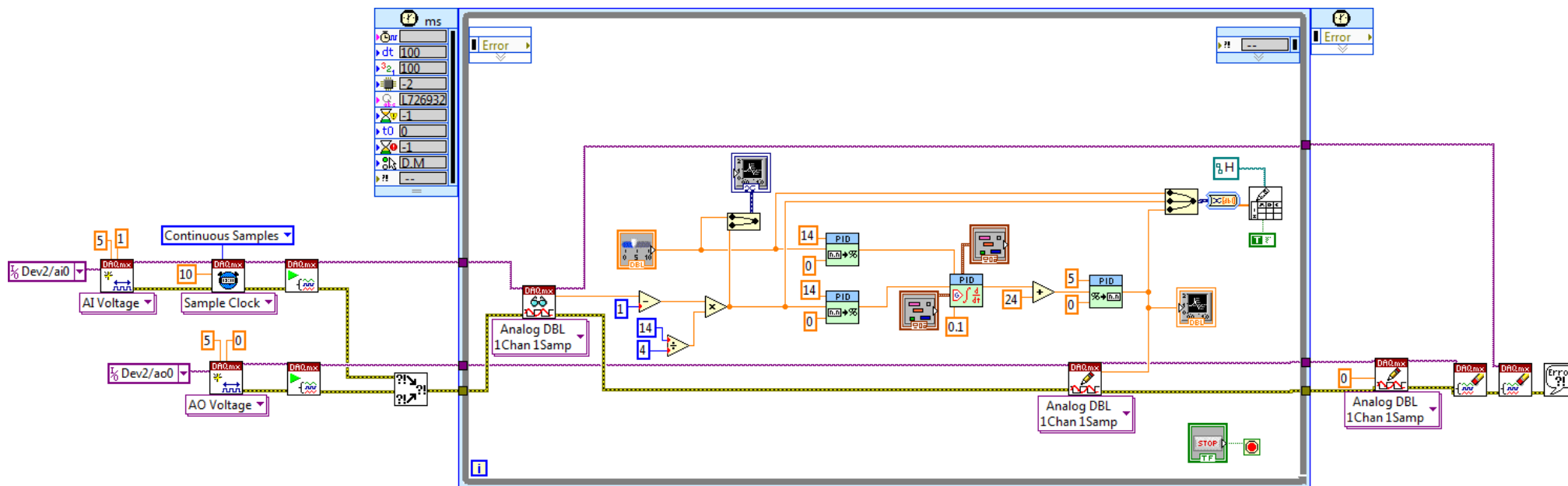


Figure F-1. LabVIEW block diagram [PID controller]

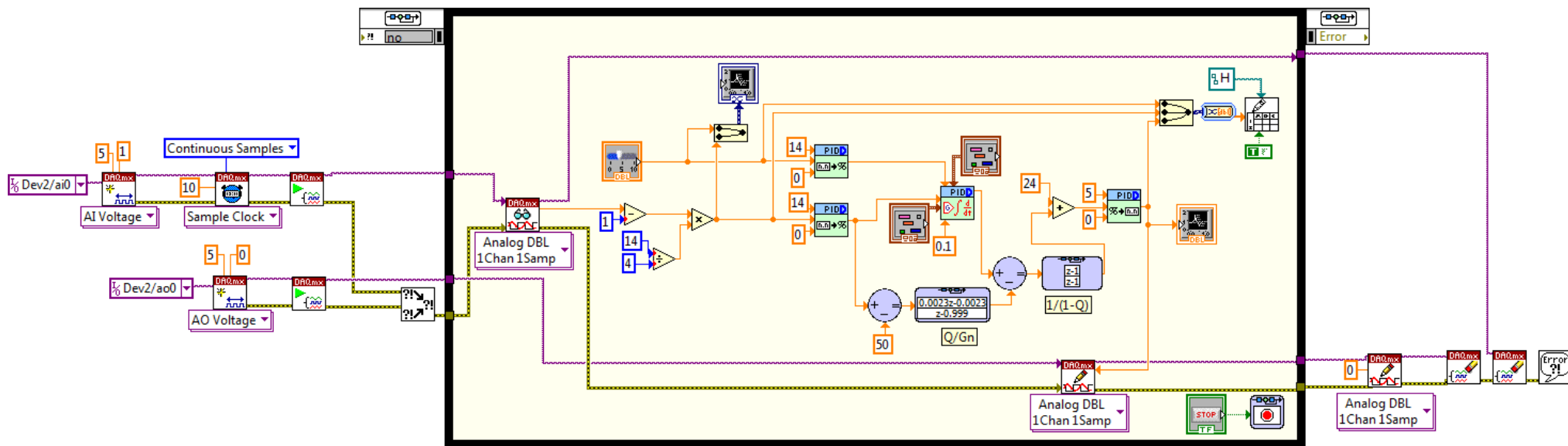


Figure F-2. LabVIEW block diagram [PID controller plus DO]

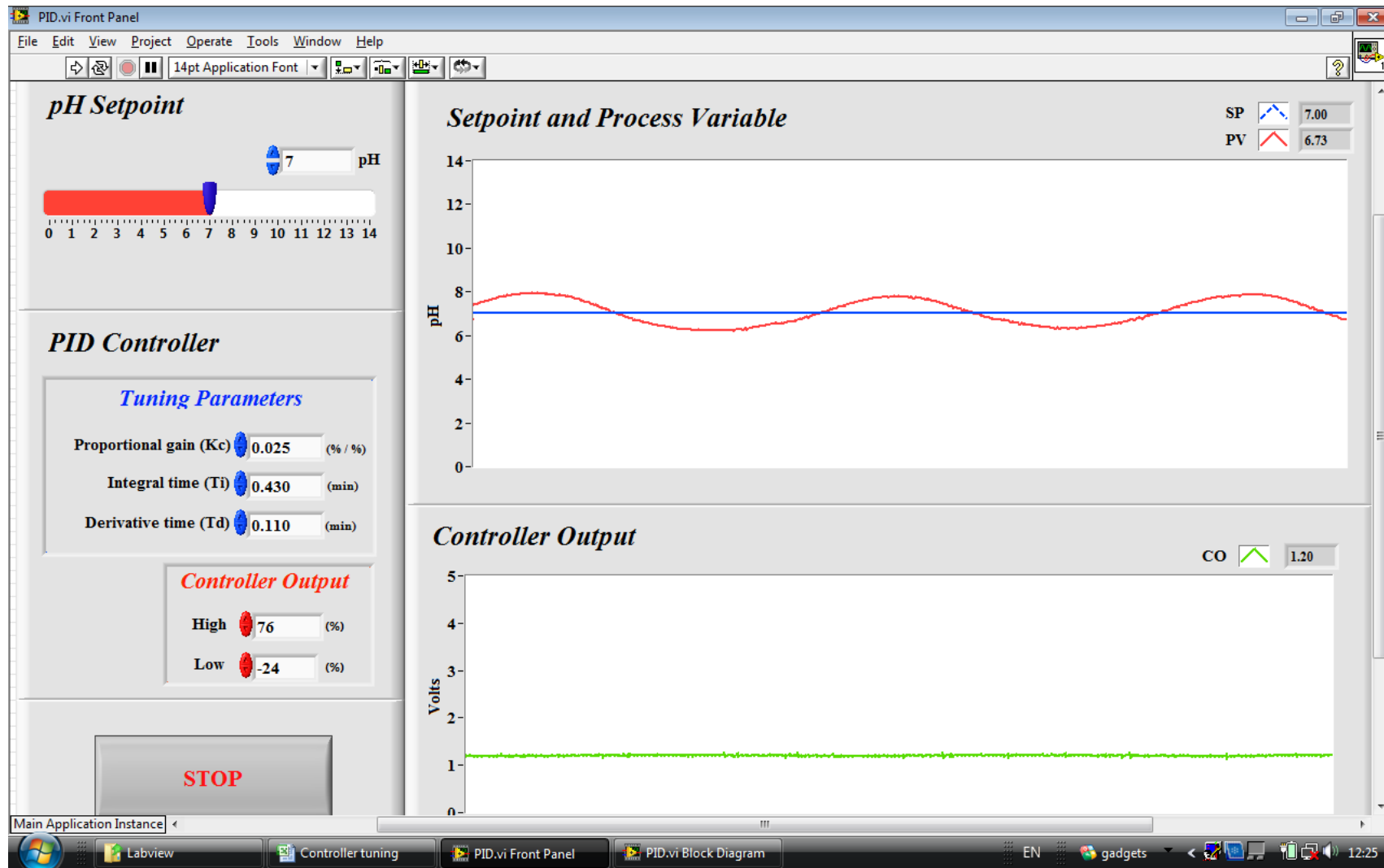


Figure F-3. LabVIEW front panel

Appendix G. Conductivity Control Loop in LabVIEW

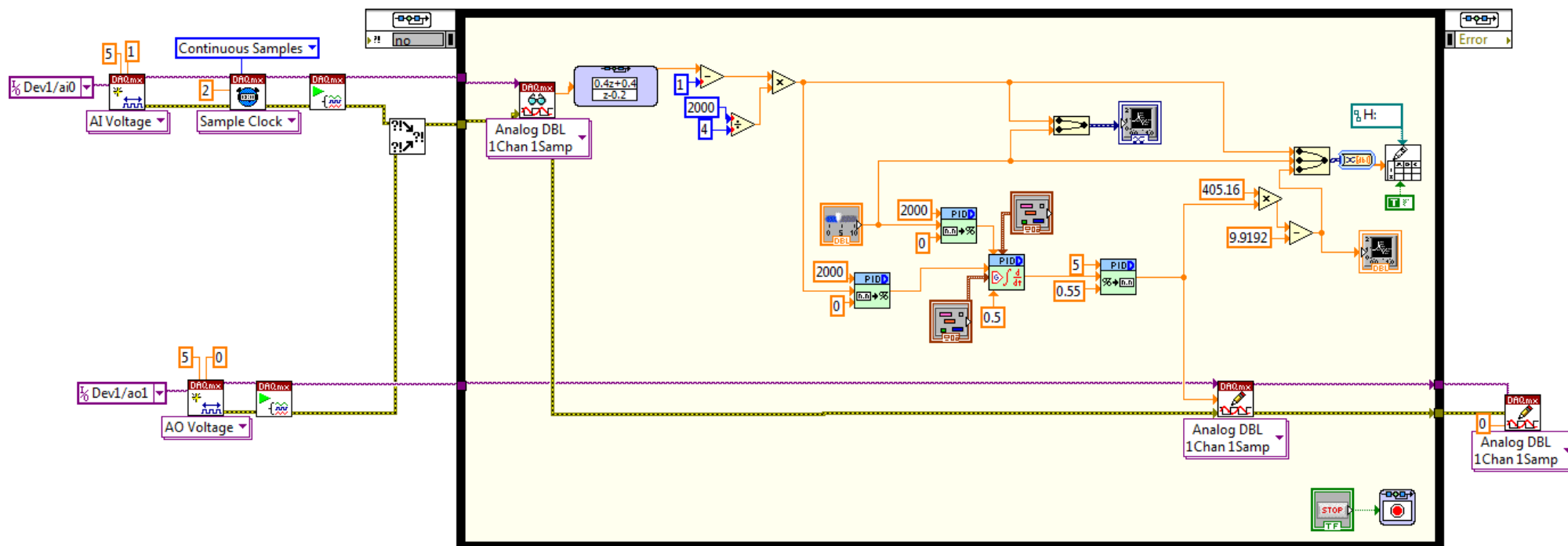


Figure G-1. LabVIEW block diagram [PI controller]

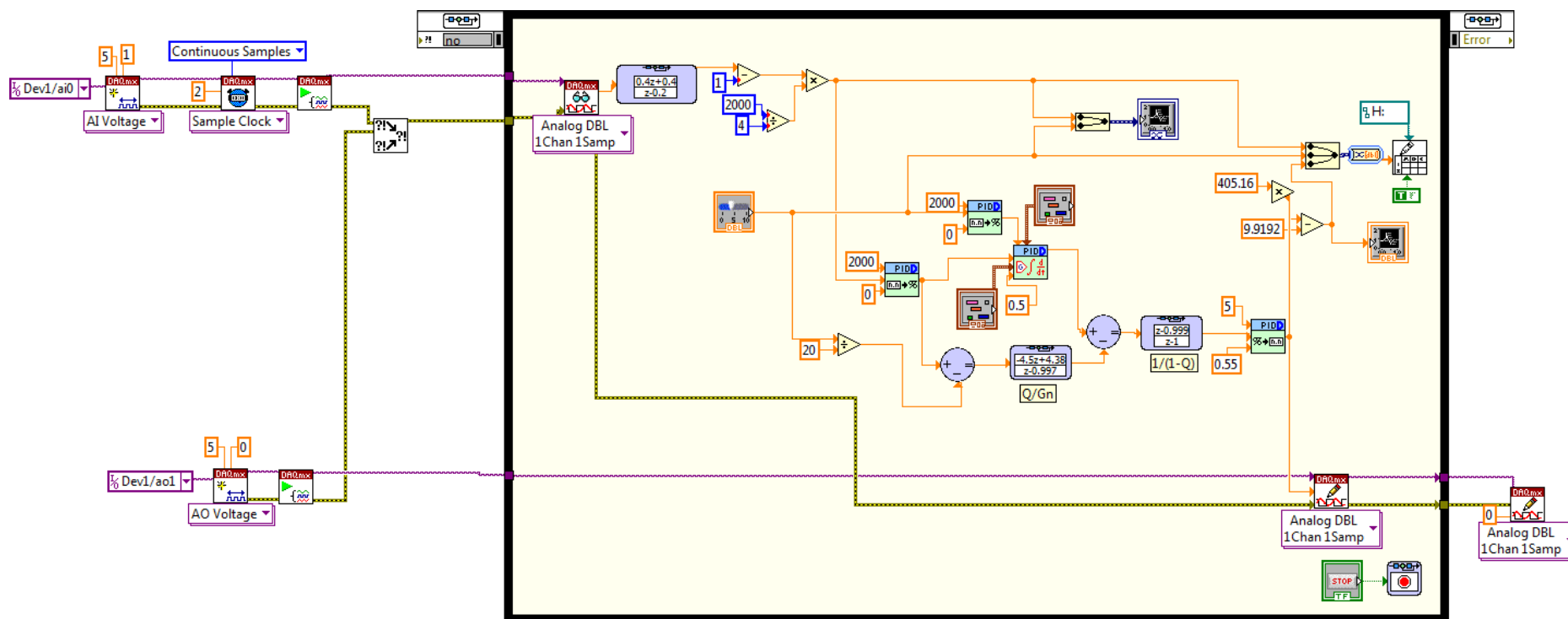


Figure G-2. LabVIEW block diagram [PI controller plus DO]

### Appendix H. Calculation of Diffusion Coefficient

The diffusion coefficient can be calculated using the Scheibel equation [H1], presented below:

$$D_{AB} = \frac{8.2 \times 10^{-8} T}{\mu V_A^{1/3}} \left[ 1 + \left( \frac{3V_B}{V_A} \right)^{2/3} \right] \quad (\text{H-1})$$

Where,  $D_{AB}$  = diffusion coefficient [ $\text{cm}^2/\text{s}$ ]

$T$  = absolute temperature [K]

$\mu$  = solution viscosity [cP]

$V_A$  = molar volume of solute [ $\text{cm}^3/\text{mol}$ ]

$V_B$  = molar volume of solvent [ $\text{cm}^3/\text{mol}$ ]

For barium sulphate in water at 25°C the following input parameters are used:

$$\mu = 0.89 \text{ cP}$$

$$W_{\text{BaSO}_4} = 233.43 \text{ g/mol}$$

$$\rho_{\text{BaSO}_4} = 4.5 \text{ g/cm}^3$$

$$W_{\text{H}_2\text{O}} = 18 \text{ g/mol}$$

$$\rho_{\text{H}_2\text{O}} = 0.997 \text{ g/cm}^3$$

Therefore, the diffusion coefficient is equal to:

$$D_{AB} = \frac{8.2 \times 10^{-8} \times 298.15}{0.89 \left( \frac{233.43}{4.5} \right)^{1/3}} \left[ 1 + \left( \frac{3 \times 18}{\frac{0.997}{233.43}} \right)^{2/3} \right] = 1.49 \times 10^{-5} \text{ cm}^2/\text{s} = 1.49 \times 10^{-9} \text{ m}^2/\text{s}$$

#### Reference

H1. Skelland, A.H.P., 1974, *Diffusional mass transfer*, Wiley: New York.

### Appendix I. Calculation of Activity Coefficient

The activity coefficient of BaSO<sub>4</sub> salt may be calculated using the following expression [I1]:

$$\log \gamma_{12} = \frac{-A_\gamma |Z_1 Z_2| \sqrt{I}}{1 + \sqrt{I}} + \frac{|Z_1 Z_2|}{|Z_1| + |Z_2|} \left[ \frac{F_1}{|Z_1|} + \frac{F_2}{|Z_2|} \right] \quad (\text{I-1})$$

Where,  $A_\gamma$  is the Debye-Huckel constant (0.511 at 25°C),  $Z$  is the ion charge number and  $I$  denotes the ionic strength, whilst,  $F_1$  and  $F_2$  are functions. The following individual ion values are required to carry out the calculations [I1].

Table I-1. Individual ion values in an aqueous solution at 25°C

Ion	Ion number	B (kg/mol)	$\delta$
Ba <sup>2+</sup>	1	0.0022	0.098
SO <sub>4</sub> <sup>2-</sup>	2	0	-0.4
Na <sup>+</sup>	3	0	0.028
Cl <sup>-</sup>	4	0.0643	-0.067

The calculation of the activity coefficient involving 0.01M feed solutions is outlined here as an example, whilst the numbers in the subscripts correspond to the ionic species present in the system (see Table I-1).

$$|Z_1| = |Z_2| = 2, \quad |Z_3| = |Z_4| = 1$$

$$I = 0.5 \sum C_i Z_i^2 = \frac{(0.01 \times 2^2) + (0.01 \times 2^2) + (0.02 \times 1^2) + (0.02 \times 1^2)}{2} = 0.06 \text{ mol/kg}$$

$$Z_{12} = \frac{Z_1 + Z_2}{2} = \frac{2+2}{2} = 2$$

$$Z_{14} = \frac{2+1}{2} = 1.5$$

$$Z_{32} = \frac{1+2}{2} = 1.5$$

$$B_{12} = B_1 + B_2 + \delta_1 \delta_2 = 0.0022 + 0 + 0.098 \times (-0.4) = -0.037 \text{ kg/mol}$$

$$B_{14} = 0.0022 + 0.0643 + 0.098 \times (-0.067) = 0.06 \text{ kg/mol}$$

$$B_{32} = 0 + 0 + 0.028 \times (-0.4) = -0.0112 \text{ kg/mol}$$

$$\bullet \bar{B}_{12} = \frac{(0.06 + 0.6 B_{12}) |Z_1 Z_2|}{\left(1 + \frac{1.5 I}{|Z_1 Z_2|}\right)^2} + B_{12} = \frac{(0.06 + 0.6 \times (-0.037)) \times 4}{\left(1 + \frac{1.5 \times 0.06}{4}\right)^2} - 0.037 = 0.1076 \text{ kg/mol}$$

$$\bullet \bar{B}_{14} = \frac{(0.06 + 0.6 \times 0.06) \times 2}{\left(1 + \frac{1.5 \times 0.06}{2}\right)^2} + 0.06 = 0.2357 \text{ kg/mol}$$

$$\dot{B}_{23} = \frac{(0.06 + 0.6 \times (-0.0112)) \times 2}{\left(1 + \frac{1.5 \times 0.06}{2}\right)^2} - 0.0112 = 0.0864 \text{ kg/mol}$$

$$F_1 = \dot{B}_{12} Z_{12}^2 C_2 + \dot{B}_{14} Z_{14}^2 C_4 = 0.1076 \times 2^2 \times 0.01 + 0.2357 \times 1.5^2 \times 0.02 = 0.0149$$

$$F_2 = \dot{B}_{12} Z_{12}^2 C_1 + \dot{B}_{32} Z_{32}^2 C_3 = 0.1076 \times 2^2 \times 0.01 + 0.0864 \times 1.5^2 \times 0.02 = 0.0082$$

$$\log \gamma_{12} = \frac{-0.511 \times 4 \times \sqrt{0.06}}{1 + \sqrt{0.06}} + \frac{4}{2+2} \left[ \frac{0.0149}{2} + \frac{0.0082}{2} \right] = -0.391$$

$$\gamma_{12} = 0.4068$$

### Reference

II. Bromley, L.A. (1973) 'Thermodynamic properties of strong electrolytes in aqueous solutions' *AIChE Journal*, **19**, pp.313-320.



## Appendix J. Semi-Analytical Model of Barium Sulphate Precipitation

The following differential equation [J1] is solved numerically to estimate the concentration profiles of the chemical species with respect to time in a homogeneous zero-dimensional reaction zone.

$$\begin{aligned} \frac{d^4 C}{dt^4} = & -2BKk_g^2(\alpha C - 1)^6 \exp\left[\frac{-A}{\ln^2(\alpha C)}\right] + \frac{14\alpha}{\alpha C - 1} \frac{dC}{dt} \frac{d^3 C}{dt^3} - \frac{86\alpha^2}{(\alpha C - 1)^2} \left(\frac{dC}{dt}\right)^2 \frac{d^2 C}{dt^2} \\ & + \frac{80\alpha^3}{(\alpha C - 1)^3} \left(\frac{dC}{dt}\right)^4 + \frac{8\alpha}{\alpha C - 1} \left(\frac{d^2 C}{dt^2}\right)^2 \end{aligned} \quad (J-1)$$

Where, the parameters and constants used in the simulations are outlined in Table J-1.

Table J-1. Simulation parameters

Notation	Description	Value/formula	units
$C$	concentration		mol/l
$t$	time		s
$A$	nucleation kinetic constant	2686 ( $S \geq 1000$ ) 67.3 ( $1 < S < 1000$ )	-
$B$	nucleation rate constant	$10^{36}$ ( $S \geq 1000$ ) $1.46 * 10^{12}$ ( $1 < S < 1000$ )	no. crystals/( $m^3 s$ )
$K$	parameter used in the model	$3k_g k_v \frac{\rho_{BaSO_4}}{W_{BaSO_4}}$	
$k_g$	growth rate constant	$4 * 10^{-11}$	m/s
$k_v$	volume shape factor	$\pi/6$	-
$\rho_{BaSO_4}$	density	4480	kg/ $m^3$
$W_{BaSO_4}$	molecular weight	233.39	kg/kmol
$\alpha$	parameter used in the model	$\frac{\gamma}{\sqrt{K_{sp}}}$	
$\gamma$	activity coefficient	see Appendix I	-
$K_{sp}$	solubility product	$1.1 * 10^{-10}$	mol <sup>2</sup> /dm <sup>6</sup>

### Reference

J1. Oncul, A.A., K. Sundmacher, A. Seidel-Morgenstern, and D. Thevenin (2006) 'Numerical and analytical investigation of barium sulphate crystallization' *Chemical Engineering Science*, **61**, pp.652-664.

## Appendix K. Therminol SP Properties

Typical physical, chemical and thermal properties:

Composition		Mixture of synthetic hydrocarbons
Appearance		Clear yellow liquid
Max. bulk temperature		315°C
Max. film temperature		335°C
Kinematic viscosity @ 40°C	DIN 51562 - 1	19.0 mm <sup>2</sup> /s (cSt)
Density @ 15°C	DIN 51757	875 kg/m <sup>3</sup>
Flash point	DIN EN 22719	166°C
	DIN 51376	177°C
Fire point	ISO 2592	218°C
Autoignition temperature	DIN 51794	366°C
Pour point	ISO 3016	-40°C
Boiling point @ 1013 mbar		351°C
Coefficient of thermal expansion		0.00096/°C
Moisture content	DIN 51777 - 1	< 150 ppm
Total acidity	DIN 51558 - 1	< 0.2 mg KOH/g
Chlorine content	DIN 51577 - 3	< 10 ppm
Copper corrosion	EN ISO 2160	<< 1a
Average molecular weight		320

Physical property formulae:

$$\text{Density (kg/m}^3\text{)} = 885.597 - 0.689367 * T(\text{°C}) + 1.9228 * 10^{-4} * T^2(\text{°C}) - 8.87642 * 10^{-7} * T^3(\text{°C})$$

$$\text{Heat Capacity (kJ/kg.K)} = 1.83369 + 0.0036172 * T(\text{°C}) - 4.94238 * 10^{-7} * T^2(\text{°C}) + 7.98115 * 10^{-10} * T^3(\text{°C})$$

$$\text{Thermal Conductivity (W/m.K)} = 0.131281 - 0.000114034 * T(\text{°C}) - 1.49876 * 10^{-8} * T^2(\text{°C}) + 1.76622 * 10^{-11} * T^3(\text{°C})$$

$$\text{Kinematic Viscosity (mm}^2\text{/s)} = e \left( \frac{798.89}{T(\text{°C})+97.7} - 2.65773 \right)$$

## ***Appendix L. Presentations and Publications***

The results of the current research project have been presented in several international conferences and also published in form of Journal articles, as outlined below:

### *Presentations*

1. 'Control of process intensified equipment: pH control in a SDR', 3<sup>rd</sup> European Conference on Process Intensification, Manchester, U.K, 20-23 June 2011.
2. 'Thermographic analysis of thin liquid films on a rotating disc' 8<sup>th</sup> International Conference on Heat Transfer, Fluid Mechanics and Thermodynamics, Mauritius, 11-13 July 2011.
3. 'Control and operation of a SDR', 22<sup>nd</sup> International Symposium on Chemical Reaction Engineering, Maastricht, the Netherlands, 2-5 September 2012.

### *Publications*

1. Ghiasy, D., K.V.K. Boodhoo, and M.T. Tham (2012) 'Control of intensified equipment: A simulation study for pH control in a spinning disc reactor' *Chemical Engineering and Processing: Process Intensification*, **55**, pp.1-7.
2. Ghiasy, D., K.V.K. Boodhoo, and M.T. Tham (2012) 'Thermographic analysis of thin liquid films on a rotating disc: Approach and challenges' *Applied Thermal Engineering*, **44**, pp.39-49.
3. Ghiasy, D., K.V.K. Boodhoo, and M.T. Tham (2012) 'Control of a Spinning Disc Reactor' Submitted to *Chemical Engineering*.